Data-driven Models and Computational Frameworks for Physically Informed Design of Compositionally Complex Alloys

Doctoral Thesis

by

Dishant Beniwal

(2021MMZ0005)

DEPARTMENT OF METALLURGICAL AND MATERIALS ENGINEERING

INDIAN INSTITUTE OF TECHNOLOGY ROPAR

June, 2024

Data-driven Models and Computational Frameworks for Physically Informed Design of Compositionally Complex Alloys

A Thesis Submitted

In Partial Fulfillment of the Requirements

for the Degree of

DOCTOR OF PHILOSOPHY

by

Dishant Beniwal

(2021MMZ0005)

DEPARTMENT OF METALLURGICAL AND MATERIALS ENGINEERING

INDIAN INSTITUTE OF TECHNOLOGY ROPAR

June, 2024

Dishant Beniwal: *Data-driven Models and Computational Frameworks for Physically Informed Design of Compositionally Complex Alloys*

Copyright © 2024, Indian Institute of Technology Ropar

All Rights Reserved

DEDICATED

TO

The wonders that dwell within the computational world.

And the minds that dream free and wild.

Declaration of Originality

I hereby declare that the work which is being presented in the thesis entitled '*Data-driven Models and Computational Frameworks for Physically Informed Design of Compositionally Complex Alloys*' has been authored by me. It presents the results of my own independent investigation/research conducted during the time period from *January 2022* to *January 2024* under the supervision of *Dr. Pratik K. Ray (Assistant Professor, Dept. of Metallurgical and Materials Engineering, IIT Ropar)*. To the best of my knowledge, it is an original work, both in terms of research content and narrative, and has not been submitted or accepted elsewhere, in part or in full, for the award of any degree, diploma, fellowship, associateship, or similar title of any university or institution. Further, due credit has been attributed to the relevant state-of-the-art and collaborations with appropriate citations and acknowledgments, in line with established ethical norms and practices. I also declare that any idea/data/fact/source stated in my thesis has not been fabricated/falsified/misrepresented. All the principles of academic honesty and integrity have been followed. I fully understand that if the thesis is found to be unoriginal, fabricated, or plagiarized, the Institute reserves the right to withdraw the thesis from its archive and revoke the associated Degree conferred. Additionally, the Institute also reserves the right to appraise all concerned sections of society of the matter for their information and necessary action. If accepted, I hereby consent for my thesis to be available online in the Institute's Open Access repository, inter-library loan, and the title & abstract to be made available to outside organizations.

Name: Dishant Beniwal

Entry Number: 2021MMZ0005

Program: PhD

Department: Metallurgical and Materials Engineering

Indian Institute of Technology Ropar

Rupnagar, Punjab 140001

Date: 11 June 2024

Certificate

This is to certify that the thesis entitled '*Data-driven Models and Computational Frameworks for Physically Informed Design of Compositionally Complex Alloys*', submitted by *Dishant Beniwal (Entry No.: 2021MMZ0005)* for the award of the degree of '*Doctor of Philosophy*' of Indian Institute of Technology Ropar, is a record of bonafide research work carried out under my guidance and supervision. To the best of my knowledge and belief, the work presented in this thesis is original and has not been submitted, either in part or full, for the award of any other degree, diploma, fellowship, associateship or similar title of any university or institution. In my opinion, the thesis has reached the standard fulfilling the requirements of the regulations relating to the Degree.

Dr. Pratik K. Ray

Department of Metallurgical and Materials Engineering

Indian Institute of Technology Ropar

Rupnagar, Punjab 140001

Date: 11 June 2024

Acknowledgement

This thesis marks the culmination of years of hard work and sincere efforts by not just me, but many individuals who made my doctoral research journey an extremely fulfilling and enriching experience. First and foremost, I express my deepest gratitude to Dr. Pratik Ray who, through his constant guidance and encouragement, has been the single most important force behind everything that I could achieve during my doctoral research. His profound knowledge and passion for all research made for amazing discussions that led me to pursue a broad range of problems that I may not have explored otherwise. His introductions and recommendations opened the doors to many collaborations and achievements, including the Prime Minister's Research Fellowship, and his work ethics have been a constant inspiration. He has been a friend, a mentor and a role model like no other, and I couldn't have dreamed of a better research supervisor to guide me on my doctoral journey.

I am deeply indebted to Dr. Ashish Sahani as I was introduced to the field of machine learning through his wonderful course on 'Applied Machine Learning'. Looking back at my journey, the decision to take his course (which happened serendipitously during discussion with Dr. Pratik Ray) was a defining moment. Dr. Sahani is a prolific researcher and entrepreneur, and is amongst the best teachers that I have ever studied from. His contributions to my growth extend far beyond the classroom teaching and I will always look up to him with admiration for a gem of a person that he is.

I would like to thank all of my research collaborators at Iowa State University and Ames Laboratory, USA who contributed at different stages in this thesis. It was wonderful to work with Dr. Duane Johnson and Dr. Prashant Singh, both of whom are well-renowned experts in DFT. Their contributions added new dimensions to our hardness prediction work. Dr. Prashant Singh also created the dataset for SRO model and discussions with him were always uniquely insightful and full of new ideas. I would like to sincerely thank Dr. Matthew Kramer and Ms. Olena Palasyuk at Ames Lab for their support in the development of EDS-PhaSe software as well as in the experimental work. Dr. Kramer's immense knowledge, impeccable attention to details and exceptional clarity of thought has been inspiring for me.

I would like to thank Dr. Gandham Phanikumar at IIT Madras who graciously allowed me to spend a month at his lab to work on induction melting and thermodynamic modelling. I vividly remember the research discussions held with them that spanned so many different research areas. I am also thankful to his PhD students, V S Hariharan and Ajith, who helped me with the experiments and made my stay at IIT Madras a wonderful experience. I would

like to thank Dr. Vikas Shivam, who was initially a postdoc at our lab at IIT Ropar and later joined CSIR-NML Jamshedpur, as we collaborated on multiple problems. In fact, it was our collaboration on studying the effect of Zn addition that sowed the seeds for development of EDS-PhaSe software and Cu addition experimental work that formed an integral part of this thesis. He is an excellent researcher and a wonderful human being, and it was a pure joy to work with him.

I am very thankful to my entire doctoral committee at IIT Ropar, which comprised Dr. Ravi Mohan Prasad, Dr. Neha Sardana, Dr. Khushboo Rakha and Dr. Srikant Padhee, for their continuous support, guidance and suggestions. I am indebted to Dr. Srikant Padhee for introducing me to atomistic modelling through his course and for his recommendations that contributed immensely to my professional growth. I am deeply thankful to Mr. Amit Kaushal who taught me how to operate the SEM and to Dr. Harpreet Singh who allowed me independent access to the SEM. This contributed immensely to my learning and enabled the microscopy work carried out in this thesis. I am thankful to the Department of Metallurgical and Materials at IIT Ropar and the IIT Ropar itself for allowing me to pursue my doctoral research there. I am thankful to the Prime Minister's Research Fellowship Scheme by Govt. of India which financially supported my PhD research.

I am extremely thankful to the past and present IDEAs Lab members at IIT Ropar – Jhalak, Santosh, Sagarika, Rudraksha, Ashish and Shrish, all of whom have been wonderful friends and a constant support throughout my PhD journey. I am also thankful to all the fellow PhD research scholars at the Department of Metallurgical and Materials Engineering, IIT Ropar who made for a wonderful work environment, excellent discussions and amazing memories that I will carry with me for life.

Last, but in no way the least, I am truly indebted to my wife Jhalak, who is also a fellow researcher, for her unwavering support through every phase of my life. She has been a best friend, an amazing companion and a wonderful human being and I am blessed to have her as my better half. I am deeply indebted to my parents and my sister who never questioned and always encouraged every life decision that I have ever taken, including the decision to enroll for a doctoral program. Their blessings and lessons have made me whatever I am today.

It's when writing this acknowledgement that the feeling truly sinks in as to how wonderful these last few years have been and that how blessed I have been.

Lay Summary

Alloys are created by mixing different elements together to improve overall properties. For many centuries, alloys have been created by first selecting a main element and then adding secondary elements to modify the properties. For example, superalloys use nickel as main element with titanium and aluminium as secondary additions for strength, and stainless steels use iron as main element with chromium as secondary addition for corrosion resistance. It was a long-held belief that mixing too many different elements together in large amounts will lead to brittle alloys that will not be useful for engineering applications. But in 2004, Prof. Brian Cantor and Prof. Jien-Wei Yeh showed that it is possible to make alloys with excellent properties by mixing five or even more elements in high concentrations. This discovery started the field of compositionally complex alloys (CCAs), which is a general name to denote alloys that have a lot of elements mixed in high concentration, and over the last 20 years, many CCAs have been discovered that show much better properties than the traditional alloys. So how does one select which elements should be mixed, and in what concentrations, to create a CCA! At first thought, this may seem trivial as one might say – why not study all the possible combinations? But, to achieve this, we would need to make more than 10^{100} alloys. To put some context as to how large this number is, imagine if every living person on earth starts making 1000 alloys every second, then in 100 years from now we would have only 10^{21} alloys. Thus, the only way to overcome this is to use theoretical calculations, computer simulations or data-driven models to predict which compositions can give good properties and to then make only those handful of alloys for further study. This is the main motivation of this thesis wherein we have developed machine learning models that can generate rapid predictions for CCAs and can thus identify compositions where either we obtain the best properties or where we see sudden changes in the properties. Since machine

learning models are quite complex and don't speak the same language as us, we have developed interfaces that, in principle, ask specific questions to these models and observe their response to build an understanding of how they function. We have also synthesized some unique and interesting alloys in our lab and analyzed their structure using microscopy to understand how elements interact with each other when they are mixed together. Thus, this thesis presents novel methodologies, models and results that shed new light on the design of CCAs.

Abstract

Compositionally complex alloys (CCAs), containing large number of elements in high concentrations, represent an astronomical design space that can span more than 10^{100} possible compositions. The properties of CCAs can be improved significantly via compositional and microstructural tuning; but the traditional methodologies i.e., experimental alloy design and ab initio calculations are not suitable for efficient exploration of CCAs owing to their vast design space. Thus, machine learning (ML) has taken a center stage in recent years and various ML models have been reported for the exploration of CCAs. But these are often treated as a black box that offers no physical insights into the decision-making process of the trained models. In this thesis, we have developed interpretation frameworks, machine learning models and computational tools that enable targeted and physically informed exploration of CCAs. To address the black-box nature of ML models, two approaches have been implemented. Firstly, a neural network based ML has been reduced into a simpler and fundamentally interpretable mathematical model that can predict the probability of occurrence of FCC and BCC phases in CCAs. Secondly, a novel model-agnostic Compositional-Stimulus and Model-Response (CoSMoR) framework has been developed to extract exact contribution of individual features. CoSMoR establishes the physical consistency of the nature of fit and provides material-specific specific insights into the decision-making process. We have also developed ML models for the prediction of short-range order (SRO) and hardness in CCAs and have validated them over a variety of complex alloy systems through comparison with *ab-initio* and experimental results wherein they reliably capture the linear, non-linear and non-monotonic changes in hardness and SRO as a function of alloy composition. We have also carried out experimental studies on CoCrNi ternary, CoCrCuNi quaternary and CoCrCuNi-M quinary alloys to probe the

effect of strong ordering and clustering binary pairs on the overall phase evolution. The strong and contrasting binary pair interactions encountered in these alloys provide a good test bed for not only validating but for also finding the limits of the ML models. To support our experimental studies and to address the challenges faced in identification and quantification of phases during microstructural characterization of CCAs using SEM-EDS data (especially when phase contrast is missing in SEM images), we have developed EDS-PhaSe software that performs phase segmentation and analysis through quantitative analysis of EDS elemental maps. All feature generation programs, trained ML models and interpretation routines developed as part of this thesis have been packaged as an open-source Python library (MAPAL).

List of Publications out of Thesis

Journal publications

1. **D Beniwal**, P Singh, S Gupta, MJ Kramer, DD Johnson, PK Ray, *Distilling physical origins of hardness in multi-principal element alloys directly from ensemble neural network models*, **npj Computational Materials**, 8, 153 (2022)

2. **D Beniwal** and PK Ray, *FCC vs. BCC phase selection in high-entropy alloys via simplified and interpretable reduction of machine learning models*, **Materialia**, 26, 101632 (2022)

3. **D Beniwal** and PK Ray, *CoSMoR: Decoding decision-making process along continuous composition pathways in machine learning models trained for material properties*, **Physical Review Materials**, 7, 043802 (2023)

4. **D Beniwal**, V Shivam, O Palasyuk, MJ Kramer, G Phanikumar, PK Ray, *EDS-PhaSe: Phase segmentation and analysis from EDS elemental map images using markers of elemental segregation*, **Metallography, Microstructure, and Analysis**, 12 (2023) 924-933.

5. **D Beniwal**, S Tripathi, P Singh, N Sardana, PK Ray, *Predicting short-range order in compositionally complex alloys using variational autoencoders*, **Under preparation**

6. **D Beniwal** and PK Ray, *MAPAL: A python library for mapping features and properties of alloys over compositional spaces*, **Under preparation**

7. **D Beniwal**, PK Ray et al., *Phase evolution in CoCrCuNi-M alloys in presence of strong ordering and clustering binary pairs*, **Under preparation**

Book chapters

1. **D Beniwal**, Jhalak, PK Ray, *Data-driven phase selection, property prediction and force-field development in Multi-Principal Element Alloys*, In: A Verma, SM Rangappa, S Ogata, S Siengchin (eds) Forcefields for Atomistic-Scale Simulations: Materials and Applications. Lecture Notes in Applied and Computational Mechanics, vol 99. Springer, Singapore (2022)

Conference presentations

1. **D Beniwal**, PK Ray, *CoSMoR: A model-agnostic interpretation framework to extract exact feature contributions along continuous composition pathways in machine learning models trained for material properties*, **IIM-ATM 2022**, Hyderabad, India, Nov 2022.

2. **D Beniwal**, PK Ray, *Extracting physical insights from compositional machine learning models trained for predicting material properties*, **ASATM**, Nanyang Technological University, Singapore, Jan 2023.

3. **D Beniwal**, PK Ray, *Materials informatics for physically informed design of multi-principal element alloys*, **ICAM^5**, NIT Warangal, India, Sept 2023.

4. **D Beniwal**, PK Ray, *Binary interactions as drivers of phase evolution in high-entropy alloys*, **IIM-ATM 2023**, Bhubaneswar, India, Nov 2023.

5. **D Beniwal**, PK Ray, *EDS PhaSe: Computational tool for phase segmentation and analysis from EDS elemental maps*, **iConFirm 2023**, IIT Ropar, India, Dec 2023.

Table of contents

Acknowledgement ..... **ix**
Lay Summary ..... **xi**
Abstract ..... **xiii**
List of Publications out of Thesis ..... **xv**
List of Tables ..... **xxi**
List of Figures ..... **xxiii**

Chapter 1 : Introduction **1**
1.1 Data-driven approach to materials science 2
1.1.1 Databases 3
1.1.2 Feature engineering 6
1.1.3 Training and validation of ML models 8
1.1.4 Machine learning algorithms 10
1.2 Data-driven models for phase selection in CCAs 11
1.2.1 Parameter-based phase selection 11
1.2.2 Inferring phase selection using Machine Learning 16
1.3 Data-driven models for mechanical behaviour of CCAs 18
1.4 Data-driven models for predicting ordering in CCAs 21
1.5 Research gaps and motivation 24
1.6 Outline of the thesis 25

Chapter 2 : Reduced mathematical model for FCC vs BCC phase selection in compositionally complex alloys **27**
2.1 Introduction 27
2.2 Development of machine learning models 29
2.3 Development of Reduced Mathematical (RM) model 32
2.3.1 Dataset for RM model 32
2.3.2 Reduced mathematical representation of ML models 33
2.3.3 Optimization and performance of reduced mathematical model 35
2.4 Feature contributions towards phase predictions 38
2.5 Exploring continuous composition variations 41

2.6 Conclusion 45
2.7 Research data 47

Chapter 3 : CoSMoR – Compositional-Stimulus and Model-Response framework to extract physical insights from machine learning models 49
3.1 Introduction 49
3.2 Methodology for development of CoSMoR 52
3.3 Implementation of CoSMoR 55
3.4 Phase selection in compositionally complex alloys 57
3.4.1 Development of ML models 57
3.4.2 Phase variations in M_x-$(CoCrFeNi)_{1-x}$ 58
3.4.3 Decoding the decision-making process in M_x-$(CoCrFeNi)_{1-x}$ 60
3.4.4 Exploring Fe_x-$(AlCoCr_{0.5}Ni_{2.5})_{1-x}$ and $(TaNb)_x$-$(MoW)_{1-x}$ alloy systems 64
3.5 Use case scenarios for CoSMoR 66
3.5.1 Evaluating the nature of fit 66
3.5.2 Revealing the drivers of change 67
3.6 Conclusion 70
3.7 Research data 72

Chapter 4 : Predicting short-range order in compositionally complex alloys using variational autoencoders 73
4.1 Introduction 73
4.2 Quantification of SRO 74
4.3 Development of the SRO database 75
4.4 Machine learning framework 76
4.4.1 Alloy representation as a binary-pair feature stack 76
4.4.2 Variational autoencoder: Architecture and training 77
4.5 Model performance and validation 80
4.5.1 Cross-validation performance 80
4.5.2 Exploring SRO as a function of composition 81
4.5.3 CoSMoR: Insights into decision-making process of ML model 83
4.6 Automated workflow for model improvements 86
4.7 Conclusions 87

Chapter 5 : Distilling physical origins of hardness in compositionally complex alloys directly from ensemble neural network models 89

5.1 Introduction 89

5.2 Development of ML models 92

5.2.1 Database for ML model development 92

5.2.2 Feature engineering and model architecture 94

5.2.3 Machine learning model training 98

5.2.4 Predictions using ensemble model 101

5.3 Methodology – ab-initio calculations and experiments 102

5.3.1 Density Functional Theory Calculations 102

5.3.2 Linear-response Theory for Short-Range Order 102

5.3.3 Experimental Methods 103

5.4 Results and discussion 103

5.4.1 Model validation 104

5.4.2 Prediction of non-linear trends in Hardness 104

5.4.3 Experimental validation in the Al-Ti-Zr-Hf alloy system 109

5.4.4 Physical insights from decision-making process of the ML model 111

5.5 Conclusions 115

5.6 Research data 117

5.7 Supplementary data 117

Chapter 6 : Phase evolution in CoCrCuNi-M alloys in presence of strong ordering and clustering binary pairs 119

6.1 Introduction 119

6.2 Methodology 122

6.2.1 Machine learning and Thermo-Calc calculations 122

6.2.2 Experimental characterization 123

6.2.3 EDS-PhaSe analysis 123

6.3 Results and discussion 124

6.3.1 Summary of Machine learning predictions 124

6.3.2 Thermodynamic framework for general analyses of the systems ..126

6.3.3 Baseline alloys: CoCrNi and CoCrCuNi 127

6.3.4 CoCrCuNi-Al 132

6.3.5 CoCrCuNi-Ti 135

6.3.6 CoCrCuNi-Zr 138
6.3.7 CoCrCuNi-Nb 141
6.3.8 CoCrCuNi-Mo 145
6.4 Conclusions 148

Chapter 7 : Conclusions and future outlook 151
7.1 Research summary and general conclusions 151
7.2 Future outlook 154

References 157

Appendix A: MAPAL: A python library for mapping features and properties of alloys over compositional spaces 179

Appendix B: EDS-PhaSe: Phase segmentation and analysis from EDS elemental map images using markers of elemental segregation 197

List of Tables

Table 1.1 List of parameter-based models developed for phase classification in CCAs [48], along with the description of parameters used and the performance of each model as measured by Tsai et al. [45] using degree of unbalance (DoU) and accuracy as metrics.....14

Table 1.2 List of ML based models for phase selection in CCAs along with the details of classification labels, dataset, features and algorithms used in the model training [48]. The accuracy of each model is also mentioned. 19

Table 1.3 List of ML based models for prediction of mechanical properties in CCAs along with details of target property, dataset, features, and algorithms used in the model training [48]. The accuracy of each model is also mentioned, wherever available.....22

Table 2.1 Mathematical expressions of alloy features used for development of machine learning model.....31

Table 4.1 Description of nine features used to create the binary feature stack shown in Figure 4.2. The feature values for all binary pairs were calculated assuming an equiatomic concentration i.e., cA=cB=0.5 78

Table 5.1 Cross-validation performance summary of ANNs with different architectures trained on various feature sets. Here, ...98

Table 5.2 ANN architectures used in the work 99

Table 5.3 Feature-sets used in this work for training ML models 99

List of Figures

Figure 1.1 A schematic representation of the multi-modal nature of data required for materials informatics 6

Figure 1.2 Key aspects of feature engineering. (a) A schematic heat map of correlation coefficient matrix showing relationship between different features (X_i) and target parameter (Y). (b) Pair of features that show high collinearity. (c) Pair of features that show low collinearity. (d) A schematic dendrogram showing hierarchical clustering of features based on their collinearity. 8

Figure 1.3 Schematic for: (a) training and validation of machine learning models, (b) K-fold cross-validation methodology, and (c) selection of optimal model while preventing underfit or overfit. 9

Figure 1.4 Overview of the machine learning model developed by Beniwal and Ray for phase selection in CCAs [19]. 16

Figure 2.1 Overview of machine learning framework used for the development of machine learning models. Two separate neural network models were trained – first for prediction of FCC phase and second for prediction of BCC phase. The input layer represents seven alloy features (listed in Table S2) and the output layer has 1 unit representing probability of occurrence of a phase (FCC or BCC). "ReLU" stands for rectified linear unit activation function. 30

Figure 2.2 Feature correlation: Pair plots of features used in this work. The linear-regression lines and Pearson's correlation coefficient (R) values have been shown in the pair-plots above the diagonal. 32

Figure 2.3 Distribution of ML predicted phases in the datasets used for fitting and validation of RM models. 33

Figure 2.4 Mathematical functions used for isolating the effect of VEC on phase stabilities. (a) Logistic function used to model the dependence of FCC and BCC occurrence probability on VEC. (b) Skew-normal function of VEC used to model the peak residuals obtained after logistic fit of phase probabilities wrt VEC. 34

Figure 2.5 Model parameters and performance of optimized RM model. (a1) FCC phase occurrence probabilities predicted by optimized RM model vs. NN model, (a2) Optimized logistic function for P(FCC) model, (a3) Optimized skew-normal function for P(FCC) model, (b1) BCC phase occurrence probabilities predicted by optimized RM model vs. NN model, (b2) Optimized logistic function for P(BCC) model, (b3) Optimized skew-normal function for P(BCC) model. 36

Figure 2.6 Performance of reduced mathematical (RM) model over validation dataset 37

Figure 2.7 Confusion matrix for RM model predictions of (a) FCC and (b) BCC class labels for 35 new alloys that were not present in the training dataset. (c) Precision, Recall and F-1 score for each class. 37

Figure 2.8 Feature contributions. (a) Weight-factors (βi) of each feature in RM model, (b) stacked frequency density plots of the contributions made by each feature towards $P(FCC)^{RM}$ and $P(BCC)^{RM}$, and (c) expressions for calculation of feature contribution values. Here, $P(Phase)^{NN}$ and $P(Phase)^{RM}$ is the phase occurrence probability predicted by NN and RM model, respectively; VEC is valence electron count, $\delta rmet$ is asymmetry in metallic radius, $\delta rcov$ asymmetry in covalent radius, δE is asymmetry in elastic modulus, $Ecoh$ is average cohesive energy, ΔHch is chemical enthalpy of mixing, and ΔHel is elastic enthalpy of mixing. 39

Figure 2.9 Plot of local mismatch in electronegativity vs. asymmetry in covalent radius over all the alloys present in experimental dataset 40

Figure 2.10 Performance of reduced mathematical (RM) model created without including chemical enthalpy and elastic enthalpy features. The exclusion of these features has no significant effect on the model performance. 40

Figure 2.11 Parameters of the reduced mathematical model created without including chemical enthalpy and elastic enthalpy features. The feature coefficients are very similar to those observed when both these features are included. 41

Figure 2.12 Comparing NN vs. reduced mathematical (RM) model predictions and feature contributions over continuous composition pathways in (a) $Al_x(CoCrFeNi)_{1-x}$, (b) $Ti_x(CrFeNi)_{1-x}$ and (c) $Mo_x(TaTiWZr)_{1-x}$. At any composition

x, feature contribution value represents exact contribution made by that feature towards the overall phase occurrence probability predicted in RM model i.e., $P(Phase)^{RM}$. In (a1, b1, c1), compositional regions with different predicted phases have been mapped at the top axes for both NN and RM models; here F is FCC and B is BCC.....42

Figure 2.13 Mathematical expressions for FCC and BCC occurrence probability obtained from symbolic regression models. 44

Figure 2.14 Performance of (a) FCC and (b) BCC model developed using symbolic regression (SR). The SR models, similar to RM models, were developed to replace the trained ML models and same fitting dataset of 4719 compositions (as used for RM models) was used to develop SR models.....45

Figure 2.15 Performance of (a) FCC and (b) BCC symbolic regression model on validation dataset comprising 2002 alloy compositions (this dataset is same as that used for validation of RM models).....45

Figure 3.1 Methodology used in CoSMoR to extract exact feature contributions along a compositional pathway. (a) Calculation of local partial dependence ($\delta Y/\delta X_i$) of target property Y with respect to feature X_i at any composition *c*. (b) Calculation of individual feature contributions towards change in phase probability for each one composition step i.e., as composition changes from $c \rightarrow c+\Delta c$. (c) Calculation of cumulative feature contributions along a continuous composition pathway wherein the initial concentration is treated as baseline. 55

Figure 3.2 Flowchart showing implementation of CoSMoR. The function blocks with purple outline and text (namely, '*create_features*' and '*make_predictions*') are the user-defined functions whereas rest of the functions are in-built in the 'cosmor' code. 57

Figure 3.3 Probability of occurrence of FCC, BCC and IM phases as predicted by machine learning models in M_x-$(CoCrFeNi)_{1-x}$ alloy systems. Phase probabilities as a function of (a) Al, (b) Cu, (c) Mn, (d) Mo, and (e) Ta addition in CoCrFeNi alloy. A phase probability (P) threshold of 0.5 has been used to indicate the presence of a particular phase, and correspondingly each plot has been divided into green and red regions representing $P \geq 0.5$ (i.e., phase presence) and $P < 0.5$ (i.e., phase absence) respectively. Predicted phase

transition boundaries have also been highlighted above the top-axis of each plot, along with the experimentally observed phases at some discrete compositions. The green dotted line (x=0.2) in each plot represents the equiatomic quinary composition. 60

Figure 3.4 Interpreting the decision-making process of phase selection ML models using CoSMoR. Cumulative contribution of each feature towards the overall phase probability P(phase) in (a-c) Al_x-$(CoCrFeNi)_{1-x}$, (e-g) Cu_x-$(CoCrFeNi)_{1-x}$ and (i-k) Mn_x-$(CoCrFeNi)_{1-x}$ alloy systems. Normalized feature values as a function of (d) Al, (h) Cu and (l) Mn concentration. The feature contributions here are cumulative contributions along the composition pathway with respect to baseline composition of x=0. 62

Figure 3.5 Interpreting the decision-making process of phase selection ML models using CoSMoR. Cumulative contribution of each feature towards the overall phase probability P(phase) in (a-c) Mo_x-$(CoCrFeNi)_{1-x}$ and (e-g) Ta_x-$(CoCrFeNi)_{1-x}$ alloy systems. Normalized feature values as a function of (d) Mo and (h) Ta concentration. The feature contributions here are cumulative contributions along the composition pathway with respect to baseline composition of x=0. 64

Figure 3.6 Interpreting the decision-making process of phase selection ML models using CoSMoR. Cumulative contribution of each feature towards the overall phase probability P(phase) in (a-c) Fe_x-$(AlCoCr_{0.5}Ni_{2.5})_{1-x}$ and (e-g) $(TaNb)_x$-$(MoW)_{1-x}$ alloy systems. Normalized feature values as a function of (d) Fe and (g) (TaNb) concentration. The feature contributions here are cumulative contributions along the composition pathway with respect to baseline composition of x=0. 66

Figure 3.7 CoSMoR applied to random forest models for FCC, BCC and Intermetallic phase prediction in Al_x-$(CoCrFeNi)_{1-x}$, Mo_x-$(CoCrFeNi)_{1-x}$, Ta_x-$(CoCrFeNi)_{1-x}$. 70

Figure 4.1 Overview of the machine learning framework. (a) Alloy representation as a 2D array (shape 14x14) containing c_ic_j values for all i-j binary pairs in the alloy where ci and cj are atomic fractions of i and j element respectively. (b) Binary pairs feature stack (3D array of shape 14x14x9) compiled through layering of 9 feature arrays containing binary pair properties as shown in Figure 4.2. (c) Transformed feature stack obtained through

element-wise multiplication of each layer in binary pairs feature stack with alloy c_ic_j array. (d) Schematic representation of variational auto-encoder with a latent space dimension of 20. (e) Predicted SRO array for the alloy comprising SRO values for all i-j binary pairs. 78

Figure 4.2 Normalized binary-pair feature arrays that were used to create the three-dimensional binary pair feature stack (F) shown in Figure 4.1b. The 1-9 feature arrays shown here correspond to the 1-9 features listed in Table 4.1..79

Figure 4.3 Schematic architecture of the variational autoencoder model used in this work. It takes the transformed feature stack of shape (14, 14, 9) as input, encodes it to a latent vector of size 20 and maps it to the output SRO array of shape (14, 14, 1)....80

Figure 4.4 Data distribution and cross-validation performance. (a) Distribution of binary pair SRO values in DFT-based training dataset and cross-validation predictions from ML model. (b) Distribution of mean absolute error in cross-validation predictions. (c) Parity plot of ML predicted SRO (ML-SRO) vs. DFT predict SRO (DFT-SRO) for binary pairs with classification accuracy and mean absolute error (MAE) metrics. (d) Confusion matrix for ML-predicted ordering and clustering behaviour of binary pairs along with precision, recall and accuracy metrics. 81

Figure 4.5 Exploring SRO variation and ML-model decision-making process (using CoSMoR) as a function of composition. DFT calculated and ML predicted SRO values of binary pairs in (a) Ti_x-$(CrFeNi)_{1-x}$ and (b) Al_x-$(TiZrHf)_{1-x}$ alloy systems. Here, only the pairs that show highest ordering/clustering tendency have been shown for each system. Cumulative contribution of individual binary pairs towards ML-predicted SRO of (a1) Cr-Fe, (a2) Fe-Ni, and (a3) Ni-Ti binary pair in Ti_x-$(CrFeNi)_{1-x}$. Cumulative contribution of individual feature towards ML-predicted SRO of (a4) Cr-Fe, (a5) Fe-Ni, and (a6) Ni-Ti binary pair in Ti_x-$(CrFeNi)_{1-x}$. Cumulative contribution of individual binary pairs towards ML-predicted SRO of (a1) Al-Ti, (a2) Hf-Zr, and (a3) Ti-Zr binary pair in Al_x-$(TiZrHf)_{1-x}$. Cumulative contribution of individual feature towards ML-predicted SRO of (a4) Al-Ti, (a5) Hf-Zr, and (a6) Ti-Zr binary pair in Al_x-$(TiZrHf)_{1-x}$. 83

Figure 4.6 Automated workflow for ML model development wherein models can be automatically retrained as and when new data is available. The green

highlighted region indicates all the processes that are automated. The red pathways indicate instances where some user intervention is required. 86

Figure 5.1 Overview of the methodology used for extracting origins of hardness: (a) CCAs hardness database development and calculation of alloy features, (b) training of neural network ensemble, (c) exploration of hardness over wide compositional spaces, (d) model interrogation to extract exact feature contributions along continuous composition pathways, (e) DFT results to probe ordering behaviour and structure stabilities, (f) experimental validation over complex alloy systems, and (g) analyzing the results to establish physical origins of hardness. 93

Figure 5.2 Dataset exploration and model validation. (a) Statistical distribution of hardness values for eight different type of crystal structures present in the dataset along with number of alloys, mean hardness, median hardness, 1.5 IQR and 25%-75% percentile range for each structure. (b) Distribution of hardness values in the training dataset (218 alloys) along with mean, median and 10%-90% percentile range of hardness. (c) Distribution of hardness values in the testing dataset (58 alloys) compiled from recent literature. (d) Parity plot of hardness predictions obtained for test dataset along with statistical performance metrics –root mean square error (RMSE), mean absolute error (MAE) and average percentage error. The shaded area represents an 80% accuracy region and the number at top right corner represents fraction of predictions with > 80% accuracy. 94

Figure 5.3 List of all the calculated features along with their mathematical expression and their Pearson's coefficient of correlation with hardness.....96

Figure 5.4 Ten shortlisted features along with their correlation coefficient with hardness and plots (a-j) of hardness vs. each shortlisted feature. Linear regression lines have been plotted along with R^2 in each plot. Data points have been color-coded based on number of phases present. 97

Figure 5.5 Significance of depth of ANNs. Parity plot for hardness predictions obtained using: (a) ANN1 and FS1, (b) ANN2 and FS1, and (c) Linear Regression (least squares). (d) Probability density of the absolute error about the MAE for predictions obtained through all three. 100

Figure 5.6 Improvement factor of (a) ANN2/ANN6 trained with different feature sets, and (b) ANNs with different architectures trained with FS2 feature-set. 101

Figure 5.7 ML predictions of hardness and corresponding formation enthalpy and SRO obtained from DFT calculations. (a) Predicted hardness contours for $Al_xTi_y(CrFeNi)_{1-x-y}$. (b) Inset shows the hardness contours in Al-poor and Ti-poor regions, along with composition trajectories along which hardness measurements and predictions are compared. (c) Experimental and ML-predicted hardness for $Ti_x(CrFeNi)_{1-x}$ with a 90% prediction-interval (PI). (d) Formation energy of the BCC alloy and (e) Pairwise SRO in $Ti_x(CrFeNi)_{1-x}$. (f) Experimental and ML-predicted hardness for $Al_xTi_y(CrFeNi)_{1-x-y}$ with a 90% prediction-interval (PI). (g) Formation energy of the BCC solid solution and (h) Pair SRO and dominant ordering pairs in $Al_xTi_y(CrFeNi)_{1-x-y}$ 107

Figure 5.8 ML predictions of hardness and corresponding DFT-predicted formation enthalpy and SRO. (a) Predicted hardness contours for $Hf_xCo_y(CrFeNi)_{1-x-y}$ system, with (b) showing an expanded view of the compositions from experiments by Ma and Shek[225]. (c) Experimental and ML-predicted hardness for $Hf_x(CoCrFeNi)_{1-x}$ alloys with a 90% prediction-interval (PI). (d) DFT formation energies showing the relative stabilities of the BCC and FCC structures. (e) DFT SRO and the main ordering and clustering pairs present 109

Figure 5.9 ML hardness predictions and corresponding DFT-predicted formation enthalpy and SRO. (a) Predicted hardness contours for $Al_xTi_y(ZrHf)_{1-x-y}$ system. (b) Experimental and ML-predicted hardness for $Al_x(TiZrHf)_{1-x}$ alloys with a 90% prediction-interval (PI). (c) DFT energy calculations shows the relative stabilities of the BCC and HCP structures. (d) DFT SRO pairs show the ordering and clustering tendencies. (e) DFT and XRD densities compared for the HCP, BCC (vacancy-stabilized) and disordered BCC (without vacancy) phases. 110

Figure 5.10 Visualizing the decision-making process of ML model. Contribution of different features toward ML hardness prediction in: (a) $Al_x(CrFeNi)_{1-x}$, (b) $Ti_x(CrFeNi)_{1-x}$, (c) $Hf_x(CoCrFeNi)_{1-x}$, and (d) $Al_x(TiZrHf)_{1-x}$ alloy systems. At any composition (x), the hardness contribution of each feature is equal to the vertical distance between that feature contribution plot and the baseline hardness value (calculated at x=0). At any x, the summation of baseline

hardness and all feature contributions will result in overall hardness. (e) Feature variations with respect to composition for alloy systems shown in (a-d). Normalized feature values have been plotted here. Feature notations: VEC-Valence electron concentration, δ_{cov}-asymmetry in covalent radius, ρ-average density, δ_E-asymmetry in Young's modulus, δ_G-asymmetry in shear modulus, ΔH^{chem}-chemical enthalpy of mixing, ΔH^{el}-elastic enthalpy of mixing. Features that had negligible contribution to hardness prediction over these composition ranges have not been included in the plots. 113

Figure 6.1 (a) Design methodology indicating the baseline compositions and the rationale for selection of alloying elements. (b) Miedema's chemical (ΔH^{chem}) and elastic ($\Delta H^{elastic}$) interaction parameters representing enthalpy change (in kJ) associated with the addition of 1 mole of solute A into an infinite amount of solvent B. ΔH^{sol} is the sum of both ΔH^{chem} and $\Delta H^{elastic}$. 122

Figure 6.2 (a) Phase fraction of FCC, BCC and Intermetallic (IM) phases as predicted by ML model along continuous composition variations in M_x-$(CoCrCuNi)_{1-x}$ alloys. (b) ML predicted Vicker's hardness in M_x-$(CoCrCuNi)_{1-x}$ alloys. (c) Comparing ML predicted and experimentally measured hardness of equiatomic alloys CoCrNi, CoCrCuNi and CoCrCuNi-M. Here, M includes {Al, Ti, Zr, Nb, Mo}. 125

Figure 6.3 Thermo-Calc predicted phase fractions in CoCrNi ternary as a function of temperature. 128

Figure 6.4 SEM-EDS results of CoCrNi. 128

Figure 6.5 XRD pattern and Rietveld-refined structures for CoCrNi ternary. 129

Figure 6.6 Thermo-Calc predicted phase fractions in CoCrCuNi quaternary as a function of temperature. 130

Figure 6.7 SEM-EDS and EDS-PhaSe results of CoCrCuNi alloy along with the phase information. The quantitative analysis of EDS data and subsequent phase segmentation was done using EDS-PhaSe [235] software that was developed as part of this thesis (Appendix B). 131

Figure 6.8 XRD pattern and Rietveld-refined structures for CoCrCuNi equiatomic quaternary. 131

Figure 6.9 Thermo-Calc predicted phase fractions in CoCrCuNi-Al equiatomic quinary as a function of temperature. 133

Figure 6.10 SEM-EDS and EDS-PhaSe results of CoCrCuNi-Al alloy along with the phase information. The quantitative analysis of EDS data and subsequent phase segmentation was done using EDS-PhaSe [235] software that was developed as part of this thesis (Appendix B) 134

Figure 6.11 XRD pattern and Rietveld-refined structures for CoCrCuNi-Al equiatomic quinary. 134

Figure 6.12 Thermo-Calc predicted phase fractions in CoCrCuNi-Ti equiatomic quinary as a function of temperature. 137

Figure 6.13 SEM-EDS and EDS-PhaSe results of CoCrCuNi-Ti alloy along with the phase information. The quantitative analysis of EDS data and subsequent phase segmentation was done using EDS-PhaSe [235] software that was developed as part of this thesis (Appendix B). 137

Figure 6.14 XRD pattern and Rietveld-refined structures for CoCrCuNi-Ti equiatomic quinary 138

Figure 6.15 Thermo-Calc predicted phase fractions in CoCrCuNi-Zr equiatomic quinary as a function of temperature. 140

Figure 6.16 SEM-EDS and EDS-PhaSe results of CoCrCuNi-Zr alloy along with the phase information. The quantitative analysis of EDS data and subsequent phase segmentation was done using EDS-PhaSe [235] software that was developed as part of this thesis (Appendix B). 140

Figure 6.17 XRD pattern and Rietveld-refined structures for CoCrCuNi-Zr equiatomic quinary 141

Figure 6.18 Thermo-Calc predicted phase fractions in CoCrCuNi-Nb equiatomic quinary as a function of temperature. 143

Figure 6.19 SEM-EDS and EDS-PhaSe results of CoCrCuNi-Nb alloy along with the phase information. The quantitative analysis of EDS data and subsequent phase segmentation was done using EDS-PhaSe [235] software that was developed as part of this thesis (Appendix B). 144

Figure 6.20 XRD pattern and Rietveld-refined structures for CoCrCuNi-Nb equiatomic quinary 144

Figure 6.21 Thermo-Calc predicted phase fractions in CoCrCuNi-Mo equiatomic quinary as a function of temperature. 147

Figure 6.22 SEM-EDS and EDS-PhaSe results of CoCrCuNi-Mo alloy along with the phase information. The quantitative analysis of EDS data and subsequent phase segmentation was done using EDS-PhaSe [235] software that was developed as part of this thesis (Appendix B). 147

Figure 6.23 XRD pattern and Rietveld-refined structures for CoCrCuNi-Mo equiatomic quinary 148

Chapter 1: Introduction

Compositionally complex alloys (CCAs) contain large number of principal elements, often five or more, in high concentrations. While various terminologies are associated with these alloys, such as High-Entropy Alloys (HEAs), multi-principal element alloys (MPEAs) and complex concentrated alloys, the central idea remains the same i.e., to explore the alloys in/around the center of multicomponent phase diagrams such that all the constituent elements are present in sufficiently high amounts (≥ 5 atomic %). Contrary to the traditional viewpoint that mixing of multiple elements in high concentrations would lead to formation of complex and brittle microstructures, in 1980s, Prof. Brian Cantor started experimenting with mixing up to 20 elements and observed the surprising formation of a single-phase structure in five-component equiatomic CoCrFeMnNi. In 2004, research groups led by Prof. Brian Cantor and Prof. Jien-Wei Yeh reported formation of simple solid-solution (SS) phases in various equiatomic alloys wherein the stability of SS phases was attributed largely to the high configurational entropy of mixing [1,2]. This new alloy design paradigm led to an explosion in research on CCAs resulting in discovery of various alloy systems with unique and promising properties. While the initial interest in CCAs was focused on finding systems that form simple SS phases, over the years it has branched into various domains involving the study of structure-property correlations, deformation mechanisms, alloy processing routes and short-range ordering behaviour [3–11].

The major challenges associated with exploration of CCAs are – a) an astronomical compositional space [8] (spanning more than 10^{100} unique compositions) that cannot be explored efficiently using time-intensive experimental route or ab-initio calculations, and b) a multitude of inter-atomic interactions (due to the presence of multiple elements in high concentrations) that need to be estimated accurately for computational modelling of CCAs. Over the last decade, data-driven models have evolved as a promising avenue for addressing these challenges. While the initial efforts (2007-2016) focused on the development of empirical and semi-empirical models to guide the phase selection in CCAs, the last few years (2018 onwards) have seen a significant shift towards the use of machine learning (ML) for exploring a broad range of aspects of CCAs such as phase selection, mechanical behaviour, corrosion behaviour and ordering behaviour.

This chapter introduces the fundamental concepts of data-driven methodologies for training and validation of ML models, followed by a review of the data-driven models and alloy design paradigms that have been developed for exploring CCAs over the last decade.

1.1 Data-driven approach to materials science

Since ages, science has relied on theoretical and empirical frameworks to understand how our physical reality works. A theoretical approach relies on an underlying theory, mathematical framework and/or hypothesis to depict a reality which may then be validated through observations. On the contrary, an empirical approach is data-centric and explores the intricate dependencies and correlations that are hidden within the observed data to gain new insights about our reality. With the advent of computer age, the data-driven approaches have gained prominence due to the – (a) significant increase in the availability and accessibility of scientific data, (b) development of improved computer algorithms for processing and analyzing the data, and (c) exponential increase in computing power that drives the implementation of complex algorithms over large datasets. Thanks to the efforts of the entire computer science

community in providing open-source tools and extensive documentation, the key developments in artificial intelligence and machine learning (ML) have now spread to various science and engineering domains. Specific to materials science, we now have a dedicated field of materials informatics that applies the principles of data science, AI and ML for the discovery and development of materials. While the type and complexity of data-driven models may change from one problem to another, the key motivations that lie at the heart of every data-driven approach include – (a) interpolation and extrapolation of trends in existing data to predict behavior of new systems, (b) understanding cause-effect relationships to develop rules or principles that link causality with observed outcomes, and (c) development of theoretical or semi-empirical frameworks that are guided by the trends identified within the data while also aligning with the underlying physical principles and theories. We will briefly discuss next the various aspects of data collection, feature engineering, model training and validation, and ML algorithms that are associated with development of ML models for materials science.

1.1.1 Databases

Gathering and storing of data lies at the core of any data-driven approach. In general, a database represents structured storage of information that can be read by machines (and often humans also). Every database follows some schema for organizing the information in a way that makes it readily accessible and can take many different forms based on the type and amount of information to be stored. Some typical examples are: a) relational databases that comprise of linked tables wherein primary keys link data within a table and foreign keys link one table with another table, b) hierarchical databases that categorize data in multiple levels using parent-child linkages, c) network databases that are similar to hierarchical databases but with additional flexibility that allows linking of children with multiple parents, and d) NoSQL databases that do not use the traditional table-based storage model and instead provide flexible schema to store data in different formats such as document databases (json objects), key-value databases or graph databases. While the

above methodologies are well suited for large scale projects involving multiple teams, it is often easier to run smaller personal projects using one's own schema for managing the data, for example – a) using excel or csv files for storing tabular data, and b) maintaining directories and files linked to an index list as a pointer.

Materials data is highly multi-modal in nature with a large variation in both the scope and the type of data. This makes the curation of materials datasets an extremely difficult task. For example, consolidating the multi-modal information such as tabular data, XRD patterns, SEM-EDS images, TEM images, electron diffraction patterns and temporal oxidation curves together is no easy task; that too when there are no clear standards on how the data is reported. Despite that, even before the age of modern AI and ML, many efforts were made to consolidate materials information. Notable amongst these are crystallographic databases (Pearson's Crystal Data, Crystallography Open Database, ICDD database) and material handbooks (ASM handbooks, Springer Handbook of Materials Data). While these have been immensely useful in guiding materials research, they have some key limitations. The crystallographic databases are limited primarily to tasks that involve retrieval, solution or refinement of structures such as in XRD peak analysis, Rietveld refinement or creation of structures for ab initio calculations. The materials handbooks on the other hand contain a wide variety of data including thermodynamic data, phase diagrams, microstructures and diffusion coefficient. But the major problems are – a) the content is not easily machine readable and thus its integration with modern data analytics and machine learning tools is difficult, and b) they are not exhaustive enough to cover all materials or applications, especially the new and upcoming ones. In recent years, web scraping and text-mining has been used to convert unstructured experimental data present in scientific articles into structured datasets that can be then used for materials informatics [12–16]. Moreover, for problems where the available data is relatively sparse (such as high-entropy alloys), researchers have manually extracted datasets from literature [17–19]. Computational approaches, especially DFT-based *ab-initio* methods, provide another avenue

for generating materials data and contrary to experimental data, it is much easier to conform to well defined schema that is essential for large scale datasets. Thus, the last decade has witnessed remarkable efforts by various consortiums around the globe towards building open-source materials databases using ab-initio calculations. Some noteworthy mentions include Materials Project [20], AFLOW [21,22] , Open Quantum Materials Database (OQMD) [23,24] and NOMAD [25]. Since these databases contain DFT-calculated information for compounds only, they do have a limitation in their application to metals and alloys where one frequently deals with solid solutions. Thus, for building data-driven approaches for such systems, the best option is to collect information from published literature, either manually or through combined use of web scraping and text-mining. The recent introduction of large language models offers some unique opportunities in automating this task and can pave the way forward for building structured experimental datasets for materials science.

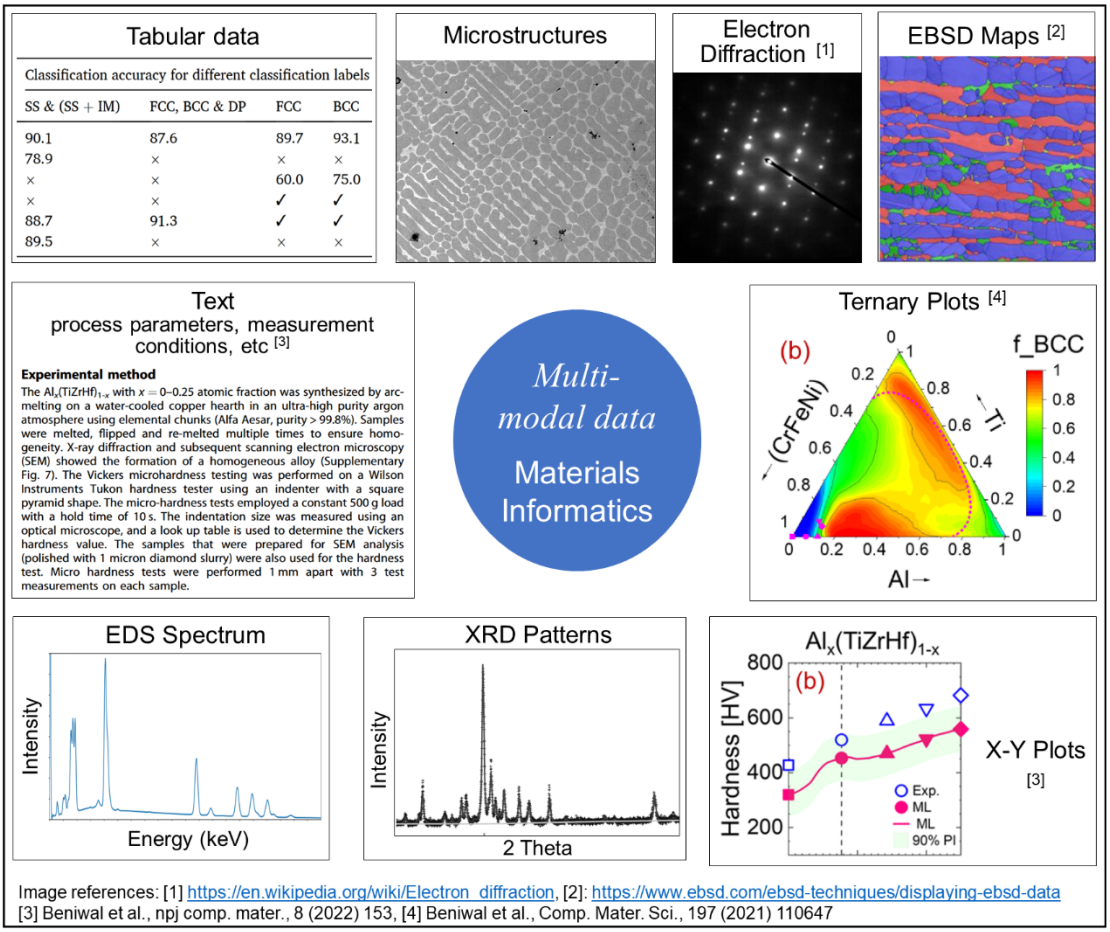

Image references: [1] https://en.wikipedia.org/wiki/Electron_diffraction, [2]: https://www.ebsd.com/ebsd-techniques/displaying-ebsd-data
[3] Beniwal et al., npj comp. mater., 8 (2022) 153, [4] Beniwal et al., Comp. Mater. Sci., 197 (2021) 110647

Figure 1.1 A schematic representation of the multi-modal nature of data required for materials informatics

1.1.2 Feature engineering

The term 'features' in context of ML models is synonymous to term 'independent variables' in the context of a mathematical function. Features act as the input for ML model wherein the ML algorithm then maps them to the output that is being predicted; similar to how a mathematical function y=f(x) maps the independent variable (x) to a dependent variable (y). Thus, the ML model essentially learns the dependencies between the input features and the model output. The features can be either numerical (continuous or discrete number values) or categorical (discrete values belonging to groups). The choice of features depends on the problem at hand. For example, suppose we are interested in predicting the strength of an alloy wherein one would need to capture the effects of composition, processing route and microstructural characteristics. The processing route can be a categorical feature that can be handled in two different ways. The first option is to use a single feature that takes discrete values based on the route, e.g. as-cast=1, heat-treated=2, rolled=3. Second option is to define a separate Boolean feature for each of the possible routes and these will individually take a value of 1 or 0 based on whether that route was followed or not. The microstructure may be defined using features such as phase fractions, phase compositions and geometrical parameters for size and shapes of phases. The composition, in simplest way, may be incorporated using concentration of each element as a separate feature. From many theoretical frameworks developed over the years, we know that composition can have several effects such as solid-solution strengthening, internal strain generation, intermetallic formation and phase transitions that may affect the strength. When we use composition directly as a feature, we are assuming that the ML model will be able to learn all of these dependencies directly. But that is not possible due to the missing pieces of information such as atomic sizes, electronegativities, interaction parameters and valency that are not available to the ML model. Thus, it is always beneficial to convert composition into physical and thermodynamic features that capture various

aspects of the alloying process and are closely linked to the output property that is being predicted. This process is akin to integrating domain knowledge into the ML model to ensure that the model learning captures the underlying physics and is not merely statistical in nature.

Before building any ML model, it is always advantageous to study the correlation between the various features and target variables present in the database. A correlation matrix is a table that expresses the correlation coefficients between variables and thus helps in visualizing the dependencies present in the data (especially if these dependencies are linear), as shown in Figure 1.2a. Pearson's [26] and Spearman's [27] correlation coefficients are the most commonly used correlation metrics. Both these coefficients can vary between -1 to +1 wherein a value of +1 or -1 indicates perfect linear relationship, positive and negative values represent direct and inverse relation respectively, and zero implies no correlation. Pearson's correlation is a measure of the linear relationship between features and assumes that the features are normally distributed, whereas Spearman's correlation is a measure of monotonicity of relationship between two features and does not assume normal distribution of features. Both Pearson's and Spearman's correlation are used only for continuous variables. If we have a binary variable, a 'point biserial' correlation coefficient [28] may be used to measure the relationship between a binary variable and a continuous variable.

Multicollinearity between features is another important aspect of the database that must be probed before building ML models as it can have a significant impact on the perceived importance of a feature and thereby may lead to an incorrect interpretation of the learning. Multicollinearity occurs due to the presence of two or more variables in the database that are highly correlated to each other, as shown in Figure 1.2(b, c). This happens often due to the introduction of dependent variables that are a function of already existing independent variables in the dataset. There are generally two ways to root out multicollinear features: a) through a detailed study of correlation matrix and feature maps, and b) through hierarchical clustering of features and creation of

a dendrogram (Figure 1.2d) that groups collinear features based on a distance matrix [29].

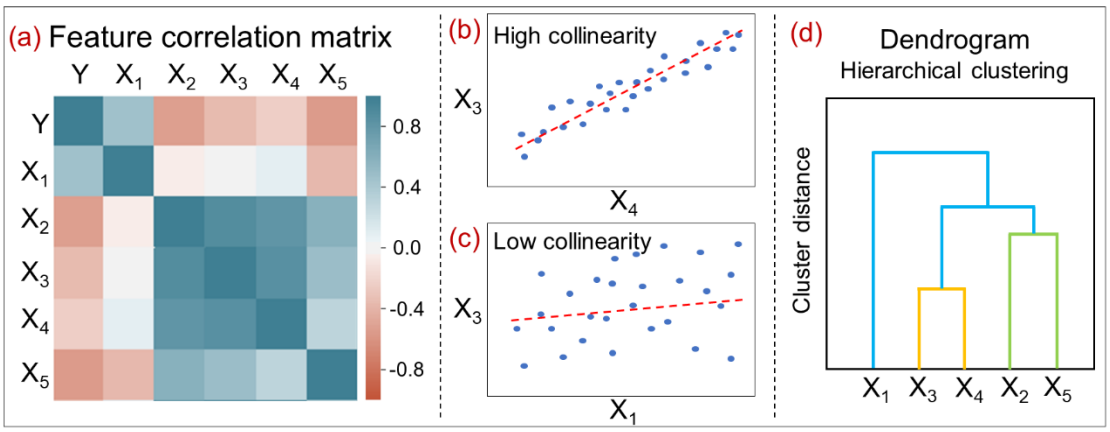

Figure 1.2 Key aspects of feature engineering. (a) A schematic heat map of correlation coefficient matrix showing relationship between different features (X_i) and target parameter (Y). (b) Pair of features that show high collinearity. (c) Pair of features that show low collinearity. (d) A schematic dendrogram showing hierarchical clustering of features based on their collinearity.

1.1.3 Training and validation of ML models

All ML frameworks operate with an underlying hypothesis that the target property is fundamentally associated with the features being used as an input for the model; and thus, the training process estimates these dependencies based on the relationships that are captured in the dataset. This approach has been used extensively in building ML models for predicting various properties and behaviour of materials (including CCAs) [30–34]. Figure 1.3a shows the schematic representation of training and validation process in development of ML models. While building ML models, the dataset is generally divided into two parts – training and test set. The training set is used to train the model whereas the test set is used to evaluate the model. The deviation of a model from actual data is evaluated using a loss function that captures the error between predicted and actual output. The form of loss function can vary depending on the type of problem; for example, regression problems generally use mean absolute error or mean square error as the loss function whereas a log-loss function is used for classification problems. The training of ML model refers to the process of modifying the ML model parameters in order to minimize this loss function. This is done iteratively using optimizer functions

that update the model parameters in each iteration using loss values. The extent of modification that an optimizer can do in each iteration is controlled coarsely using a learning rate parameter. Depending on the size of the dataset, the training to test split generally ranges from 80:20 to 50:50. For sparse datasets, a better approach is to use K-fold cross validation that ensures that the model is exposed to all data points at least once, as shown in Figure 1.3b. During the training process, both training and test loss are monitored as a function of iterations, and the best-performing model is generally selected based on the minimization of test loss, as shown in Figure 1.3c. For non-deterministic ML models such as neural networks, that can show high variance based on different initialization conditions, use of ensemble models is often desirable. An ensemble comprises of multiple models that provide independent predictions for the same input which are then clubbed to get an average or median prediction as the final output.

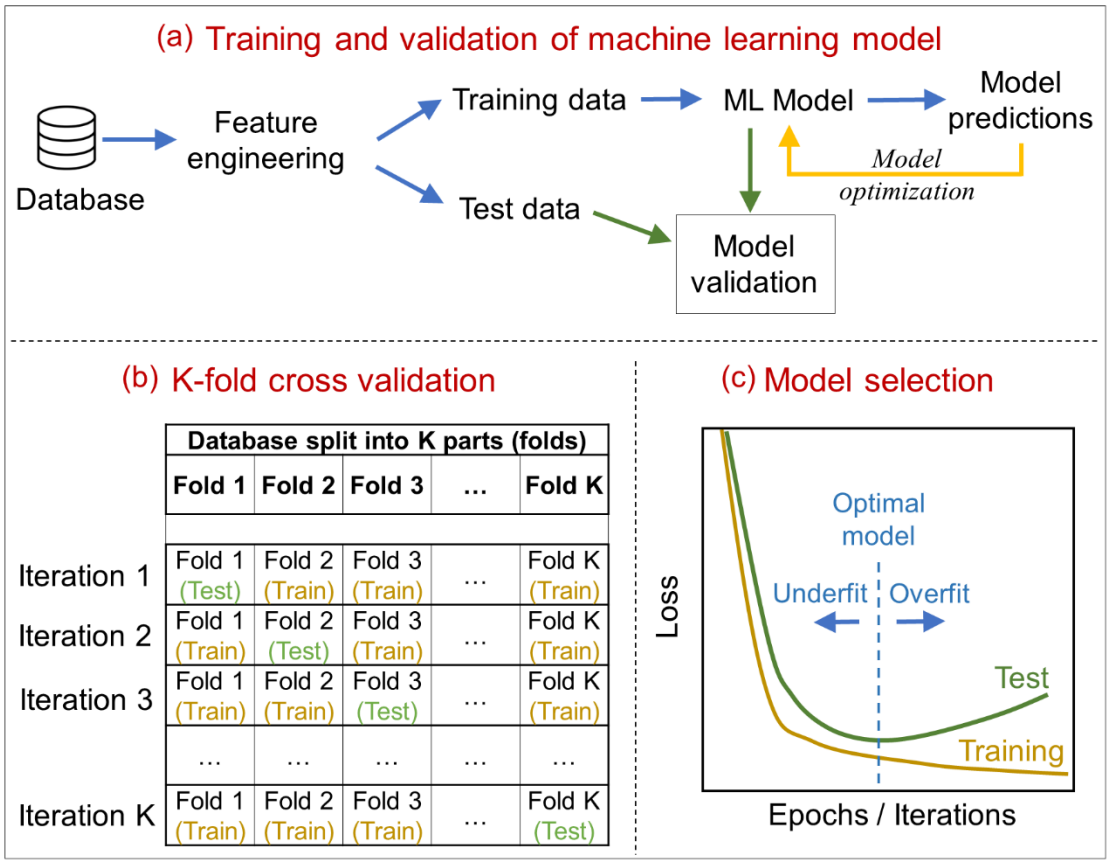

Figure 1.3 Schematic for: (a) training and validation of machine learning models, (b) K-fold cross-validation methodology, and (c) selection of optimal model while preventing underfit or overfit.

1.1.4 Machine learning algorithms

While all ML methodologies are aimed at identifying relationships hidden in the data in one way or another, these are broadly classified into three categories: a) Supervised learning – a target (output) variable is predicted from a set of descriptors (inputs) through generation of a function that maps inputs to target, b) Unsupervised learning – there is no specific target variable, but instead inherent dependencies between variables are exposed through different techniques such as clustering of population into groups, and c) Reinforcement learning – the model is trained to make specific decisions in such a way that it trains itself continuously through exposure to an environment wherein it is rewarded and punished from desired and undesired predictions respectively.

Some of the commonly used ML algorithms include linear regression, logistic regression, decision tree, support vector machine (SVM), naïve-bayes, k-nearest neighbours (kNN), K-Means clustering, random forest, gradient boosting and neural networks [35]. Amongst all these algorithms, neural networks have gained significant attention in the recent years due to their capability to: a) learn both linear and non-linear relationships in data, b) adapt to various kinds of input data structures like structured tables, images with spatial relationships, signals with temporal relationships and videos with both spatial and temporal relationships, and c) perform both regression and classification tasks with extremely high accuracy. But despite these advantages, neural networks suffer from their lack of interpretability since it is difficult to make out the exact decision-making process learnt by the model. To address this, there are some methodologies that have been adopted to impart interpretability or explainability to these models [36–39]. The choice of algorithm is often dictated by three factors: a) the type of decision boundaries that are to be learnt, b) the type of task i.e., regression or classification and the nature of target variable, and c) the amount of interpretability desired from the trained model.

1.2 Data-driven models for phase selection in CCAs

They physical properties of an alloy are strongly dependent on the phases present, and thus, a targeted alloy design approach requires prior knowledge of the phases that will form in an alloy. This becomes a challenge for CCAs since the mixing of different elements can result in a variety of single-phase or multi-phase microstructures containing solid solution (SS) phases and Intermetallics (IM). Thus, the phase selection in CCAs has been by-far the most explored problem and numerous data-driven methodologies have been implemented over the years to address it. These approaches have been classified into two categories here: a) parameter-based approaches wherein a single or combination of parameters have been used to draw phase classification boundaries, and b) ML-based approaches wherein a group of features have been used to train ML algorithms for phase prediction.

1.2.1 Parameter-based phase selection

Since the initial interest in CCAs was focused around finding alloys with simple SS phases, a major portion of the earlier work in data-driven phase selection was centered around two key classifications: a) whether the alloy will form only simple SS phases, only IM phases or a combination of both! and b) whether the structure of SS phase will be FCC or BCC!

<u>Predicting formation of simple-solid-solution vs. intermetallic phases</u>: The empirical and semi-empirical rules for predicting the formation of SS and IM phases in CCAs are generally based on two types of parameters: a) thermodynamic parameters such as configurational entropy of mixing (ΔS_{mix}) and mixing enthalpy (ΔH_{mix}), and b) lattice distortion parameters such as size asymmetry, strain energy and geometric packing state. The configurational entropy of mixing is calculated as: $\Delta S_{mix} = -R\sum_{i=1}^{n} c_i \ln c_i$, where R is the universal gas constant and c_i is the concentration of ith element. The enthalpy of mixing is calculated using Takeuchi's extended regular solution model [40] as: $\Delta H_{mix} = \sum_{i=1,\ i\neq j}^{n} 4\Delta H_{ij}^{mix} c_i c_j$, where ΔH_{ij}^{mix} is the mixing enthalpy of equiatomic binary *i-j* calculated using Miedema's model [41,42]. While various

improvements have been proposed for ΔH_{mix} calculations in ternary systems [43,44], they are yet to be extended to multi-component alloys. Table 1.1 lists the existing parameter-based models for predicting formation of simple SS phases in CCAs along with the performance of each model as reported by Tsai et al. [45] in a recent study. These rules lay out the conditions under which only simple SS phases will be observed i.e., outside these regions IM phases are predicted to appear in the alloy. While a variety of parameters are used in these rules, the key underlying principles comprise: a) high ΔS_{mix} stabilizes the SS phases, b) large negative ΔH_{mix} drives compound formation and a large positive ΔH_{mix} leads to clustering, c) large asymmetry in atomic sizes destabilizes the SS phases due to introduction of lattice strains, and d) presence of atomic-pairs with high intermetallic formation tendency (i.e., high $\Delta H_{IM}/\Delta H_{mix}$ ratio) promotes appearance of IM phases. Here, we refer to ordering as the tendency of elements to mix with each other, in a periodic manner (at least locally) and clustering as the tendency for elements to segregate away from each other forming elemental clusters in case of binary systems. It is important to note that while these rules give some general insights into SS vs. IM stability in CCAs, the performance of these parameter-based models is not very good as they exhibit low accuracy and high degree of unbalance, as seen in Table 1.1. This is primarily due to: a) the simplistic nature of these rules as they utilize only a few parameters that are insufficient to directly capture all of the physics associated with the alloying process, and b) the small size of datasets used to formulate these rules. To overcome this, ML based phase prediction models have gained significant attention in recent years and have been discussed in the next section.

<u>FCC/BCC structure prediction</u>: In 2011, Guo et al. [46] proposed Valence Electron Count (VEC) as a criterion for delineating the stability of FCC and BCC SS wherein VEC ≥ 8, ($6.7 \leq$ VEC < 8) and VEC<6.87 results in formation of FCC, (FCC+BCC) and BCC SS phases respectively. This simple rule has stood the test of time and has been reinforced in numerous later works wherein VEC appears as the single most important factor in determining BCC vs. FCC stability. But, at the same time, it is important to point out two limitations of this rule: a) it

cannot explain FCC/BCC stability variations in systems wherein VEC remains constant for e.g., Fe_x-$(AlCoCr_{0.5}Ni_{2.5})_{1-x}$ [47], and b) there are exceptions to the bounds of 6.7 and 8 put on VEC since these have been estimated statistically and do not represent strict absolute boundaries for FCC/BCC stability. Recently, Beniwal and Ray [19] identified electronegativity (χ_{Allen}) and cohesive energy (E_{coh}) as additional parameters to guide identification of FCC vs. BCC stability domains based on binary-feature maps. They reported an improved empirical classification criterion: BCC (VEC < 6.8 and E_{coh} > 3.55 eV), FCC (VEC > 8 and E_{coh} < 5.25 eV) and BCC + FCC (6.8 < VEC < 8 and 3.55 eV < E_{coh} < 5.25 eV).

Table 1.1 List of parameter-based models developed for phase classification in CCAs [48], along with the description of parameters used and the performance of each model as measured by Tsai et al. [45] using degree of unbalance (DoU) and accuracy as metrics

Model Ref.	**Criterion**	**Description of parameters**	**Performance** [45]	
			DoU	**Accuracy**
Yang and Zhang, 2012 [49]	$\Omega \geq 1.1$ & $\delta_r \leq 0.066$	$\Omega = T_m \Delta S_{mix}/\Delta H_{mix}$ $\delta_r = \sqrt{\sum_{i=1}^{n} c_i \left(1 - \frac{r_i}{\bar{r}}\right)^2}$ where, T_m and $\bar{r}$ are average melting temperature and average atomic radius respectively obtained using rule-of-mixture; c_i is the concentration of ith element; and n is the number of elements in alloy $\Delta S_{mix} = -R \sum_{i=1}^{n} c_i \ln c_i$ $\Delta H_{mix} = \sum_{i=1,\ i\neq j}^{n} 4\Delta H_{ij}^{mix} c_i c_j$ where, ΔH_{ij}^{mix} is the mixing enthalpy of equiatomic binary *i-j* calculated using Miedema's model [41]	83%	48%
Guo et al., 2013 [50]	$-11.6 < \Delta H_{mix} < 3.2$ kJ mol^{-1} & $\delta_r < 0.066$	$\Delta H_{mix} = \sum_{i=1,\ i\neq j}^{n} 4\Delta H_{ij}^{mix} c_i c_j$ $\delta_r = \sqrt{\sum_{i=1}^{n} c_i \left(1 - \frac{r_i}{\bar{r}}\right)^2}$ where, ΔH_{ij}^{mix} is the mixing enthalpy of equiatomic binary *i-j* calculated using Miedema's model [41], $\bar{r}$ is average atomic radius obtained using rule-of-mixture; c_i and r_i is the concentration and radius of ith element; and n is the number of elements in alloy	53%	61%
Wang et al., 2015 [51]	$-11.6 < \Delta H_{mix} < 3.2$ kJ mol^{-1} & $\gamma < 1.175$	$\gamma = \omega_S/\omega_L$ $\omega_S = (1 - \sqrt{((r_S + \bar{r})^2 - \bar{r}^2)/(r_S + \bar{r})^2})$ $\omega_L = (1 - \sqrt{((r_L + \bar{r})^2 - \bar{r}^2)/(r_L + \bar{r})^2})$ where, r_S and r_L are the radii of smallest and largest atoms in alloy	10%	54%
Singh et al., 2014 [52]	$\Lambda > 0.96$	$\Lambda = \Delta S_{mix}/{\delta_r}^2$ $\Delta S_{mix} = -R \sum_{i=1}^{n} c_i \ln c_i$ $\delta_r = \sqrt{\sum_{i=1}^{n} c_i \left(1 - \frac{r_i}{\bar{r}}\right)^2}$	-38%	63%

Model Ref.	Criterion	Description of parameters	Performance [45]	
			DoU	Accuracy
		where, $\bar{r}$ is average atomic radius obtained using rule-of-mixture; c_i and r_i is the concentration and radius of ith element; and n is the number of elements in alloy		
Ye et al., 2015 [53]	$\phi \geq 20$	$\phi = (\Delta S_{mix} - S_H)/\lvert S_E \rvert$ $S_H = \lvert \Delta H_{mix} \rvert / T_m$ where, S_E is the excess configurational entropy of mixing [54]	-23%	61%
Troparevsky et al., 2015 [55]	$-T_{ann}\Delta S_{mix} < \Delta H_f <$ 3.57 meV/atom	ΔH_f is the formation enthalpy (ΔH_{ij}^{IM}) of most stable binary IM compound (i-j) possible in alloy. ΔH_{ij}^{IM} values for various i-j pairs were calculated by authors using DFT calculations.	-45%	72%
Senkov & Miracle, 2016 [56]	$\kappa_1^{cr} > \Delta H_{IM}/\Delta H_{mix}$	$\kappa_1^{cr} = T_m \Delta S_{mix}(1-\kappa_2)/\lvert \Delta H_{mix} \rvert$ $\kappa_2 = 0.6$ (assessed using a sub-lattice model)	-12%	72%
King et al., 2016 [57]	$\Phi \geq 1$	$\Phi = -\Delta G_{SS}/\lvert \Delta G_{max} \rvert$ $\Delta G_{SS} = \Delta H_{mix} - T_m \Delta S_{mix}$ where, ΔH_{mix} includes chemical, elastic and structural contributions [41]; ΔG_{max} is the highest (segregation) or lowest (intermetallic) Gibbs free energy amongst all binary systems that are possible from elements constituting the alloy	-84%	63%

1.2.2 Inferring phase selection using Machine Learning

To overcome the limitations posed by parameter-based models, a large number of ML based models have been reported in recent years to predict phase selection in CCAs [19,58–65], as listed in Table 1.2. A majority of these models are directed towards predicting whether the alloy will contain only simple SS phases or if it will contain IM phases; and only a few models focus on the identification of crystal structure of SS phases [19,58,61]. The implementation of ML requires a database to start out with; and for phase selection, the database must contain phase information of each alloy obtained via. experimental characterization or first-principles calculations. The phase information is further encoded into integer labels, for e.g., (SS→0, SS+IM→1, and IM→2) or (FCC→0, BCC→1, and FCC+BCC→2), wherein these labels comprise the target space for model training. For a more exhaustive multi-label classification, the phase information can also be encoded as a 3-element binary vector as shown by Beniwal and Ray [19], wherein the vector-elements correspond to presence of FCC, BCC and IM phases, i.e., (FCC→[1,0,0], FCC+BCC→[1,1,0], FCC+BCC+IM→[1,1,1], and so on). Here, the model is trained to predict this 3-element binary vector for each alloy i.e., it predicts the probability of occurrence of each phase – FCC, BCC and IM. This approach allows a seven-label classification wherein both SS vs. IM and FCC vs. BCC classifications can be achieved without compromising the model accuracy [19], as shown in Figure 1.4.

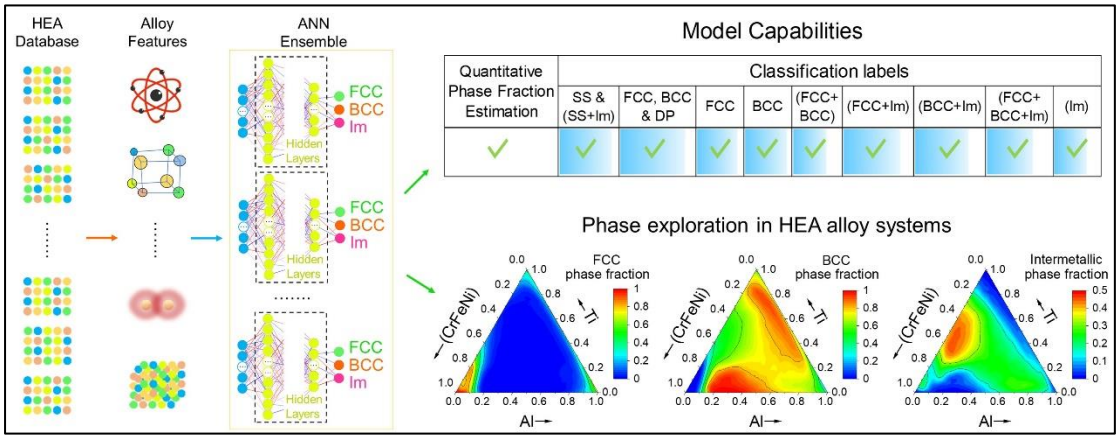

Figure 1.4 Overview of the machine learning model developed by Beniwal and Ray for phase selection in CCAs [19].

For ML implementation, each alloy is represented through a set of descriptors that capture the atomic, chemical, physical or thermodynamic information about the alloy. An extensive list of such descriptors for CCAs has been provided by Roy and Balasubramanian [66]. The features for ML model are selected based on their statistical correlation and physical relevance to alloy phase stability, and the parameter-based models discussed earlier provide a useful guide as to which descriptors are important for phase predictions. VEC, atomic size asymmetry, cohesive energy, enthalpy of mixing and entropy of mixing are amongst the most common features that appear repeatedly in ML models for phase prediction in CCAs.

Table 1.2 lists the various ML models, along with the information about dataset, features, algorithms, and performance, that have been developed over the last three years for predicting phase selection in CCAs. These models exhibit a considerably higher classification accuracy as compared to the parameter-based models listed in Table 1.1. This is primarily due to two reasons: a) the multi-dimensional nature of classification boundaries learnt by ML models due to the use of large number of features, and b) use of larger datasets which amounts to more training examples for the model to learn from. Through continuous improvements in the ML models, a large pool of material descriptors is now available for use as model features and the feature selection process is often carried out based on statistical correlation, intuitive physical significance and/or feature-importance study. A systematic study to identify the multi-collinearity and physical-overlapping of these features is still lacking.

The usual label classification approach only predicts presence/absence of a phase and does not give any idea about the quantitative phase fractions. In a recent work, Beniwal and Ray [19] proposed an approach wherein the predicted probabilities of occurrence of phases are treated as a measure of phase stabilities and are thereby transformed into phase fraction estimates. This was achieved this through a combined use of 3-element binary vectors, that capture phase information, along with a softmax function in the output layer

of the neural network that restricts the model outputs such that the summation of outputs (phase fractions) cannot exceed a value of 1. The ability of the model to capture both linear and non-linear variations in the phase fractions of FCC, BCC and IM phases, as a function of alloy composition, was demonstrated over a variety of CCAs through comparison with experimental and CALPHAD results [19].

1.3 Data-driven models for mechanical behaviour of CCAs

Since CCAs span an astronomical compositional space, the ability to predict mechanical properties is imperative for targeted alloy design. Various ML models, as listed in Table 1.3, have been reported in recent years for prediction of mechanical properties such as hardness, Young's Modulus and elastic constants [58,67–72]. Table 1.3 also presents details concerning the dataset, features, algorithm and performance for each model. In one of the earlier works, Chang et al. [68] developed a simple neural network model to predict the Vickers hardness of Al-Co-Cr-Cu-Fe-Mn-Mo-Ni containing alloy systems. They used elemental concentrations as the model inputs, which makes the implementation easy but renders the model unusable for probing alloy systems that are away from this 8-element space used to train the model. Thus, all future works have used a more robust and general modelling approach wherein the compositional inputs are replaced with composition-dependent physical and thermodynamic features that are relevant to alloy hardness. Since the hardness of an alloy is closely associated with the type of phases present, a significant overlap can be seen between the features that have been used for phase selection (Table 1.2) and hardness (Table 1.3) in CCAs. A variety of ML algorithms, as listed in Table 1.3, have been used to model the Vickers hardness, Young's modulus and elastic constants in CCAs using physical descriptors (such as radius asymmetry, melting temperature, density, elastic modulus asymmetry and VEC) and thermodynamic descriptors (enthalpy and entropy of mixing).

Table 1.2 List of ML based models for phase selection in CCAs along with the details of classification labels, dataset, features and algorithms used in the model training [48]. The accuracy of each model is also mentioned.

Model Ref.	**Classification Labels**	**Training Dataset**	**Features**	**ML algorithms**	**Classification Accuracy**
Islam et al., 2018 [59]	AM, SS, IM	Exp., 118 alloys	ΔH_{mix}, ΔS_{mix}, δ_r, VEC, $\Delta\chi$	Neural Network	83%
Huang et al., 2019 [60]	SS, SS+IM, IM	Exp., 401 alloys	ΔH_{mix}, ΔS_{mix}, δ_r, VEC, $\Delta\chi$	K-nearest neighbours, Support Vector Machine, Neural Network	SS vs. IM: 86.7% SS+IM vs. IM: 94.3% SS vs SS+IM: 78.9%
Li & Guo, 2019 [61]	FCC, BCC, NSP (Not forming Single Phase SS)	Exp., 322 alloys	ΔH_{mix}, ΔS_{mix}, δ_r, VEC, $\Delta\chi$, T_m	Support Vector Machine	BCC:60%; FCC:75%; NSP:98%
Zhou et al., 2019 [62]	AM, SS, IM	Exp., 601 alloys (binary, ternary & higher-order alloys)	ΔH_{mix}, ΔS_{mix}, δ_r, VEC, $\Delta\chi$, T_m, $\bar{r}$, $\bar{\chi}$, δ_{T_m}, ΔK, ΔVEC, $(\Delta H_{mix})_{LM}$, $\bar{K}$	Neural Network, Convolutional Neural Network, Support Vector Machine	AM:95.6% SS:97.8% IM:92.2%
Roy et al., 2020 [58]	FCC, BCC, FCC+BCC	Exp., 329 alloys	$\Delta\chi_{Pauling}$, ΔH_{mix}, ΔS_{mix}, δ_r, Λ, T_m, a_m, Ω, Δa, ΔT_m	Gradient Boost Classification	70%

Model Ref.	Classification Labels	Training Dataset	Features	ML algorithms	Classification Accuracy
Zhang et al., 2020 [63]	FCC, BCC, FCC+BCC, SS, NSS (Not forming SS)	Exp., 550 alloys	A total of 70 material descriptors used	Linear Discriminant Analysis, Decision Tree, Naïve Bayes Classification, Neural Network, Random Forest, Support Vector Machine	FCC, BCC, FCC+BCC: 88.7% SS, NSS: 91.3%
Jaiswal et al., 2021 [64]	FCC, BCC, FCC+BCC	Exp., 664 alloys	ΔH_{mix}, ΔS_{mix}, δ_r, VEC, $\Delta\chi$, T_m, $\bar{\chi}$, Ω	Logistic Regression, Random Forest, Support Vector Machine, Decision Tree, Gradient Boosting Decision Tree, Neural Network	86%
Lee et al., 2021 [65]	SS, IM, SS+IM, AM	Exp., 989 alloys	ΔH_{mix}, ΔS_{mix}, δ_r, VEC, $\Delta\chi$, T_m, $\bar{r}$, $\bar{\chi}$, δ_{T_m}, ΔK, ΔVEC, $(\Delta H_{mix})_{LM}$, $\bar{K}$	Deep Neural Network, Bayesian optimization, Generative Adversarial Network	SS: 89% SS+IM: 90% IM: 94% AM: 100%
Beniwal & Ray, 2021 [19]	FCC, BCC, FCC+BCC, FCC+IM, BCC+IM, FCC+BCC+IM, IM	Exp., 323 alloys	δ_r^{cov}, δ_r^{met}, ΔH_{mix}, ΔH_{el}, ΔS_{mix}, VEC, ρ, δ_E, δ_G, δ_K, $\bar{\chi}_{Allen}$, E_{coh}, $\delta_{E_{coh}}$, δ_{V_m}	Deep Neural Network Ensemble	FCC: 90%, BCC: 93%, FCC+BCC: 70%, FCC+IM: 82%, BCC+IM: 77%, FCC+BCC+IM: 71%, IM:71%

1.4 Data-driven models for predicting ordering in CCAs

The ordering behaviour of alloys represents the phenomenon where symmetry of the atomic arrangement is broken while the overall crystal structure remains the same. The extent of ordering in an alloy can be described through Warren-Cowley short-range order (SRO) parameter [73] α_l^{ij} that is defined as: $\alpha_l^{ij} = 1 - \frac{P_l^{i|j}}{c_i}$, where c_i is the concentration of atom i, and $P_l^{i|j}$ is the probability of finding atom i at the l-th neighbor for a given atom j. The α_l^{ij} value is calculated for multiple atomic configurations followed by an ensemble averaging. Thus, the SRO for a CCA is not a single value but is instead a matrix that contains one SRO parameter for each unique binary present in the alloy. Moreover, the SRO parameter of each binary-pair is affected not only by that binary itself but by all the atomic interactions that exist in a material simultaneously. Owing to the limited dataset and immense physical complexity associated with manifestation of SRO in CCAs, there is hardly any ML model in literature that attempts to predict it.

To bypass the complexities associated with multi-valued SRO matrix, Yin et al. [74] developed an alternative Variational Autoencoder (VAE)-based order parameter that compresses the ordering information into a single valued parameter. VAEs are based on 3D convolutional neural networks (CNNs) and allow encoding of the information into lower-dimensional latent variables in such a way that the data can be reconstructed through decoding process [75,76]. Their model input comprises a cubic lattice where the atoms sit at BCC lattice sites and each atom type was placed in a different channel. Each feature extraction (convolutional) layer, except for the final output layer, is followed by an average pooling layer. A dataset of 10^5 BCC-lattice based atomic configurations, comprising both ordered and disordered configurations, was generated using DFT-based Monte Carlo simulations at different temperatures; and an 80% to 20% split was used for training and testing respectively. Manhattan Distance metric [77], calculated in the VAE latent space, was used as an order parameter for order-disorder phase transitions which satisfies the

Table 1.3 List of ML based models for prediction of mechanical properties in CCAs along with details of target property, dataset, features, and algorithms used in the model training [48]. The accuracy of each model is also mentioned, wherever available.

Model Ref.	**Target Property**	**Training Dataset**	**Features**	**ML algorithms**	**Model Performance**
Chang et al., 2019 [68]	Vickers Hardness	Exp., 91 alloys	c_{el} $(el = Al, Co, Cr, Cu, Fe, Mn, Mo, Ni)$	Neural Network	R^2=0.94; MAE=36 HV
Rickman et al., 2019 [67]	Vickers Hardness	Exp., 82 alloys	ΔH_{mix}, ΔS_{mix}, δ_r, T_m, Ω, δ_E, VEC	Canonical-Correlation Analysis, Genetic Algorithm	-
Wen et al., 2019 [69]	Vickers Hardness	Exp., 155 alloys	ΔH_{mix}, ΔS_{mix}, δ_r, Ω, Λ, VEC, $\Delta\chi$, γ, $(\Delta\chi)_{LM}$, e/a, E_{coh}, η, $(\delta)_{LM}$, A, F, w, $\bar{G}$, δ_G, $(\Delta G)_{LM}$, μ	Linear Regression, Polynomial Regression, Support Vector Regression, Neural Network, K-nearest neighbour	Best Model: Support Vector Regression RMSE=68
Roy et al., 2020 [58]	Young's Modulus	Exp., 87 alloys	$\Delta\chi_{Pauling}$, ΔH_{mix}, ΔS_{mix}, δ_r, Λ, T_m, a_m, Ω, Δa, ΔT_m	Gradient Boost Regression	MAE = 36 GPa Avg. % Error=18.2%
Khakurel at al., 2021 [71]	Young's Modulus	Exp., Two datasets (154 & 96 alloys)	$\Delta\chi_{Pauling}$, ΔH_{mix}, ΔS_{mix}, δ_r, Λ, T_m, a_m, Ω, Δa, ΔT_m, VEC	Gradient Boosting, XGBoost, Random Forest, Ada Boost, Support Vector Regression, Regression (Lasso, Ridge & Gaussian)	Best Model: Gradient Boosting Only Refractory dataset: MAE=6.2 GPa, R^2=0.9 All dataset: MAE=10.4 GPa, R^2=0.71

Model Ref.	**Target Property**	**Training Dataset**	**Features**	**ML algorithms**	**Model Performance**
Revi et al., 2021 [70]	Elastic Constants	Materials Project, 1229 binary alloys	$\bar{r}$, $\bar{\chi}$, $\overline{IP}$, $\bar{\rho}$, VEC, T_m, $\bar{K}$, $\bar{C}$, $\bar{k}$, $\bar{v}$	Linear Regression, Random Forest, Neural Network	Best Model: Random Forest MAE=23.5 (DFT)/ 19.3 (Exp.)
Yang et al., 2022 [72]	Vickers Hardness	Exp., 370 alloys	VEC, T_m, Δm, ΔCol, ΔV	Support Vector Regression	RMSE=75 R^2=0.88

properties that: i) it should have non-zero values in ordered phase and approach zero in disordered phase, and ii) its second-order moment should peak at phase transitions. Yin et al. [74] applied this scalar VAE-based order parameter to study phase transitions in MoNbTaW, MoNbTaVW & $Al_xCoCrFeNi$ CCAs; and observed that even though it cannot capture all the physical information related to phase transitions, it has the capability of quantifying degree of ordering and phase-transition temperatures.

1.5 Research gaps and motivation

While various ML models have been reported for predicting phase selection and mechanical properties in CCAs, the aspects related to model interpretation and physical consistency of the model learning are often ignored. Moreover, while the primary aim of ML models for CCAs is to explore the vast compositional space, most reports only analyze the statistical performance over discrete compositions and don't probe deeper into how well the model learning interpolates or extrapolates along continuous compositional variations. We believe that these nuances are of utmost importance in establishing the reliability and applicability of ML models and thus, in this thesis, we will develop data-driven models and computational frameworks for CCAs with three key tenets: a) Firstly, we want to ensure that the ML models are not treated as black-box models and will thus develop methodologies that can impart physical meaning to the model learning, b) Secondly, we will develop ML models for SRO and hardness prediction in CCAs and will explore their variation over continuous compositional pathways while using the interpretation methodologies to extract physical insights, and c) Finally, we will experimentally study alloy compositions which show interesting and contrasting physics that can help in both validating as well as finding limitations of the ML models.

1.6 Outline of the thesis

Chapter 1 provides an introduction to materials informatics, reviews the current state of the art and contains brief description of data-driven methodologies including feature engineering, types of machine learning models and their training and validation process. It also lists key literature related to the data-driven exploration of phase selection, mechanical properties and ordering behavior in CCAs.

Chapter 2 builds on our prior work on phase selection [19] (not included in the thesis) and presents a mathematical model for FCC vs. BCC phase selection in CCAs that was developed through the reduction of complex neural network models into a significantly simpler and interpretable mathematical expression. This work presents a promising way for imparting interpretability to ML models through their reduction to simpler, but meaningful, frameworks.

Chapter 3 presents a novel model-agnostic **Co**mpositional-**S**timulus and **Mo**del-**R**esponse (CoSMoR) framework that can be applied to any composition-based ML model (irrespective of the algorithm used) to calculate the exact contribution of each feature towards the manifestation of target material property along a continuous compositional pathway. It showcases the capabilities of CoSMoR through its implementation on understanding phase selection in CCAs.

Chapter 4 presents a novel ML framework for predicting the short-range order in CCAs using variational auto-encoders that map a three-dimensional representation of all the binary interactions in an alloy to a two-dimensional SRO matrix containing Warren-Cowley SRO parameters for each unique binary. The model is further integrated with CoSMoR to extract contributions of binary pairs and physical features towards the manifestation of SRO in any given alloy system.

Chapter 5 presents a ML model for hardness prediction in CCAs that captures the essential physical and thermodynamic features contributing to hardness

and allows high-throughput exploration of multi-dimensional compositional space. The model is validated over diverse alloy systems that pose unique challenges due to the presence of ordering and clustering pairs, as well as vacancy-stabilized novel structures. The model is further integrated with CoSMoR to distill the physical origins of hardness in these alloys, as seen by the ML model.

Chapter 6 presents experimental studies on CoCrNi ternary, CoCrCuNi quaternary and CoCrCuNi-M quinary alloys to probe the effect of strong ordering and clustering binary pairs on the overall phase evolution. The strong and contrasting binary pair interactions encountered in these alloys provide a good test bed for not only validating but for also finding the limits of the hardness and phase selection models developed in earlier chapters.

Chapter 7 presents a concise summary as well as the future outlook for the research presented in this thesis.

Chapter 2: Reduced mathematical model for FCC vs BCC phase selection in compositionally complex alloys

2.1 Introduction

The exact quantitative rules governing phase stabilities in CCAs are not well-understood, despite a reasonable qualitative understanding, which poses a challenge for predicting phase stabilities and phase fractions in these systems. Traditionally, phase stability has been studied theoretically using a variety of techniques such as the CALPHAD method [78], DFT calculations [79] or even semi-empirical thermodynamics such as extended Miedema's model [80]. Each of these techniques have their own limitations – the CALPHAD approach is limited by the availability of a sufficiently extensive database; DFT calculations are inherently limited for solid solutions and are computationally expensive; Miedema's approach, though convenient, does not capture the entire physics and has relatively low accuracy compared to the other methods [81,82]. Of late, ML based approaches have endeavored to fill this gap [83–85]. While various ML models have been developed for phase prediction in CCAs [48,83,86–93], these suffer from a general lack of interpretability since the exact decision-making process is hidden. This limits the physical insights that can be obtained

---

This chapter has been published as a research article in 'Materialia'

D Beniwal and PK Ray, *FCC vs. BCC phase selection in high-entropy alloys via simplified and interpretable reduction of machine learning models*, **Materialia**, 26 (2022) 101632

DOI: https://doi.org/10.1016/j.mtla.2022.101632

from these models. Recently, explanatory model analysis techniques (such as Ceteris-Paribus profiles, breakDown analysis, SHapley Additive exPlanations and compositional-stimulus model-response study) have been applied to extract insights into the decision-making process of ML models for CCAs [37,72,94–96]. While these approaches do not make the ML models more interpretable by design, they do enable extraction of important physical insights from trained models based on local and global sensitivity of the model. An alternative data-driven approach is symbolic regression (SR) that creates fundamentally interpretable models by searching the space of mathematical expressions to identify a mathematical model that best fits the given dataset [38,97–101]. Since the formulation of best-fit model in SR is driven primarily by the statistical metrics, the final model form is often susceptible to be unrepresentative of any physical phenomenon. As an alternative to these approaches and with the aim of building a mathematical expression for occurrence probability of FCC and BCC phases in CCAs, here we present a mathematical reduction of physics-based and data-driven neural network (NN) models that were trained to predict the probability of occurrence of FCC and BCC phases in CCAs. The reduced model imparts interpretability through quantification of feature contributions towards phase occurrence probabilities and thus, exposes the decision-making process over discrete as well as continuous compositional spaces.

The mixing of different elements in large concentrations in CCAs can result in a variety of phases including simple solid solution (SS) phases and intermetallics (IM). The structure of SS phase has a huge impact on the mechanical properties since BCC phases are generally associated with higher strength and hardness as compared to FCC phases [95]. Thus, an a-priori phase information is critical for targeted alloy design. Initially, various parameter-based models [102–109] were developed for predicting phase boundaries; but these suffered from low accuracy and high degree of unbalance due to the smaller dataset size and simplistic nature of fit [110]. Guo et al. [111] proposed a Valence Electron Count (VEC) based criteria to determine the occurrence of

FCC and BCC phases in CCAs: FCC (VEC ≥ 8), FCC+BCC (6.87 ≤ VEC < 8), and BCC (VEC<6.87). While this simple rule has been reinforced in various later works [112,113], it has two limitations: a) it fails to explain variation in FCC/BCC phase stabilities in constant VEC systems for e.g., Fe_x-$(AlCoCr_{0.5}Ni_{2.5})_{1-x}$ [114], and b) the bounds of VEC=6.87 and 8 were determined empirically and thereby do not represent strict boundaries for FCC or BCC phase stabilities. Also, apart from VEC, other physical parameters such as cohesive energy can also play an important role in determining FCC/BCC phase boundaries [83]. To overcome this, in the reduced mathematical (RM) model developed here, we have isolated the effect of VEC on FCC and BCC phase occurrence to enable further assessment of the effect of other features on the FCC and BCC phase occurrence in CCAs.

2.2 Development of machine learning models

We first elucidate the model setup used for development of ML models [83]. Each alloy in the dataset was assigned two labels [F, B]; wherein F is presence (F=1) or absence (F=0) of FCC phase and B is presence (B=1) or absence (B=0) of BCC phase. Thus, any given alloy can have four possible phase configurations represented by [F, B] labels: [1, 0] → FCC; [0, 1] → BCC; [1, 1] → (FCC+BCC), and [0, 0] → (neither FCC nor BCC). To predict the alloy phase configuration, we developed two separate ensemble models. The first model predicts only F label i.e., it predicts whether FCC phase will be present or not. The second model predicts only B label i.e., it predicts whether BCC phase will be present or not. Since each of these models employs a sigmoid activation function in output layer, the output ranges between [0, 1] and has been interpreted as the predicted probability of occurrence of a phase [$P(FCC)^{NN}$ and $P(BCC)^{NN}$]; where superscript NN represents Neural Network. A probability value threshold of 0.5 was used for phase classification i.e., a phase is present if $P(phase)^{NN} \geq 0.5$ and absent if $P(phase)^{NN} < 0.5$ [83]. Thus, the combination of outputs from these two models can now span all four phase configurations mentioned earlier. For e.g., if both $P(FCC)^{NN}$ and $P(BCC)^{NN}$ are ≥ 0.5, then the alloy is predicted to have both (FCC+BCC) phases; whereas if $P(FCC)^{NN} \geq 0.5$

but $P(BCC)^{NN} < 0.5$, then the alloy is predicted to have only FCC phase. This methodology has also been depicted schematically in Figure 2.1.

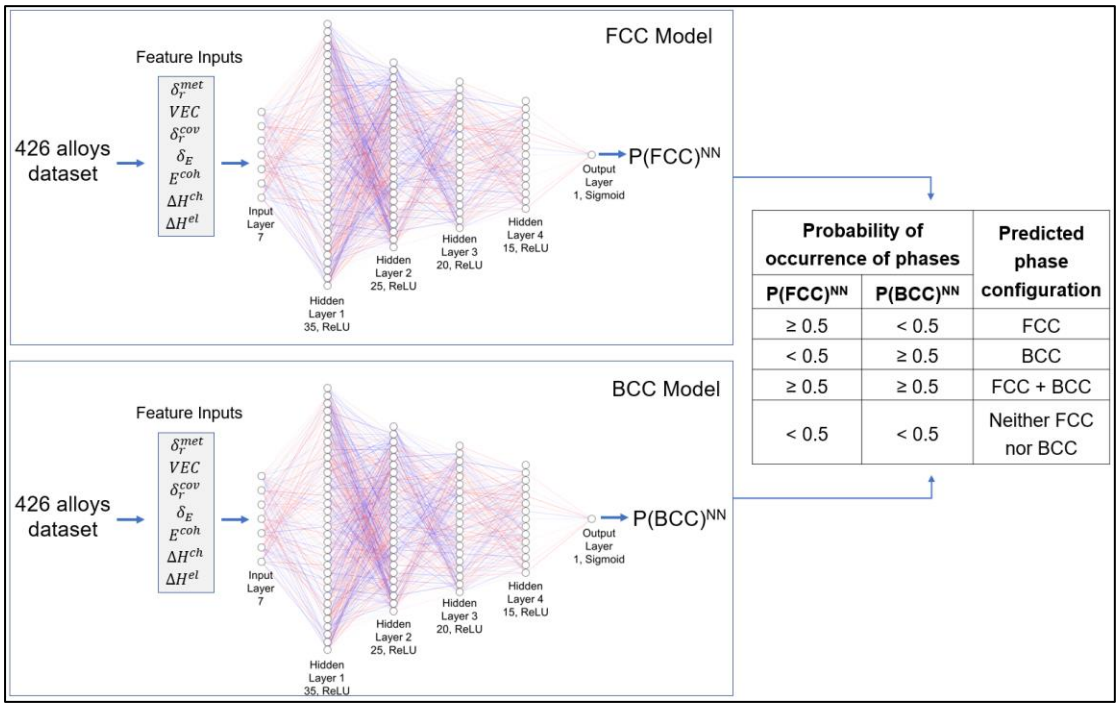

Probability of occurrence of phases		Predicted phase configuration
$P(FCC)^{NN}$	$P(BCC)^{NN}$	
≥ 0.5	< 0.5	FCC
< 0.5	≥ 0.5	BCC
≥ 0.5	≥ 0.5	FCC + BCC
< 0.5	< 0.5	Neither FCC nor BCC

Figure 2.1 Overview of machine learning framework used for the development of machine learning models. Two separate neural network models were trained – first for prediction of FCC phase and second for prediction of BCC phase. The input layer represents seven alloy features (listed in Table S2) and the output layer has 1 unit representing probability of occurrence of a phase (FCC or BCC). "ReLU" stands for rectified linear unit activation function.

Each model was trained using a set of seven alloy features: F = {Valence Electron Count (VEC), Metallic radius asymmetry (δ_r^{met}), Covalent radius asymmetry (δ_r^{cov}), Elastic modulus asymmetry (δ_E), Average cohesive energy (E^{coh}), Chemical enthalpy of mixing (ΔH^{ch}), Elastic enthalpy of mixing (ΔH^{el})}, as listed in Table 2.1. The Miedema's chemical enthalpy of mixing (S. No. 6) was calculated in accordance with Miedema's model [115–117] and takes into account the interfacial surface energy for non-ionic interfaces and dipole-layer energy for ionic interfaces. The elastic enthalpy of mixing (S. No. 7) was calculated using the classical elasticity method by Eshelby and Friedel [116–118]. The binary enthalpies were extended to high-entropy alloys using the extended regular solid solution model proposed by Takeuchi and Inoue [119]. In our prior work [19], we have shown that these features are capable of capturing the phase selection in CCAs. A dataset of 426 as-cast CCAs,

containing experimentally observed room temperature phase information, was used to train the ML models. The dataset contained 293 alloys wherein BCC phase was present and 195 alloys wherein FCC phase was present. These include 71 alloys where both FCC and BCC phases were present. Also, there were 9 alloys that contained neither FCC nor BCC phase. The FCC and BCC phase prediction ML models exhibited a cross-validation accuracy of 95% and 91% respectively. For the training of neural networks, 'Binary Crossentropy' loss function and 'SGD' optimizer was used with a learning rate of 0.01. All features were normalized within [0,1] range using min-max normalization. The correlation between features has been visualized in the form of a scatter-matrix plot in Figure 2.2. The ML models developed here are consistent with our previously reported model for the prediction of phase fractions in CCAs [83]; which has been shown to accurately predict the phases and phase fractions over a wide range of CCAs with an accuracy of 91% for FCC and 97% for BCC phase [83].

Table 2.1 Mathematical expressions of alloy features used for development of machine learning model.

S. No.	Feature	Feature Description	Calculation
1	VEC	Valence electron count	$\sum_{i=1}^{N} c_i \, VEC_i$
2	δ_r^{met}	Metallic radius asymmetry	$\sqrt{\sum_{i=1}^{N} c_i \left(1-\frac{r_i}{\bar{r}}\right)^2}$
3	δ_r^{cov}	Covalent radius asymmetry	$\sqrt{\sum_{i=1}^{N} c_i \left(1-\frac{r_i}{\bar{r}}\right)^2}$
4	δ_E	Young's elastic modulus asymmetry	$\sqrt{\sum_{i=1}^{N} c_i \left(1-\frac{E_i}{\bar{E}}\right)^2}$
5	E^{coh}	Average cohesive energy	$\sum c_i \, E_{coh,i}$
76	ΔH_{SS}^{chem}	Miedema's chemical enthalpy of mixing	$\sum_{i<j} 4H_{ij}^{chem,L} \, c_i c_j$
7	ΔH^{el}	Elastic enthalpy of mixing	$\sum_{i<j} 4H_{ij}^{el} \, c_i c_j$

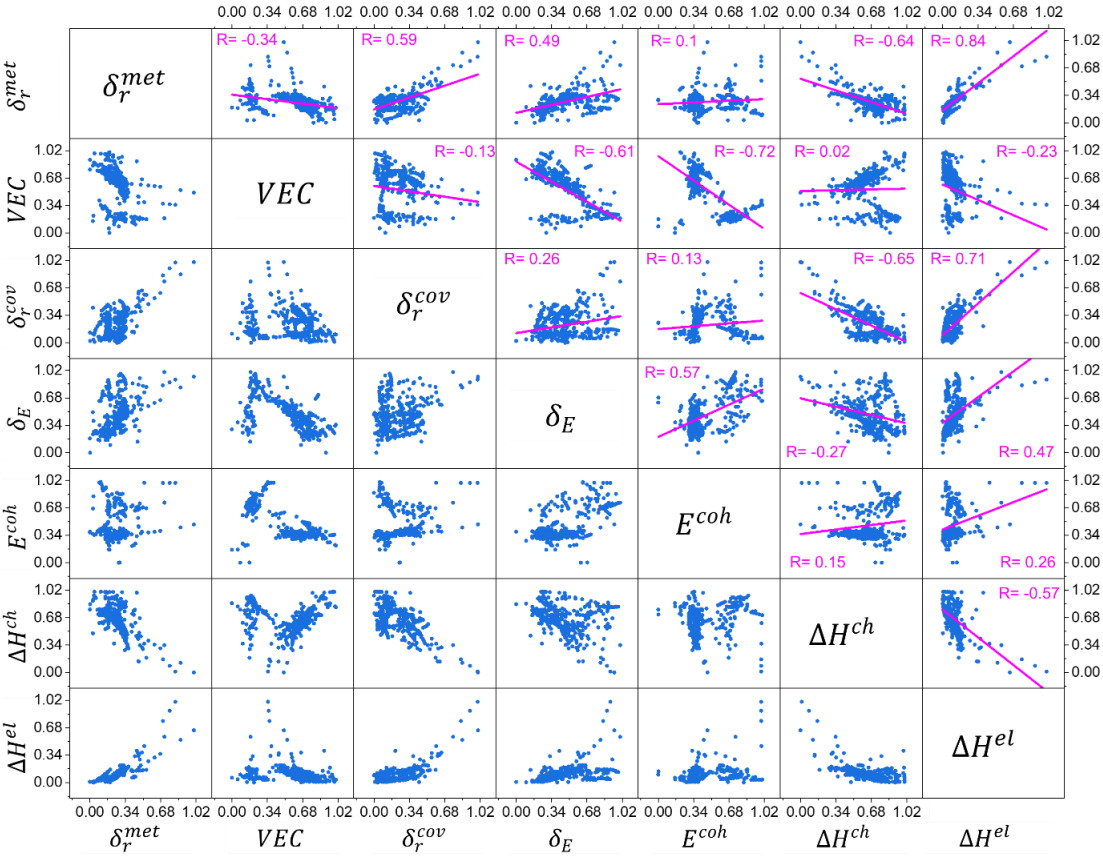

Figure 2.2 Feature correlation: Pair plots of features used in this work. The linear-regression lines and Pearson's correlation coefficient (R) values have been shown in the pair-plots above the diagonal.

2.3 Development of Reduced Mathematical (RM) model

2.3.1 Dataset for RM model

Since the RM model is aimed as a simplistic and interpretable replacement for the ML model, it needs to capture the learning achieved by the trained ML model. This was achieved by fitting and validating the RM model on predictions generated from the trained ML models. We considered a 13-element space [E = {Al, Ti, V, Cr, Mn, Fe, Co, Ni, Cu, Zn, Zr, Nb, Mo}]. Within this space E, the number of unique equiatomic alloys with n number of elements is $^{13}C_n$. Thus, the number of unique equiatomic alloys with 5 elements is 1287 (=$^{13}C_5$), with 6 elements is 1716 (=$^{13}C_6$) and with 7 elements is 1716 (=$^{13}C_7$). Adding these together, we created a dataset of 4719 alloys and [P(FCC)^{NN}, P(BCC)^{NN}] values were obtained for each of the alloy using trained ML models. This dataset was used to fit the RM model for FCC and BCC

phases. Similarly, another dataset of 2002 (=$^{13}C_8$ + $^{13}C_9$) unique equiatomic alloys with 8 and 9 elements from the element space E was created for validation of the RM model. The distribution of ML predicted phases in these datasets has been shown in Figure 2.3.

Fitting dataset for RM model (Equiatomic alloys with 5,6 & 7 elements)	
Phases predicted from ML model	**No. of alloys**
FCC present →	2307
BCC present →	2909
Both FCC & BCC present →	721
Neither FCC nor BCC →	224

Validation dataset for RM model (Equiatomic alloys with 8 & 9 elements)	
Phases predicted from ML model	**No. of alloys**
FCC present →	1042
BCC present →	1235
Both FCC & BCC present →	384
Neither FCC nor BCC →	109

Figure 2.3 Distribution of ML predicted phases in the datasets used for fitting and validation of RM models.

2.3.2 Reduced mathematical representation of ML models

As seen in Figure 2.4a, the NN-predicted phase probabilities i.e., $P(FCC)^{NN}$ and $P(BCC)^{NN}$ show a strong dependence on VEC wherein $P(FCC)^{NN}$ transitions from 0→1 and $P(BCC)^{NN}$ transitions from 1→0 as VEC increases. This dependence is very similar to the behaviour of a generalized logistic function which allows – a) non-linear scaling, b) limiting the output between 0 and 1, and c) variation in both the shape and size of the activation window. Thus, to isolate this effect of VEC on phase probabilities, we used a logistic function ($f_{logistic}^{phase}$) that has three parameters – M (maximum value), k (logistic growth rate), and x_o (x value of sigmoid's midpoint):

$$f_{logistic}^{phase}(VEC) = \frac{M}{1 + e^{-k(VEC - x_o)}}$$

Equation 2.1

Since the phase probabilities cannot be explained completely by VEC alone, we now focus on the residuals left by this fit. The absolute residuals obtained from here i.e., $|P(phase)^{NN} - f_{logistic}^{phase}(VEC)|$ appear to peak at intermediate values of VEC, as seen in Figure 2.4b. We hypothesize that these residuals represent the effect of features other than VEC on phase probabilities. The distribution of

residuals seen in Figure 2.4b indicates that while the actual contribution of these features will depend on their individual values, the maximum possible contribution from these features in any alloy is a function of the VEC value of that alloy. We used a skew-normal function ($f_{skew-norm}^{phase}$) [120,121] to model this dependence of peak value of residuals on VEC as seen in Figure 2.4b. This function has four parameters – A (scaling factor), ξ (location), ω (scale), and α (shape):

$$f_{skew-norm}^{phase}(VEC) = \frac{A}{\sqrt{2\pi}\omega}\, exp\left[-\frac{(VEC-\xi)^2}{2\omega^2}\right] erfc\left[-\frac{\alpha(VEC-\xi)}{\sqrt{2}\omega}\right]$$

Equation 2.2

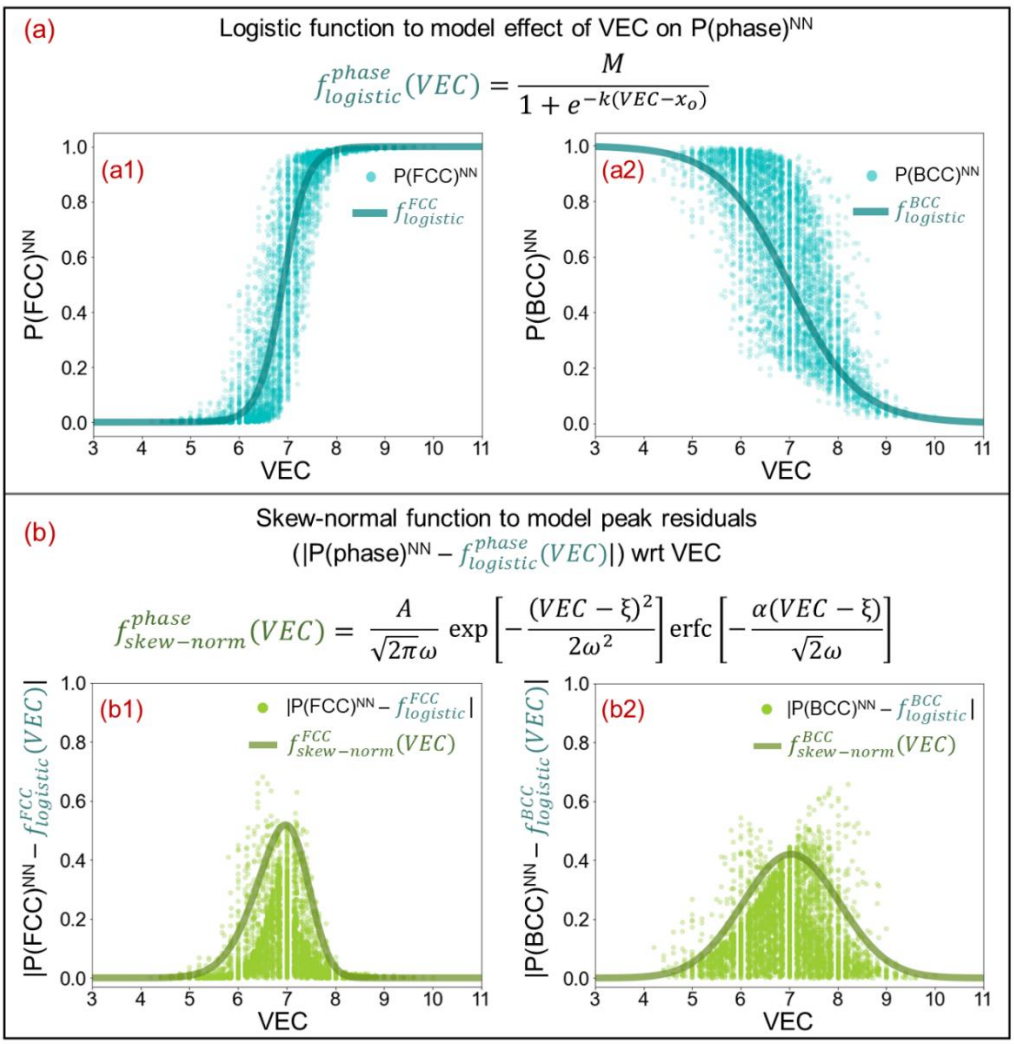

Figure 2.4 Mathematical functions used for isolating the effect of VEC on phase stabilities. (a) Logistic function used to model the dependence of FCC and BCC occurrence probability on VEC. (b) Skew-normal function of VEC used to model the peak residuals obtained after logistic fit of phase probabilities wrt VEC.

Thus, we have modelled the residuals, i.e. [P(phase)^{NN} – $f_{logistic}^{phase}(VEC)$], as a linear function of all feature values (except VEC) that have been scaled by the $f_{skew-norm}^{phase}(VEC)$ function. For any given alloy, the overall phase probability predicted by the reduced mathematical (RM) model, $P(phase)^{RM}$, has been modelled as:

$$P(phase)^{RM} = f_{logistic}^{phase}(VEC) + \left[\beta_0 + \sum_{i \in F \setminus \{VEC\}} \beta_i \left[f_{skew-norm}^{phase}(VEC) * X_i \right] \right]$$

Equation 2.3

Here 'F' denotes the feature set {VEC, δ_r^{met}, δ_r^{cov}, δ_E, E^{coh}, ΔH^{ch}, ΔH^{el}}, '$F \setminus \{VEC\}$' represents feature set excluding VEC, 'β_0' is the bias factor of linear fit, 'β_i' represents the weight-factor for i^{th} feature in '$F \setminus \{VEC\}$', and X_i represents the normalized value of ith feature in '$F \setminus \{VEC\}$'.

2.3.3 Optimization and performance of reduced mathematical model

The model thus developed (Equation 2.3) was further optimized and its performance was evaluated using the process elucidated here. The final model has a total of seven parameters – three logistic function parameters (M, k, x_o) and four skew-normal function parameters (A, ξ, ω, α). For any given set of these parameters, we performed a fit of Equation 2.3 wrt P(phase)^{NN} to yield the values of β_0 and β_i, and the quality of fit thus obtained was quantified using the R^2 score. For the optimization of model parameters, we used (1 – R^2) as the objective function that was minimized using the LM-BFGS-B algorithm [122,123], which is a limited-memory (LM) implementation of Broyden–Fletcher–Goldfarb–Shanno (BFGS) algorithm with simple bound constraints. The objective-function minimization was carried out using the 'L-BFGS-B' solver in 'optimize' method of 'SciPy' library for Python [124]. The code used for the optimization process has been uploaded on GitHub, as detailed in §2.7. Figure 2.5 shows the optimized functions and parameters, along with the performance of the optimized RM model with respect to the NN model, for both FCC and BCC phase. The (classification accuracy (CA), R^2 score) of FCC and BCC model is (CA=97.2%, R^2=0.966) and (CA=92.1%, R^2=0.906),

respectively. A similar performance [(CA=97.1%, R^2=0.966) for FCC and (CA=91.1%, R^2=0.906) for BCC] was also obtained over the validation set that comprised 2003 compositions that were not used in the RM model development process (Figure 2.6). The optimized RM model also shows a good classification accuracy (93% for FCC and 84% for BCC) over the experimental dataset comprising 426 CCAs. The RM model performance was further validated through comparison with experimentally observed phases over a set of 35 new alloy compositions (compiled from recent literature) that were not present in the training dataset (Figure 2.7).

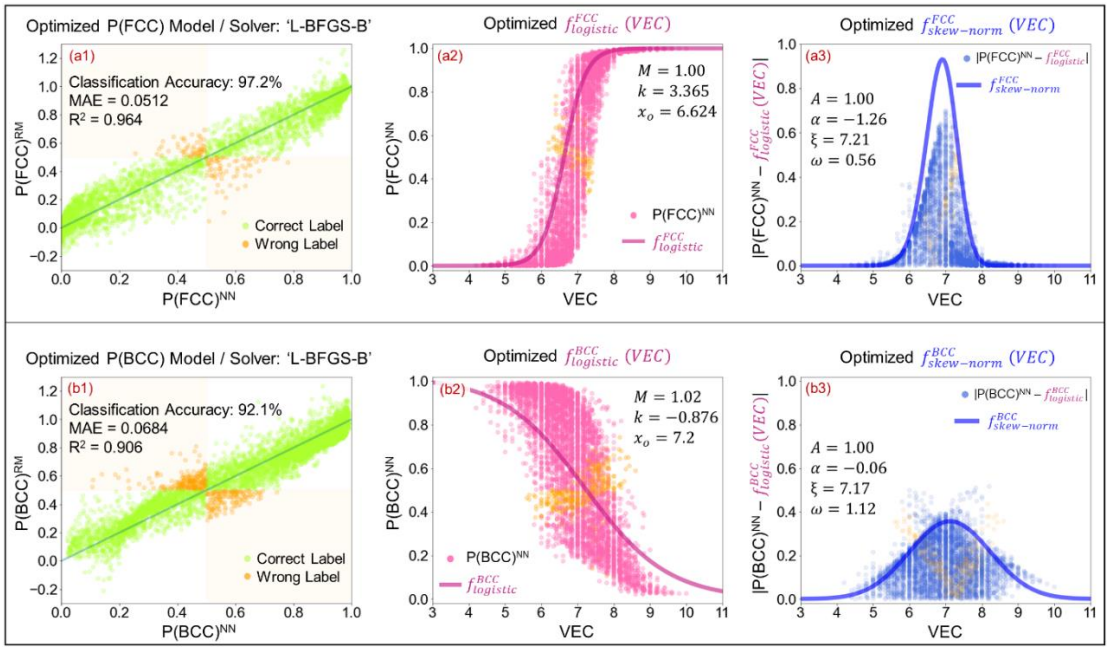

Figure 2.5 Model parameters and performance of optimized RM model. (a1) FCC phase occurrence probabilities predicted by optimized RM model vs. NN model, (a2) Optimized logistic function for P(FCC) model, (a3) Optimized skew-normal function for P(FCC) model, (b1) BCC phase occurrence probabilities predicted by optimized RM model vs. NN model, (b2) Optimized logistic function for P(BCC) model, (b3) Optimized skew-normal function for P(BCC) model.

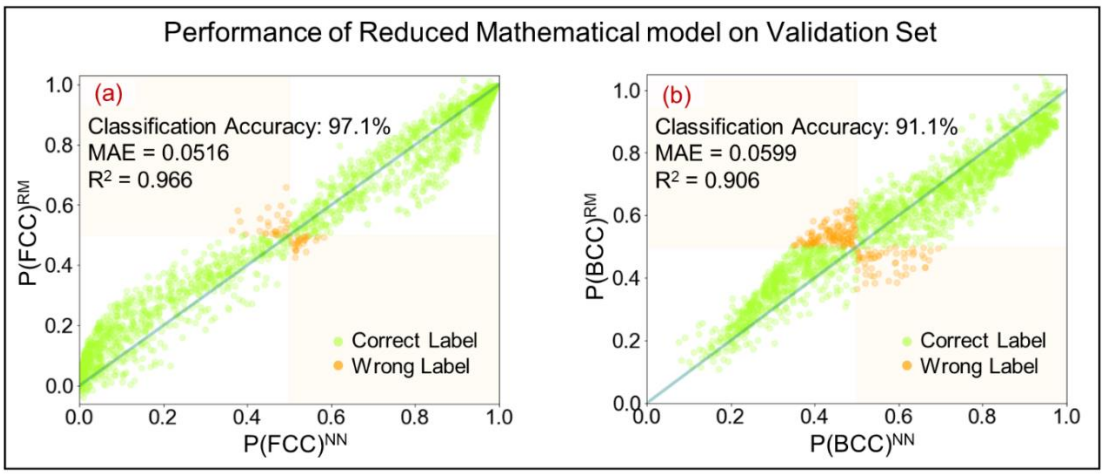

Figure 2.6 Performance of reduced mathematical (RM) model over validation dataset

Confusion-Matrix for FCC Class

(a)

		RM-Model		
		FCC-present	FCC-absent	
Exp	FCC-present	**10**	**5**	**66.67**
	FCC-absent	**0**	**20**	
		100		

Confusion-Matrix for BCC Class

(b)

		RM-Model		
		FCC-present	FCC-absent	
Exp	FCC-present	**30**	**0**	**100**
	FCC-absent	**5**	**0**	
		85.71		

(c)

Class	**Precision (P)**	**Recall (R)**	**F-1 score** 2(P*R)/(P+R)
FCC	100%	66.67%	80.0%
BCC	85.71%	100%	92.3%

Figure 2.7 Confusion matrix for RM model predictions of **(a)** FCC and **(b)** BCC class labels for 35 new alloys that were not present in the training dataset. **(c)** Precision, Recall and F-1 score for each class.

2.4 Feature contributions towards phase predictions

The NN models, by themselves, do not allow direct insights into the decision-making process since the exact mathematical form is either not easily visualizable or is not easily comprehensible when visualized. Therefore, a variety of indirect methods are often used to impart some interpretability (local or global) to the model by approximating the decision-making process. As an alternative approach, the RM model developed here replaces the NN models with a simplified mathematical model that enables direct and exact quantification of the feature contributions towards prediction of FCC and BCC phase occurrence probabilities. The magnitude of weight-factors (β_i), as listed in Figure 2.8a, gives an estimation of the relative contribution of features; whereas the sign of β_i indicates whether the relationship between P(Phase)^{RM} and feature value is direct (positive β_i) or inverse (negative β_i). That said, the β_i value alone is not sufficient as the actual feature contribution is also a function of $f_{skew-norm}^{phase}$ and actual feature (X_i) values. For any given alloy probed through the RM model, the contribution of VEC can be quantified as '$f_{logistic}^{phase}(VEC)$', whereas the contribution of any other feature i can be measured as '$\beta_i \left[f_{skew-norm}^{phase}(VEC) * X_i \right]$', as shown in Figure 2.8(b, c).

δ_r^{met}, δ_r^{cov}, δ_E, and E^{coh} show significant, but opposite, contributions in the FCC and BCC phase models, whereas ΔH^{ch} and ΔH^{el} appear as the least significant features for both FCC and BCC phases. Both E^{coh} and δ_r^{met} show a direct and inverse relationship with P(BCC)^{RM} and P(FCC)^{RM} respectively, thereby indicating that high cohesive energy and metallic radius asymmetry favours the occurrence of BCC phase over FCC phase. The role of E^{coh} is consistent with the observations in another recent work where it was shown to be an important classifier for FCC and BCC phases in CCAs [83]. This also aligns with the fact that high E^{coh} usually leads to a higher melting temperature (T_m) and high T_m metals generally favor a more open structure (i.e., BCC as compared to FCC) due to the higher entropy. The δ_r^{met} contribution seems to align with the fact that the BCC structures are more open (with lower packing fraction) as

compared to FCC and can thus accommodate larger atomic size differences. Unlike (E^{coh} and δ_r^{met}), δ_r^{cov} and δ_E show an inverse and direct relationship with P(BCC)^{RM} and P(FCC)^{RM} respectively. In the periodic table, covalent radius (r^{cov}) decreases and electronegativity (χ^{Allen}) increases as we move from left-to-right along a particular period; and thus, a high covalent-radius asymmetry (δ_r^{cov}) would also result in a large local mismatch in electronegativity (as confirmed in Figure 2.9) indicating the formation of stronger bonds which might favor formation of more close packed structure (FCC). The weak contribution from ΔH^{ch} and ΔH^{el} was further confirmed through the observation of no appreciable change in the model performance even upon their removal from the RM model (Figure 2.10 & Figure 2.11).

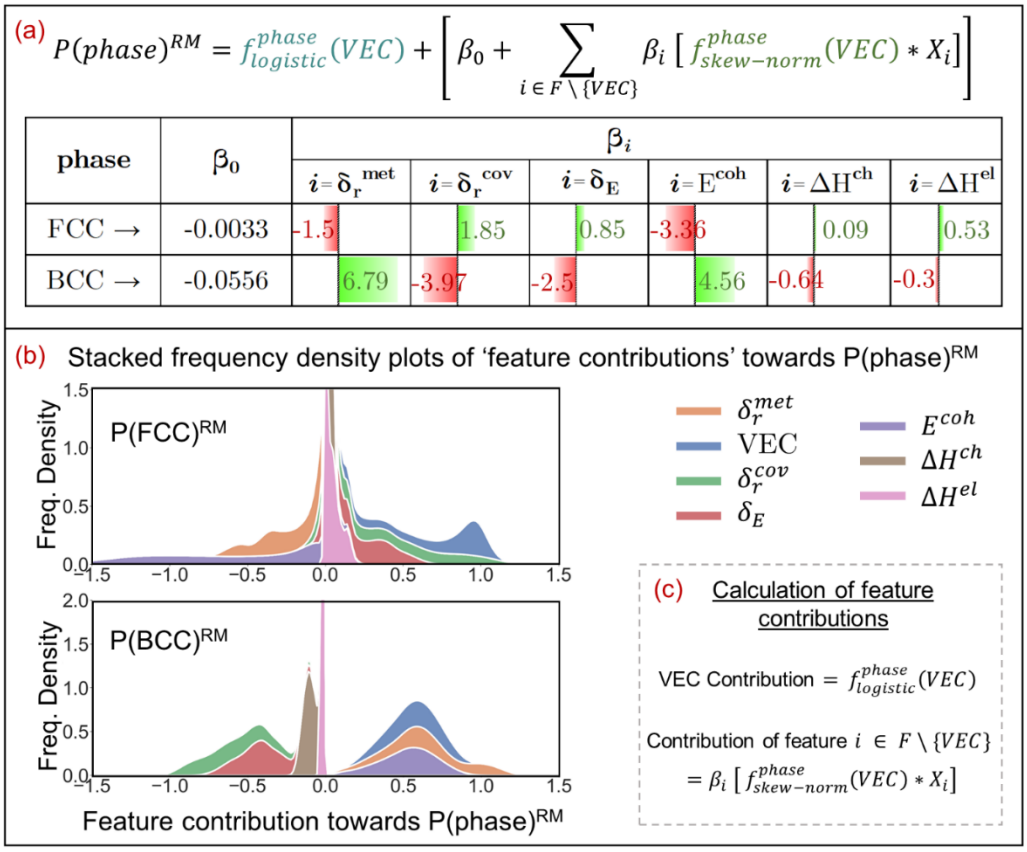

Figure 2.8 Feature contributions. (a) Weight-factors (β_i) of each feature in RM model, (b) stacked frequency density plots of the contributions made by each feature towards P(FCC)RM and P(BCC)RM, and (c) expressions for calculation of feature contribution values. Here, P(Phase)NN and P(Phase)RM is the phase occurrence probability predicted by NN and RM model, respectively; VEC is valence electron count, δ_r^{met} is asymmetry in metallic radius, δ_r^{cov} asymmetry in covalent radius, δ_E is asymmetry in elastic modulus, E^{coh} is average cohesive energy, ΔH^{ch} is chemical enthalpy of mixing, and ΔH^{el} is elastic enthalpy of mixing.

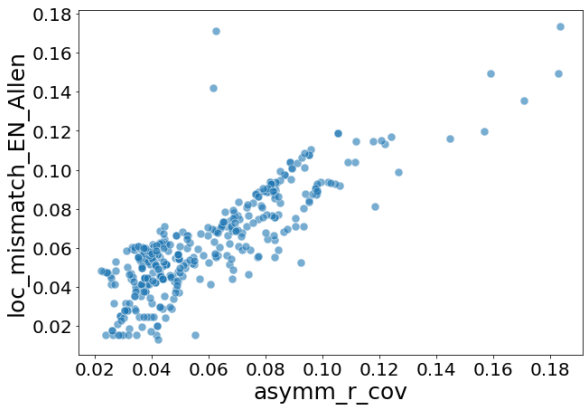

Figure 2.9 Plot of local mismatch in electronegativity vs. asymmetry in covalent radius over all the alloys present in experimental dataset

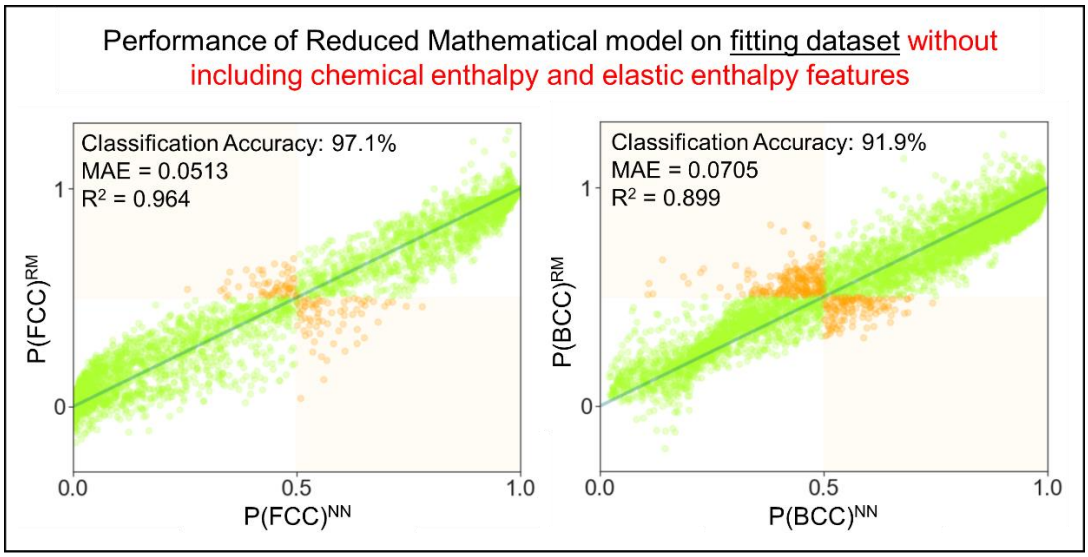

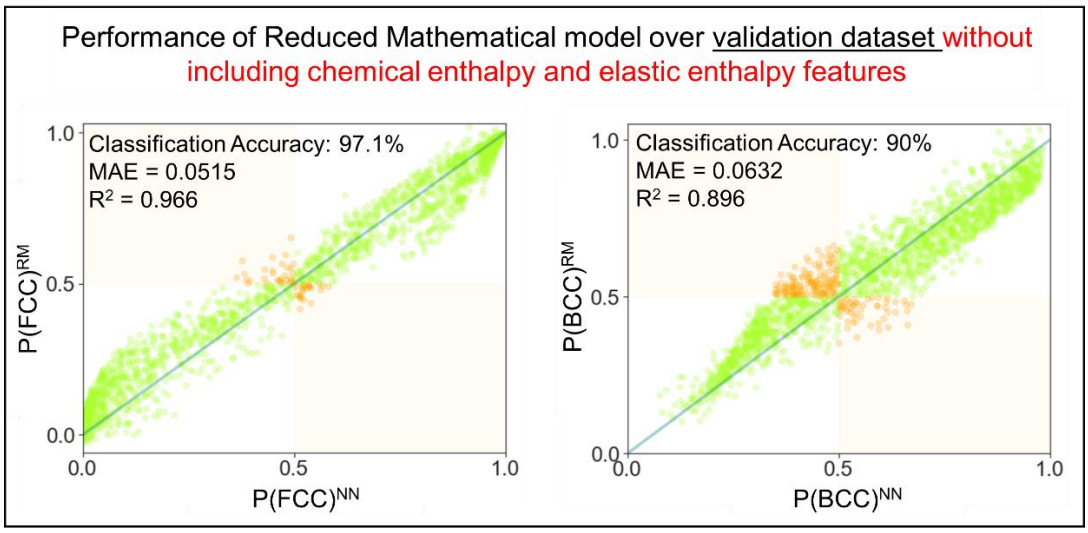

Figure 2.10 Performance of reduced mathematical (RM) model created without including chemical enthalpy and elastic enthalpy features. The exclusion of these features has no significant effect on the model performance.

phase	β_0	β_i			
		$i = \delta_r^{met}$	$i = \delta_r^{cov}$	$i = \delta_E$	$i = E^{coh}$
FCC →	-0.0011	-1	1.8	0.87	-3.2
BCC →	0.0071	6.47	-3.36	-2.52	3.8

Figure 2.11 Parameters of the reduced mathematical model created without including chemical enthalpy and elastic enthalpy features. The feature coefficients are very similar to those observed when both these features are included.

2.5 Exploring continuous composition variations

To further probe the feature contributions and the consistency between NN and RM model, we explored continuous composition variations in three alloy systems – $Al_x(CoCrFeNi)_{1-x}$, $Ti_x(CrFeNi)_{1-x}$ and $Mo_x(TaTiWZr)_{1-x}$, as shown in Figure 2.12. The NN model predictions closely match the previously reported phase stabilities in these systems [125–127]. The RM model also correctly predicts – a) the FCC → (FCC+BCC) → BCC transitions as Al and Ti is added to $Al_x(CoCrFeNi)_{1-x}$ (Figure 2.12a1) and $Ti_x(CrFeNi)_{1-x}$ (Figure 2.12b1), respectively, and b) BCC as the stable structure throughout the $Mo_x(TaTiWZr)_{1-x}$ system (Figure 2.12c1). Moreover, the phase occurrence probability trends predicted by the RM model closely follow the predictions from NN model in all three systems, although the BCC-RM model does predict occurrence of BCC phases at slightly lower Al and Ti concentrations as compared to NN model.

The feature contributions measured through the RM model provide insights into the decision-making process of the model. The FCC → BCC transition in $Al_x(CoCrFeNi)_{1-x}$ appears to be driven primarily by the decrease in VEC due to Al addition along with the large contributions from E^{coh} and δ_r^{met} values associated with this system, as seen in Figure 2.12a. A similar observation is made in $Ti_x(CrFeNi)_{1-x}$ also, where FCC → BCC transition occurs with Ti addition (Figure 2.12b), but here the considerable increase in δ_r^{cov} with Ti addition also contributes significantly and causes smoothening of gradients of $P(Phase)^{RM}$ with respect to Ti concentration thereby leading to a larger compositional range over which the transition occurs as compared to

$Al_x(CoCrFeNi)_{1-x}$. In $Mo_x(TaTiWZr)_{1-x}$ (Figure 2.12c), the structure at x=0 is predicted to be BCC due to a low VEC value of 4.75 for equiatomic (TaTiWZr). With Mo addition, the VEC value increases very gradually (from 4.75 at x=0 to 5.5 at x=0.6) and thus, we don't see any transition being predicted by the RM or NN model.

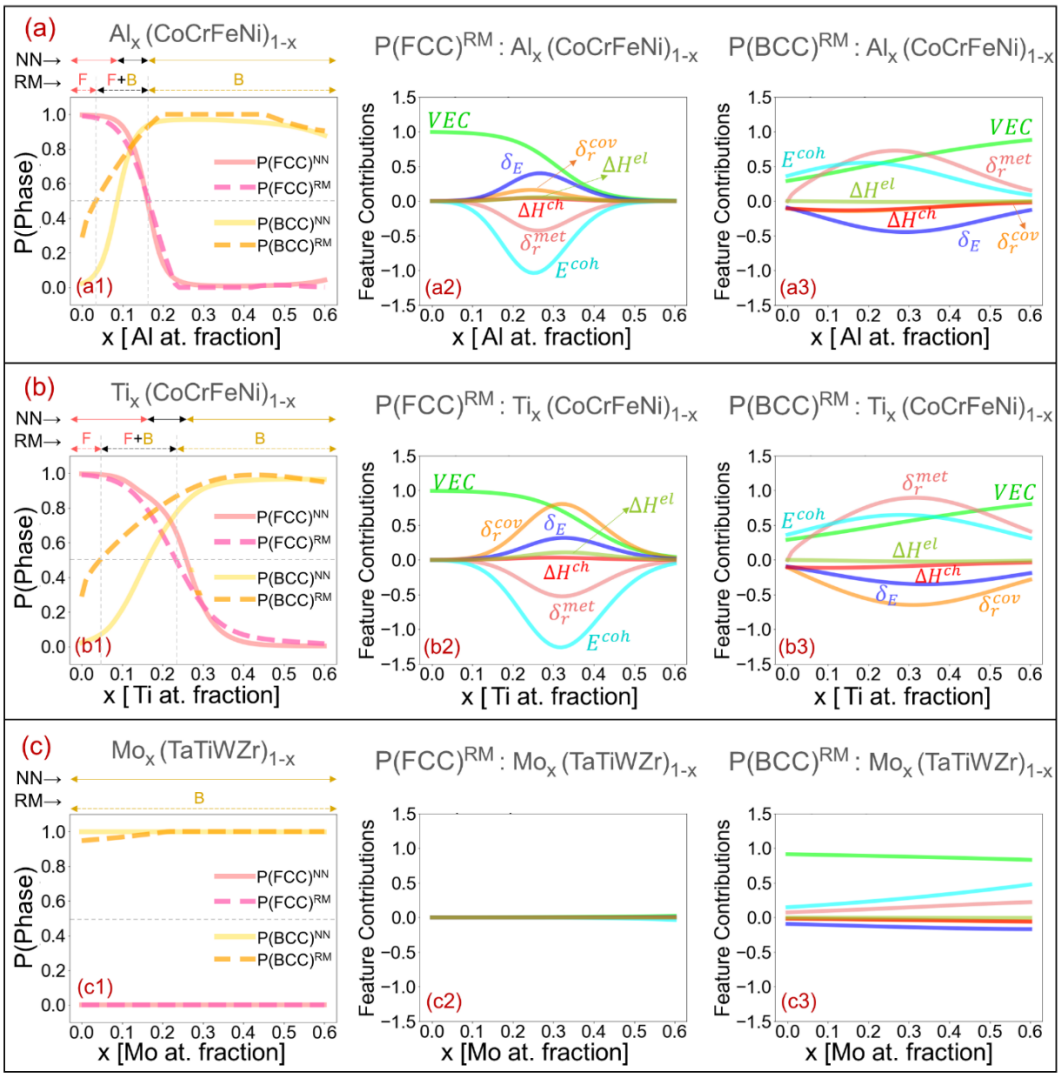

Figure 2.12 Comparing NN vs. reduced mathematical (RM) model predictions and feature contributions over continuous composition pathways in (a) Alx (CoCrFeNi)1-x, (b) Tix (CrFeNi)1-x and (c) Mox (TaTiWZr)1-x. At any composition x, feature contribution value represents exact contribution made by that feature towards the overall phase occurrence probability predicted in RM model i.e., P(Phase)RM. In (a1, b1, c1), compositional regions with different predicted phases have been mapped at the top axes for both NN and RM models; here F is FCC and B is BCC.

The RM model developed in this work takes a mathematical form that was inspired by the physical intuition based on a well-documented idea that VEC is a key (but not the only) factor that dictates formation of FCC and BCC

structures in CCAs. While the RM model performs quite well, it poses a question as to whether it is indeed the best-fit mathematical model. To probe this, we performed symbolic regression (SR) using "Feyn" python module [128] that implements "QLattice". QLattice is a supervised machine learning tool for symbolic regression that composes functions together to build mathematical models between the inputs and output in the dataset. The available mathematical functions include – addition, multiply, squared, linear, tanh, gaussian, exponential, logarithmic and inverse. The following parameters were used for symbolic regression: number of epochs = 10; maximum complexity = 15; loss function = mean squared error. The mathematical forms of best-fit SR models have been shown in Figure 2.13. and the performance has been shown in Figure 2.14 and Figure 2.15. The SR models don't show any significant improvement with respect to the RM model. However, the form of SR models is quite arbitrary and it is difficult to assign a physical meaning or significance to the mathematical form and constants obtained here. Thus, the RM model is superior in the sense that it enables clear interpretation of the model form as well as the feature contributions.

FCC Model

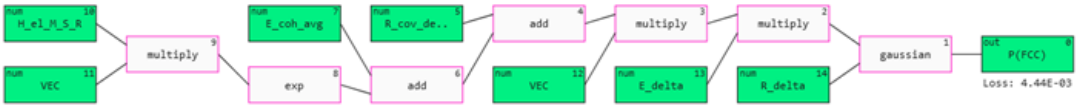

FCC SR Model Equation:

```
0.0215647 + 1.00615*np.exp(-859.228*(0.805176 - VEC)**2*(1 -
0.74332*E_delta)**2*(E_coh_avg - 0.486242*R_cov_delta + 0.229008*np.exp((-2.57774*H_el
- 1.14137)*(1.3974*VEC - 0.981104)) - 0.253279)**2 - 0.215091*(R_delta -
0.00931492)**2)
```

$$P(FCC) = \mathbf{A} + \mathbf{B}e^{\mathbf{C}(\mathbf{D}-V)^2(1-\mathbf{E}\delta_E)^2\left(E^{coh}-\mathbf{F}\delta_r^{cov}+\mathbf{G}e^{(\mathbf{H}\Delta H^{el}-\mathbf{I})(\mathbf{J}V-\mathbf{K})}-\mathbf{L}\right)^2-\mathbf{M}\left(\delta_r^{met}-\mathbf{N}\right)^2}$$

Where; A=0.0215647; B=1.00615; C=−859.228; D=0.805176; E=0.74332; F=0.486242; G=0.229008; H=−2.57774; I=1.14137; J=1.3974; K=0.981104; L=0.253279; M=0.215091; N=0.00931492

BCC Model

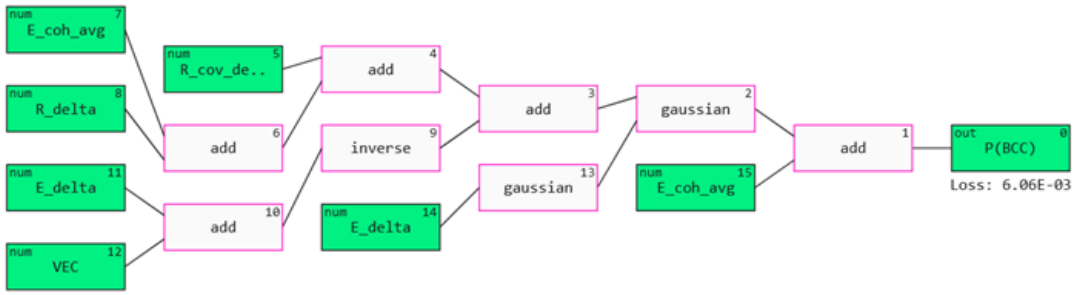

BCC SR Model Equation:

```
- 0.230101 + 0.760363*E_coh_avg + 0.822534*np.exp(-13.168*(0.223822*E_coh_avg -
0.50224*R_cov_delta + R_delta + 0.34678 + 0.389722/(0.34549*E_delta + 0.519464*VEC
- 1.05674))**2 - 2.0*np.exp(-46.5514*(E_delta - 0.073299)**2))
```

$$P(BCC) = \mathbf{A} + \mathbf{B}E^{coh} + \mathbf{C}e^{\mathbf{D}\left(\mathbf{E}E^{coh}-\mathbf{F}\delta_r^{cov}+\delta_r^{met}+\mathbf{G}+\frac{\mathbf{H}}{(\mathbf{I}\delta_E+\mathbf{J}V-\mathbf{K})}\right)^2-\mathbf{L}e^{\mathbf{M}(\delta_E-\mathbf{N})^2}}$$

Where; A=−0.230101; B=0.760363; C=0.822534; D=−13.168; E=0.223822; F=0.50224; G=0.34678; H=0.389722; I=0.34549; J=0.519464; K=1.05674; L=2.0; M=−46.5514; N=0.073299

Figure 2.13 Mathematical expressions for FCC and BCC occurrence probability obtained from symbolic regression models.

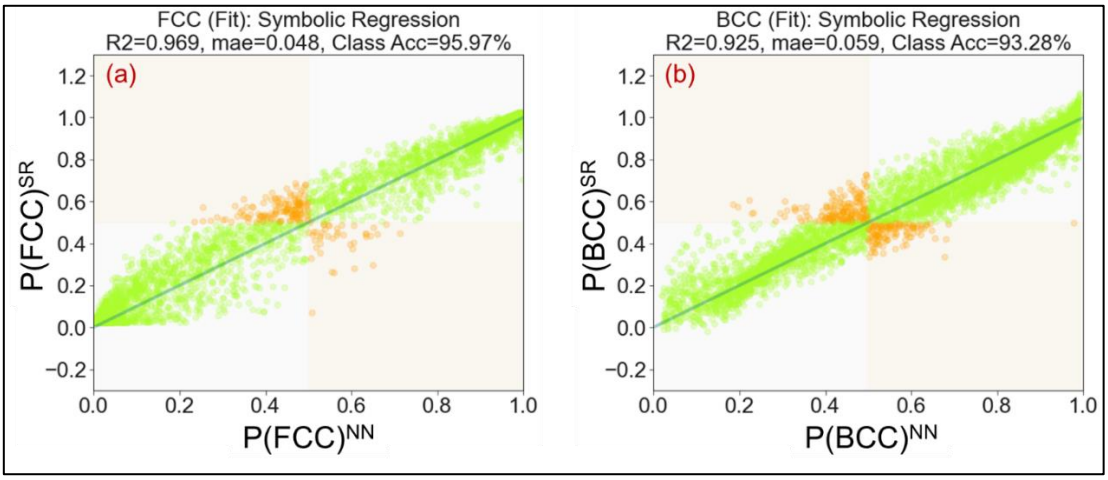

Figure 2.14 Performance of **(a)** FCC and **(b)** BCC model developed using symbolic regression (SR). The SR models, similar to RM models, were developed to replace the trained ML models and same fitting dataset of 4719 compositions (as used for RM models) was used to develop SR models.

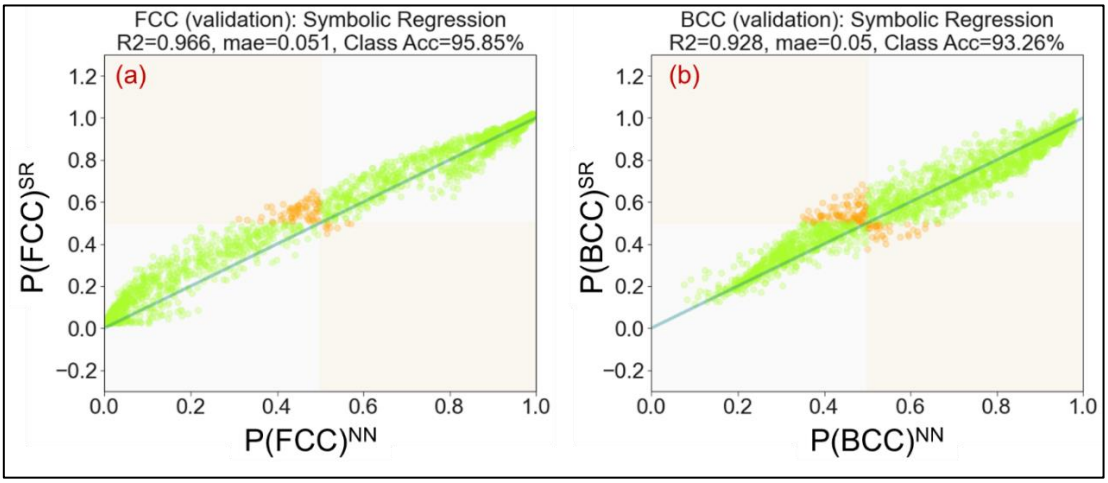

Figure 2.15 Performance of **(a)** FCC and **(b)** BCC symbolic regression model on validation dataset comprising 2002 alloy compositions (this dataset is same as that used for validation of RM models)

2.6 Conclusion

In summary, we have presented in this chapter a mathematical reduction, driven by physical intuition and statistical inference, of a NN-based ML model that was trained to predict FCC and BCC phase occurrence probabilities in high-entropy alloys. The reduced mathematical model replaces the complex ML model with a simplified and interpretable mathematical function that

allows direct insights into the decision-making process. The mathematical model shows good consistency with the experimental database and ML model over both discrete and continuous compositions in a variety of systems. More importantly, it enables a direct quantitative estimation of feature contributions towards phase occurrence probabilities and thus allows a glimpse into the decision-making process followed by the model. While VEC remains the main driver for FCC ↔ BCC transitions, wherein very high and low VEC values result in FCC and BCC respectively, other features (namely – metallic radius asymmetry, cohesive energy, covalent radius asymmetry and elastic modulus asymmetry) also contribute significantly towards the phase stabilities when VEC values lie in the intermediate range. The cohesive energy and metallic radius asymmetry seem to show direct and inverse relationship with BCC and FCC phase occurrence respectively, whereas the covalent radius asymmetry and elastic modulus asymmetry seems to show inverse and direct relationship with BCC and FCC phase occurrence, respectively. The approach presented here highlights a possible way of imparting some interpretability to ML models through their reduction to simpler, but meaningful, frameworks. Moreover, identification of a reduced model essentially replaces the complex ML model with a simple mathematical relation leading to huge computational gains with minimal accuracy loss, thereby enabling a rapid assessment of phase selection over wide compositional spaces.

While the reduced model shows good accuracy, few key limitations must be noted: (a) the feature contributions derived from the reduced model are not "exact" with respect to the ML model decision-making and thus some information loss is inevitable; (b) the modelled contribution of feature variations are scaled by a function dependent on VEC value and thus, might be suppressed in alloy systems where VEC changes are extremely subtle and (c) other aspects such as vacancy stabilization of structures (which though rarely observed, have been reported for medium entropy alloys [129]) have been ignored. To address some of these challenges, in the next chapter, we present a different methodology to extract the decision-making process of any

composition-based ML model by quantifying the exact contribution of each feature towards the overall prediction.

2.7 Research data

The code and datasets used for the development of machine learning model and reduced mathematical model are available at:

https://github.com/IDEAsLab-Materials-Informatics/reduced-math-model-FCCvsBCC-HEAs

Chapter 3: CoSMoR – Compositional-Stimulus and Model-Response framework to extract physical insights from machine learning models

3.1 Introduction

The application of machine learning (ML) in materials science has seen tremendous growth in recent years[30,34,48,130–132]. Compositional ML models, that use a combination of composition and elemental properties as input features, have been used extensively for the prediction of a wide variety of materials phenomena such as phase selection[19,37,58,60,133], mechanical properties[67,72,95], oxidation behavior[134–138], structure stability[139,140] and alloy discovery[141–147]. Given the success of these ML models even on unseen compositional space, there is a strong possibility that these models are capturing the underlying physical principles using the input material descriptors, even though these decisions are often hidden due to the complicated form assumed by ML models (especially deep neural networks). This introduces exciting avenues for uncovering physical insights from the trained ML models through the decoding of their decision-making process. Here, we have developed the **Co**mpositional **S**timulus and **Mo**del **R**esponse (**CoSMoR**) framework that discretizes the compositional space and calculates

---

This chapter has been published as a research article in 'Physical Review Materials'

D Beniwal and PK Ray, *CoSMoR: Decoding decision-making process along continuous composition pathways in machine learning models trained for material properties*, **Physical Review Materials**, 7 (2023) 043802

DOI: *https://doi.org/10.1103/PhysRevMaterials.7.043802*

the exact feature contributions along any given compositional pathway. This is done by combining the partial-local-dependence (PLD) of ML model (with respect to each feature) with the sensitivity of that feature (with respect to the composition) at each composition step.

With the growing applicability and reliability of ML for materials science, the interpretability of these models has appeared at the forefront in recent years[94,148–151]. As discussed eloquently by Lipton [152] and Oviedo et al. [149], the term 'interpretability', and the expectations surrounding it, can be quite subjective since it is associated with a lot of technical jargon such as explainability, simulability, decomposability, algorithmic transparency, understandability, etc. Thus, it is imperative to define *a priori* the expectations for any framework that aims at decoding the decision-making process of ML models. In this regard, we describe here the four attributes of interpretation obtained from **CoSMoR** framework:

(a) **Type of explanation**: Suppose we have a base alloy B. If we start adding another component A to this base alloy i.e., we move along A_xB_{1-x} composition pathway, then **CoSMoR** provides the exact contribution of each feature towards the changes in ML predicted property with respect to the base alloy composition.

(b) **Correctness of model explanation**: The feature contributions calculated by **CoSMoR** along a composition pathway are not relative or indicative metrics of feature importance, but are instead quantitatively exact with respect to the model decision-making process. For example, suppose we have a hardness ML model that predicts an increase of 100 HV when 10 at. percent Al is added to CrFeNi base alloy, then implementation of **CoSMoR** will tell exactly how much did each feature contribute towards this overall increase of 100 HV hardness as predicted by the ML model.

(c) **Causation for model understanding**: The existing interpretation methodologies such as partial dependence plots, accumulated local effects, Local interpretable model-agnostic explanations (LIME) and

SHapley Additive exPlanations (SHAP) provide an understanding of how important each feature is towards the overall model decision-making. But, from an alloy design perspective, it is much more meaningful to understand the model decision making with respect to compositional variations because: (i) the direct point of control in alloy design is the elemental composition, not the feature values, (ii) the features cannot be varied independently since any alloying addition will affect all features, and (iii) the features cannot be changed by any arbitrary amount or to any arbitrary set of values since the elements have a fixed set of properties and we have direct control over only the alloy composition. Since **CoSMoR** probes feature contributions as a function of composition, the causality for model understanding obtained from **CoSMoR** is rooted in compositional variations rather than arbitrary feature variations.

(d) **Scope of explanation (local/global)**: In the context of compositional ML models, the scope of explanation from any interpretation framework may be defined as – (i) local if the understanding obtained is at a single composition value for example, calculating the partial dependence of model output on each feature for a given alloy (similar to SHAP values), and (ii) global if the understanding obtained reflects in general how the feature manifests in the model decision making for example, formulation of surrogate models with simplified and interpretable mathematical forms. While local explanations tend to be more accurate with respect to the model decision making process, they are valid only for a fixed composition value. On the other hand, the global explanations can span a much more expansive compositional space, but the understanding becomes generalized, though approximate. **CoSMoR** aims at combining the best of these two approaches to provide material-specific insights. Fundamentally, the explanation obtained from **CoSMoR** is local in nature as it calculates feature contributions for each composition step at a time. But the scale of understanding is not

limited to a single composition point, and instead a complete continuous composition pathway can be probed. Moreover, composition pathways defined as A_xB_{1-x} can span a considerable compositional space since components A and B can be either elements or any stoichiometric combination of elements.

3.2 Methodology for development of CoSMoR

In **CoSMoR** framework, the compositional space is represented by atomic fraction (and not weight fraction). Further, it is discretized using a composition step size variable denoted by Δc. This is a user input parameter; for e.g., in §2.4 (where **CoSMoR** has been applied to phase selection in CCAs), a composition step size value of 0.01 has been used that represents 0.01 at. fraction (i.e., 1 at. %). Consider a hypothetical compositional ML model that takes F number of input features (denoted as X_i, $i \in [1,2,3,\ldots F]$) to predict a single target parameter Y. At any composition c, we have a set of all feature values. **CoSMoR** is built on the hypothesis that if the composition changes by a discrete amount Δc, then the resultant change in prediction Y can be represented exactly as an accumulation of contributions from all features, i.e.:

$$[\Delta Y]_{c \to c+\Delta c} = \sum_{i=1}^{F} [\Delta Y(X_i)]_{c \to c+\Delta c}$$

Equation 3.1

The partial dependence (PD) of ML model on any feature is reflected by the sensitivity of the ML model to an independent change in that feature. But this PD value depends on the value of all the other features also i.e., at different compositions the PD values will be different. Thus, the term partial-local-dependence (PLD) is used to denote the fact that any PD calculation is valid only locally (i.e., at a particular composition value only). As shown schematically in Figure 3.1a, PLD of the model with respect to feature X_i at any composition c is calculated by changing the value of feature X_i by a small amount δX_i, while keeping all the other features same, and measuring the

change in model output δY. Thus, the PLD (denoted as $m_c^{X_i}$) with respect to feature X_i at composition c is calculated as: $m_c^{X_i} = \left(\frac{\delta Y}{\delta X_i}\right)_c$. Here, δX_i is a user input parameter whose value will depend on the scale of each feature. If all features were normalized to a uniform scale (as recommended for ML model development), same value of δX_i may be used for all features; for e.g., in §3.4 we used a value of 0.02 for δX_i since all features were normalized to [0, 1] scale.

Once we know the PLD values with respect to each feature at composition c, we can calculate the contribution of each feature for any discrete composition change. Suppose we change the composition by one step size i.e., we move from $c \rightarrow c + \Delta c$. For this composition step, as shown in Figure 3.1b, the contribution of any feature X_i (denoted as $[\Delta Y]_{c \rightarrow c+\Delta c}^{X_i}$) towards the overall change in target Y can be calculated as the product of PLD and feature change, i.e.:

$$[\Delta Y]_{c \rightarrow c+\Delta c}^{X_i} = m_c^{X_i} \, [\Delta X_i]_{c \rightarrow c+\Delta c}$$

Equation 3.2

where, $[\Delta X_i]_{c \rightarrow c+\Delta c}$ is the change in value of feature X_i as composition changes from $c \rightarrow c + \Delta c$.

With this, now we can explore the exact contribution of each feature along a continuous composition pathway, as shown schematically in Figure 3.1c. Suppose we take an initial baseline composition c_0 and start increasing the concentration in steps of Δc. After N steps, the concentration is $c_0 + N\Delta c$, and the cumulative contribution of any feature X_i towards the overall change in Y prediction is calculated as:

$$[\Delta Y]_{c_0 \rightarrow c_0+N\Delta c}^{X_i} = \sum_{n=1}^{N} \left[m_{c_0+(n-1)\Delta c}^{X_i} \, [\Delta X_i]_{c_0+(n-1)\Delta c \rightarrow c_0+n\Delta c} \right]$$

Equation 3.3

CoSMoR returns both the step-wise as well as the cumulative feature contributions along a composition pathway, as shown in Figure 3.1c. While the

user is afforded the flexibility to use any or both of these, in most use cases, cumulative contributions may be the preferred choice since plotting these provides a clear and intuitive visualization of both the local changes (represented by variations in slope) as well as cumulative effect (with respect to baseline composition) for feature contributions. Plotting these cumulative feature contributions as a function of compositional variation provides two key insights. Firstly, quantitively-accurate relative contributions of features can be ascertained, which can in turn be associated with the underlying physical phenomena represented by the features. Secondly, different composition pathways can be compared and the similarities or differences in the underlying physics can be understood by comparing these feature contributions. While the **CoSMoR** methodology to extract exact feature contributions will remain same for all ML models, the interpretation of these contributions will be problem-specific. As an example, in §3.4, we have presented the application of **CoSMoR** to phase selection problem in CCAs.

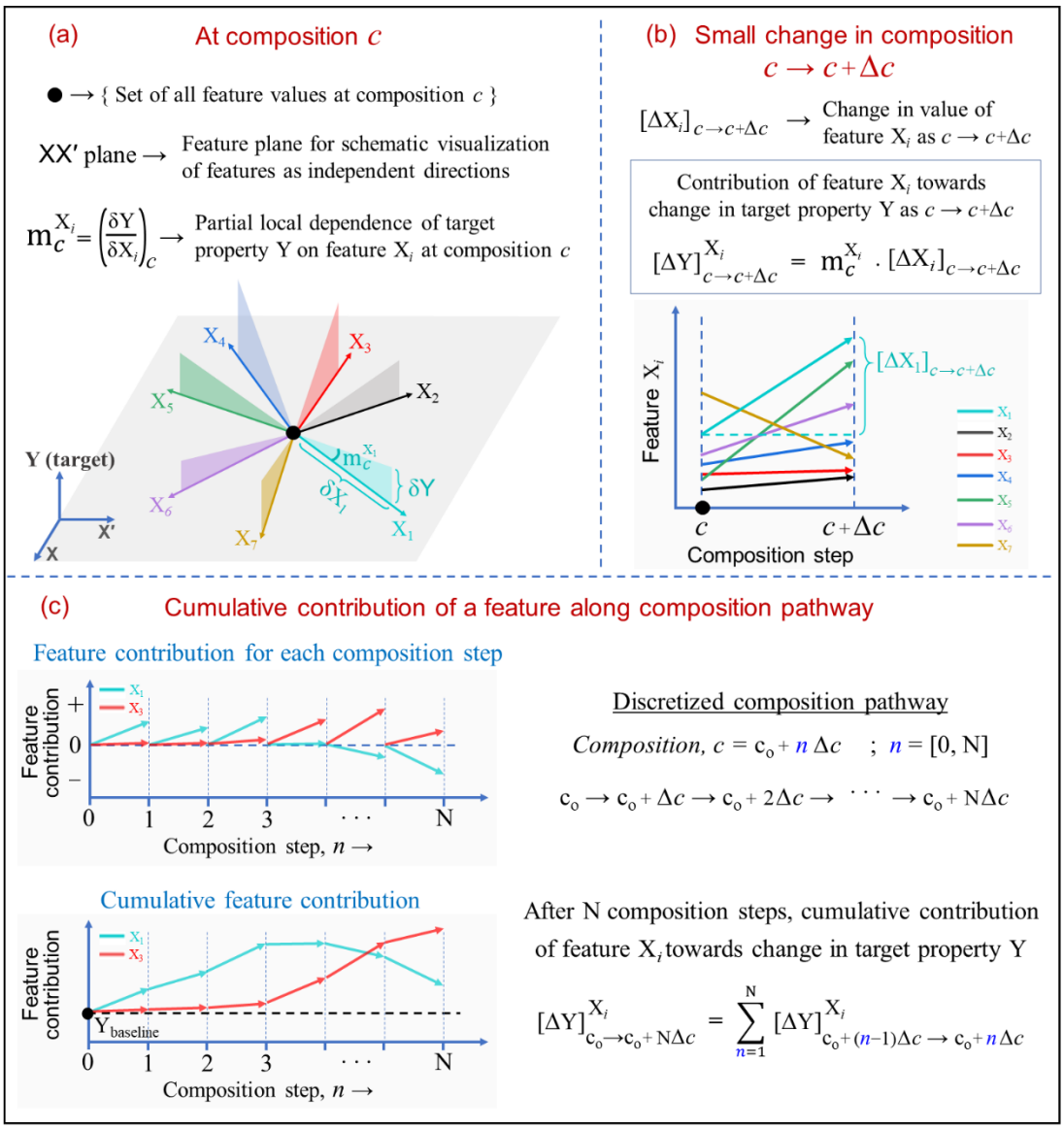

Figure 3.1 Methodology used in CoSMoR to extract exact feature contributions along a compositional pathway. (a) Calculation of local partial dependence ($\delta Y/\delta X_i$) of target property Y with respect to feature X_i at any composition c. (b) Calculation of individual feature contributions towards change in phase probability for each one composition step i.e., as composition changes from $c \rightarrow c+\Delta c$. (c) Calculation of cumulative feature contributions along a continuous composition pathway wherein the initial concentration is treated as baseline.

3.3 Implementation of CoSMoR

While it is possible to implement **CoSMoR** with any programming language (as long as the concerned ML model can be loaded into it), in our work, we have developed it using Python. The workflow starts with the creation of 'cosmor' class and Figure 3.2 shows the flowchart depicting the implementation of **CoSMoR** methodology. We first go over the user inputs required for 'cosmor' class. A composition pathway is represented as a pseudo-

binary system (A_xB_{1-x}) where components A and B can be either elements or stoichiometric combination of elements, for e.g., 'Al', 'AlTi', 'Al2Ti' and 'AlTi2Ni' are all valid component inputs. The concentration of component A (i.e., x) is used as the independent variable and thus, the user must specify that component as A whose concentration has to be varied. For e.g., if effect of 'Al' addition to 'Cu2NiTi' has to be studied, then component A will be 'Al' and component B will be 'Cu2NiTi'. The composition step size (Δc) input is specified in atomic fraction (typically 0.01) and is used to discretize the composition space. The upper and lower bounds for the composition pathway are also required in the form of 'start concentration of component A' and 'end concentration of component A'. These are specified in atomic fractions and must lie between [0, 1] with the additional constraint that start composition is less than end composition. Finally, feature step size (δX_i) input is required for the calculation of PLD values of model with respect to each feature. The current code assumes same value of δX_i for all features and is thus suitable for models where normalized features are used. This functionality will be expanded in future updates to support the use of non-normalized features.

The implementation requires six core functions, as shown in Figure 3.2. Two of these, viz. '*create_features*' and '*make_predictions*', would be specific to each model and thus have to be defined by the user, which the user would have created during the development of ML model. The '*create_features*' function takes the compositions (generated by '*create_alloys*' function) as an input and returns feature values for each composition. The '*make_predictions*' function takes these feature values as input and generates the ML prediction for each composition. More information into the development of these functions, along with examples, has been provided in the code repository at GitHub (§3.7). Rest of the functions are model agnostic and thus do not require any user modification.

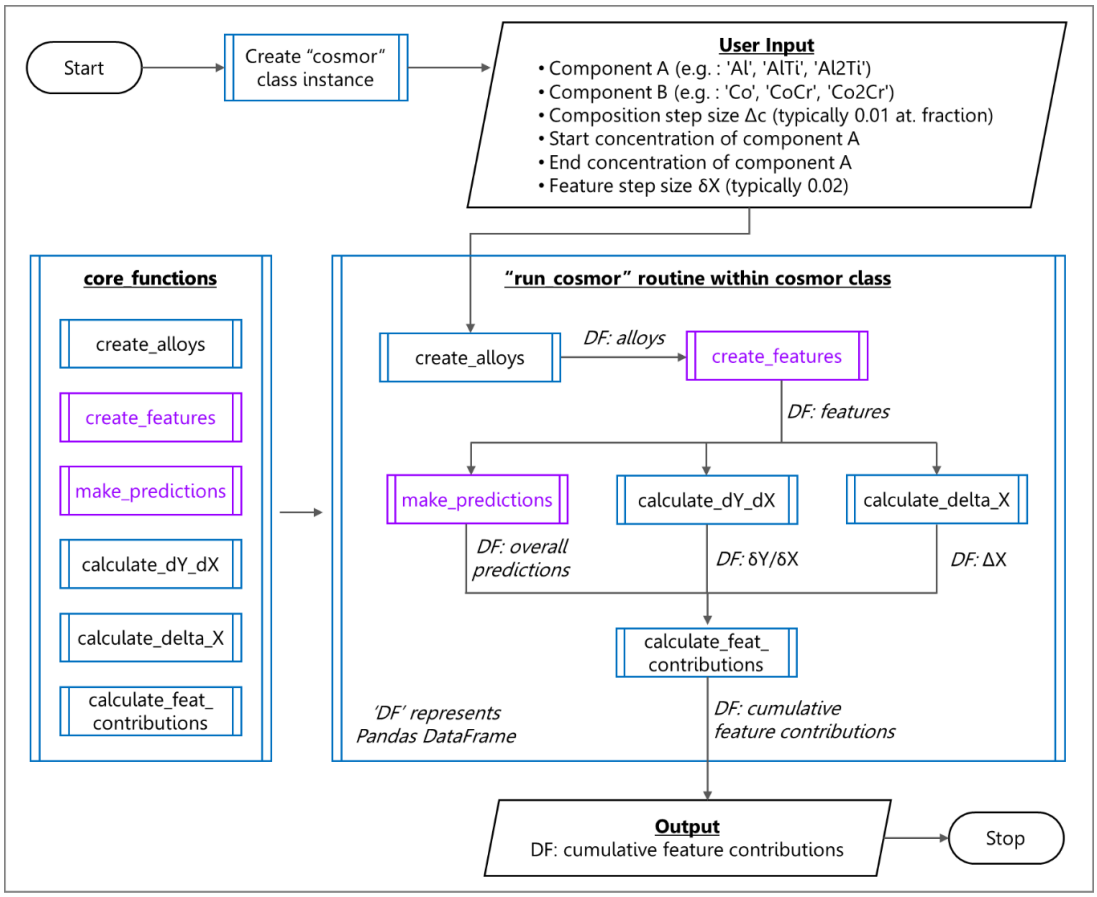

Figure 3.2 Flowchart showing implementation of CoSMoR. The function blocks with purple outline and text (namely, '*create_features*' and '*make_predictions*') are the user-defined functions whereas rest of the functions are in-built in the 'cosmor' code.

3.4 Phase selection in compositionally complex alloys

To demonstrate the application and importance of **CoSMoR** framework, we have applied it to probe the phase selection in CCAs.

3.4.1 Development of ML models

The ML models used here have been reported in our previous work[153]. The training dataset for these models was compiled from the database reported by Borg et al.[154] that contains 426 CCAs with experimentally observed phase information in as-cast condition at room temperature. While the dataset is small, we have shown in our previous works [19,153] that the model learning aligns well with the experimental results in a wide variety of alloy systems. Three separate artificial neural network models were trained for predicting the probability of occurrence of phases. The first model predicts only the

probability of FCC phase i.e. P(FCC), the second model predicts only the probability of BCC phase i.e. P(BCC) and the third model predicts only the probability of IM phase P(IM). Since these probabilities are independent of each other, they can individually vary between [0, 1] and their summation does not have to be equal to 1. While predicting the presence or absence of a phase, a probability threshold of 0.5 has been used i.e., the model predicts the presence of a phase if the predicted P(phase) ≥ 0.5. To elaborate, P(IM) = 0.6 means that the probability for IM phase to occur is 0.6 and we would conclude that it is present based on the threshold of 0.5. But it gives no information on whether FCC and BCC phases are present or absent. For that, we would need to look separately at P(FCC) and P(BCC) values. These models were driven by physics-based features that have been shown to be correlated with phase stabilities in CCAs[19] and a cross-validation accuracy of 91, 95 and 76 % was obtained for BCC, FCC and IM phase respectively. The feature-set comprised of seven features – {Metallic radius asymmetry (δ_{met}), Valence electron count (VEC), Covalent radius asymmetry (δ_{cov}), Elastic modulus asymmetry (δ_E), Average cohesive energy (E^{coh}), Chemical enthalpy of mixing (ΔH^{chem}), Elastic enthalpy of mixing (ΔH^{el})}. Since the focus here is on the implementation of **CoSMoR** to gain physical insights, more details related to the training, validation and performance of these models can be obtained from previous work[153].

3.4.2 Phase variations in M_x-$(CoCrFeNi)_{1-x}$

Since **CoSMoR** brings forth the decision-making process of the ML model along continuous composition pathways, it is pertinent to ascertain whether the ML model is even capable of capturing the continuous variations in the first place. For this purpose, we probed the effect of various element additions (Al, Cu, Mn, Mo and Ta) on phase evolution in CoCrFeNi. Equiatomic quaternary CoCrFeNi is a medium-entropy reduced Cantor alloy that exhibits FCC solid solution phase in as-cast condition [155,156]. We selected CoCrFeNi as the base alloy since the effect of different alloying elements has been studied experimentally for this system [156–169]; and thus, these compositions can be been used as validation checkposts for the phase mappings predicted through

ML model. Figure 3.3 shows the predicted occurrence probabilities of FCC, BCC and IM phases as a function of different alloying additions in CoCrFeNi quaternary along with the experimentally observed phases at some discrete compositions. With the addition of Cu and Mn, only FCC phase is predicted throughout the composition range of 0-0.4 at. fraction, as seen in Figure 3.3(b, c). This matches the experimental observations for Cu [162,165,168] and Mn [157,164] variations.

Addition of Al to CoCrFeNi increases the occurrence probability of BCC phase, as seen in Figure 3.3a, and the model predicts formation of stable BCC phase beyond 9 at. % Al; this aligns closely with the experimental observations made by Chou et al. [169] wherein the alloy structure transitioned from single phase FCC to dual-phase (FCC+BCC) as Al concentration was increased from 8.57 to 11.1 at. %. The model predicts a decrease in occurrence probability of FCC phase as Al increases and the structure transitions completely to BCC phase above 16 at. % Al; this complete transition from FCC→BCC phase has also been observed experimentally by Cieslak et al. [163] and Chou et al. [169] above 15.7 and 20 at. % Al respectively. The model also predicts existence of IM phases above 20 at. % Al; which aligns with the formation of B2 phase above 20 at. % Al, as observed experimentally [163]. Thus, the effect of continuous Al variation has been captured accurately by the ML model as the learned transition boundaries align very closely with experimental observations.

Addition of Mo or Ta to (CoCrFeNi) induces a strong IM formation tendency, as seen in Figure 3.3(d, e), and the model predicts a transition from FCC phase to a dual-phase (FCC+IM) structure above 7 at. % Mo and 3 at. % Ta. This aligns with the experimental studies for varying Mo [160] and Ta [159,161] concentration which showed the formation of IM phase at 9 at. % Mo and 2.5 at. % Ta. Also, the predicted occurrence probability of BCC phase remains comfortably below the 0.5 threshold and thus no BCC phase formation is predicted with Mo or Ta addition in (CoCrFeNi).

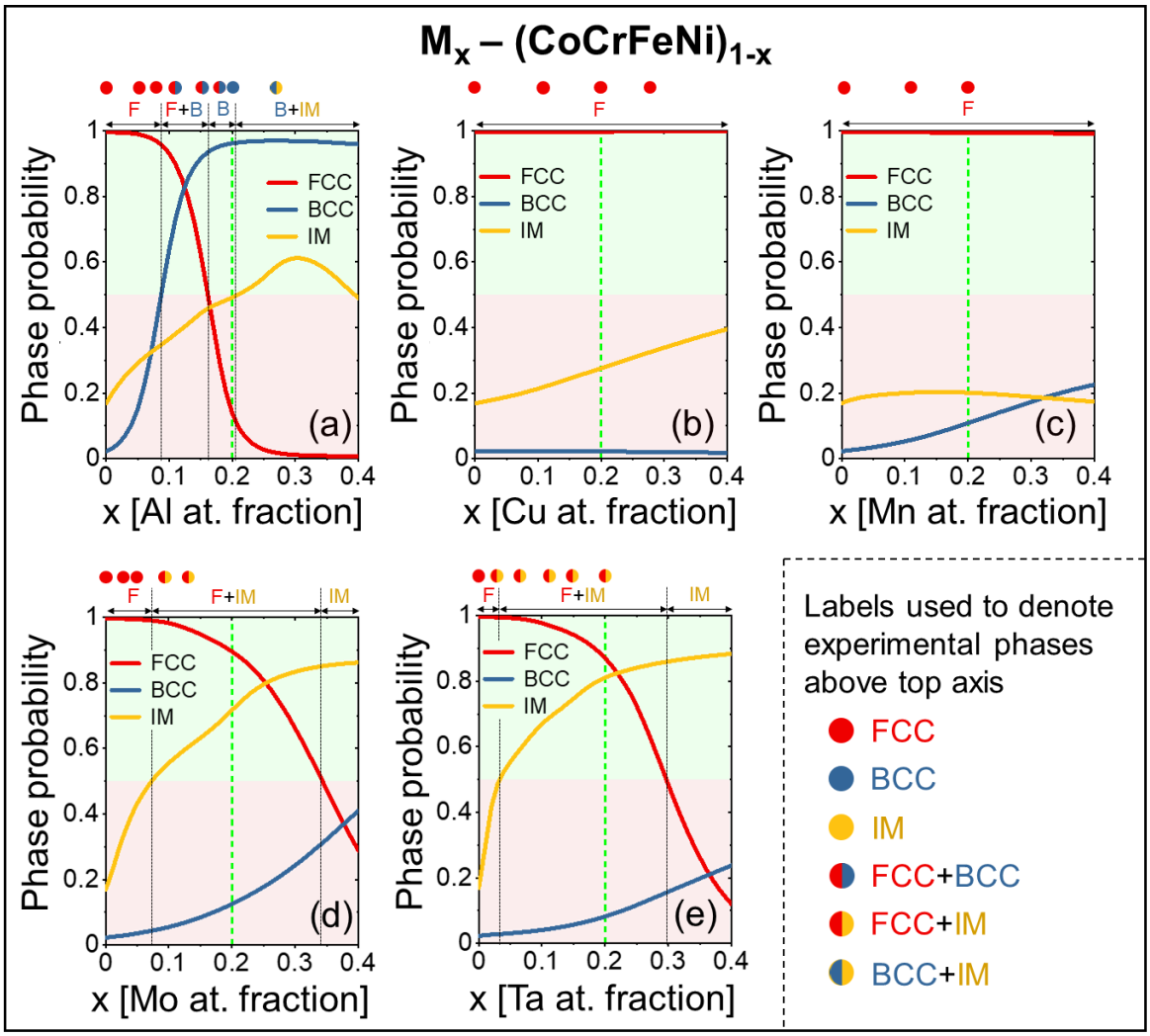

Figure 3.3 Probability of occurrence of FCC, BCC and IM phases as predicted by machine learning models in M_x-$(CoCrFeNi)_{1-x}$ alloy systems. Phase probabilities as a function of (a) Al, (b) Cu, (c) Mn, (d) Mo, and (e) Ta addition in CoCrFeNi alloy. A phase probability (P) threshold of 0.5 has been used to indicate the presence of a particular phase, and correspondingly each plot has been divided into green and red regions representing P≥0.5 (i.e., phase presence) and P<0.5 (i.e., phase absence) respectively. Predicted phase transition boundaries have also been highlighted above the top-axis of each plot, along with the experimentally observed phases at some discrete compositions. The green dotted line (x=0.2) in each plot represents the equiatomic quinary composition.

3.4.3 Decoding the decision-making process in M_x-$(CoCrFeNi)_{1-x}$

To understand the decision-making process used by the ML model for predicting phase probabilities, we implemented **CoSMoR** to calculate exact contribution of individual features towards FCC, BCC and IM phase probabilities in M_x-$(CoCrFeNi)_{1-x}$ alloy systems probed in §3.4.2. The feature contributions in these alloy systems, along with normalized feature values, have been plotted in Figure 3.4 and Figure 3.5 wherein x=0 has been used as

the baseline composition. A quick observation of these trends shows that: **(a)** the feature contributions vary non-linearly, sometimes even non-monotonically, with respect to feature values, **(b)** same features contribute differently towards occurrence probability of different phases, viz. FCC, BCC and IM, and **(c)** the relative importance of features changes as we move from one system to another. These observations indicate that the decision-making process of the ML model is not purely statistical, and that it updates dynamically as the alloy system changes; thereby highlighting the cognizance of the model to underlying physics that drives the phase selection process in CCAs. Here, we discuss the findings that stand out on closer inspection.

VEC and δ_{met} contributions dominate the occurrence probability of FCC and BCC phases, as seen with respect to addition of Al, Mo or Ta to (CoCrFeNi) in Figure 3.4(a, b) Figure 3.5(a, b) and Figure 3.5(e, f), respectively. As Al, Mo or Ta concentration increases, VEC decreases whereas δ_{met} increases, but both VEC and δ_{met} contribute strongly towards a decrease in FCC and increase in BCC phase probability. Also, the magnitude of feature contributions changes sharply in the FCC→BCC transition domain (9-16 at. % Al) observed from experimental studies[163,169]. This aligns with the previous observations wherein VEC has been shown to be strongly associated with the stability of FCC and BCC phases[111,153,170,171]. Contrary to these systems, the addition of Cu or Mn to (CoCrFeNi) does not induce any significant change in the occurrence probability of FCC or BCC phase, as seen in Figure 3.4(e, f) and Figure 3.4(i, j) respectively. Even though δ_{met} increases with addition of Mn (Figure 3.4l), its contribution towards FCC and BCC phase probability is negligible and marginal respectively. This aligns with previous observations[153] that the VEC acts as a classifier wherein the importance of not only VEC , but also that of the other features, towards occurrence of FCC/BCC phases is dictated by the VEC value. As seen with Al addition, the contributions of all features towards P(FCC) and P(BCC) sees a sudden changes beyond a threshold VEC value. Thus, it appears that the model has successfully

learnt these physics-based relationships to establish the stability of FCC and BCC phases in CCAs.

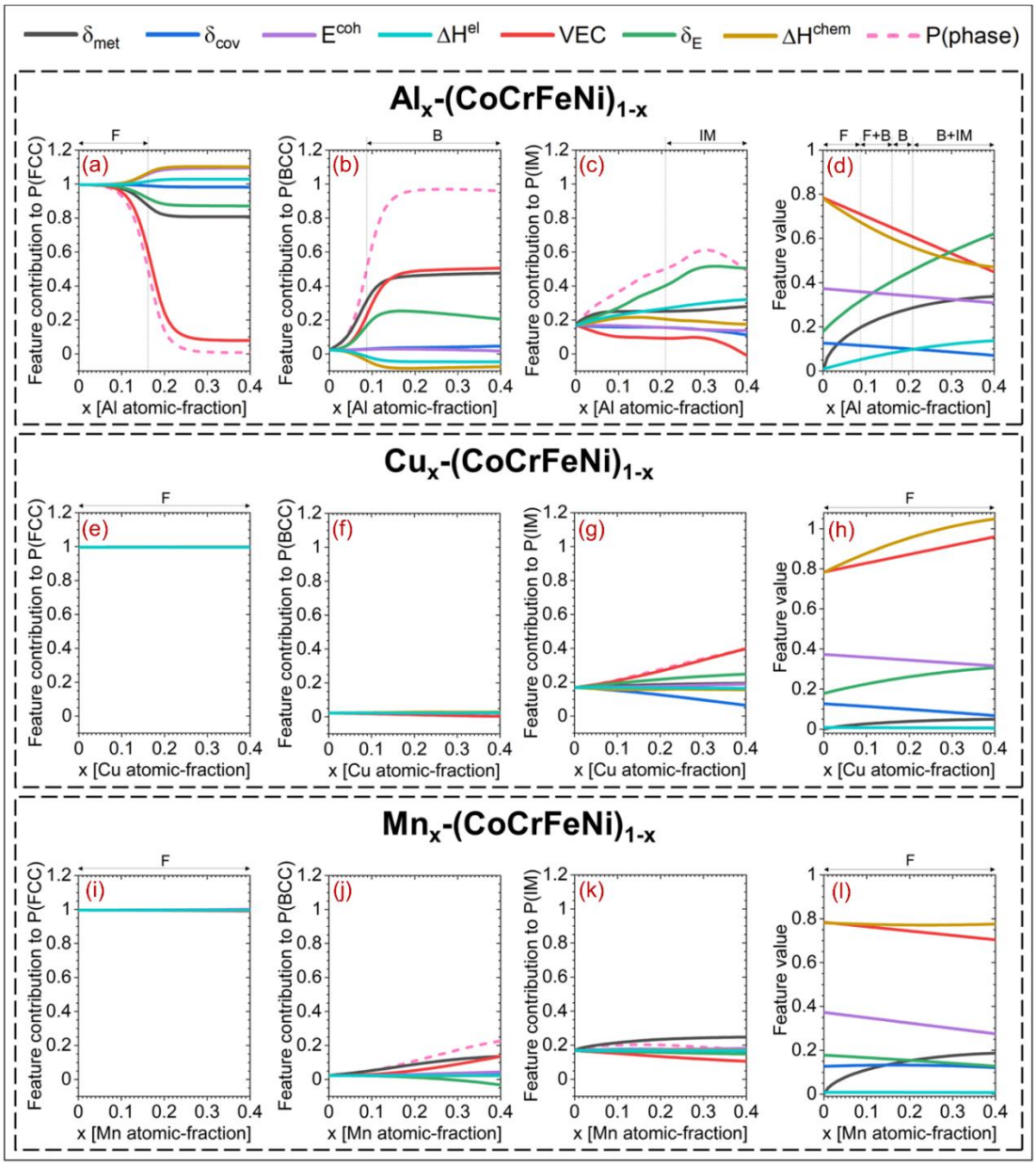

Figure 3.4 Interpreting the decision-making process of phase selection ML models using CoSMoR. Cumulative contribution of each feature towards the overall phase probability P(phase) in (a-c) Al_x-$(CoCrFeNi)_{1-x}$, (e-g) Cu_x-$(CoCrFeNi)_{1-x}$ and (i-k) Mn_x-$(CoCrFeNi)_{1-x}$ alloy systems. Normalized feature values as a function of (d) Al, (h) Cu and (l) Mn concentration. The feature contributions here are cumulative contributions along the composition pathway with respect to baseline composition of x=0.

While FCC and BCC phase occurrence is dominated by VEC and δ_{met}, the IM phase probability in M_x-$(CoCrFeNi)_{1-x}$ [M={Al, Mo, Ta}] is dominated by three

feature contributions: δ_{cov}, δ_E and ΔH^{el}. With the addition of Al, both δ_E and ΔH^{el} increase (Figure 3.4d) and consequently drive the formation of IM phase to a large extent (Figure 3.4c), but the contribution of δ_E to IM formation is considerably more due to a much steeper increase in δ_E feature value. On the other hand, with addition of Mo and Ta, δ_{cov} and ΔH^{el} contribute significantly toward the IM phase formation, whereas the contribution of δ_E is almost negligible, as seen in Figure 3.5(c, g). This is because δ_{cov} increases sharply with Mo and Ta addition whereas δ_E saturates at low values, as seen in Figure 3.5(d, h). To read further into these observations, we need to discuss how these features (δ_{cov}, δ_E and ΔH^{el}) could be correlated to the formation of intermetallics. The bond formation in metals and alloys always has some covalent character[172] that is expected to be affected by δ_{cov}, which is a measure of asymmetry in bond lengths when constituent elements participate in covalent bond formation. The covalent nature is especially dominant in the intermetallics wherein a large δ_{cov} can dictate preferential formation of certain atomic-pairs and coordination symmetries corresponding to favorable atomic-size ratios. The Young's modulus (E) is correlated to the strength of interatomic bonds as it can be estimated from the potential energy vs. separation curve. Since multiple elemental interactions are possible in CCAs, δ_E is an indirect measure of the asymmetry in bond-strengths of different atomic-pairs. A high δ_E would indicate the presence of certain atomic pairs with considerably higher or lower bond-strengths that may promote ordering or clustering tendencies, and thus, dictate formation of intermetallics. The elastic enthalpy of mixing ΔH^{el}, calculated using the classical elasticity method by Eshelby and Friedel[173–175], is a measure of the elastic energy generated due to the internal strains induced by size asymmetry between constituent elements. Since the calculation of ΔH^{el} considers both local distortion (through volume corrections) and bonding characteristics (indirectly through shear and bulk modulus), a large ΔH^{el} represents instability induced in the solid-solution phase due to excessive strain-energy and is expected to result in the formation of ordered structures that can relieve some of this strain-energy. Thus, all three features, viz. δ_{cov}, δ_E and ΔH^{el}, are closely correlated to the IM phase formation

in CCAs, and the fact that ML model gives significant and selective weightage to these features strongly indicates that it has successfully learnt the underlying physics.

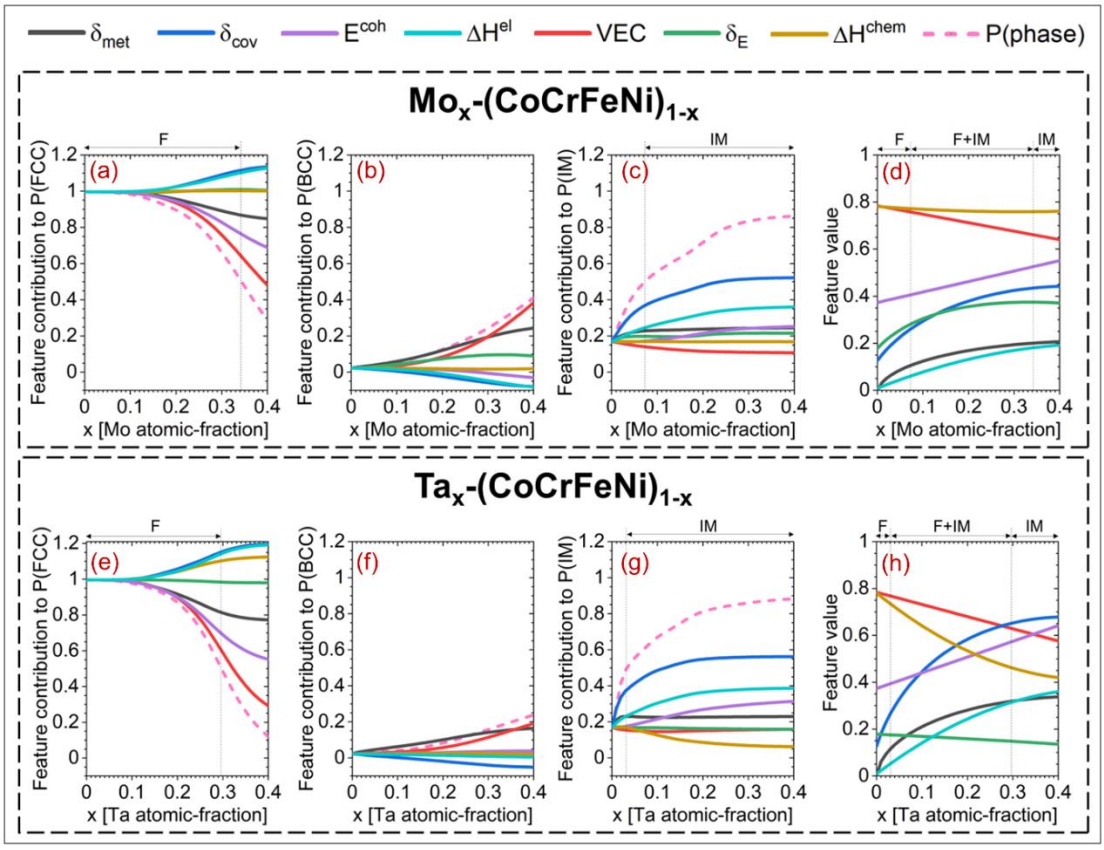

Figure 3.5 Interpreting the decision-making process of phase selection ML models using CoSMoR. Cumulative contribution of each feature towards the overall phase probability P(phase) in (a-c) Mo_x-$(CoCrFeNi)_{1-x}$ and (e-g) Ta_x-$(CoCrFeNi)_{1-x}$ alloy systems. Normalized feature values as a function of (d) Mo and (h) Ta concentration. The feature contributions here are cumulative contributions along the composition pathway with respect to baseline composition of x=0.

3.4.4 Exploring Fe_x-$(AlCoCr_{0.5}Ni_{2.5})_{1-x}$ and $(TaNb)_x$-$(MoW)_{1-x}$ alloy systems

The implementation of **CoSMoR** in M_x-$(CoCrFeNi)_{1-x}$ alloy systems shows a strong dependence of FCC and BCC phase occurrence on VEC. This poses an interesting question as to whether the ML model can capture phase stabilities in systems where VEC remains constant. To address this, we looked at Fe_x-$(AlCoCr_{0.5}Ni_{2.5})_{1-x}$ alloy system that maintains a constant VEC of 8 and has been studied experimentally by Liu et al.[47]. One would expect this system to have

FCC phase throughout the compositional range, but Liu et al. observed a transition from (FCC+BCC) dual-phase structure at x=0 to an almost single-phase FCC structure at x=0.47. The ML model captures this transition almost perfectly, as seen in Figure 3.6(a, b), and the interpretation framework reveals that the extinction of BCC phase accompanying Fe addition is driven primarily by the decrease in δ_{met} and δ_E. δ_{met} is a measure of metallic radius asymmetry between the component elements and increase in δ_{met} contributes to an increase in BCC and decrease in FCC phase probability, as seen in Figure 3.4(a, b), Figure 3.5(a, b, e, f) and Figure 3.6b. This is expected since BCC phase, due to its more open structure, can accommodate the larger size asymmetry more easily as compared to the close packed FCC phase.

CoSMoR was further used to explore another interesting alloy system that contradicts some of the earlier observations related to IM formation. In M_x-$(CoCrFeNi)_{1-x}$ alloy systems, δ_{cov}, δ_E and ΔH^{el} features contribute strongly towards the occurrence of IM phases. Especially with Al addition, the increase in δ_E contributed significantly to the formation of IM phases at high Al concentration. But on the contrary, $(TaNb)_x$-$(MoW)_{1-x}$ system shows a very steep increase in δ_E value as (TaNb) concentration increases (Figure 3.6h), but experimentally no IM formation is observed in this system[176]. This raises an interesting question as to whether the ML model can predict this behaviour and how this decision would be made based on all feature values. The ML model does not predict any IM formation in this system, as seen in Figure 3.6g, which aligns with the experimental observations[176] wherein TaNbMoW forms a simple single-phase BCC structure. This can be attributed to the fact that all the other drivers for IM formation are virtually non-existent in this system since: **(a)** there are no significant lattice strains as δ_{met} and ΔH^{el} are almost zero, and **(b)** no strong chemical interactions as $-6.38<\Delta H^{chem}<-0.22$ kJ/mol, and **(c)** δ_{cov} is almost zero. This indicates that a high δ_E alone is not sufficient for IM formation, and that the model understands these nuances in the feature variations that are associated with occurrence of IM phases.

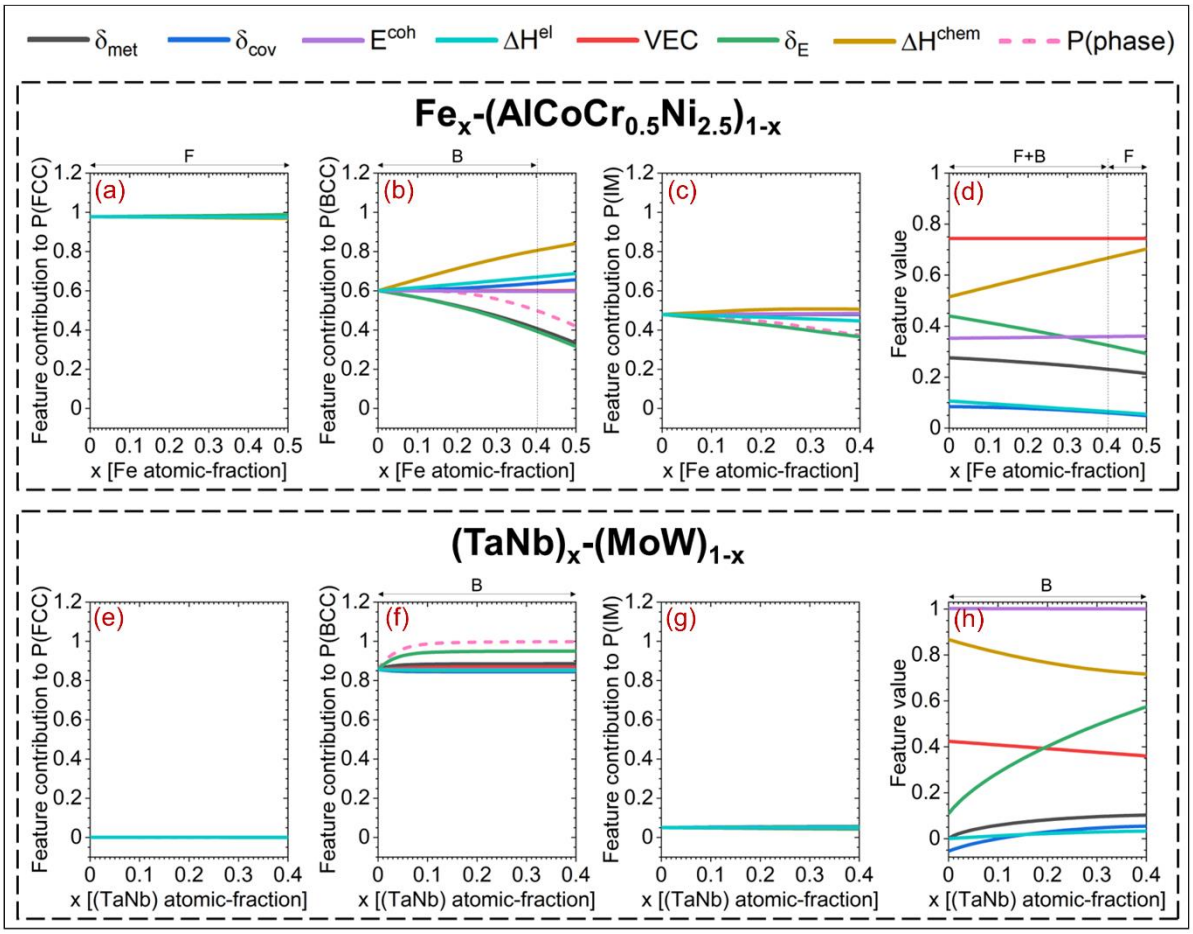

Figure 3.6 Interpreting the decision-making process of phase selection ML models using CoSMoR. Cumulative contribution of each feature towards the overall phase probability P(phase) in (a-c) Fe_x-$(AlCoCr_{0.5}Ni_{2.5})_{1-x}$ and (e-g) $(TaNb)_x$-$(MoW)_{1-x}$ alloy systems. Normalized feature values as a function of (d) Fe and (g) (TaNb) concentration. The feature contributions here are cumulative contributions along the composition pathway with respect to baseline composition of x=0.

3.5 Use case scenarios for CoSMoR

CoSMoR is a generalized framework that can be applied to any ML model (irrespective of the type or complexity of the models and features used) provided that the model has been built using features that are a direct function of material composition. Here we discuss the scenarios wherein **CoSMoR** can be used to evaluate, interpret and improve the compositional ML models that have been built for predicting material properties.

3.5.1 Evaluating the nature of fit

The development and optimization of ML models is driven by the maximization of statistical performance that is quantified using a variety of

metrics such as mean absolute error, R^2 value, percentage error, precision, recall etc. But while the statistical nature of fit is routinely evaluated, the physical nature of the fit (which implies the consistency between the ML model decision-making process and the known physical rules) is often ignored resulting in a big question mark as to how well the model is expected to perform when extrapolated to novel compositions. It is an even bigger problem when using ML models (such as neural networks) that have multiple minima corresponding to similar statistical performance but different learning states, since now one can end up with different models with similar statistical performance. **CoSMoR** addresses these concerns by enabling the evaluation of physical nature of fit for compositional ML models through the comparison of feature contributions with well-established physical rules. For example, VEC is known to have a strong impact on FCC and BCC phase stability in CCAs and thus when we probe the model decision-making process in M_x-$(CoCrFeNi)_{1-x}$ alloys with **CoSMoR**, the fact that VEC contributions closely follow the P(FCC) and P(BCC) variations strongly indicates that the model has learnt this rule. On the other hand, if it had so happened that VEC contributions didn't align with the P(FCC) and P(BCC) variations, we could have safely rejected the model even if it showed good statistical accuracy. Thus, users can validate the physical consistency of their compositional ML models by using **CoSMoR**.

3.5.2 Revealing the drivers of change

The black-box treatment of ML models obscures their decision-making process leaving open questions as to how exactly the model outcomes are computed. Implementation of **CoSMoR** provides the exact feature contributions along specific composition pathways and thus reveals material-specific insights into what drives the changes in target property as predicted by the ML model. This understanding can be both at feature level and physical level, as elaborated here.

Firstly, **CoSMoR** identifies features that drive the changes as a function of composition which can lead to new fundamental insights and design

principles. For example, since the advent of data-driven models for CCAs, the intermetallic formation has been frequently assumed to be driven by large metallic radius asymmetry (δ_{met}). But the implementation of **CoSMoR** in this work shows that it is actually the covalent radius asymmetry that is considerably more critical for intermetallic formation, and that δ_{met} is more relevant for FCC and BCC phase stability rather than intermetallic formation. Similarly, even though δ_{met} and elastic enthalpy of mixing (ΔH^{el}) features are highly correlated, the intermetallic formation is predominantly driven by ΔH^{el}. Thus, **CoSMoR** can provide new insights into the relevance and significance of features used in the ML model.

Secondly, when combined with experimental observations and *ab-initio* calculations, **CoSMoR** can lead to insights into the physical origins of the target property predicted by the ML model. Suppose we have a compositional ML model that uses a set of input material descriptors (such as VEC, δ_{met}, δ_{cov}, ΔH^{el}, etc.) to predict the strength of an alloy. Using **CoSMoR**, we can identify the origin of strength at feature level while the DFT calculations and experimental results can assist in identification of baselines as to what these origins at feature level may represent at a physical level within the material. For example, one of the expected observations in this case would be that whenever FCC↔BCC transitions occur, the contribution of VEC towards the resultant changes in strength becomes significant. Such baselines, once established, will allow exploring the novel compositional spaces using **CoSMoR** to predict not only the variations in predicted property, but also the underlying physical phenomena that may be responsible for these variations. In our previous work[95], we have shown how this methodology can be used to extract physical origins of hardness in CCAs.

The model-agnostic implementation offered by **CoSMoR** allows its use for both continuous as well as discrete decision-based models such as decision trees and random forest (RF). To illustrate this, we developed RF models for the same problem presented in this work i.e., presence/absence of FCC, BCC and IM phases in CCAs and implemented **CoSMoR** to probe the decision-making

process of these RF models along some of the compositional spaces. The performance of these models is inferior to the neural network models and they were developed only to illustrate the applicability of **CoSMoR** to such models. The results in Figure 3.7 show that **CoSMoR** successfully brings out the contribution of different features towards the phase occurrence for these RF models also. The instability of PLDs (which may occur in such discrete models) at phase transition boundaries does not appear to be a problem for FCC and BCC models. But, for the IM model, we do see instability in both the model output as well as the feature contributions. In fact, the instability in feature contributions could largely be due to the instability in the model output itself because the IM RF model was the least accurate model with F1 score of 0.74 as compared to FCC and BCC models with F1 score of 0.92 and 0.94 respectively. Thus, while the breakdown of continuous models using **CoSMoR** will always be more accurate as compared to that for decision-based models, we believe that certain best practices can improve the performance for RF models: (a) Reducing the complexity of the RF by controlling the depth and splitting criteria, (b) Preventing overfit of the model, and (c) Improving generality of the model by using bootstrapping or other techniques.

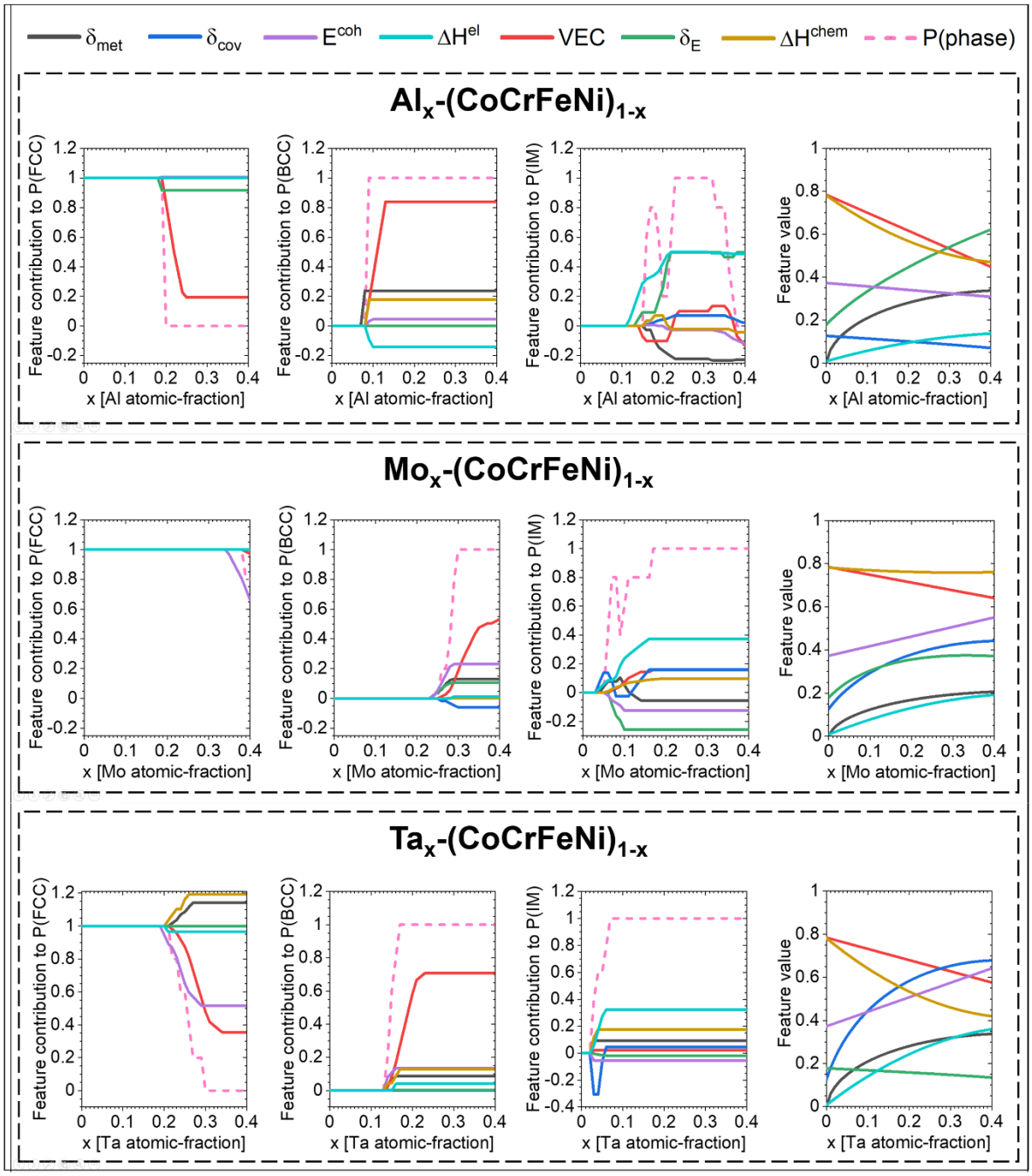

Figure 3.7 CoSMoR applied to random forest models for FCC, BCC and Intermetallic phase prediction in Al_x-$(CoCrFeNi)_{1-x}$, Mo_x-$(CoCrFeNi)_{1-x}$, Ta_x-$(CoCrFeNi)_{1-x}$.

3.6 Conclusion

In this chapter, we have presented the model-agnostic **Co**mpositional **S**timulus and **Mo**del **R**esponse (**CoSMoR**) framework, which is an interpretation framework capable of decoding the decision-making process of machine

learning models trained for material properties along continuous compositional pathways. A compositional pathway is defined as a pseudo-binary A_xB_{1-x} where components A and B can be either elements (e.g., 'Al' or 'Ti') or any stoichiometric combination of elements (e.g., 'CrFe', 'Cr_2Fe' or 'Cr_2FeNi_2'). As composition changes, the ML model predictions also change; but the variations in model predictions cannot be explained if the ML model is treated as a black-box. **CoSMoR** addresses this by calculating the exact contribution of each feature along any compositional pathway based on the partial-local-dependence of ML model (with respect to each feature) and the sensitivity of that feature (with respect to the composition). **CoSMoR** offers three unique advantages. Firstly, it adopts a model agnostic approach and thus can be applied to any compositional ML model, irrespective of the algorithm used. Secondly, the causality of model understanding is shifted to variations in alloy composition rather than some arbitrary feature variations. This enables integration of the understanding derived from **CoSMoR** with *ab-initio* calculations and experimental results to correlate the feature contributions with physical phenomenon. Thirdly, the feature contributions extracted by **CoSMoR** are quantitatively exact with respect to the model decision-making process. This enables direct and reliable comparison between multiple composition pathways to assess similarities and differences between how ML model treats these different alloy systems. We have showcased the importance of **CoSMoR** through implementation on phase selection problem in compositionally complex alloys. Individual feature contributions towards predicted phase probabilities in a variety of alloy systems, viz. M_x-$(CoCrFeNi)_{1-x}$ [M={Al, Cu, Mn, Mo, Ta}], Fe_x-$(AlCoCr_{0.5}Ni_{2.5})_{1-x}$ and $(TaNb)_x$-$(MoW)_{1-x}$ were obtained using **CoSMoR**. The interpretation results show that the ML model has learnt the underlying physics associated with phase stability and point toward the features that are essential for predicting relative stability of FCC/BCC phases and formation of Intermetallic phase. Thus, **CoSMoR** enables a systematic and insightful exploration of compositional spaces using ML models to not only validate the physical nature of fit but to also extract material-specific insights as to how the target property manifests in a material.

3.7 Research data

The **CoSMoR** code, along with the examples, is available at 'IDEAsLab-Materials-Informatics' organization page on GitHub at:

https://github.com/IDEAsLab-Materials-Informatics/CoSMoR

Chapter 4: Predicting short-range order in compositionally complex alloys using variational autoencoders

4.1 Introduction

The presence of multiple elements in high concentrations in CCAs results in complex interatomic interactions that may lead to microstructural complexity via intermetallic formation and/or phase separation into multiple solid-solution phases. Even the disordered phases often exhibit atomic short-range order (SRO) owing to the presence of energetically favorable atom pairs. While SRO has been long known to affect the mechanical, electrical and magnetic properties in a variety of materials, its impact on the properties of CCAs has gained significant attention only in the recent years [5,7,95,177–179]. The experimental measurement of SRO is extremely difficult and thus density functional theory (DFT) based computational techniques have been the mainstay for study of SRO in materials. But even these pose a difficulty when applied to CCAs owing to the extremely large number of possible atomic configurations in any given quaternary or higher-order alloy. This problem is further compounded by the astronomical compositional space for CCAs, thereby making the high-throughput exploration of SRO in CCAs with DFT-based techniques an extremely difficult task. Furthermore, any given pair with identical composition, may show starkly different SRO depending upon the

---

D Beniwal, S Tripathi, P Singh, N Sardana, PK Ray, *Predicting short-range order in compositionally complex alloys using variational autoencoders*, **Under preparation**

alloy chemistry. As an example, one can consider the Al-Cr binary pair. In an AlFeCoCrNi alloy, this pair typically shows clustering, with Al and Cr staying away from each other. The same pair, upon the addition of Zn, shows a complete reversal in their tendency to cluster apart and order together instead [133]. In this work, we present a novel machine learning (ML) framework to reliably classify all binary pairs in a given CCA as ordering or clustering and to quantitatively predict the SRO parameter for each binary pair, dependent on the overall alloy composition. Any given alloy composition is first transformed into a unique three-dimensional feature stack (comprising of binary pair descriptors) which is then mapped to a two-dimensional matrix of SRO parameters using a variational autoencoder. As the study of SRO in CCAs is still in a nascent stage, a significant stream of data is expected to appear in the coming times. Thus, to enable easy integration with future data, the ML framework has been wrapped as an automated workflow that can quickly and automatically retrain the models as and when more data becomes accessible.

4.2 Quantification of SRO

The SRO in a material arises from preferential occurrence of atomic pairs that can be conveniently quantified using Warren-Cowley parameters [177,178,180–182] which measure the extent to which spatial correlation of atoms varies relative to a perfectly random atomic distribution. While a binary alloy has single SRO parameter, a multicomponent alloy has multiple SRO parameters, one for each possible binary pair (μ-ν), that are defined as:

$$\alpha_{\mu\nu}^{(r)} = 1 - \frac{P_{\mu\nu}^{(r)}}{c_\mu c_\nu}$$

Equation 4.1

where $P_{\mu\nu}^{(r)}$ is the probability of finding μ-ν pair within a neighbor distance (shell) r, and c_μ and c_ν are the overall concentrations of μ and ν elements in the alloy respectively. If all elements are distributed randomly, $P_{\mu\nu}^{(r)}$ is equal to $c_\mu c_\nu$ and thus $\alpha_{\mu\nu}^{(r)} = 0$ for all values of r; implying no SRO in the material. If μ and

ν attract each other, $P_{\mu\nu}^{(r)} > c_\mu c_\nu$ and $\alpha_{\mu\nu}^{(r)} < 0$; whereas if they repel each other, $P_{\mu\nu}^{(r)} < c_\mu c_\nu$ and $\alpha_{\mu\nu}^{(r)} > 0$. Thus, the Warren-Cowley SRO parameters have a finite range $\left(-\frac{\min(c_\mu,c_\nu)^2}{c_\mu c_\nu} \leq \alpha_{\mu\nu}^{(r)} \leq 1\right)$ wherein the positive SRO indicates clustering apart and the negative SRO indicates ordering together.

4.3 Development of the SRO database

The SRO database used in this work was developed by Prashant Singh at Ames Lab, USA. The density-functional theory-based thermodynamic linear-response theory developed by Singh et al. [177] allows calculation of Warren-Cowley SRO parameters $\alpha_{\mu\nu}(\mathbf{k};T)$ for all pairs simultaneously in a N-component system such as CCAs. After which, the real-space parameters $\alpha_{\mu\nu}^{ij}$ are obtained over neighbor shells by inverse-Fourier transform, as done experimentally. The SRO dictates the pair probabilities $P_{\mu\nu}^{ij} = c_\mu^i c_\nu^j\left(1 - \alpha_{\mu\nu}^{ij}(T)\right)$ in disordered alloys with temperature T [3]. The free energy from DFT, the linear-response is analytically expanded to second-order in site-occupation probabilities (i.e., concentrations) c_μ^i and c_ν^j for atom-types μ, ν at lattice sites i,j to obtain the chemical stability (Hessian) matrix $S_{\mu\nu}^{(2)}(\mathbf{k};T)$ for the disorder alloy represented in the thermodynamically-averaged unit cell [177]. Importantly, $S_{\mu\nu}^{(2)}(\mathbf{k};T)$ are thermodynamically averaged chemical pair-interchange energies for all μ-ν pairs, which dictate the SRO directly from the electronic structure (dispersion) of the homogeneously disordered alloy.

The SRO database, created by Prashant Singh at Ames Lab, USA, comprised of 41 unique alloys that include ternary, quaternary and quinary alloys and span a compositional space of 14 elements – {Al, Ti, V, Cr, Mn, Fe, Co, Ni, Zr, Nb, Mo, Hf, Ta, W}. The total number of binary pairs within these 41 alloys equals 240. For the implementation of ML framework, the tabular dataset was then transformed into three-dimensional binary feature arrays (that act as the input) and two-dimensional SRO matrix (that acts as the output). This transformation process has been detailed in §4.4.1.

4.4 Machine learning framework

The formulation of Warren-Cowley parameters (as discussed in §4.2) indicates that the SRO for μ-ν atomic pair depends on two terms viz. $P_{\mu\nu}^{(r)}$ and $c_\mu c_\nu$. The $c_\mu c_\nu$ term is trivial as it is simply the product of individual element concentrations c_μ and c_ν. But the $P_{\mu\nu}^{(r)}$ term is non-trivial as it effectively captures atomic distribution in favorable configurations dictated by binary interactions. Since $c_\mu c_\nu$ becomes a constant as soon as the alloy composition is fixed, $P_{\mu\nu}^{(r)}$ may be thought of as a transformation factor that modifies $c_\mu c_\nu$ value to yield SRO of μ-ν pair. But the key point to note is that while $c_\mu c_\nu$ depends only on concentration of elements in μ-ν atomic pair, $P_{\mu\nu}^{(r)}$ is influenced by the behaviour and properties of all the binary pairs that exist in the material. This aligns with previous observations wherein SRO appears to be governed by the strength of interactions between multiple pairs of elements rather than simple chemical or physical characteristics [178,179,183]. The fundamental hypothesis behind the ML methodology adopted in this work is that – **(a)** given a fixed alloy composition, the Warren-Cowley SRO parameters can be determined if we simultaneously know the strength of interactions for all possible atomic pairs, and **(b)** the interaction strength of an isolated binary pair is linked to the thermodynamic and physical features associated with the interaction of constituent elements.

4.4.1 Alloy representation as a binary-pair feature stack

To implement the above hypothesis, we represent each alloy with a two-dimensional $c_i c_j$ array ($\mathbf{C}$) of shape (14x14) wherein the index of rows (i) and columns (j) map to the element list: {Al, Ti, V, Cr, Mn, Fe, Co, Ni, Zr, Nb, Mo, Hf, Ta, W}, as shown in Figure 4.1a. Here, the non-diagonal elements take a value of $c_i c_j$ i.e., $\mathbf{C}_{ij}\big|_{i\neq j} = c_i c_j$ whereas the diagonal elements take a value of zero i.e., $\mathbf{C}_{ij}\big|_{i=j} = 0$. The $\mathbf{C}$ array is further rescaled to [0, 1] range using min-max normalization with 0 and 0.25 as minimum and maximum values of $c_i c_j$. Thus, any alloy within the compositional space of these 14 elements can be

mapped to a unique **C** array of form shown in Figure 4.1a. Similarly, the full set of SRO parameters of all binary pairs in an alloy are represented as an SRO array (**S**) of shape (14x14) as shown in Figure 4.1e. We create a separate three-dimensional feature stack (**F**) of shape (14x14x9), as shown in Figure 4.1b, that contains 9 binary feature arrays (each of shape 14x14) stacked on top of each other. The nine binary features used here have been detailed in Table 4.1 and the feature arrays (containing values for all atomic pairs) have been shown in Figure 4.2. Each layer of **F** array is individually rescaled to [0, 1] range using min-max normalization and this normalized binary feature stack **F**, containing values of all features for all binary pairs, acts as a reference stack. For each alloy, a new transformed feature stack (**T**), as shown in Figure 4.1c, is created by elementwise multiplication of **C** array with each layer of **F** i.e., $\mathbf{T}_{kij} = \mathbf{F}_{kij}.\mathbf{C}_{ij}$. Since **C** is unique for each alloy, **T** is also a unique three-dimensional representation of each alloy composition. Thus, the machine learning approach in this work has been framed using the transformed feature stack **T** as the input representation of each alloy that is then mapped to the SRO array **S** using variational autoencoders, as depicted in Figure 4.1.

Figure 4.2 Figure 4.3 Figure 4.4 Figure 4.5 Figure 4.6

4.4.2 Variational autoencoder: Architecture and training

A variational autoencoder (VAE) is a probabilistic generative model, built on neural network architecture, that comprises of two components – encoder and decoder. The encoder compresses the input to a significantly reduced latent space that is sampled from a distribution whereas the decoder decompresses the latent space and maps it back to a higher dimensional space. The architecture of the VAE model used in this work has been shown schematically in Figure 4.3. The VAE takes the transformed feature stack **T** of shape (14x14x9) as input and the encoder transforms it to a latent vector of size 20 which is then expanded and mapped to the SRO array **S** of shape (14x14x1) by the decoder.

Table 4.1 Description of nine features used to create the binary feature stack shown in Figure 4.2. The feature values for all binary pairs were calculated assuming an equiatomic concentration i.e., c_A=c_B=0.5

#	Description	Abbreviation	Formula for A-B binary pair
1	Miedema's chemical enthalpy of mixing	ΔH^{ch}	$c_A c_B\ (f_B^A . \Delta \bar{H}_{A\ in\ B}^{int} + f_A^B . \Delta \bar{H}_{B\ in\ A}^{int})$
2	Miedema's elastic enthalpy of mixing	ΔH^{el}	$c_A c_B (c_B\ \Delta \bar{H}_{A\ in\ B}^{el} + c_A\ \Delta \bar{H}_{B\ in\ A}^{el})$
3	Valence electron count	VEC	$c_A . \mathrm{VEC}_A + c_B . \mathrm{VEC}_B$
4	Spin magnetic moment	μ_S	$c_A . \mu_S^A + c_B . \mu_S^B$
5	Mismatch in Allen Electronegativity	$\Delta\chi$	$c_A c_B \lvert \chi_A - \chi_B \rvert$
6	Mismatch in electron density over Wigner-Seitz cell boundary	Δn_{ws}	$c_A c_B \lvert n_{ws}^A - n_{ws}^B \rvert$
7	Mismatch in metallic radius	Δr_{met}	$c_A c_B \lvert r_{met}^A - r_{met}^B \rvert$
8	Mismatch in covalent radius	Δr_{cov}	$c_A c_B \lvert r_{cov}^A - r_{cov}^B \rvert$
9	Mismatch in elastic modulus	ΔE	$c_A c_B \lvert E_A - E_B \rvert$

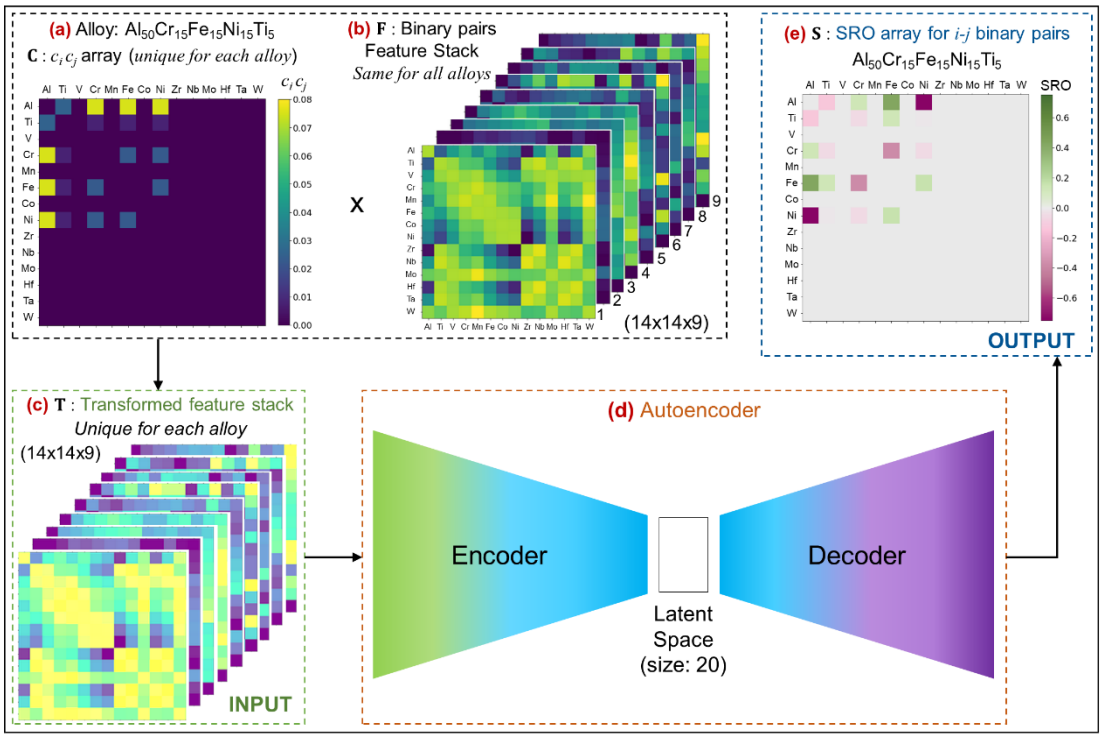

Figure 4.1 Overview of the machine learning framework. (a) Alloy representation as a 2D array (shape 14x14) containing $c_i c_j$ values for all i-j binary pairs in the alloy where ci and cj are atomic fractions of i and j element respectively. (b) Binary pairs feature stack (3D array of shape 14x14x9) compiled through layering of 9 feature arrays containing binary pair properties as shown in Figure 4.2. (c) Transformed feature stack obtained through element-wise multiplication of each layer in binary pairs feature stack with alloy $c_i c_j$ array. (d) Schematic representation of variational auto-encoder with a latent space dimension of 20. (e) Predicted SRO array for the alloy comprising SRO values for all i-j binary pairs.

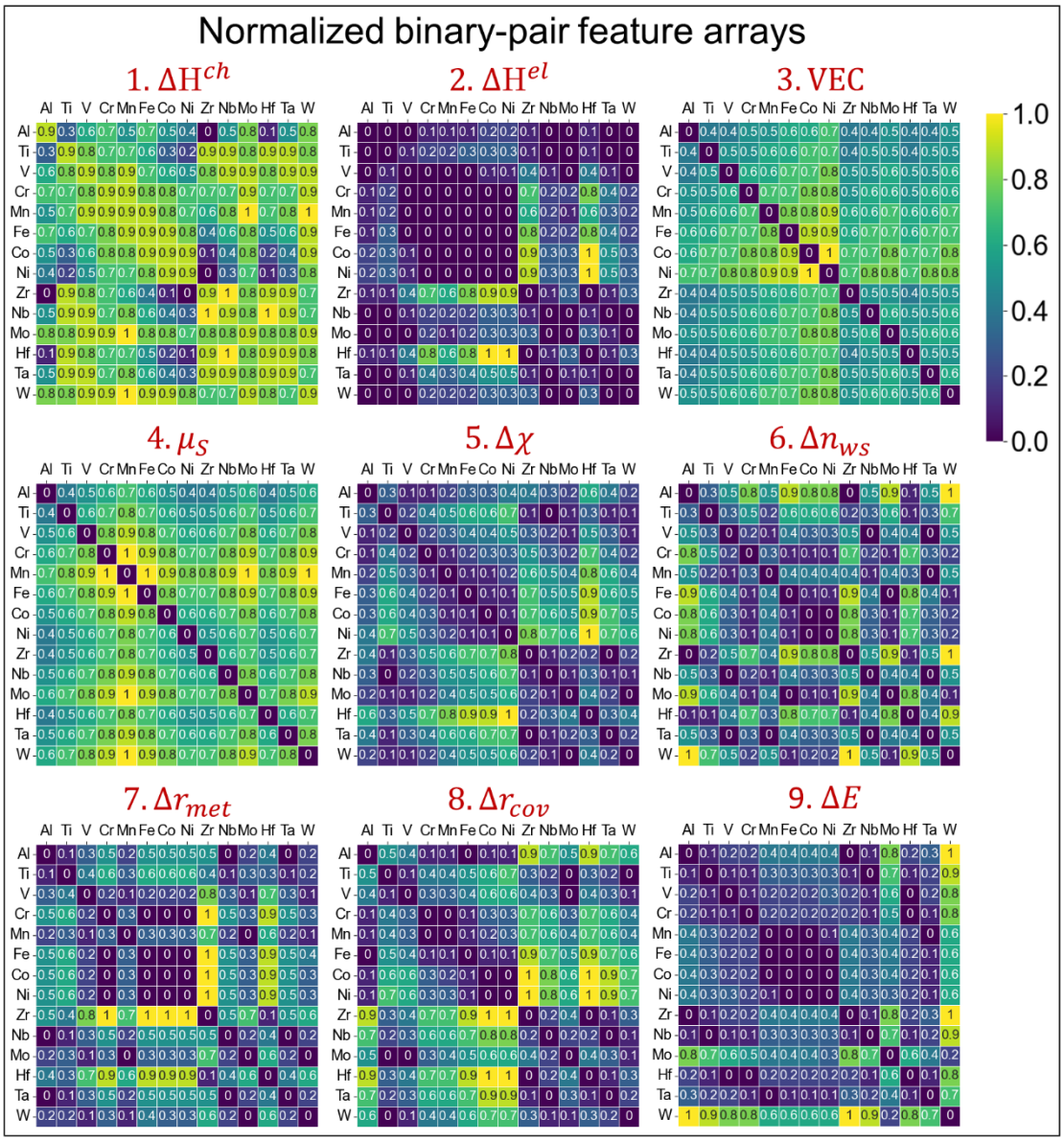

Figure 4.2 Normalized binary-pair feature arrays that were used to create the three-dimensional binary pair feature stack (F) shown in Figure 4.1b. The 1-9 feature arrays shown here correspond to the 1-9 features listed in Table 4.1.

The generated array **S** contains the SRO parameters of all possible binary pairs in the alloy. While **S** is supposed to be symmetric about the diagonal, the output from the decoder does not have this inherent constraint; thus, a transformation, wherein $\mathbf{S} = (\mathbf{S} + \mathbf{S}^{\mathbf{T}})/\mathbf{2}$, is carried out to ensure the symmetric nature of predicted SRO array. Since neural network models are non-deterministic in nature, we created an ensemble of VAE models to build an overall generalized model. The dataset was shuffled with five different random states and for each shuffled dataset, five training runs (each with fresh initialization of model parameters) were carried out wherein five-fold cross validation was

implemented in each run. This resulted in (5x5x5 = 125) VAE models that were clubbed as an ensemble wherein the median value from the ensemble predictions was used as the final prediction. Python | 3.10.2, tensorflow | 2.8.0 and Keras | 2.8.0 were used for implementing the VAE models. For the training of each model, Adam optimizer was used with a learning rate of 0.0005. The loss function comprised of two parts: reconstruction loss and KL divergence loss.

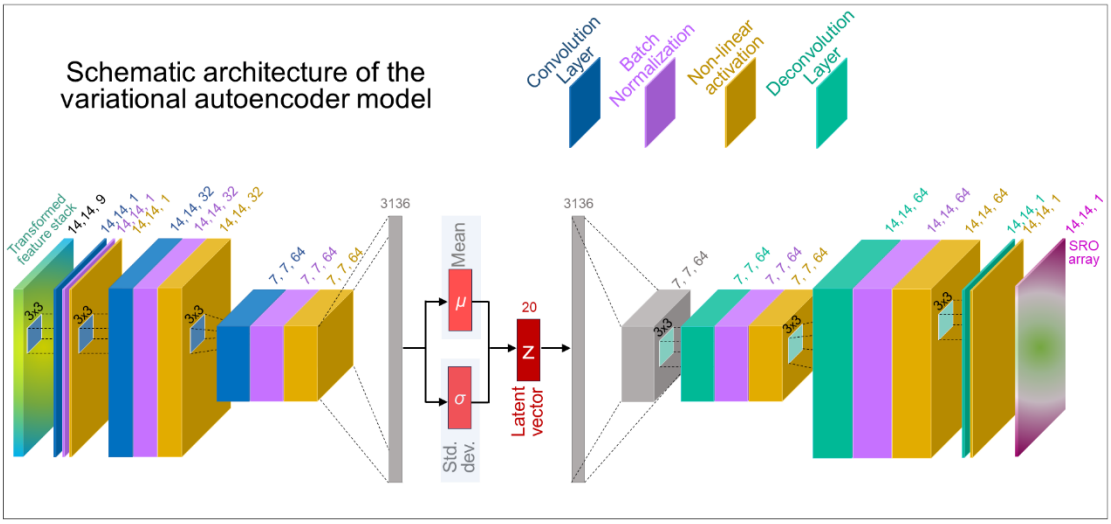

Figure 4.3 Schematic architecture of the variational autoencoder model used in this work. It takes the transformed feature stack of shape (14, 14, 9) as input, encodes it to a latent vector of size 20 and maps it to the output SRO array of shape (14, 14, 1).

4.5 Model performance and validation

4.5.1 Cross-validation performance

The cross-validation performance and confusion matrix of the ML model, as shown in Figure 4.4c, exhibits a high classification accuracy of 94.2% when classifying the type of SRO (ordering or clustering) that each atomic pair would exhibit in an alloy. Out of the total 240 atomic pairs in the dataset, the model made incorrect classification for only 14 atomic pairs. Figure 4.4d shows the confusion matrix and although the number of ordering pairs (=147) is significantly more than the clustering pairs (=93), the model does not show any significant bias and exhibits good accuracy for prediction of both ordering and clustering behaviour. Figure 4.4a shows the distribution of SRO values in both the DFT database and the ML predictions and Figure 4.4b shows the

distribution of mean absolute error. The quantitative prediction of binary-pair SRO values also exhibits a low mean absolute error of 0.08 with respect to the absolute SRO values in the DFT-database that range from -1.05 to 0.732.

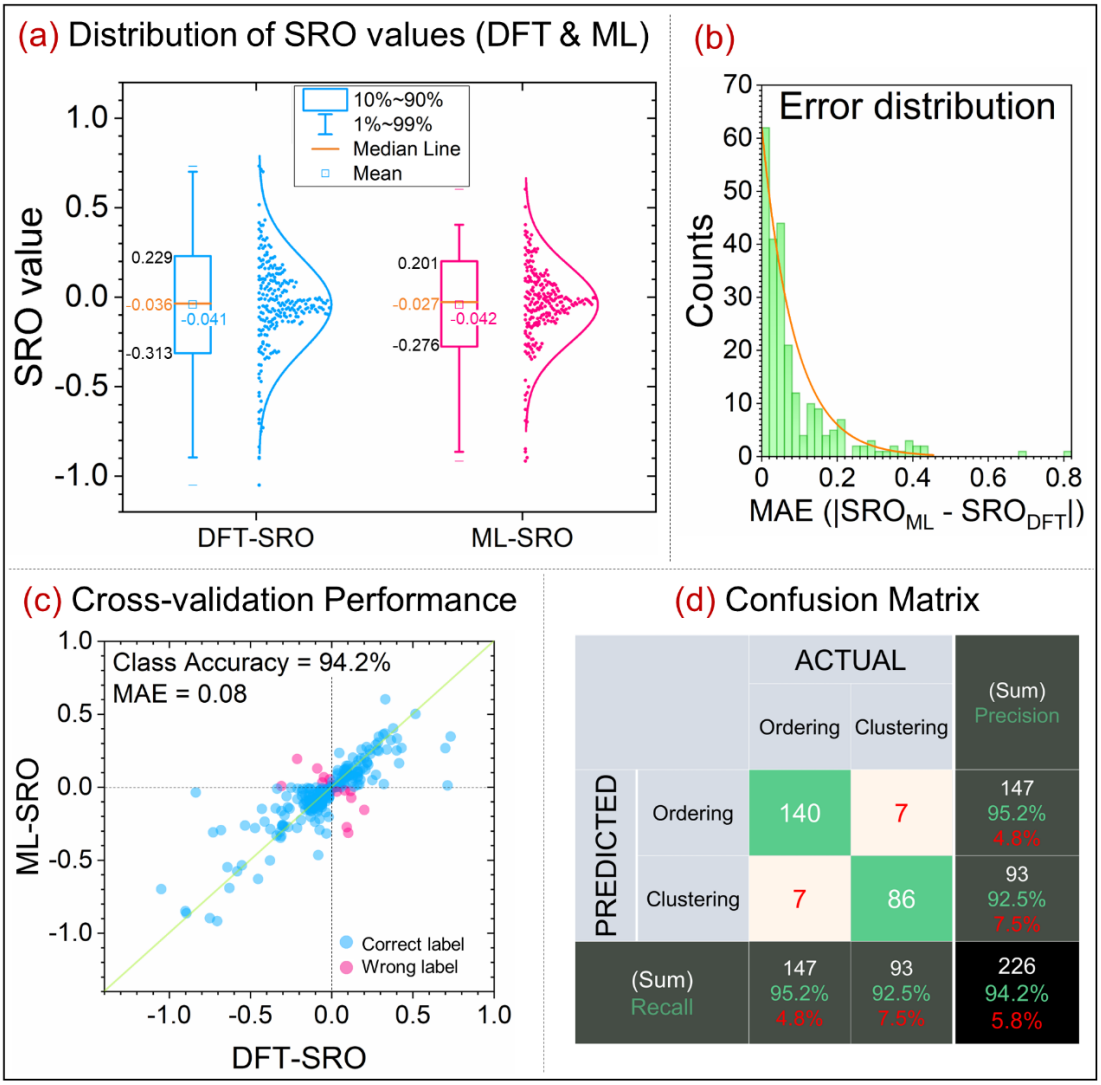

Figure 4.4 Data distribution and cross-validation performance. (a) Distribution of binary pair SRO values in DFT-based training dataset and cross-validation predictions from ML model. (b) Distribution of mean absolute error in cross-validation predictions. (c) Parity plot of ML predicted SRO (ML-SRO) vs. DFT predict SRO (DFT-SRO) for binary pairs with classification accuracy and mean absolute error (MAE) metrics. (d) Confusion matrix for ML-predicted ordering and clustering behaviour of binary pairs along with precision, recall and accuracy metrics.

4.5.2 Exploring SRO as a function of composition

While the model shows good performance over discrete compositions, as seen in Figure 4.4, it is imperative to observe the decision-making behaviour of the model along continuous compositional variations to ascertain two key aspects: **(a)** how well does the model interpolate or extrapolate the learning to new

compositions! and **(b)** can the model capture non-linear and non-monotonic changes in SRO associated with compositional variation! Thus, we predicted the SRO parameters in two alloy systems viz. Ti_x-$(CrFeNi)_{1-x}$ and Al_x-$(TiZrHf)_{1-x}$ along continuous compositional changes and compared them with SRO values calculated using DFT, as shown in Figure 4.5. The negative and positive SRO values reflect ordering and clustering tendencies respectively. The model correctly identifies [Fe-Ni] and [Cr-Fe] as the dominant clustering and ordering pair respectively in CrFeNi alloy. With addition of Ti to CrFeNi, SRO of the clustering pair [Fe-Ni] initially increases at low Ti concentrations and then decreases at higher Ti concentrations (Figure 4.5a). The ML model accurately captures this non-monotonic SRO variation. Moreover, the [Ni-Ti] pair sees a sudden increase in the ordering SRO as Ti concentration increases and at some point, between 15-25% Ti, the [Ni-Ti] pair takes over as the dominant ordering pair. The ML model also predicts a similar sudden increase in ordering tendency of [Ni-Ti] pair wherein it overtakes [Cr-Fe] at around 18% Ti to become the dominant ordering pair. Similarly, in Al_x-$(TiZrHf)_{1-x}$ system (Figure 4.5b), the ML model correctly predicts [Ti-Zr] and [Hf-Zr] as the dominant ordering and clustering pairs respectively in absence of Al. Further, with addition of Al to TiZrHf, the ML model accurately predicts the increase in ordering tendency of [Al-Ti] pair to become the dominant ordering pair above 9% Al. The number of DFT-calculated SRO points in Figure 4.5(a, b) are quite limited owing to the difficulty associated with rapid generation of DFT based SRO data. Thus, while the ML-SRO predictions appear to follow the trends indicated by DFT-SRO data points, more DFT-SRO data is needed to comment conclusively about the DFT-SRO trends over continuous composition variations.

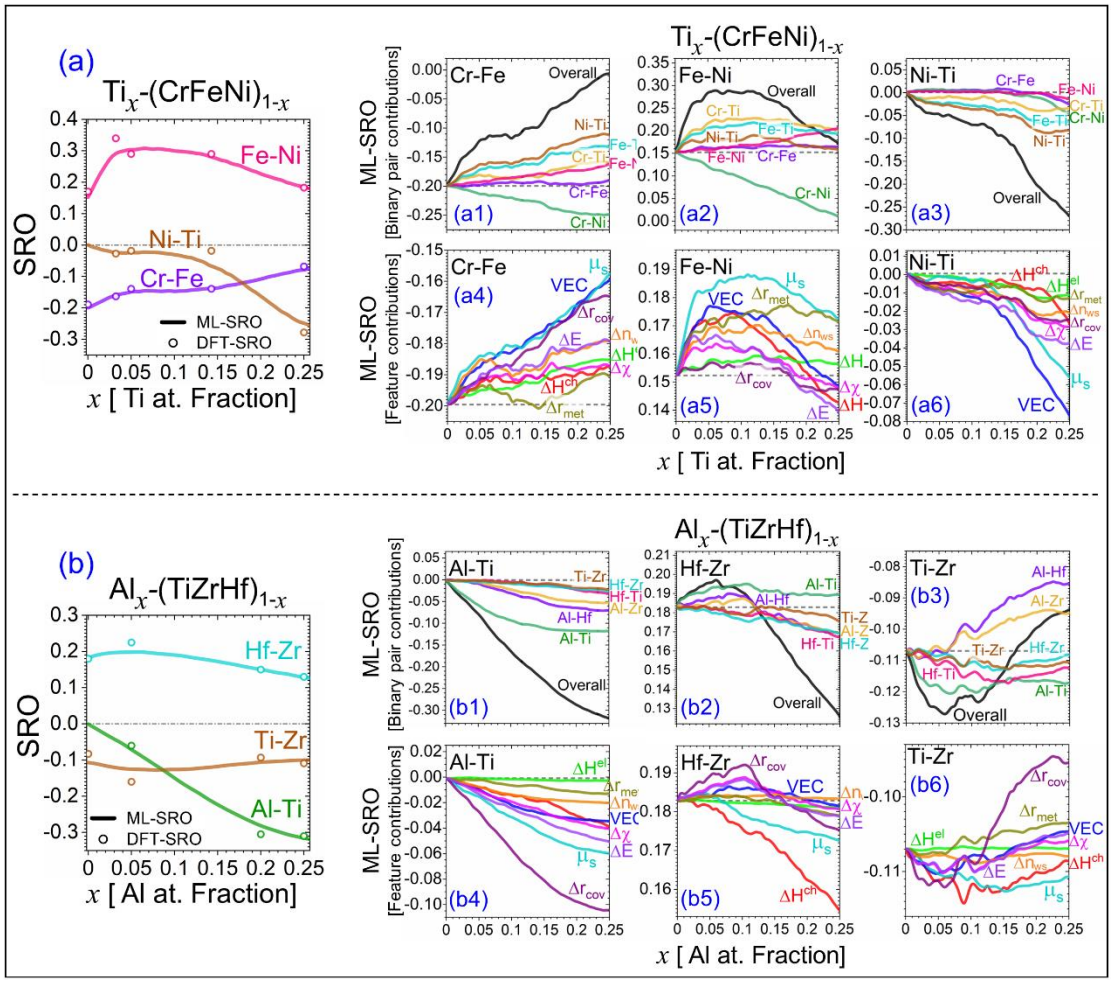

Figure 4.5 Exploring SRO variation and ML-model decision-making process (using CoSMoR) as a function of composition. DFT calculated and ML predicted SRO values of binary pairs in (a) Ti_x-$(CrFeNi)_{1-x}$ and (b) Al_x-$(TiZrHf)_{1-x}$ alloy systems. Here, only the pairs that show highest ordering/clustering tendency have been shown for each system. Cumulative contribution of individual binary pairs towards ML-predicted SRO of (a1) Cr-Fe, (a2) Fe-Ni, and (a3) Ni-Ti binary pair in Ti_x-$(CrFeNi)_{1-x}$. Cumulative contribution of individual feature towards ML-predicted SRO of (a4) Cr-Fe, (a5) Fe-Ni, and (a6) Ni-Ti binary pair in Ti_x-$(CrFeNi)_{1-x}$. Cumulative contribution of individual binary pairs towards ML-predicted SRO of (a1) Al-Ti, (a2) Hf-Zr, and (a3) Ti-Zr binary pair in Al_x-$(TiZrHf)_{1-x}$. Cumulative contribution of individual feature towards ML-predicted SRO of (a4) Al-Ti, (a5) Hf-Zr, and (a6) Ti-Zr binary pair in Al_x-$(TiZrHf)_{1-x}$.

4.5.3 CoSMoR: Insights into decision-making process of ML model

As seen in Figure 4.5(a, b), the ML model can capture the non-linear and non-monotonic changes in SRO over continuous compositional variations. But this raises important questions pertaining to the decision-making process of the ML model, for example – a) Which features control the SRO value of a binary pair in any given alloy system? b) Are same features important for all binary pairs or do different features become dominant for different binary pairs in an alloy? c) Does feature importance change as we move from one alloy system to

another? d) Is the SRO value of a binary pair controlled by features of that binary pair only or by the features of other binary pairs as well? Answering these questions can provide key insight into the decision-making process of the ML model. With this motivation, we used Compositional-Stimulus and Model-Response (CoSMoR) [36] framework to extract the exact contribution of features towards the predicted SRO of each binary pair as a function of composition. As seen in Figure 4.1c, the effective number of input features for any given alloy is equal to $N_f \times N_p$; where N_f is the number of features used in the binary-pair feature stack (=9 in this model as shown in Figure 4.1b) and N_p is the number of unique binary pairs present in an alloy (=6 for quaternary alloys). Thus, as we change composition of Ti_x-$(CrFeNi)_{1-x}$ and Al_x-$(TiZrHf)_{1-x}$ quaternary alloy systems, the variation in ML-SRO arises from (9×6=54) feature contributions. CoSMoR calculates the quantitative contribution of each feature with respect to the ML-SRO value for baseline composition at x=0. As it is difficult to visualize 54 variations in a legible manner, we have combined these contributions in two different ways. Firstly, contributions of all features associated with a binary pair are combined together to represent the cumulative effect of that particular binary pair and have been visualized in Figure 4.5(a1-a3, b1-b3). For example, the 'Cr-Ni' curve in Figure 4.5a1 shows the combined contribution of all nine features associated with 'Cr-Ni' binary pair on the ML-SRO of Cr-Fe pair in Ti_x-$(CrFeNi)_{1-x}$ alloy system. Secondly, contributions of all binary pairs for a given feature are clubbed together to represent the cumulative effect of each physical feature and have been visualized in Figure 4.5(a4-a6, b4-b6). For example, the 'VEC' curve in Figure 4.5a4 shows the combined contribution of 'VEC' feature of all six binary pairs on the ML-SRO of Cr-Fe pair in Ti_x-$(CrFeNi)_{1-x}$ alloy system.

We highlight here some insights gained from the breakdown of the ML model decision-making using CoSMoR. The ML-SRO of a binary pair is not dictated by its own properties but has strong contributions from other binary pairs as well. In fact, in some cases, it may be dictated entirely by other binaries. For example, in Ti_x-$(CrFeNi)_{1-x}$, the SRO of Cr-Fe (Figure 4.5a1) and Fe-Ni (Figure

4.5a2) binaries is controlled majorly by other binary pairs whereas that of Ni-Ti (Figure 4.5a3) is controlled strongly by Ni-Ti pair itself. Similarly, in Al_x-$(TiZrHf)_{1-x}$, the SRO of Ti-Zr is controlled by other binary pairs whereas that of Al-Ti is controlled strongly by Al-Ti pair itself. Further, in an alloy system, the same binary pair can drive clustering for some atomic pairs and ordering for others. For example, in Ti_x-$(CrFeNi)_{1-x}$, Ni-Ti pair contribution drives the clustering in Cr-Fe pair (Figure 4.5a1) whereas it drives the ordering of Ni-Ti pair itself (Figure 4.5a3). Similarly, in Al_x-$(TiZrHf)_{1-x}$, the Al-Ti pair contribution strongly drives the ordering in Al-Ti (Figure 4.5b1) and Ti-Zr (Figure 4.5b3) pair whereas it promotes clustering in Hf-Zr pair (Figure 4.5b2). These observations align with the fundamental understanding that the SRO in an alloy arises from favorable atomic configurations controlled by binary pair interactions wherein the preferential ordering/clustering of one atomic pair affects the other pair probabilities also since the overall concentration is fixed.

Moving to the cumulative effect of physical features, we observe that within an alloy system, the contribution of a particular feature to the ordering behavior can vary drastically from one binary pair to another. For example, in Ti_x-$(CrFeNi)_{1-x}$, VEC and μ_S contributions lower the ordering tendency for Cr-Fe pair (Figure 4.5a4) whereas they strongly drive the ordering tendency for Ni-Ti pair (Figure 4.5a6). Also, a feature that dominates SRO for one binary pair may not be significant for another binary pair. For example, in Ti_x-$(CrFeNi)_{1-x}$, Δr_{cov} contributes significantly to SRO for Cr-Fe pair (Figure 4.5a4) but not so much for Fe-Ni pair (Figure 4.5a5). Moreover, a feature that has huge significance in one alloy system may not be of particular importance in determining SRO for another alloy system. For example, in Ti_x-$(CrFeNi)_{1-x}$, VEC contributes strongly to SRO for Cr-Fe, Fe-Ni and Ni-Ti pairs (Figure 4.5(a4-a6)) but in Al_x-$(TiZrHf)_{1-x}$, it does not play a major role in controlling the SRO of binary pairs (Figure 4.5(b4-b6)). Overall, these insights support the initial hypothesis (§4.4) behind the ML methodology in this work viz., SRO in an alloy can be predicted provided we have simultaneous knowledge of alloy chemistry

(which controls $c_\mu c_\nu$ terms that represent μ-ν pair frequency) and physical features of all binary pairs (which control the strength of pair interactions).

4.6 Automated workflow for model improvements

The study of SRO in CCAs is still in its early stages and the current model was trained on a limited dataset of 41 CCAs (comprising 240 binary pairs). But with the growing research interest, a significant amount of data on SRO parameters for various CCAs is expected to appear in the coming years. In view of this, it is vital to ensure easy upgradability of the model as and when new SRO data appears. To achieve this, we have wrapped our ML model development

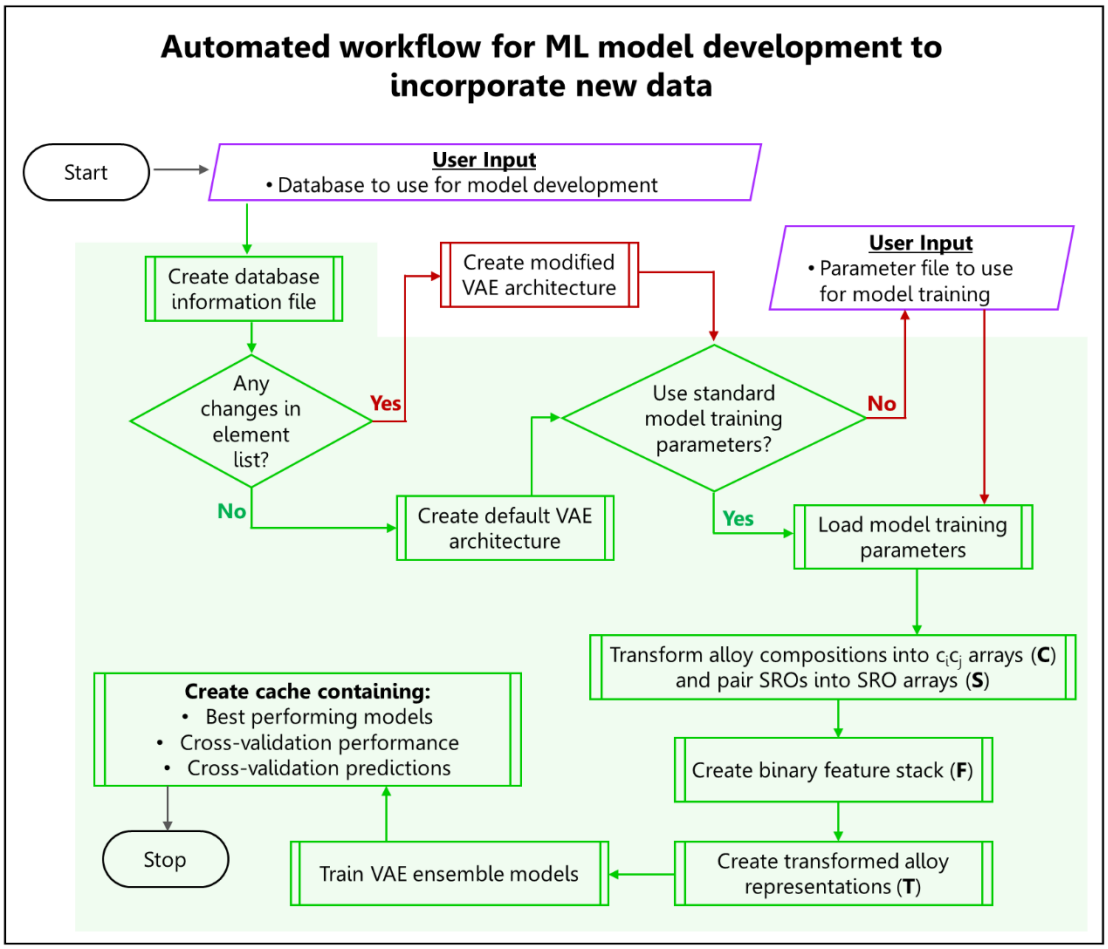

Figure 4.6 Automated workflow for ML model development wherein models can be automatically retrained as and when new data is available. The green highlighted region indicates all the processes that are automated. The red pathways indicate instances where some user intervention is required.

process as an automated workflow wherein – **(a)** the models can be retrained automatically, with or without user intervention, using updated datasets, **(b)**

addition of new elements, if required, can be handled with just some tweaking of VAE architecture, and **(c)** the model selection, ensemble building and performance evaluation proceeds automatically. The automated workflow and database generation method are summarized in Figure 4.6.

4.7 Conclusions

In summary, we have presented here a novel machine learning framework for predicting the Warren-Cowley SRO parameters in CCAs. The methodology developed relies on the hypothesis that the manifestation of SRO is governed primarily by the atom-pair interactions and that simultaneous knowledge of the interaction tendencies of all possible atomic pairs in a given alloy can point towards the SRO parameters. This has been implemented by expressing each alloy as a unique three-dimensional feature stack that encapsulates the physical and thermodynamic properties of all atomic pairs. Variational autoencoders are then used to map this three-dimensional feature stack to the two-dimensional SRO array that contains SRO parameters for all binary pairs within the alloy. The ML model, comprising an ensemble of autoencoders, is shown to be capable of reliably classifying the type of SRO (ordering or clustering) for each binary pair within an alloy. Moreover, it also captures the non-linear and non-monotonic changes in SRO as a function of continuous compositional changes. The implementation of CoSMoR shows that, for each binary pair SRO in a given alloy system, the model captures the intricate contributions from all the different binary pairs and physical features. Further, the model effectively captures how these contributions change when we move from one alloy system to another. To enable integration of new research data with the models developed here, the entire development process has been wrapped as an automated workflow that can retrain the models with no or minimal user intervention.

Chapter 5: Distilling physical origins of hardness in compositionally complex alloys directly from ensemble neural network models

5.1 Introduction

Compositionally complex alloys (CCAs) present unique challenges including an astronomically large composition space (with more than 10^{78} possible alloy compositions[184]) and a multitude of interactions arising from mixing four or more principal elements (N≥4) that cannot be precisely explained or predicted with the existing thermodynamic and physical models. *Ab-initio* calculations can accurately predict the phase stability and physical properties[127,185,186]; however, they are time-intensive when extended to finite temperatures and thus are not well-suited as an exploratory tool. Similarly, experimental exploration of the composition space becomes expensive and time intensive. Given these constraints, coupled with a reasonably large volume of data on these alloys generated over the past decade, machine learning (ML) based approaches have rapidly gained traction[187–191]. A classic shortcoming of ML is that models with fewer parameters tend to be physically interpretable, though less accurate, while those with larger number of parameters tend to be more accurate but lose the interpretability.

This chapter has been published as a research article in 'npj Computational Materials'

D Beniwal, P Singh, S Gupta, MJ Kramer, DD Johnson, PK Ray, *Distilling physical origins of hardness in multi-principal element alloys directly from ensemble neural network models*, **npj Computational Materials**, 8 (2022) 153

DOI: *https://doi.org/10.1038/s41524-022-00842-3*

Hardness is an important quantity from engineering perspective as it is a measure of a material's ability to resist localized plastic-deformation, scratching, or indentation. Knowledge of hardness can be critical because high hardness in an alloy is often associated with reduced ductility that may limit its use[192]. In the past few years, ML models have been reported and applied to CCAs to predict mechanical properties[193–197], thermal properties[195] and phase selection[83,89,91,198]. Chang et al.[194] implemented an artificial neural network (ANN), with a single hidden layer and three nodes, to predict hardness of AlCoCrFeMnNi high-entropy alloys (dataset size of 91 alloys) using composition-weighted hardness, density and atomic mass as features. Wen et al.[197] explored the hardness of AlCoCrCuFeNi system (dataset size of 155 alloys) using multiple ML algorithms (linear/polynomial regression, support vector machines, decision trees and ANNs) based on elemental compositions and twenty other material features. While both these models are quite useful and display good accuracy, they were trained on datasets spanning eight and six-element composition space, respectively. This leaves out a significant number of alloy systems, especially refractory CCAs, which cannot be explored reliably using these models. Rickman et al.[193] developed a more comprehensive approach employing a canonical-correlation analysis to predict the hardness of CCAs (dataset size of 82 alloys) using seven features built from elemental and thermodynamic parameters, and further used a genetic algorithm to search for high-hardness quinary alloys from a sixteen-element composition-space. While accurate, these models do not probe deeper into the nature of fit achieved by ML approach, thereby failing to assess the physical consistency of learning achieved – a challenge that we seek to address here through a combination of deconstructed ML predictions coupled with *ab-initio* stability analysis.

Single-phase CCAs can provide fundamental insights into the correlation between physical and mechanical properties;[199–201] however, the multi-phase alloys allow greater flexibility in tailoring the microstructure leading to improved properties.[202–206] Also, one expects discontinuous variations in

physical properties as we move across phase boundaries in multi-phase systems. This necessitates the development of strategies that can narrow down the regions of interest by rapidly exploring compositional spaces to provide approximate, but representative, insights into the targeted properties. Ideally, the model should also closely mirror the changes in microstructure assemblages, as well as the ordering that drives precipitate formation indicated by the phase transformations and capture the non-linear variation in physical properties due to change in alloy chemistry. As we develop this model for hardness prediction of CCAs, it is pertinent to ask: (i) What elemental and thermodynamic variables (or combination thereof) can best describe alloy hardness? (ii) Can a combination of these variables, some of which vary linearly, be combined to predict non-linear response in the system? And, (iii) Is the ML model's decision-making process a mere statistical fit or does it capture some fundamental insights into the physical origins of hardness?

In this chapter, we present a ML strategy (Figure 5.1) that employs an ensemble of ANNs, driven by elemental and alloying descriptors, to rapidly predict and explore the hardness of CCAs over vast compositional spaces. ANNs, inspired by biological neural networks, are capable of learning non-linear relationships and thus excel in predictive modelling of material properties[197,207–209] as they can learn complex unknown functions from a stream of data[210]. To address the high variance of ANNs, we implement a model averaging ensemble learning technique combining output from 165 trained networks to give a final prediction. The material descriptors used for training are shortlisted from an extensive pool of 22 features based on their fundamental relevance and statistical correlation with respect to hardness. The model is trained over a dataset[211] of 218 CCAs and is validated using a test dataset of 58 alloys compiled from recent literature (these were not included in model training), followed by experimental validation for $TiZrHfAl_x$ system.

The ML model together with density-functional theory (DFT) is essential to minimize the gap in our understanding of the physical origin of mechanical response in CCAs. Therefore, for arbitrary CCAs, selected set of compositions

were analyzed using DFT[212] total-energy and electronic-structure calculations and DFT-based thermodynamic linear-response theory[79,186] to assess chemical short-range order to capture/identify the physics, including phase stability, electronic effects, and short-range ordering/clustering and its relation to ML-predicted hardness. ML models, neural networks particularly, often face criticism due to their treatment as a black-box that severely limits the understanding of the decision-making process. To overcome this, we have used the CoSMoR framework (presented in Chapter 3) to reveal the decision-making process for critical insights as to how the ML model learns the physical origins of hardness through different features. Our explainability analysis approach identifies the origin of hardness at the feature level while the DFT calculations assist in identification of baselines as to what these origins at feature level may represent at an atomistic level within the material.

5.2 Development of ML models

5.2.1 Database for ML model development

A training dataset of 218 unique as-cast alloys, with experimentally measured hardness values, was extracted from the database compiled by Gorsse et al.[211] The data consists of single- and multi-phase alloys, as shown in Figure 5.2a, and these comprise of 3d-transition-metals, refractory-metals and select main-group elements. The hardness values in the training dataset span from 109 to 905 HV with the distribution profile as shown in Figure 5.2b. The region above 800 HV is very thinly populated. While there are some outliers lying beyond the 1.5 interquartile range (IQR) in single-phase BCC/FCC alloys, Figure 5.2a, these have not been excluded from the training as we believe these alloys could be critical for capturing the underlying physics that may not be apparent in other alloys. The model was validated using a separate test dataset comprising 58 alloys (provided in §5.7 Supplementary data) compiled from recent literature. The test dataset was not used for model training. It spans a

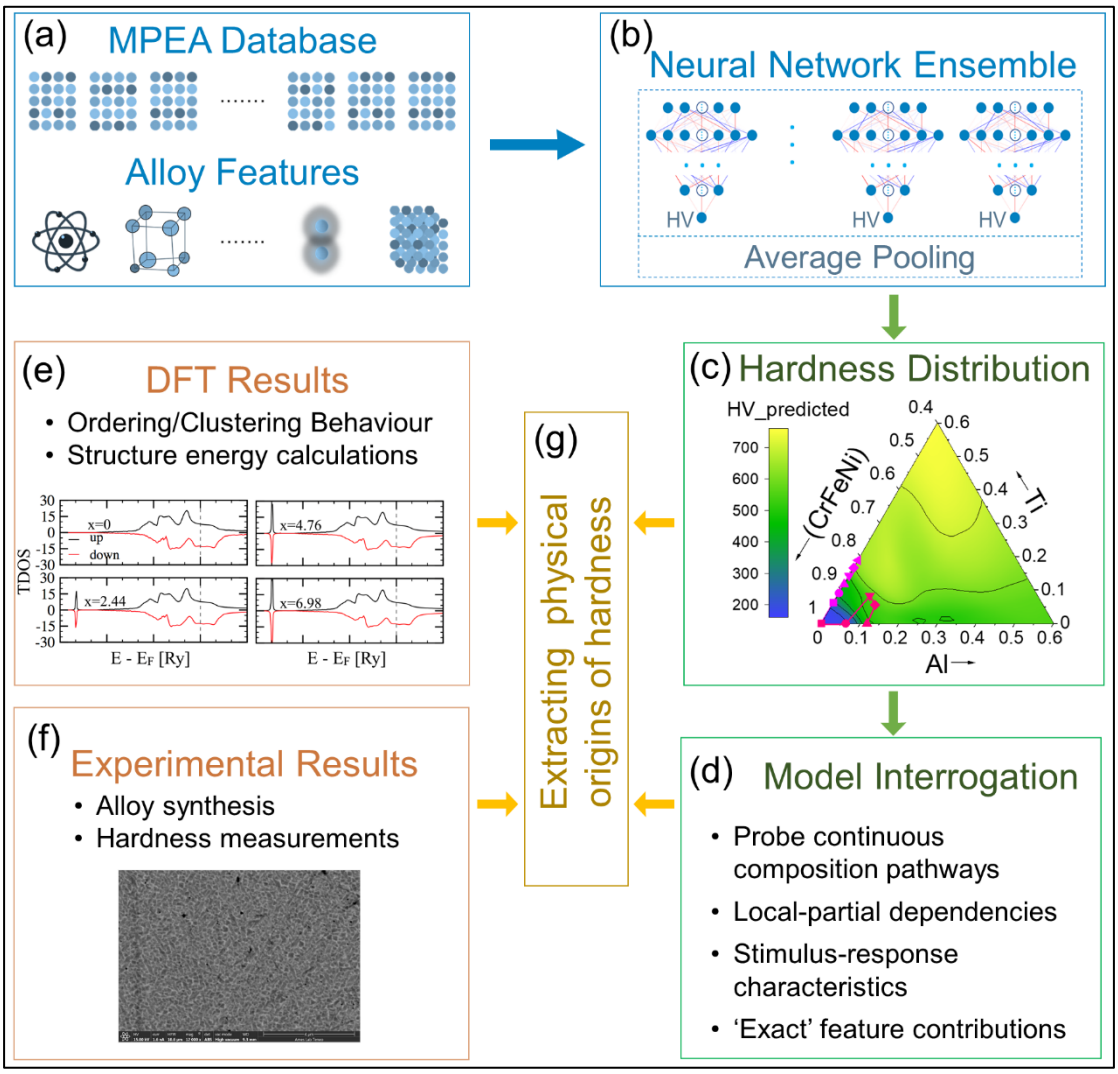

Figure 5.1 Overview of the methodology used for extracting origins of hardness: (a) CCAs hardness database development and calculation of alloy features, (b) training of neural network ensemble, (c) exploration of hardness over wide compositional spaces, (d) model interrogation to extract exact feature contributions along continuous composition pathways, (e) DFT results to probe ordering behaviour and structure stabilities, (f) experimental validation over complex alloy systems, and (g) analyzing the results to establish physical origins of hardness.

composition space of 15 elements and contains alloys with hardness ranging from 123 HV to 894 HV, with a mean hardness value of 459 HV. The test set has a wide hardness distribution, as seen in Figure 5.2c, similar to that of the training set, and this diversity ensures that the performance of ML model on the test set is a good representation of its predictive ability.

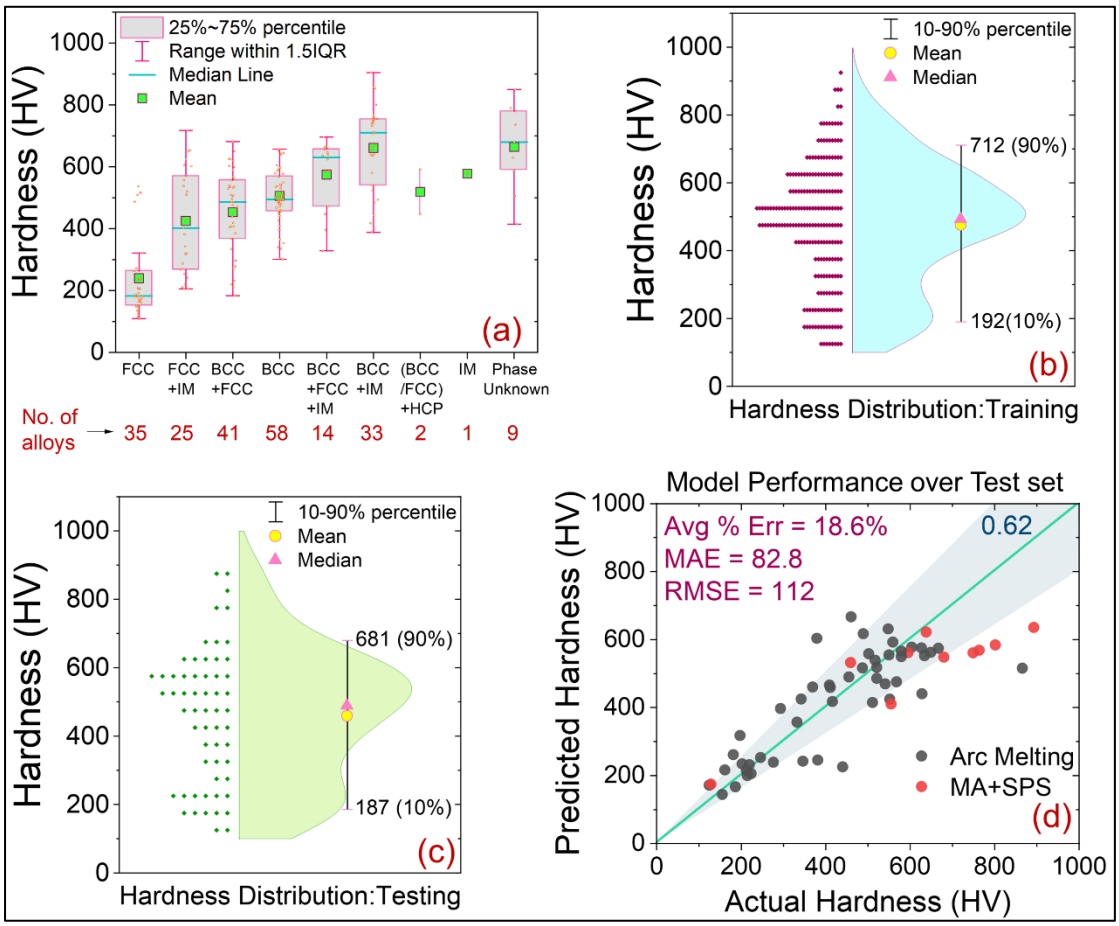

Figure 5.2 Dataset exploration and model validation. (a) Statistical distribution of hardness values for eight different type of crystal structures present in the dataset along with number of alloys, mean hardness, median hardness, 1.5 IQR and 25%-75% percentile range for each structure. (b) Distribution of hardness values in the training dataset (218 alloys) along with mean, median and 10%-90% percentile range of hardness. (c) Distribution of hardness values in the testing dataset (58 alloys) compiled from recent literature. (d) Parity plot of hardness predictions obtained for test dataset along with statistical performance metrics –root mean square error (RMSE), mean absolute error (MAE) and average percentage error. The shaded area represents an 80% accuracy region and the number at top right corner represents fraction of predictions with > 80% accuracy.

5.2.2 Feature engineering and model architecture

We explored a set of 22 features comprising of elemental and alloying descriptors. The features have been classified as-such to highlight two different characteristics of an alloy: a) the elemental descriptors represent alloy properties that may be a direct extension of the properties possessed by component elements, and b) the alloying descriptors represent changes that occur when different elements interact with each other during alloy formation. Figure 5.3 lists these features along with the expressions used to calculate them and the Pearson's correlation coefficient for each feature as a measure of its

linear association with hardness. The elemental descriptors are characteristic of the elemental composition of the alloy and were calculated as either composition-weighted average or as an asymmetry-measure over the component elements. The chemical and elastic enthalpies of mixing associated with alloy formation were calculated using Miedema's model[108,119,213,214]. The configurational entropy depends only on the relative amount of constituents while being independent of their identity, and has been shown to be the primary stabilizing factor for disordered phases in CCAs[215]. YZ parameter represents a thermodynamic parameter developed by Yang and Zhang[102] that was shown to be a good descriptor of the phases present in CCAs. Figure 5.4 lists the ten shortlisted features that were used for training the ANNs and also visualizes the variation of hardness with each feature along with the linear regression lines and R^2 values. Feed-forward back-propagation ANNs with twelve different architectures (Table 5.2) were trained using ten feature-sets (Table 5.3) with Vickers hardness as the target value. For three feature-sets, a multiple linear regression was also performed to act as a baseline measure of ANN performance. These ANNs (ANN1, ANN2, …, ANN12) were used with the aim to ascertain if the depth of neural network will be significant in controlling the model performance. This was of specific interest since a non-linear relationship was observed between the features and hardness, and deep neural networks have been conclusively shown to perform better at learning non-linear relationships [216]. The number of layers in the neural networks used in this work range from two in ANN1 to seven in ANN12. Since the hardness prediction is a regression problem, the output layer in all ANN architectures employs rectified linear unit (ReLU) activation function. For the hidden layers, we have used a combination of sigmoid and ReLU activation functions. The hardness of an alloy is a strong function of its crystal structure and the same can also be seen in Figure 5.2a where the mean hardness value increases as we move from FCC to BCC crystal structure and the presence of intermetallic phases also hardens the alloy. This strong dependence indicates that the neural network may make accurate hardness predictions only if it is capable of classifying the alloy crystal structure based on input features. Past

research has shown that it is possible to predict the phases present in CCAs using the thermodynamic descriptors included in our feature sets [108,171,217]. Thus, we believe that hidden layers with sigmoid activation functions may be able to learn such correlations without explicitly training the network for crystal structure classification. This belief was strengthened by test runs wherein ANNs with combination of ReLU and sigmoid hidden layers performed considerably better than those with only ReLU hidden layers.

	Feature	*Calculation*	*Correlation with Hardness*
1	*Metallic Radius Asymmetry*, δ_{met}	$\sqrt{\sum_{i=1}^{N} c_i \left(1-\frac{r_i}{\bar{r}}\right)^2}$	0.53
2	*Valence e⁻ Concentration*, $\mathrm{VEC}_{\mathrm{alloy}}$	$\sum_{i=1}^{N} c_i\ \mathrm{VEC}_i$	-0.33
3	*Covalent Radius Asymmetry*, δ_{cov}	$\sqrt{\sum_{i=1}^{N} c_i \left(1-\frac{r_i}{\bar{r}}\right)^2}$	0.47
4	*Average Density*, $\bar{\rho}$	$\sum c_i \rho_i$	-0.26
5	*Average melting temperature*, $\bar{T}_{\mathrm{m}}$	$\sum c_i T_{\mathrm{m},i}$	0.04
6	*Average Elastic Modulus*, $\bar{E}$	$\sum c_i E_i$	-0.15
7	*Elastic Modulus Asymmetry*, δ_{E}	$\sqrt{\sum_{i=1}^{N} c_i \left(1-\frac{E_i}{\bar{E}}\right)^2}$	0.52
8	*Average Shear Modulus*, $\bar{G}$	$\sum c_i G_i$	-0.16
9	*Shear Modulus Asymmetry*, δ_{G}	$\sqrt{\sum_{i=1}^{N} c_i \left(1-\frac{G_i}{\bar{G}}\right)^2}$	0.56
10	*Average Bulk Modulus*, $\bar{B}$	$\sum c_i B_i$	0.02
11	*Bulk Modulus Asymmetry*, δ_{B}	$\sqrt{\sum_{i=1}^{N} c_i \left(1-\frac{G_i}{\bar{G}}\right)^2}$	0.24
12	*Average Compressibility*, $\bar{\beta}$	$\sum c_i \beta_i$	0.02
13	*Compressibility Asymmetry*, δ_{β}	$\sqrt{\sum_{i=1}^{N} c_i \left(1-\frac{\beta_i}{\bar{\beta}}\right)^2}$	0.1
14	*Average Electronegativity*, $\bar{\chi}_{\mathrm{allen}}$	$\sum c_i \chi_i$	-0.17
15	*Average Hardness*, $\overline{\mathrm{HV}}$	$\sum c_i \mathrm{HV}_i$	0.18
16	*Molar Volume Asymmetry*, $\delta_{\mathrm{V_m}}$	$\sqrt{\sum_{i=1}^{N} c_i \left(1-\frac{V_{\mathrm{m},i}}{\bar{V}_{\mathrm{m}}}\right)^2}$	0.53
17	*Average Cohesive Energy*, $\overline{E^o}$	$\sum c_i E_i^o$	0.09
18	*Cohesive Energy Asymmetry*, $\delta_{\mathrm{E^o}}$	$\sqrt{\sum_{i=1}^{N} c_i \left(1-\frac{E_i^o}{\bar{E}^o}\right)^2}$	0.26
19	*YZ Parameter*, Ω	$\frac{T_{\mathrm{m}}\Delta\bar{\mathrm{S}}_{\mathrm{mix}}}{\lvert\Delta\bar{\mathrm{H}}_{\mathrm{mix}}\rvert}$	-0.17
20	*Configurational Entropy of Mixing*, $\Delta\bar{\mathrm{S}}_{\mathrm{config}}$	$-\mathrm{R}\sum_{i=1}^{N} c_i\ (\ln c_i)$	0.43
21	*Miedema's Chemical Enthalpy of Mixing*, $\Delta\bar{\mathrm{H}}_{\mathrm{SS}}^{\mathrm{chem}}$	$\sum_{i<j} 4H_{ij}^{\mathrm{chem}}\ c_i c_j$	-0.62
22	*Elastic Enthalpy of Mixing*, $\Delta\bar{\mathrm{H}}_{\mathrm{SS}}^{\mathrm{el}}$	$\sum_{i<j} 4H_{ij}^{\mathrm{el}}\ c_i c_j$	0.56

Figure 5.3 List of all the calculated features along with their mathematical expression and their Pearson's coefficient of correlation with hardness.

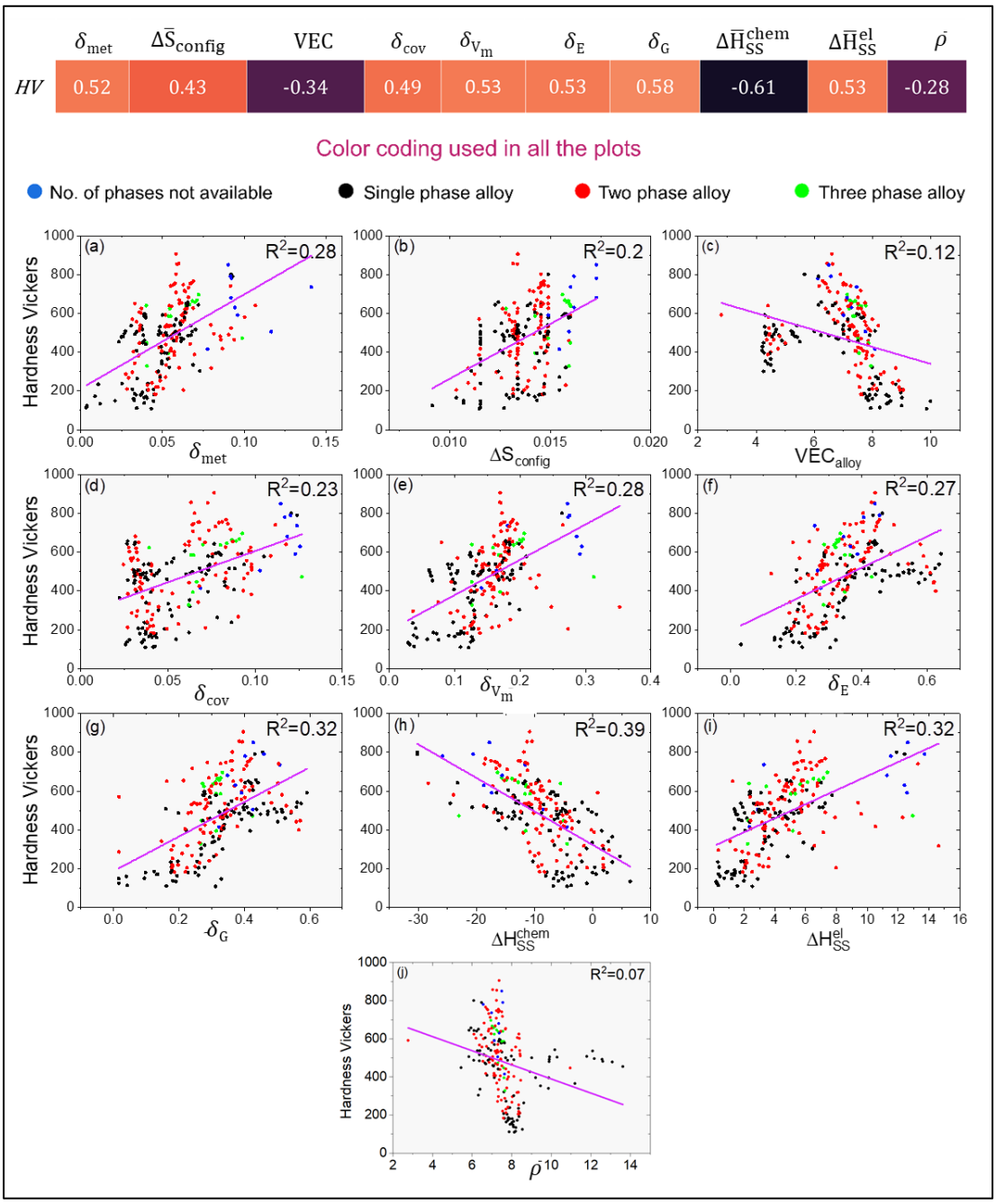

Figure 5.4 Ten shortlisted features along with their correlation coefficient with hardness and plots (a-j) of hardness vs. each shortlisted feature. Linear regression lines have been plotted along with R^2 in each plot. Data points have been color-coded based on number of phases present.

Table 5.1 Cross-validation performance summary of ANNs with different architectures trained on various feature sets. Here,

$$\text{Improvement Factor of model i, } IF_i = \left(\frac{100}{4}\right)\left[\left(\frac{R2_i - R2_{L|FS1}}{R2_{L|FS1}}\right) + \left(\frac{RMSE_{L|FS1} - RMSE_i}{RMSE_{L|FS1}}\right) + \left(\frac{MAE_{L|FS1} - MAE_i}{MAE_{L|FS1}}\right) + \left(\frac{\%Err_{L|FS1} - \%Err_i}{\%Err_{L|FS1}}\right)\right]$$

where: L|FS1 refers to Lin Regression Algorithm (S. No. 1) which has been used as baseline measure

S.No.	ML Algorithm	Feature Set	R2	RMSE	MAE	Avg. % error	Improvement Factor (IF)
1	Lin Reg	FS1	0.52	124.0	103	28.60%	0
2	Lin Reg	FS2	0.549	122.0	101.6	27.50%	3.09
3	Lin Reg	FS3	0.55	122.0	99.8	26.70%	4.28
4	ANN1	FS1	0.726	95.0	69.4	18.10%	33.08
5	ANN1	FS2	0.831	74.8	52.7	13.44%	50.34
6	ANN2	FS1	0.81	78.0	55.6	14.70%	46.87
7	ANN2	FS2	0.847	71.5	50.2	13.02%	52.76
8	ANN2	FS3	0.849	71.4	50.5	12.63%	53.15
9	ANN2	FS4	0.794	84.8	55.7	14.88%	44.54
10	ANN2	FS5	0.822	78.7	51.7	12.86%	49.84
11	ANN3	FS2	0.844	71.9	48.8	12.87%	52.96
12	ANN4	FS2	0.851	70.3	48.6	12.78%	53.77
13	ANN5	FS2	0.854	69.7	50.6	13.29%	53.12
14	ANN6	FS2	0.847	71.9	47.9	12.67%	53.53
15	ANN6	FS6	0.811	79.5	54.0	14.69%	47.01
16	ANN6	FS7	0.799	82.4	53.6	13.29%	47.15
17	ANN6	FS8	0.825	76.7	53.7	13.68%	49.18
18	ANN6	FS9	0.837	74.6	52.4	12.71%	51.38
19	ANN7	FS2	0.832	75.0	51.4	13.13%	50.94
20	ANN8	FS2	0.852	70.3	50.1	13.29%	53.02
21	ANN9	FS2	0.843	72.3	51.4	13.34%	51.84
22	ANN10	FS2	0.828	75.9	52.8	13.79%	49.66
23	ANN11	FS2	0.840	73.6	51.0	13.72%	51.21
24	ANN12	FS2	0.832	76.2	50.8	13.02%	50.92
25	ANN2	FS10	0.835	74.0	49.6	12.51%	52.21

5.2.3 Machine learning model training

The standard practices followed while training all the models have been elucidated here. To ensure equal importance to all features during the training and for good convergence, the range of each feature was rescaled to [0, 1] range using min-max normalization. For every training process, five-fold cross validation was used and thus the training-set to test-set size ratio was always 80:20. Each cross validation was independent of the others i.e., trained weights

Table 5.2 ANN architectures used in the work

Architecture	**Layer Units**	**Activation Functions**
ANN1	25,1	sigmoid, ReLU
ANN2	20,15,10,1	sigmoid, sigmoid, ReLU, ReLU
ANN3	20,15,10,5,1	sigmoid, sigmoid, sigmoid, ReLU, ReLU
ANN4	20,15,10,5,1	sigmoid, sigmoid, ReLU, ReLU, ReLU
ANN5	25,20,15,1	sigmoid, sigmoid, ReLU, ReLU
ANN6	25,20,15,10,1	sigmoid, sigmoid, sigmoid, ReLU, ReLU
ANN7	25,20,15,10,5,1	sigmoid, sigmoid, sigmoid, ReLU, ReLU, ReLU
ANN8	40,30,20,10,1	sigmoid, sigmoid, sigmoid, ReLU, ReLU
ANN9	60,45,30,15,1	sigmoid, sigmoid, sigmoid, ReLU, ReLU
ANN10	40,30,20,10,5,1	sigmoid, sigmoid, sigmoid, sigmoid, ReLU, ReLU
ANN11	60,40,30,20,10,1	sigmoid, sigmoid, sigmoid, sigmoid, ReLU, ReLU
ANN12	40,35,25,15,10,5,1	sigmoid, sigmoid, sigmoid, sigmoid, ReLU, ReLU, ReLU

Table 5.3 Feature-sets used in this work for training ML models

Feature Set	Features Present
FS1	δ_{met}, $\Delta\bar{S}_{\mathrm{config}}$, $\mathrm{VEC}_{\mathrm{alloy}}$, $\Delta\bar{H}_{SS}^{\mathrm{chem}}$, $\Delta\bar{H}_{SS}^{\mathrm{el}}$
FS2	$\mathrm{VEC}_{\mathrm{alloy}}$, δ_{cov}, δ_{E}, $\Delta\bar{H}_{SS}^{\mathrm{chem}}$, $\Delta\bar{H}_{SS}^{\mathrm{el}}$, $\bar{\rho}$
FS3	$\mathrm{VEC}_{\mathrm{alloy}}$, δ_{cov}, δ_{E}, δ_{G}, $\Delta\bar{H}_{SS}^{\mathrm{chem}}$, $\Delta\bar{H}_{SS}^{\mathrm{el}}$
FS4	$\mathrm{VEC}_{\mathrm{alloy}}$, δ_{cov}, $\delta_{\mathrm{V_m}}$, δ_{E}, δ_{G}, $\Delta\bar{H}_{SS}^{\mathrm{chem}}$, $\Delta\bar{H}_{SS}^{\mathrm{el}}$
FS5	$\Delta\bar{S}_{\mathrm{config}}$, $\mathrm{VEC}_{\mathrm{alloy}}$, δ_{cov}, δ_{E}, δ_{G}, $\Delta\bar{H}_{SS}^{\mathrm{chem}}$, $\Delta\bar{H}_{SS}^{\mathrm{el}}$
FS6	δ_{met}, $\mathrm{VEC}_{\mathrm{alloy}}$, δ_{E}, $\Delta\bar{H}_{SS}^{\mathrm{chem}}$, $\Delta\bar{H}_{SS}^{\mathrm{el}}$, $\bar{\rho}$
FS7	δ_{met}, $\Delta\bar{S}_{\mathrm{config}}$, $\mathrm{VEC}_{\mathrm{alloy}}$, δ_{E}, $\Delta\bar{H}_{SS}^{\mathrm{chem}}$, $\Delta\bar{H}_{SS}^{\mathrm{el}}$, $\bar{\rho}$
FS8	δ_{met}, $\Delta\bar{S}_{\mathrm{config}}$, $\mathrm{VEC}_{\mathrm{alloy}}$, $\delta_{\mathrm{V_m}}$, δ_{E}, $\Delta\bar{H}_{SS}^{\mathrm{chem}}$, $\Delta\bar{H}_{SS}^{\mathrm{el}}$, $\bar{\rho}$
FS9	δ_{met}, $\Delta\bar{S}_{\mathrm{config}}$, $\mathrm{VEC}_{\mathrm{alloy}}$, $\delta_{\mathrm{V_m}}$, δ_{E}, δ_{G}, $\Delta\bar{H}_{SS}^{\mathrm{chem}}$, $\Delta\bar{H}_{SS}^{\mathrm{el}}$, $\bar{\rho}$
FS10	δ_{met}, $\Delta\bar{S}_{\mathrm{config}}$, $\mathrm{VEC}_{\mathrm{alloy}}$, δ_{cov}, $\delta_{\mathrm{V_m}}$, δ_{E}, δ_{G}, $\Delta\bar{H}_{SS}^{\mathrm{chem}}$, $\Delta\bar{H}_{SS}^{\mathrm{el}}$, $\bar{\rho}$

or initialized parameters were not carried forward. All performance results are from models trained on the randomized data with same seed to ensure uniformity of training/test sets between all models. This allows fair comparison of performance between models while ruling out any bias due to dataset. Python 3.8.1 and associated open-source libraries have been used for developing all the models reported here. We have used pandas|1.0.3 and numpy|1.18.2 for data processing, scikit-learn|0.22.2 and statsmodels|0.11.1 for linear regression and statistical analysis, and tensorflow|2.2.0rc2 and

keras | 2.3.1 for implementation of ANNs. All ANNs were trained using mean absolute error (MAE) loss function and Adam optimizer with a learning rate of 0.02. The performance of each ANN was calculated using only the cross-validation results, i.e., for each alloy, only that prediction was considered when it was part of the validation set and thus did not participate in the training process. For any given training process, the predictions of each validation set were recorded and statistical analysis (R^2, RMSE, MAE and average percentage error) was done on the combined predictions from all validation sets. Averaging of statistical scores from validation sets was not done as it would bring in bias by giving more/less importance to a particular validation set. The cross-validation performance for each trained model is detailed in Table 5.1 and the effect of model architecture and feature set has been visualized in Figure 5.5 and Figure 5.6.

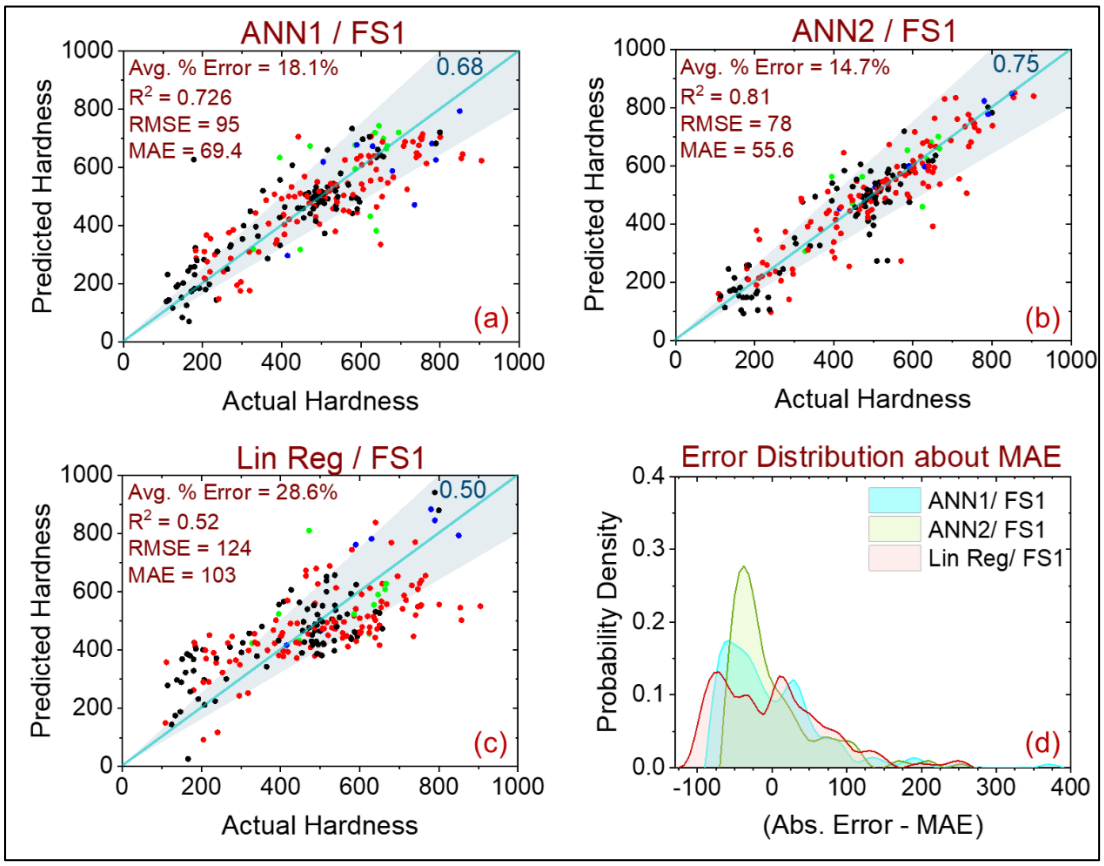

Figure 5.5 Significance of depth of ANNs. Parity plot for hardness predictions obtained using: (a) ANN1 and FS1, (b) ANN2 and FS1, and (c) Linear Regression (least squares). (d) Probability density of the absolute error about the MAE for predictions obtained through all three.

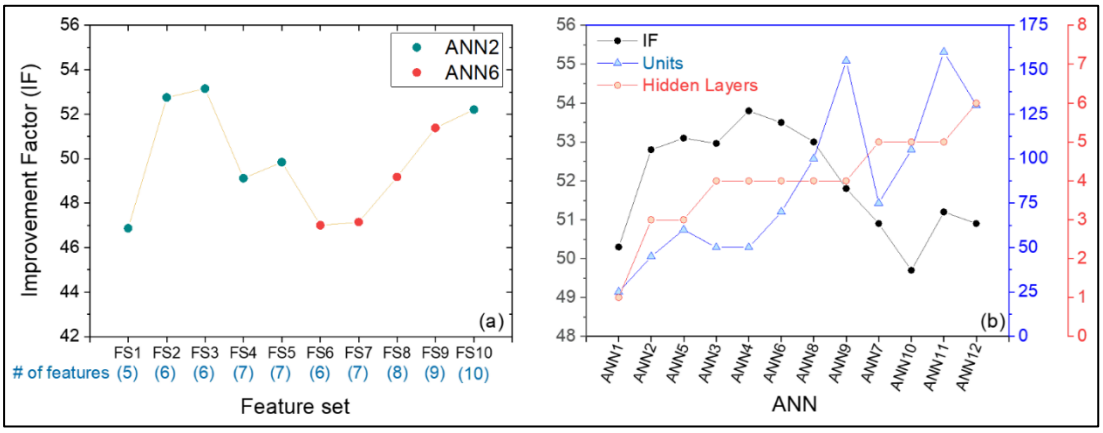

Figure 5.6 Improvement factor of (**a**) ANN2/ANN6 trained with different feature sets, and (**b**) ANNs with different architectures trained with FS2 feature-set.

5.2.4 Predictions using ensemble model

The final ML model consists of an ensemble of 165 trained ANN models which were selected based on their cross-validation performance scores. A model averaging technique is used wherein the final prediction is calculated as an average of the 165 predictions (one from each trained model present in the ensemble). The ML model developed here requires only a single user input viz. name of the alloy (for e.g., AlCo2CrFe0.5Ni) for predicting the hardness as the composition and features required by each ANN are calculated automatically by supporting scripts.

We generated hardness predictions (ternary contour plots in Figure 5.7, 5.8 and 5.9) over vast compositional spaces by reducing the compositional degree of freedom in CCAs through clubbing of elements into binary or ternary components. For example, in Figure 5.7a, AlTiCrFeNi system is broken into three components – Al, Ti and an equiatomic ternary (CrFeNi). This allows representation of CCAs composition space on a ternary plot. The first step is to create alloy compositions spaced by 1 atomic %, thereby leading to 5151 unique compositions. The ML model is used to predict the hardness at each of these compositions and the results are plotted as a predicted hardness contour on a ternary plot.

5.3 Methodology – ab-initio calculations and experiments

The DFT calculations for phase stability and ordering behavior were done by Dr. Prashant Singh and Prof. Duane Johnson at Ames Lab, USA. The experimental fabrication and hardness measurement for $Al_x(TiZrHf)_{1-x}$ alloys was done by Dr. Shalabh Gupta and Dr. Matthew Kramer at Ames Lab, USA.

5.3.1 Density Functional Theory Calculations

The density-functional theory (DFT) based Korringa-Kohn-Rostoker (KKR) Greens' function method combined with the coherent potential approximation (CPA) was used to calculate total energy of arbitrary solid-solution alloys[212]. The KKR-CPA performs configurational averaging simultaneously with charge self-consistency, which properly includes alloy-induced Friedel impurity-charge screening. For DFT, we used the Perdew-Burke-Ernzerhof (PBE) exchange-correlation functional for solids[218]. We employed a site-centered, spherical-harmonic basis that includes *s, p, d*, and *f* -orbital symmetries (i.e., l_{max}=3) in all calculations. The self-consistent charge density was obtained from the Green's function using a complex-energy contour integration and Gauss-Laguerre quadrature[212] (with 24-point semi-circular mesh enclosing the bottom to the top of the valence states). An equally spaced *k*-space mesh of 24 × 24 × 24 was used for Brillouin zone integrations. The core electrons were treated fully relativistically (includes spin-orbit coupling), while semi-core/valence electrons were treated scalar relativistically (i.e., neglecting spin-orbit coupling).

5.3.2 Linear-response Theory for Short-Range Order

Thermodynamic linear-response theory was used to calculated Warren-Cowley SRO parameters[79], i.e., $\alpha_{\mu\nu}^{ij}$, where $\mu\nu$ denote elements pairs in the alloys and ij are lattice sites in the crystal. For a homogeneous solid-solution alloy with a set of compositions $\{c_\mu^i\}$, the SRO dictates pair probabilities $P_{\mu\nu}^{ij} = c_\mu^i c_\nu^j(1-\alpha_{\mu\nu}^{ij})$ that potentially can affect chemical short-range order[127], as

well as mechanical behavior[219]. For a dominant **k**-space wavevector $\mathbf{k} = \mathbf{k}_o$, the SRO diverges at the spinodal temperature (T_{sp}) due to absolute instability in the correlated fluctuations, i.e., $\boldsymbol{\alpha}_{\mu\nu}^{-1;s,s'}(\mathbf{k}_o;T_{sp})=0$ (where s,s′ denote the independent sublattice in the structure), and provides an estimate for SRO and the order-disorder or miscibility temperature[79]. This first-principles theory of SRO is based on the electronic structure of the alloy; therefore, it directly embodies underlying electronic and alloying effects (like band-filling, hybridization, atomic-size, or Fermi-surface nesting[220]).

5.3.3 Experimental Methods

The $Al_x(TiZrHf)_{1-x}$ with x = 0-0.25 atomic fraction was synthesized by arc-melting on a water-cooled copper hearth in an ultra-high purity argon atmosphere using elemental chunks (Alfa Aesar, purity > 99.8%). Samples were melted, flipped and re-melted multiple times to ensure homogeneity. The Vickers microhardness testing was performed on a Wilson Instruments Tukon hardness tester using an indenter with a square pyramid shape. The micro-hardness tests employed a constant 500 g load with a hold time of 10 s. The indentation size was measured using an optical microscope, and a look up table is used to determine the Vickers hardness value. Micro hardness tests were performed 1 mm apart with 3 test measurements on each sample.

5.4 Results and discussion

The ML model was trained on databases available in the literature[211]. The model was validated using three different approaches – (a) Direct comparison with discrete hardness measurements of alloys across different alloy systems. (b) Validation of model predictions in systems with continuously varying compositions, where non-linear increases in hardness have been reported. And (c) experimental validation of model predictions for the $TiZrHfAl_x$ CCAs. The ML model predictions have been combined with *ab-initio* calculations in cases (b) and (c) for understanding the physics of the process and how well is it reflected by the ML model.

5.4.1 Model validation

The ML model, comprising of an ensemble of 165 trained ANNs, was used to predict the hardness of each alloy present in test set. Figure 5.2d shows the prediction results and performance metrics obtained for the test set. An average percentage error of 18.6% and mean absolute error of 82.8 HV was obtained on the test set, with 62% (75% if only as-cast alloys are considered) of predictions lying within 80% accuracy region. The alloys in test set were prepared with either vacuum arc melting (denoted by black dots) or through mechanical alloying (MA) plus spark plasma sintering (SPS) route (denoted by red dots, MA+SPS). Both the as-cast and (MA+SPS) alloys were kept in the test set to highlight the fact that the final model, trained on only as-cast alloys, is more prone to underpredict the hardness of alloys made through (MA+SPS) route. Thus, although the test set accuracy (~82%) is slightly lower in comparison with cross-validation accuracy (~87%), the model captures the experimentally measured hardness with a reasonable accuracy.

5.4.2 Prediction of non-linear trends in Hardness

Having established a good statistical performance of our model for discrete alloy compositions, we perform the next step in our validation, namely exploration of continuously varied composition space and prediction of non-linear variations in hardness. This validation can be accomplished only if the model can correctly identify both the continuous monotonic (near linear) and discontinuous (non-linear) variation of hardness due to subtle changes in alloying chemistry. The discontinuity in hardness values may arise from formation of new phases resulting in different microstructural assemblage as a result of compositional variations. The new crystal structures can have significantly different nearest neighbors (and hence bonding) as well as completely different slip systems affecting the resistance to localized plastic deformation. One also expects that significant incipient ordering, which may arise near phase boundaries as the composition is varied continuously prior to the actual phase separation/transformation, may be responsible for controlling

the "width" of the non-linear jumps in hardness. As shown previously, hardness depends on the nature of the atomic bonding[172,221]. The bond strength is mainly driven by constituent elements and their properties, such as electronegativity, that control the electronic-structure behavior[222]. Thus, we anticipate a dependence of CCA hardness on its overall electronic structure. Therefore, comparing electronic-structure behavior with hardness in the CCAs should reveal contributions from electronic mechanism.

Hence, we have explored a CCA system – $Al_xTi_y(CrFeNi)_{1-x-y}$ – that had the adequate microstructural complexity along with reported experimental hardness values over a range of compositions[223,224]. We have also investigated the $Hf_xCo_y(CrFeNi)_{1-x-y}$ system, where Hf content is seen to affect the ordering process. Notably, Co has a room temperature crystal structure similar to Ti and is expected to form a solid solution with CrFeNi, while Hf is expected to exhibit a strong clustering effect. As such, we assessed $Hf_xCo_y(CrFeNi)_{1-x-y}$ and compared the model predictions with the experimental measurements reported by Ma and Shek[225].

The interest in $Al_xTi_y(CrFeNi)_{1-x-y}$ system stems from the role of Al in promoting B2 ordering in a number of systems[79,186]. Ti does not have as pronounced an effect on ordering as Al, but Ti-containing systems do exhibit formation of intermetallics[223,224,226]. Figure 5.7a shows the contour plot of hardness predictions for the entire composition range of Al_xTi_y $(CrFeNi)_{1-x-y}$ system. An inset (in Figure 5.7b) shows an expanded view where experimental measurements are available. Predicted and actual hardness values are compared (Figure 5.7c) for five $Ti_x(CrFeNi)_{1-x}$ compositions (x = 0.0625 – 0.1666) studied by Gao et al.[224] to investigate the effect of Ti addition. Both the measurements and the predicted values show a near-linear monotonic increase and there is an excellent agreement in general trends, although absolute values are underpredicted. To understand the underlying reason for the deviation of predicted hardness, we performed phase stability (E_{form}) analysis in Figure 5.7d, and found that increasing Ti stabilizes the BCC structure, which mirrors the trends in hardness. This stabilization is also borne out by the experiments,

where increased Ti content led to a reduction of the FCC phase fraction, as well as increase in the BCC phase fraction. Additionally, minor amounts of intermetallic phases begin to form (ε-phase, Ni_3Ti at low Ti and the R-phase, $Ni_{2.67}Ti_{1.33}$ at higher Ti). Figure 5.2a indicates that the training dataset included only a very small amount of intermetallics (1) or multi-phase mixtures (14) – FCC+BCC+IM. Presumably, the data available was too sparse for greater accuracy. Enhanced E_{form} strongly correlates with charge sharing due to increased hybridization among constituent elements and suggests towards increased bond strength in $Ti_x(CrFeNi)_{1-x}$. The bonding behavior is dependent on local environment; therefore, we hypothesize that it should directly impact the local electronic properties, such as short-range order. The SRO strength of $Ti_x(CrFeNi)_{1-x}$, calculated using thermodynamic linear-response theory[79], is shown in Figure 5.7e. We found that the SRO of dominant pairs (Cr-Ni pair at x=0; and Ti-Ni pair x=0.0629-0.189) increases with increasing Ti. The stronger SRO also indicates increased concentration fluctuations, which directly correlates with stronger bonding character arising from increased hybridization. This bonding/hybridization effect is an aspect that has not been considered in the ML model directly due to a paucity of data on which the model could be trained. Nonetheless, the model does include the formation enthalpy, as estimated by Miedema's semi-empirical model as a feature, which is expected to correlate with bonding. At this stage, we note that Miedema's model provides a reasonable agreement with experimental measurements of formation enthalpies but it does not seem to capture the effect of Ti adequately. As a result, the elemental descriptors for Ti in Miedema's model must be adjusted and this is another potential source of error.

As Al is added (with corresponding decrease in the amount of Ti) and we move from the quaternary $Ti_xCrFeNi$ to the quinary $Al_xTi_y(CrFeNi)_{1-x-y}$, the accuracy of the model is seen to improve with excellent agreement between experimental measurements and ML predictions, as seen in Figure 5.7f. Significantly, the ML

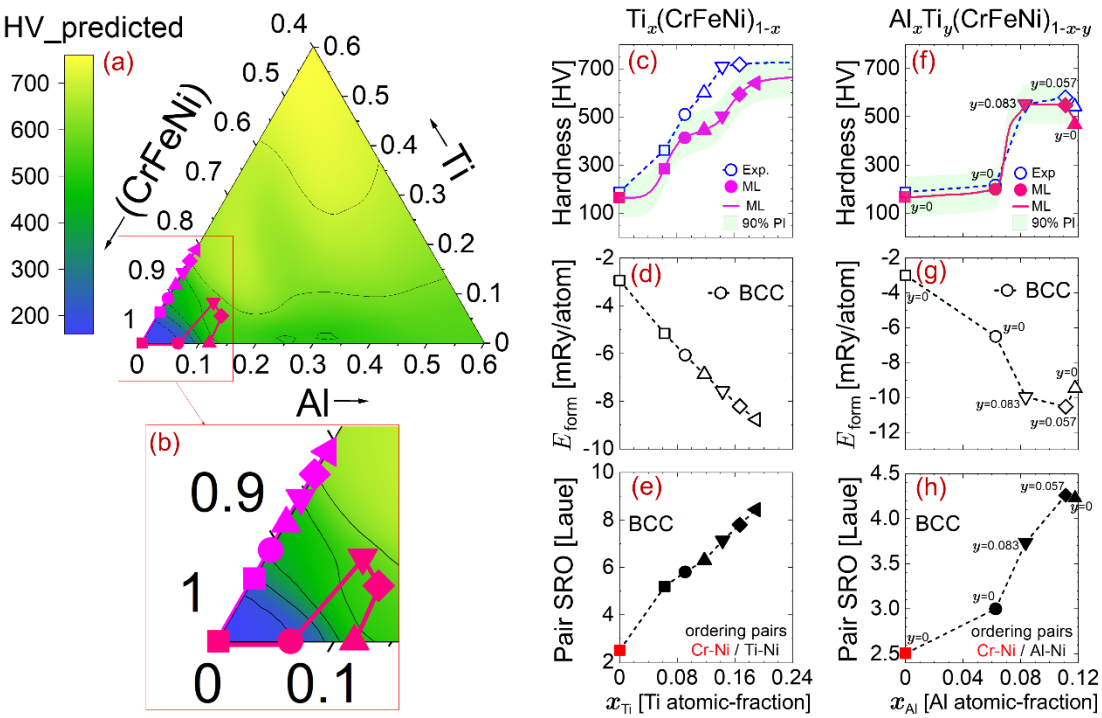

Figure 5.7 ML predictions of hardness and corresponding formation enthalpy and SRO obtained from DFT calculations. (a) Predicted hardness contours for $Al_xTi_y(CrFeNi)_{1-x-y}$. (b) Inset shows the hardness contours in Al-poor and Ti-poor regions, along with composition trajectories along which hardness measurements and predictions are compared. (c) Experimental and ML-predicted hardness for $Ti_x(CrFeNi)_{1-x}$ with a 90% prediction-interval (PI). (d) Formation energy of the BCC alloy and (e) Pairwise SRO in $Ti_x(CrFeNi)_{1-x}$. (f) Experimental and ML-predicted hardness for $Al_xTi_y(CrFeNi)_{1-x-y}$ with a 90% prediction-interval (PI). (g) Formation energy of the BCC solid solution and (h) Pair SRO and dominant ordering pairs in $Al_xTi_y(CrFeNi)_{1-x-y}$.

is able to predict the non-linear increases in hardness as a function of composition. A comparison with experiments[223] and prior phase stability calculations[83] indicates that Al addition results in a structural change, with the simple FCC structure transforming to a three-phase mixture (FCC + BCC + Intermetallic). We investigated this further here. We performed DFT calculations for phase stability[127] (Figure 5.7g) and short-range order (SRO) of CCAs[79,227], in particular the strength of dominant pairs (Figure 5.7h). Our DFT calculations (which embody quantum mechanics) provide robust E_{form} prediction in CCAs[127,220]. Clearly, the trends in E_{form} and SRO pair strength match with hardness in Figure 5.7f, i.e., our model is able to capture the electronic-structure-driven features yielding a non-linear change in hardness. The possible reason for small or no error in hardness of $Al_xTi_y(CrFeNi)_{1-x-y}$ comes from the fact that SRO contribution is very weak compared to $CrFeNiTi_x$,

and the relative amount of Ti is lower in comparison to the quaternary alloy; hence, errors associated with Miedema's calculation of formation enthalpies is minimized.

The hardness contours for the Hf-Co-(CrFeNi) system are shown in Figure 5.8a where Figure 5.8b gives an expanded view of the region investigated experimentally by Ma and Shek[225]. The model predicts a strong dependence of hardness on the Hf content, as the predicted hardness contours in Figure 5.8a are almost entirely dictated by the amount of Hf present in the system. The predictions accurately follow the experimental hardness[225] values shown in Figure 5.8c. The hardness variation in this system is relatively linear. The E_{form} in Figure 5.8d clearly shows that Hf destabilizes the FCC phase. Stability predictions show good agreement with experiments as the hypoeutectic microstructures and Laves phases increase with increasing %Hf[225]. With the addition of Hf, the $Hf_x(CoCrFeNi)_{1-x}$ CCAs transformed from a single-phase FCC structure at x = 0 to (C15 Laves + FCC phases) at x = 0.09. Hypoeutectic microstructures were obtained from x = 0.024-0.069 and a fully eutectic structure with lamellas of FCC and C15 Laves phase was found at x = 0.09[225]. This result raises a question whether the intermetallic phase contributes significantly to the hardness in the hyper-eutectic region. The other possibility would be enhanced contributions to hardness due to ordering or clustering in the solid solution phase itself. To explore this aspect, we calculated the SRO pair strength using DFT. The SRO pair strength in Figure 5.8e is even more interesting as $Hf_x(CoCrFeNi)_{1-x}$ at x = 0 shows weak ordering behavior with SRO pair strength of 2.51 Laue (Cr-Ni pair) but adding Hf (x > 0) promotes clustering (clustering is often related to unstable density of states at the Fermi-level[43]. The clustering strength of dominant Hf-Cr pair (21-29 Laue) shows monotonic increase with increasing %Hf. Clustering in Hf-Cr pairs suggests that Hf does not thermodynamically prefer to sit around Cr, i.e., Hf promotes phase separation. In some cases, the presence of multiple phases in CCAs improves hardness as the multiple phases with different grain sizes and grain orientation can strengthen the alloy. Thus, it is possible that the Hf-Cr

clustering drives the eutectic phase formation and eventually contributes to enhanced hardness through the formation of second phase intermetallics.

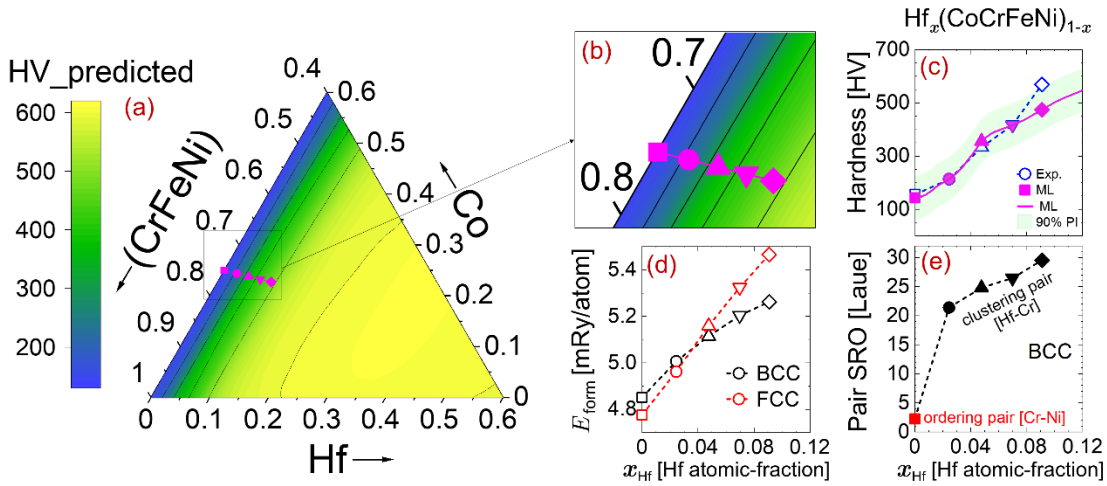

Figure 5.8 ML predictions of hardness and corresponding DFT-predicted formation enthalpy and SRO. (a) Predicted hardness contours for $Hf_xCo_y(CrFeNi)_{1-x-y}$ system, with (b) showing an expanded view of the compositions from experiments by Ma and Shek[225]. (c) Experimental and ML-predicted hardness for $Hf_x(CoCrFeNi)_{1-x}$ alloys with a 90% prediction-interval (PI). (d) DFT formation energies showing the relative stabilities of the BCC and FCC structures. (e) DFT SRO and the main ordering and clustering pairs present.

5.4.3 Experimental validation in the Al-Ti-Zr-Hf alloy system

While the $Al_xTi_y(CrFeNi)_{1-x-y}$ and $Hf_xCo_y(CrFeNi)_{1-x-y}$ systems provided a study in contrast displaying ordering and clustering tendencies, respectively, in neither of these two systems were defects (like vacancies) noted to play a prominent role. However, the formation of a vacancy-stabilized phase was recently discovered in the $Al_x(TiZrHf)_{1-x}$ system, where values of $x > 0.125$ promote the formation of a new type gamma-brass (4-vacancy ordered) phase[186]. Such phases were absent from the training dataset and, therefore, the ML model is not necessarily expected to give accurate predictions. Nonetheless, this creates an opportunity for understanding whether the vacancies play a significant role in the hardness. Furthermore, it should be noted that the crystal structure of ternary TiZrHf is hcp, which is also absent from the training dataset. Hence, we choose to measure the hardness in the $Al_x(TiZrHf)_{1-x}$ system to test the limits of the ML model.

The model was observed to underpredict the hardness by a maximum of 18% across the compositions studied. Nonetheless, the model was able to capture the trends in hardness quite accurately. Figure 5.9a shows the predicted hardness contours in the $Al_xTi_y(ZrHf)_{1-x-y}$ system, while Figure 5.9b shows the comparison of predicted and experimentally measured hardness. The values are significantly under-predicted by the ML model, which is indicative that the quantitative predictions by model may be limited in cases where significant vacancy-ordering or occurrence of the hcp structure occurs. This in itself is not a surprising result since the CCAs database used for training the model consists largely of cubic solid solution alloys with few multi-phase alloys with a constituent intermetallic phase. It is, however, interesting to observe that the model still predicts the general trends in hardness.

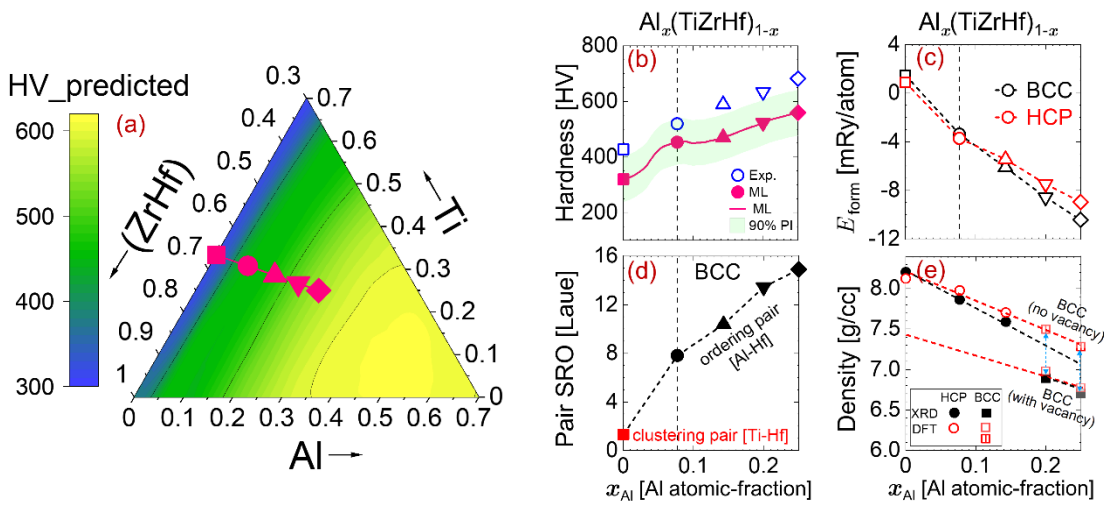

Figure 5.9 ML hardness predictions and corresponding DFT-predicted formation enthalpy and SRO. (a) Predicted hardness contours for $Al_xTi_y(ZrHf)_{1-x-y}$ system. (b) Experimental and ML-predicted hardness for $Al_x(TiZrHf)_{1-x}$ alloys with a 90% prediction-interval (PI). (c) DFT energy calculations shows the relative stabilities of the BCC and HCP structures. (d) DFT SRO pairs show the ordering and clustering tendencies. (e) DFT and XRD densities compared for the HCP, BCC (vacancy-stabilized) and disordered BCC (without vacancy) phases.

In Figure 5.9c, we plot alloy phase stability and overall, a monotonous change in E_{form} was found except a jump at Al=0.0749 atomic faction. The similar jump was also observed in hardness in Figure 5.9b, i.e., the ML model is able to capture the electronic and size effect through valence-electron count and atomic-radii, respectively. The reason for jump in hardness is obvious as alloy undergoes a phase transformation (hcp→bcc) at Al=0.0749; however, it still

does not explain why ML model underestimates the hardness by 15-20%. Similar to $Ti_x(CrFeNi)_{1-x}$, the enhanced E_{form} in $Al_x(TiZrHf)_{1-x}$ can well correlate to improved bond strength that can directly impact the local properties, such as short-range order. In Figure 5.9d, we plot DFT-derived SRO pair strength of dominant pairs in BCC phase. At Al=0, the clustering in Ti-Hf pairs is the dominant mode, which suggests that Ti and Hf want to phase separate and form a two-phase region. Moreover, adding Al stabilizes the bcc phase, as shown in Figure 5.9c. For Al>0, the $Al_x(TiZrHf)_{1-x}$ shows ordering and Al-Hf is the dominant SRO pair. In going from clustering mode for Al=0 to ordering mode for Al>0 in Figure 5.9d, a jump in SRO pair strength and hardness is seen in Figure 5.9b at same Al atomic fraction. Recently, Singh et al.[186] studied $Al_x(TiZrHf)_{1-x}$ CCAs and found that vacancies stabilize the BCC phase at higher Al content, whereas competing (BCC/HCP) phases were found in Al-poor region. The abrupt change in $Al_x(TiZrHf)_{1-x}$ densities with 7.45 at.% vacancies matches with X-ray measured density in Figure 5.9e[186]. Clearly, the ANN model is able to capture the trends of experiments and electronic features but underpredicts the hardness. In $Al_x(TiZrHf)_{1-x}$, both SRO and vacancies have significant contribution on alloy properties, however, the ML model was not trained with these quantities.

5.4.4 Physical insights from decision-making process of the ML model

The results presented thus far highlight the accuracy of ML model along with its ability to predict non-linear hardness variations associated with phase transitions in a variety of CCAs. But this still leaves two fundamental questions. What is the decision-making process followed by the ML model? Are these decisions purely statistical in nature or do they capture the fundamental physics that can lead to insights into the physical origins of hardness? To address these questions, we have probed the nature of the fit using CoSMoR (detailed in Chapter 3) that exposes the exact contribution of each feature towards the predicted hardness over continuous composition variations. Notably, CoSMoR does not just rank the features based on their perceived or indicative importance, but gives directly the exact quantitative contribution of

each feature towards decision-making. Also, CoSMoR ensures that the causality for model understanding is not some arbitrary change in feature values but instead the alloy composition which is the direct point-of-control in alloy design.

The hardness contribution of each feature (as obtained from CoSMoR) and overall hardness variation for $Al_x(CrFeNi)_{1-x}$, $Ti_x(CrFeNi)_{1-x}$, $Hf_x(CoCrFeNi)_{1-x}$, and $Al_x(TiZrHf)_{1-x}$ CCAs is shown in Figure 5.10. The non-linear decision making of the ML model is evident through the non-linear contribution of select features to hardness. Additionally, it appears that the origin of non-linear response arises due to a combination of features, some of which result in near-linear response while the others serve to "classify" the structure of the system in almost a step-like manner, which introduces the non-linearity. For example, the VEC, that acts as a classifier for phase selection (FCC and/or BCC), seems to plateau over a range where further variation in VEC does not affect structural changes.

The CoSMoR results, in tandem with first-principles DFT calculations, conclusively shows that the model is cognizant of the underlying physics such as relative phase stability, phase transitions, SRO and solid-solution strengthening. There are four key insights obtained from the breakdown of ML model. Firstly, the hardness contribution of VEC is strikingly different in $Al_x(CrFeNi)_{1-x}$, $Ti_x(CrFeNi)_{1-x}$ and $Hf_x(CoCrFeNi)_{1-x}$ CCAs even though the VEC varies almost identically. The ML model gives significant importance to VEC in $Al_x(CrFeNi)_{1-x}$ in the composition range where FCC→ BCC phase transition is expected based on experimental observations[223,228]. In $Ti_x(CrFeNi)_{1-x}$, VEC contribution is lower, in line with the lower BCC stability obtained from Ti addition as compared to Al, as seen in Figure 5.7(d, g). In contrast, addition of Hf in $Hf_x(CoCrFeNi)_{1-x}$ does not induce this FCC→ BCC transition[225] and the VEC contribution towards predicted hardness in ML

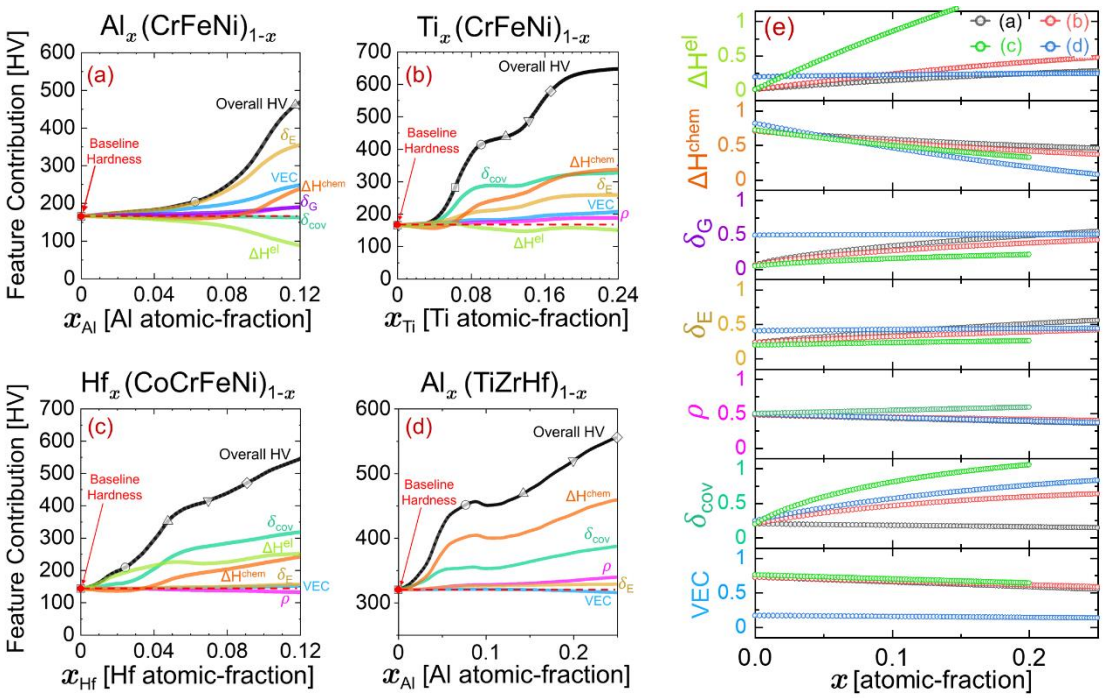

Figure 5.10 Visualizing the decision-making process of ML model. Contribution of different features toward ML hardness prediction in: (a) $Al_x(CrFeNi)_{1-x}$, (b) $Ti_x(CrFeNi)_{1-x}$, (c) $Hf_x(CoCrFeNi)_{1-x}$, and (d) $Al_x(TiZrHf)_{1-x}$ alloy systems. At any composition (x), the hardness contribution of each feature is equal to the vertical distance between that feature contribution plot and the baseline hardness value (calculated at x=0). At any x, the summation of baseline hardness and all feature contributions will result in overall hardness. (e) Feature variations with respect to composition for alloy systems shown in (a-d). Normalized feature values have been plotted here. Feature notations: VEC-Valence electron concentration, δ_{cov}-asymmetry in covalent radius, ρ-average density, δ_E-asymmetry in Young's modulus, δ_G-asymmetry in shear modulus, ΔH^{chem}-chemical enthalpy of mixing, ΔH^{el}-elastic enthalpy of mixing. Features that had negligible contribution to hardness prediction over these composition ranges have not been included in the plots.

model is also negligible. This is significant as FCC→ BCC transitions in CCAs have been linked to VEC in past[111,127,171] and the hardness of BCC structures is significantly higher; and thus, it appears that the ML model has successfully "learned" these nuances that are critical for accurate hardness prediction.

Secondly, the contributions of chemical mixing enthalpy (ΔH^{chem}) and asymmetry in covalent radius (δ_{cov}) toward hardness prediction are quite significant and follow each other closely (except for $Al_x(CrFeNi)_{1-x}$ where the value of δ_{cov} changes only slightly with Al addition, thereby resulting in its negligible contribution to hardness). The hardness contributions of ΔH^{chem} and δ_{cov} in ML model are strongly linked to the ordering tendencies, as they are

negligible at low SRO values but kick in suddenly as SRO increases beyond ~4-5 Laue; this happens at ~10 at.% Al in $Al_x(CrFeNi)_{1-x}$, ~4 at.% Ti in $Ti_x(CrFeNi)_{1-x}$ and ~3 at.% Al in $Al_x(TiZrHf)_{1-x}$, as seen from Figure 5.7(e, h), Figure 5.9d and Figure 5.10(a, b, d). Also, while both ΔH^{chem} and δ_{cov} contributions follow ordering tendencies, δ_{cov} appears to be considerably more dominant where intermetallic formation occurs, as seen for $Ti_x(CrFeNi)_{1-x}$ and $Hf_x(CoCrFeNi)_{1-x}$ systems in Figure 5.10(b, c), both of which exhibit strong intermetallic formation[224,225]. The contributions to hardness from ΔH^{chem} and δ_{cov} also appear to be sensitive to phase transformations as their slopes change significantly wherever phase transitions appear. In $Al_x(TiZrHf)_{1-x}$, Figure 5.10d, this coincides with HCP→BCC transition as Al increases from 7.7 to 14.2 at.%, as seen in Figure 5.9b, and in $Ti_x(CrFeNi)_{1-x}$, the two non-linear jumps in ΔH^{chem} and δ_{cov} hardness contributions, as seen in Figure 5.10b, coincide with the formation of ε-phase (Ni_3Ti , HCP) at low Ti concentrations and a metastable R-phase ($Ni_{2.67}Ti_{1.33}$) at higher concentrations[224]. This insight is significant as the short-range order and the nature of metallic bonds have been linked to intermetallic formation and mechanical properties in previous studies[172,219]. The ML model appears to be able to capture these dependencies quite accurately through variations in ΔH^{chem} and δ_{cov}.

The third insight is from the hardness contributions from asymmetry in Young's Modulus (δ_E), which appear to be more direct wherein a larger increase in δ_E manifests as a more significant increase in hardness; as can be seen for $Al_x(CrFeNi)_{1-x}$ which shows the highest increase in δ_E among the systems studied and consequently exhibits highest contribution of δ_E towards ML predicted hardness. But, note that the hardness contribution of δ_E is not linear with respect to feature value and appears to follow similar trends as ΔH^{chem} and δ_{cov}, which are linked to ordering and phase transformations. This is along expected lines, because the Young's modulus can be calculated in principle from the interatomic potential-energy (U) vs. separation (r) curve, where the force $F = -\partial U/\partial r$. At constant pressure and negligible volume changes, $\delta U \approx dH$. A larger δ_E would indicate the presence of a pair of atoms

where one species has a higher bond strength (and hence higher stiffness or larger Young's modulus) and the other has a lower bond strength. It has been observed empirically for minerals that higher is the localization of the electron density, higher is the bond strength. In Miedema's model, the value of ΔH^{chem} is a function of the difference in the Wigner-Seitz cell boundary electron density and will likely predict a higher value of ΔH^{chem} for the atomic species pair described above.

Finally, the elastic mixing enthalpy (ΔH^{el}) increases monotonically with respect to composition (x) in all systems studied here, but its contribution to hardness prediction shows striking differences and shifts from negative to negligible to strongly positive contribution as we move from $Al_x(CrFeNi)_{1-x}$ to $Ti_x(CrFeNi)_{1-x}$ to $Hf_x(CoCrFeNi)_{1-x}$ system. Addition of Hf to CoCrFeNi causes a significant increase in ΔH^{el} and the Hf-Cr pair has a strong clustering tendency, as shown in Figure 5.9e, indicating that Hf does not prefer sitting next to Cr. Recently, Roy et al.[229] have demonstrated that lattice distortion can be used for estimating solid-solution hardening in high-entropy alloys, where the solute-atom dislocation interaction energy was calculated as a function of shear modulus, solute-atom–dislocation-core distance and local strain. The distance from dislocation core is influenced by atomic size (i.e., molar volume) with smaller atoms segregating easily to dislocation cores and the local strain is influenced by the radius asymmetry. ΔH^{el} captures these nuances to some extent as it reflects both the local distortion and the bonding characteristics. Figure 5.10c shows that the hardness increase predicted by ML model at low Hf concentration (<3 at.%) originates almost entirely from ΔH^{el} contribution, indicating that the ML model is able to correctly predict the hardness variations accompanying phase separation processes driven by a combination of weak ordering parameter and high elastic strain energy.

5.5 Conclusions

In summary, our machine-learning (ML) framework identifies in the decision-making process the essential feature sets, non-linear responses, and the

underlying correlated physics – here, for hardness in compositionally complex alloys (CCAs). Our ML model utilizes an ensemble of 165 independent neural networks that are driven by physical features to predict the hardness of CCAs; wherein each network is trained on a diverse dataset using elemental and alloying descriptors. The model successfully predicts hardness variations in a wide variety of CCAs and closely follows the ordering behaviour and phase transitions observed from first-principles calculations. The decoding of ML model, achieved through implementation of CoSMoR, indicates that the underlying physics is being captured through predictors of atomic-interactions (such as formation enthalpy and bonding characteristics) and local-lattice distortion (such as size-asymmetry, elastic-enthalpy and strain-energy) along with a phase classifier (VEC). Our proposed ML framework presents a promising way of efficiently exploring wide compositional spaces in CCAs.

While the ML model is generally successful, it appears that small discrepancies with the experimental measurements stem from: (i) discrepancies in experimental and calculated enthalpies that can become significant for systems containing elements prone to multiple oxidation states such as Ti – an artifact that is carried over from Miedema's approach, and (ii) lack of explicit information on crystal structure and SRO parameters, neither of which is known without *a priori* experiments and/or DFT calculations. Improvements in the proposed model will, therefore, require accurate prediction of short-range order parameters and crystal structures from elemental properties and improved description of thermodynamic interactions. For example, it is well known that the short-range order in disordered alloys may affect mechanical response[230], therefore, it is important for future models to effectively capture such effects on material properties. In next chapter, we try to address some of these issues by developing a machine learning model for prediction of short-range order in CCAs.

5.6 Research data

The training dataset used for the development of machine learning model was collected from https://doi.org/10.1016/j.dib.2018.11.111[211]. The processed training dataset with normalized feature values as well as the codes used for trailing of machine learning models are available at GitHub: https://github.com/IDEAsLab-Materials-Informatics/ML-hardness-MPEAs. The test dataset of 58 alloys compiled for this work is available in Supplementary data (§5.7).

5.7 Supplementary data

Test dataset of 58 CCAs compiled from recent literature along with their actual and predicted values.

S. No.	Alloy Name	Actual (HV)	Predicted (HV)	Ref
1	AlCoFeNiTi	635	552	Edalati et al.: 10.1016/j.msec.2020.110908
2	CrFeNiNb 0.1 Ti 0.2	512	414	Zhang et al: 10.1016/j.msea.2019.138212
3	CrFeNiNb 0.1 Ti 0.3	629	439	Zhang et al: 10.1016/j.msea.2019.138212
4	CrFeNiNb 0.1 Ti 0.4	867	515	Zhang et al: 10.1016/j.msea.2019.138212
5	AlCoCr0.5Fe0.5Ni2.5	343	424	Liu et al.: 10.1016/j.jallcom.2020.153881
6	AlCoCr0.5Fe1.5Ni2.5	294	396	Liu et al.: 10.1016/j.jallcom.2020.153881
7	AlCoCr0.5Fe2.5Ni2.5	247	251	Liu et al.: 10.1016/j.jallcom.2020.153881
8	AlCoCr0.5Fe3.5Ni2.5	224	204	Liu et al.: 10.1016/j.jallcom.2020.153881
9	Al 10.86 Cr 20.93 Fe 22.48 Mn 22.11 Ni 23.62	553	423	Dewangan et al.: 10.1016/j.jallcom.2020.153766
10	Al 10.47 Cr 20.18 Fe 20.67 Mn 21.32 Ni 22.78 W 3.59	503	557	Dewangan et al.: 10.1016/j.jallcom.2020.153766
11	Al 10.11 Cr 19.49 Fe 20.93 Mn 20.59 Ni 22 W 6.89	490	616	Dewangan et al.: 10.1016/j.jallcom.2020.153766
12	Al 7.95 Cr 15.32 Fe 16.45 Mn 16.19 Ni 17.29 W 26.8	461	666	Dewangan et al.: 10.1016/j.jallcom.2020.153766
13	Al 5.66 Co 18.87 Cr 18.87 Fe 18.87 Mn 18.87 Ni 18.87	125	170	Chang et al.: 10.1007/s11837-019-03704-4
14	Al 11 Co 18 Cr 22 Fe 22 Mn 5 Ni 22	198	316	Chang et al.: 10.1007/s11837-019-03704-4
15	Al 30.5 Co 16 Cr 18.5 Fe 16.5 Mn 5 Ni 13.5	522	517	Chang et al.: 10.1007/s11837-019-03704-4
16	Al 30 Co 6 Cr 35 Fe 6 Mn 18 Ni 5	605	577	Chang et al.: 10.1007/s11837-019-03704-4
17	Al 25.5 Co 9 Cr 35 Fe 10 Mn 15.5 Ni 5	628	574	Chang et al.: 10.1007/s11837-019-03704-4
18	Al 24 Co 18 Cr 35 Fe 10 Mn7.5 Ni 5.5	650	561	Chang et al.: 10.1007/s11837-019-03704-4
19	Al 8 Co 25 Cu 18 Fe 25 Ni 25	129	173	Fu et al.: https://doi.org/10.1016/j.actamat.2016.01.050.
20	Al 10 Co 17 Fe 35 Mo 6 Ni 34	182	260	Menou et al.: 10.1016/j.matdes.2018.01.045
21	Fe 40 Mn 14 Ni 10 Cr 10 Al 15 Si 10 C 1	596	560	Jain et al.: https://doi.org/10.1016/j.jallcom.2020.155013
22	Al 35 Cr 14 Mg 6 Ti 35 V 10	460	531	Chauhan et al: 10.1016/j.jallcom.2019.153367

S. No.	Alloy Name	Actual (HV)	Predicted (HV)	Ref
23	Mo 0.5 VNbTi	370	459	Xiang et al.: 10.1016/j.jallcom.2019.153352
24	Mo 0.5 VNbTiCr 0.25	410	465	Xiang et al.: 10.1016/j.jallcom.2019.153352
25	Mo 0.5 VNbTiCr 0.5	456	489	Xiang et al.: 10.1016/j.jallcom.2019.153352
26	Mo 0.5 VNbTiCr 0.75	488	515	Xiang et al.: 10.1016/j.jallcom.2019.153352
27	Mo 0.5 VNbTiCr 1	518	538	Xiang et al.: 10.1016/j.jallcom.2019.153352
28	Mo 0.5 VNbTiCr 1.5	580	565	Xiang et al.: 10.1016/j.jallcom.2019.153352
29	Mo 0.5 VNbTiCr 2	668	573	Xiang et al.: 10.1016/j.jallcom.2019.153352
30	Al 19.2 Co 28 Fe 28 Ni 24.8	556	409	Avila-Rubio et al: 10.1016/j.apt.2020.02.008
31	Al 17.6 Co 22.6 Fe 24.2 Ni 22.1 Mo 13.5	639	621	Avila-Rubio et al: 10.1016/j.apt.2020.02.008
32	Al 14.6 Co 21.5 Fe 22.6 Ni 20.4 Ti 20.9	681	547	Avila-Rubio et al: 10.1016/j.apt.2020.02.008
33	Al 13.7 Co 18.3 Fe 19.5 Ni 17.9 Mo 14.4 Ti 16.2	894	635	Avila-Rubio et al: 10.1016/j.apt.2020.02.008
34	TiAlMoSiW	803	583	Kanyane et al.: 10.1016/j.matpr.2020.02.095
35	Ti 0.25 AlMoSi 0.25 W 0.1	750	560	Kanyane et al.: 10.1016/j.matpr.2020.02.095
36	Ti 0.3 Al Mo Si 0.3 W 0.1	765	568	Kanyane et al.: 10.1016/j.matpr.2020.02.095
37	CoCrFeNi	156	143	Ma and Shek: 10.1016/j.jallcom.2020.154159
38	CoCrFeNiHf 0.1	213	214	Ma and Shek: 10.1016/j.jallcom.2020.154159
39	CoCrFeNiHf 0.2	333	356	Ma and Shek: 10.1016/j.jallcom.2020.154159
40	CoCrFeNiHf 0.3	417	416	Ma and Shek: 10.1016/j.jallcom.2020.154159
41	CoCrFeNiHf 0.4	569	474	Ma and Shek: 10.1016/j.jallcom.2020.154159
42	Al 0.6 CrCuFeMnNi	220	230	Mitrica et al.: 10.1016/j.matchemphys.2019.122555
43	AlCrCoFeNiTi	380	603	Mitrica et al.: 10.1016/j.matchemphys.2019.122555
44	Al 0.33 CrCuFeMn 0.33 NiSi 0.33	441	224	Mitrica et al.: 10.1016/j.matchemphys.2019.122555
45	Al 0.5 CrFeMnNi 0.5	412	458	Mitrica et al.: 10.1016/j.matchemphys.2019.122555
46	FeCoNiCuMo 0.2	162	215	Soni et al.: 10.1016/j.vacuum.2020.109173
47	FeCoNiCuMo 0.4	203	233	Soni et al.: 10.1016/j.vacuum.2020.109173
48	FeCoNiCuMo 0.6	277	237	Soni et al.: 10.1016/j.vacuum.2020.109173
49	FeCoNiCuMo 0.8	347	241	Soni et al.: 10.1016/j.vacuum.2020.109173
50	FeCoNiCuMo 1	382	244	Soni et al.: 10.1016/j.vacuum.2020.109173
51	AlCrCuFeNiV 0.2	522	485	Huang et al.: 10.1016/j.vacuum.2019.109129
52	AlCrCuFeNiV 0.6	560	592	Huang et al.: 10.1016/j.vacuum.2019.109129
53	AlCrCuFeNiV 1	549	630	Huang et al.: 10.1016/j.vacuum.2019.109129
54	CrFeNi	187	165	Zhang et al.: 10.1016/j.msea.2019.138566
55	CrFeNiAl 0.2	215	199	Zhang et al.: 10.1016/j.msea.2019.138566
56	CrFeNiAl 0.4	542	468	Zhang et al.: 10.1016/j.msea.2019.138566
57	CrFeNiAl 0.3 Ti 0.3	551	554	Zhang et al.: 10.1016/j.msea.2019.138566
58	CrFeNiAl 0.4 Ti 0.2	580	548	Zhang et al.: 10.1016/j.msea.2019.138566

Chapter 6: Phase evolution in CoCrCuNi-M alloys in presence of strong ordering and clustering binary pairs

6.1 Introduction

In this chapter, we present the experimental results on phase selection and hardness in the CoCrNi, CoCrCuNi and CoCrCuNi-M (M={Al, Ti, Zr, Nb, Mo}) alloy systems that were studied to – (a) validate the ML models for phase selection and hardness prediction that were developed in previous chapters, (b) study the effect of strong ordering/clustering binary pairs on phase evolution in CCAs and (c) establish limiting conditions and boundaries for the ML model. The rationale for selecting these systems is grounded in our recent work, which showed that Zn addition to AlCrFeCoNi leads to the rarely seen preferential ordering of Al-Cr binary pair, indicating that the presence of strong clustering or ordering pairs can drive unexpected behavior in CCAs [133]. Since the alloy development with Zn is difficult (especially, when synthesized via casting, owing to its very low boiling point), we included Cu in this work as it also introduces strong ordering/clustering with the 3d and 4d transition metals. The addition of Cu, however, introduces additional complexities, especially with respect to the presence of refractory metals, since the databases used for model development had only one composition that included a Cu-Mo pair and no compositions with a Cu-Nb pair. Thus, in addition to being a more

---

D Beniwal, PK Ray et al., Phase evolution in CoCrCuNi-M alloys in presence of strong ordering and clustering binary pairs, **Under preparation**

practical option than Zn, this also provided us with a means of testing the limits of the models developed.

The base alloy composition is the equiatomic ternary CoCrNi medium entropy alloy, chosen since it is known to form a single-phase solid solution. The alloy compositions were selected through careful chemical additions to this ternary base alloy system to synthesize quaternary and quinary alloys such that each alloy had at least one strong ordering or clustering pair present in it. CoCrNi has been studied extensively in recent years[231,232]. It shows a highly stable single-phase FCC structure that aligns with the expectations since – (a) it has a high average valence electron count (VEC) of 8.33 which suggests higher stability of FCC phase over BCC phase according to empirical VEC-based rule [46], (b) all binary pairs in CoCrNi show low, albeit negative chemical interaction parameters, and very low elastic interaction parameters (Figure 6.1) indicating the potential of developing an entropy stabilized solid solution alloy (low, but negative, i.e., attractive interactions indicate alloying while the entropic stabilization is expected to drive the system towards a structurally ordered, but chemically disordered solid solution), which also suggests no preferential ordering/clustering that may be driven by chemical interactions, and (c) there is no indication of large lattice strains in the alloy owing to the similar atomic sizes of Co, Cr and Ni and negligible elastic interaction parameters of all binary pairs (Figure 6.1b). The role of the interaction parameters offers physical and quantitative insights into the process of alloying and segregation [133]. Hence, we include a separate section on this topic (§6.3.26.3.2) ahead of our discussion of the experimental results.

The addition of Cu results in phase separation leading to two FCC phases (CoCrNi based FCC and Cu rich FCC) [233]. This again aligns with the binary pair properties since even though Cu does not introduce any significant lattice strains in CoCrNi, it does have a positive chemical interaction parameter with all the other elements, especially Cr (Figure 6.1b), indicating a preferential tendency to cluster into a separate Cu rich phase. As discussed in the previous chapters, we refer to ordering as the tendency of elements to mix with each

other, in a periodic manner (at least locally) and clustering as the tendency for elements to segregate away from each other forming elemental clusters in case of binary systems. These observations suggest that binary pair properties can be a significant driver for phase evolution in CCAs and hence, to test this hypothesis, we added Cu to CoCrNi as our quaternary addition.

A host of quinary additions were then investigated systematically. The compositions studied in this work include – base alloys (CoCrNi and CoCrCuNi) and CoCrCuNi-M alloys where M={Al, Ti, Zr, Nb, Mo}. Al was selected as one of the candidates due to its propensity to promote B2 ordering [3,7,177]. The choice of Ti and Zr as the second class of quinary additions was dictated by identical VEC for both the elements, while introducing a significant size mismatch (Ti has an atomic radius of 140pm while Zr has an atomic radius of 155pm). As we move from Al → Ti → Zr, the VEC and nature of chemical interactions remains similar (Figure 6.1b) but the atomic sizes (and consequently the elastic interaction parameters and hence elastic strains) increase significantly. The third and final category of quinary additions included Nb and Mo. These two elements differ in their VECs (with Mo having one more valence electron than Nb). Both Mo and Nb have very similar atomic size (approx. 145pm each). This allows for exploring the effect of VEC when the size doesn't change. Also, since the training databases for phase selection and hardness prediction ML models contained only one alloy with Mo-Cu pair and no alloys with Nb-Cu pair, these systems can help ascertain limits of the ML models. Furthermore, the choice of the quinary additions (i.e., Al and the four early transition metals – Ti, Zr, Nb and Mo) ensure that the overall VEC of the alloys progressively decreases from a range which can be safely classified as FCC to values at the VEC classification boundaries which can potentially lead to interesting phase selection behavior with BCC and/or intermetallic phases likely to emerge. While the overall VEC decreases in comparison to the base ternary CoCrNi alloy, as we move from Zr → Nb → Mo, the VEC increases for the set of quinary alloys and the chemical interactions (especially for M-Cu

pair) change drastically. In this sense, such a choice of model systems creates an ideal testbed for the ML models developed so far.

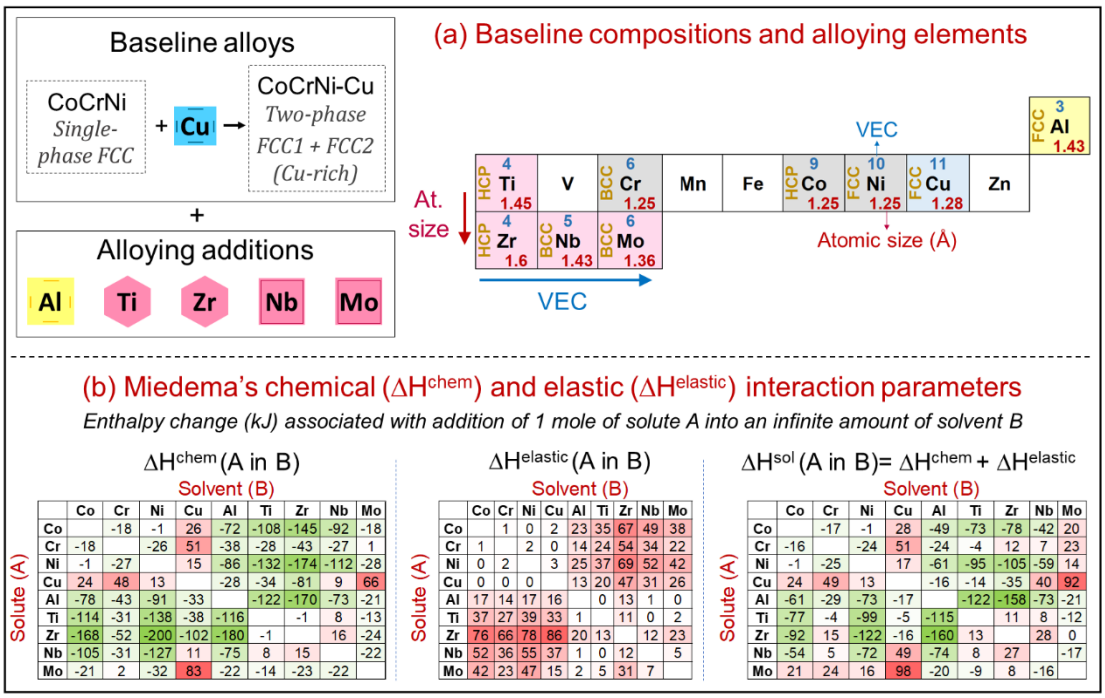

Figure 6.1 (a) Design methodology indicating the baseline compositions and the rationale for selection of alloying elements. (b) Miedema's chemical (ΔH^{chem}) and elastic ($\Delta H^{elastic}$) interaction parameters representing enthalpy change (in kJ) associated with the addition of 1 mole of solute A into an infinite amount of solvent B. ΔH^{sol} is the sum of both ΔH^{chem} and $\Delta H^{elastic}$.

6.2 Methodology

6.2.1 Machine learning and Thermo-Calc calculations

The machine learning calculations were done to predict the phase fractions and Vicker's hardness for – a) base alloy compositions (CoCrNi and CoCrCuNi) and b) M_x-$(CoCrCuNi)_{1-x}$ alloy systems along continuous addition of an alloying element to CoCrCuNi. The phase fractions were predicted using a ML model developed by us in a prior work [19]. The Vicker's hardness values were predicted using the ML model [95] developed as part of this thesis in Chapter 5. The thermodynamic calculations for prediction of stables phases (as a function of temperature) were carried out using Thermo-Calc software with TCHEA5 database.

6.2.2 Experimental characterization

Alloy ingots were prepared through arc melting of high purity (≥99.9%) elements (procured from Alfa Aesar and Sigma-Aldrich) on a water-cooled copper hearth in an inert argon gas environment. Each alloy was remelted at least five times to ensure chemical homogeneity. The as-cast alloy ingots were sectioned and polished for further characterization. Structural characterization was done through X-ray diffraction (XRD, PANalytical XPERT-PRO) using Co Kα radiation with $\lambda(K\alpha_1)$ = 1.78901 Å and $\lambda(K\alpha_2)$ = 1.7929 Å. The XRD data was Rietveld-refined using the GSAS-II code [234]. Microstructural characterization was done using a Scanning Electron Microscope (SEM, JEOL-6610LV) equipped with a tungsten filament electron gun. Along with SEM, the chemical composition and elemental distribution maps were generated using Energy Dispersive Spectroscopy (EDS, Bruker). Vicker's hardness of each sample was measured with a micro hardness tester (Zwick Roell) using 100 gf load and 10 seconds dwell time. Ten hardness measurements were done for each alloy to obtain an average hardness value and associated uncertainty estimates.

6.2.3 EDS-PhaSe analysis

The elemental maps obtained from SEM-EDS were analyzed using the EDS-PhaSe software [235] that was developed as part of this thesis to perform quantitative analysis from EDS data. EDS-PhaSe was published recently [235] and is also included as Appendix B in this thesis. The phase segmentation and analysis routine of EDS-PhaSe involves three steps – (a) first, the element maps obtained from EDS are converted into estimated composition maps (atomic/weight percent), (b) secondly, various markers of elemental segregation are calculated for spatial visualization of any preferential segregation of element pairs within the scanned region, and c) thirdly, masks are created interactively using threshold conditions to generate phase segmented micrograph along with the estimates of phase compositions. The EDS-PhaSe phase compositions shown in the figures in this chapter represent

the average composition of each phase calculated by EDS-PhaSe after phase segmentation.

6.3 Results and discussion

6.3.1 Summary of Machine learning predictions

Figure 6.2a shows the ML-predicted phase fractions of FCC, BCC and Intermetallic (IM) phases and Figure 6.2b shows the ML-predicted Vicker's hardness for M_x-$(CoCrCuNi)_{1-x}$ alloy systems. For all alloys, the hardness trends closely follow the FCC → BCC phase transitions and IM formation predicted by phase selection model, thereby indicating that the models are physically consistent with each other. ML predictions show a significant IM formation for all alloying elements except Al which shows IM formation at only high concentrations (around equiatomic). With Al addition, the hardness increase correlates directly with the FCC→BCC phase transition beyond 8 at.% Al. Addition of Zr, Nb or Ti causes a steep increase in hardness, even at low concentrations, that correlates with the strong IM formation predicted by the ML model for these systems. Figure 6.2c shows the comparison between ML-predicted and experimentally measured Vicker's hardness for CoCrNi and CoCrCuNi base alloys and M_x-$(CoCrCuNi)_{1-x}$ equiatomic alloys. The ML models closely capture the hardness for base alloys and CoCrCuNi-(Al/Ti/Zr) alloys but a significant deviation is observed for CoCrCuNi-(Nb/Mo) alloys. Figure 6.2b shows that the ML model is predicting a steep increase in hardness with Nb addition at equiatomic composition and that the predicted hardness increases to ~600 HV at 25 at.% Nb. Thus, the model is correctly predicting large increase in hardness with Nb, albeit at slightly higher concentrations. The discrepancy in hardness prediction with Mo addition coincides with the underpredicted IM formation tendency which, as we will see later in §6.3.7, does not match with the experimental observations wherein the Mo rich intermetallic phase is actually the major phase in CoCrCuNi-Mo alloy. The errors in ML-predictions for CoCrCuNi-Mo alloy possibly arise from the exceptionally large positive mixing enthalpy of this alloy since all Mo-pairs

(Mo-Cu in particular) have a positive interaction parameter (ΔH^{sol}), as seen in Figure 6.1. The database used for the training of ML models did not have alloys with such large positive mixing enthalpies; hence, the model is extrapolating into a prediction space that is quite far from the training space, leading to underprediction of both the IM formation and hardness. This allows us to recognize a limiting condition for our ML models wherein we can expect the intermetallic formation and hardness values to be significantly underpredicted for alloys with exceptionally large mixing enthalpy values. That said, the ML models, as a whole, align well with the experimentally observed trends in IM phase formation and hardness values for all of the other alloys studied here.

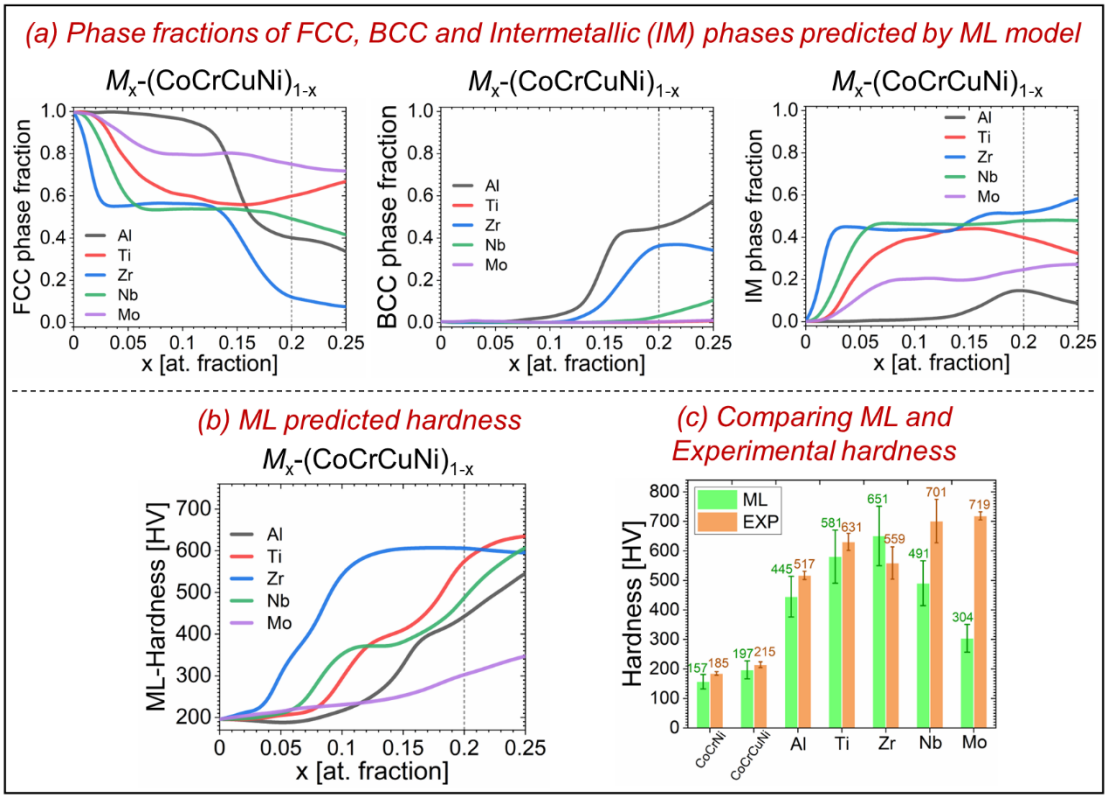

Figure 6.2 (a) Phase fraction of FCC, BCC and Intermetallic (IM) phases as predicted by ML model along continuous composition variations in M_x-$(CoCrCuNi)_{1-x}$ alloys. (b) ML predicted Vicker's hardness in M_x-$(CoCrCuNi)_{1-x}$ alloys. (c) Comparing ML predicted and experimentally measured hardness of equiatomic alloys CoCrNi, CoCrCuNi and CoCrCuNi-M. Here, M includes {Al, Ti, Zr, Nb, Mo}.

6.3.2 Thermodynamic framework for general analyses of the systems

Before embarking on a detailed discussion of the experimental work, we outline here a basic thermodynamic framework that has been used for a rather intuitive and qualitative assessments of the results. For developing a qualitative physical understanding, we resort to Miedema's semi-empirical model [41,236], while ThermoCalc calculations and Machine Learning predictions offer more quantitative insights (albeit not as physically intuitive).

The Miedema approach involves deconstructing the enthalpy of alloys into three contributions – chemical (originating from electronic interactions as atoms are brought close to form an alloy), elastic (originating from size mismatch coupled with the elastic moduli, i.e., a sense of the activation barrier to alloying in systems with atomic size mismatches forming an alloy, essentially requiring atoms to be squeezed together or stretched, depending on whether there is a positive or negative size mismatch) and structural (which is somewhat analogous to the different lattice stabilities proposed by Kauffman [237] while developing the Calphad method, although in Miedema's scheme, the effects are not nearly quite as pronounced). Generally, the structural contribution in Miedema's approach is small and often neglected. Miedema and his coworkers developed a model for estimating the interaction parameters in a sub-regular formalism (i.e., $H_{A/B}$ – the interaction parameter when a B atom is brought in infinite dilution in an A element – and $H_{B/A}$ are different). Miedema listed these chemical interaction parameters (which we replicate partially in Table 6.1). Additionally, Miedema incorporated Eshelby's model of elastic interactions to estimate elastic contributions to the enthalpy through which analogous elastic interaction parameters can be calculated, also listed in Figure 6.1b for binary pairs relevant in this work. The interaction parameters indicate how strongly the elements want to stay close (negative values of interaction parameters), whereby the energetics can become more favorable if the atoms are ordered ideally or how strongly the elements want to stay apart (positive interaction parameters), whereby similar atoms cluster together, apart from the other atoms. Of course, the process of ordering and clustering is not

determined solely from binary pair enthalpy or binary interaction parameters, especially when other elements are present, as we had seen in the previous chapter 4 where we modelled short range ordering and clustering; nonetheless, as our analysis indicated, the interactions do have a significant contribution. It is important that we understand this since we will be discussing the partitioning of elements in our experiments within this framework.

While Miedema's model allows for an intuitive qualitative understanding of our results, it is not very accurate quantitatively. Therefore, we shall also sometimes refer to Thermo-Calc results and results from our own ML models as we study the concentrations and phase fractions estimated using EDS analyses and Rietveld refinement of XRD data.

6.3.3 Baseline alloys: CoCrNi and CoCrCuNi

CoCrNi has been studied extensively in the literature and has been observed to have a single-phase FCC structure. As noted earlier in §6.1, the single-phase FCC structure of CoCrNi aligns well with the various criteria viz., VEC, atomic size asymmetry and binary pair interaction parameters, that are correlated strongly to the phase evolution in CCAs. The ML predictions (Figure 6.2a) also indicate a single-phase FCC phase, as does the Thermo-Calc analysis (Figure 6.3) of the equiatomic ternary. We observed a microstructure comprising a single phase with FCC structure (a=3.569 Å), as seen in Figure 6.4 and Figure 6.5, which is in agreement with the literature results as well as our ML model and Thermo-Calc calculations. No second phase formation or preferential elemental segregation was observed in SEM-EDS results.

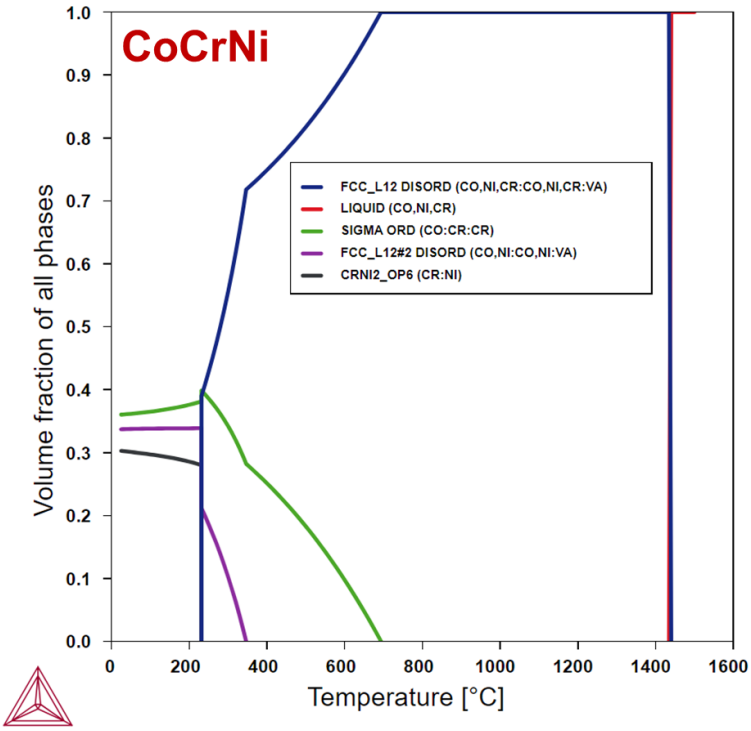

Figure 6.3 Thermo-Calc predicted phase fractions in CoCrNi ternary as a function of temperature.

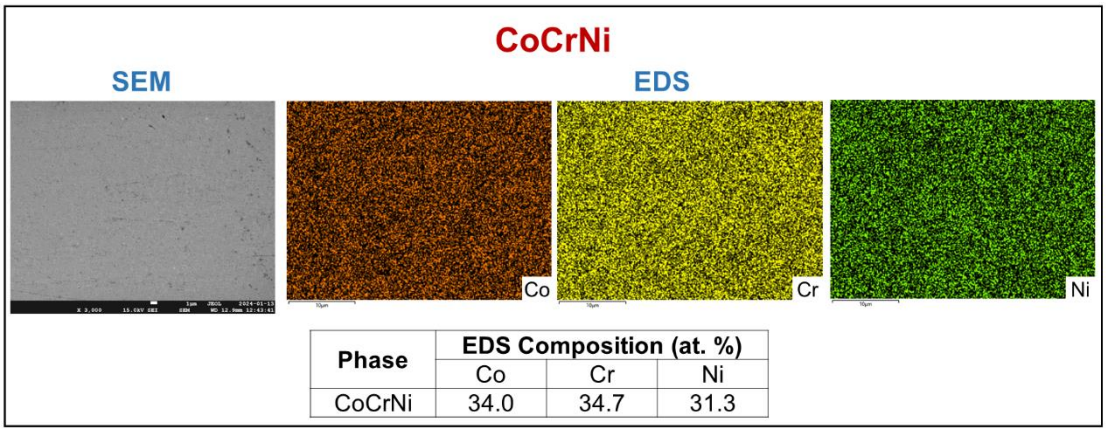

Phase	EDS Composition (at. %)		
	Co	Cr	Ni
CoCrNi	34.0	34.7	31.3

Figure 6.4 SEM-EDS results of CoCrNi.

The base alloy system for our investigations here is formed by addition of Cu to the CoCrNi ternary in equiatomic proportions resulting in a CoCrCuNi quaternary system. As seen in a previous study by Derimow et al. [233] and our own results here (Figure 6.7 and Figure 6.8), the addition of Cu to CoCrNi causes phase separation into two FCC phases – a CoCrNi rich FCC phase (a=3.572 Å) and a Cu rich FCC phase (a=3.605 Å). In general, in a binary system, Cu and Ni have excellent solid solubility and conform to the classic Hume-Rothery rules for the formation of a substitutional solid solution.

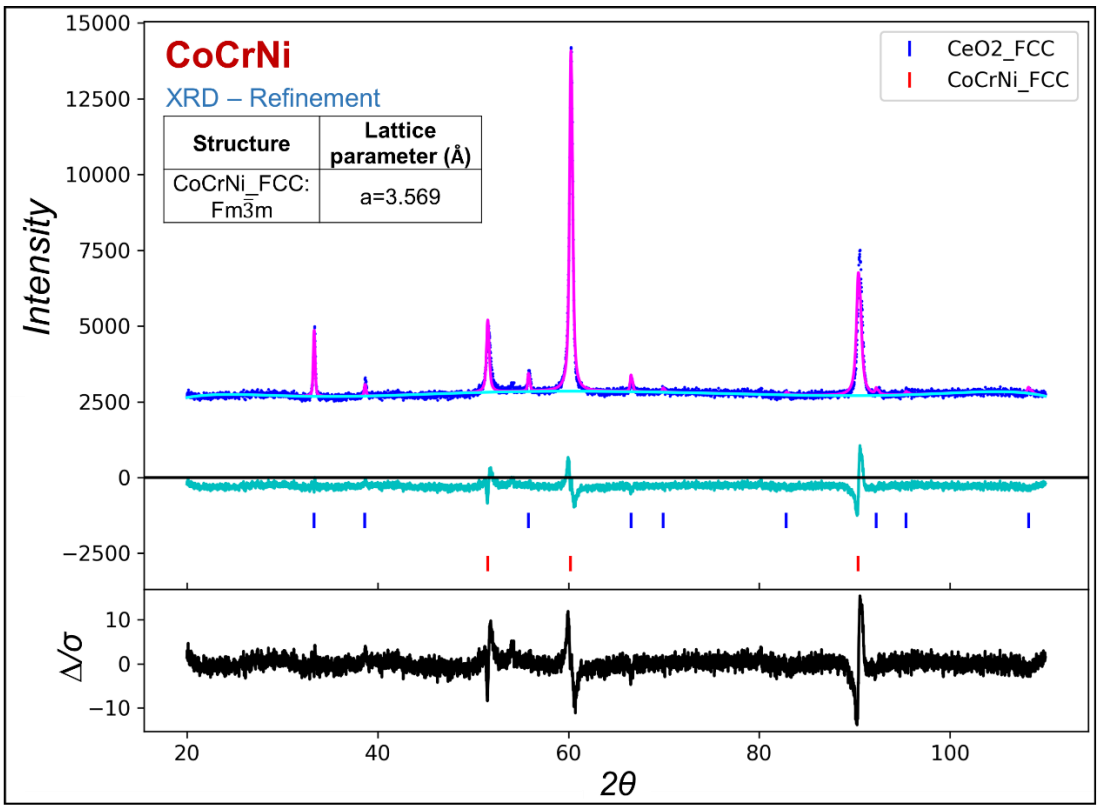

Figure 6.5 XRD pattern and Rietveld-refined structures for CoCrNi ternary.

However, at lower temperatures, the Cu-Ni system is known to undergo phase separation resulting in the formation of a Cu rich and Ni rich solid solution [238]. Nonetheless, Figure 6.1b indicates that all the three binary pairs with Cu (Cu-Co, Cu-Cr and Cu-Ni – especially Cu-Cr) have strongly positive interaction parameters which promotes clustering of Cu atoms and inducing phase separation into Cu rich regions and CoCrNi regions. Both these regions, however, are FCC type structures. This is reflected in our ML model results in Figure 6.2a which shows the existence of only FCC without any quinary alloying, as well as in the ThermoCalc results in Figure 6.6. The phase compositions obtained from EDS are shown in Figure 6.7.

The minor solubilities of Co, Cr and Ni in the Cu rich phase stems from two sources – minimizing the overall Gibbs free energy of the system to arrive at a suitable CoCrNi composition with a low enough enthalpy and high enough entropy and a Cu rich phase where the positive interactions with minor additions between the binaries are overcome largely through an increased entropy. It is instructive to note that the concentrations are in the order of

interaction parameters, i.e., with Cu-Cr having the highest chemical interaction parameters (but low elastic interaction parameters due to similar size), the concentration of Cr is the least in the Cu rich phase. The Cu-Co interactions are less strongly positive which allows for a greater concentration of Co (albeit, a greater size mismatch and hence higher elastic contributions to the enthalpy ensures that the Co concentration, though greater than Cr is not significantly larger). The Cu-Ni binary pair has the lowest positive chemical interaction parameters and has a negligible atomic size mismatch. Consequently, the solubility of Ni is highest in the Cu rich phase. Cr, Co and Ni are all higher melting elements in comparison to Cu. Therefore, quite likely, the CoCrNi phase would be the primary solidifying phase. This line of reasoning is also in agreement with Thermo-Calc results. When the CoCrNi rich phase solidifies as dendritic region (DR), the Cr cannot accommodate too much Cu and pushes majority of Cu to the interdendritic (ID) region resulting in a Cu rich (~70% Cu) ID phase. As some Cu (~10 at.%) does go into the CoCrNi rich phase, we observe a very minor increase in its lattice parameter from 3.569 Å (without Cu) to 3.572 Å (with Cu).

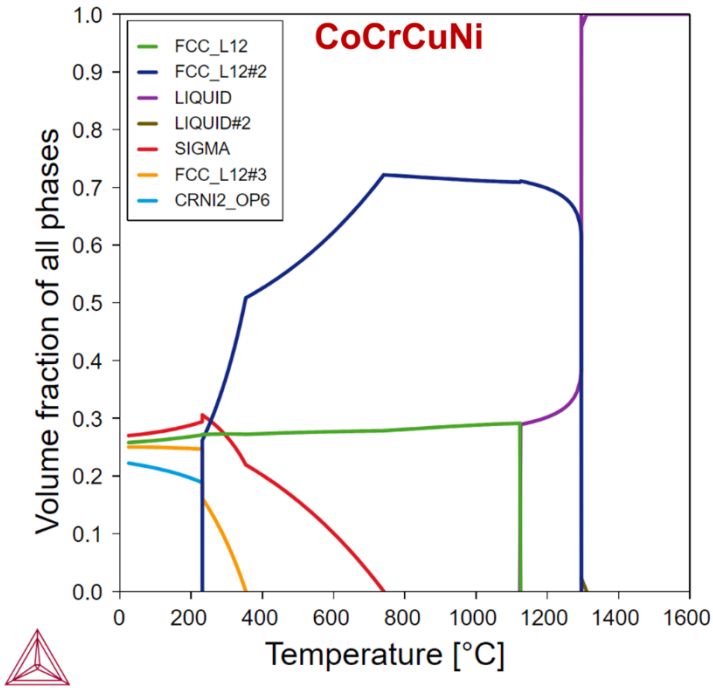

Figure 6.6 Thermo-Calc predicted phase fractions in CoCrCuNi quaternary as a function of temperature.

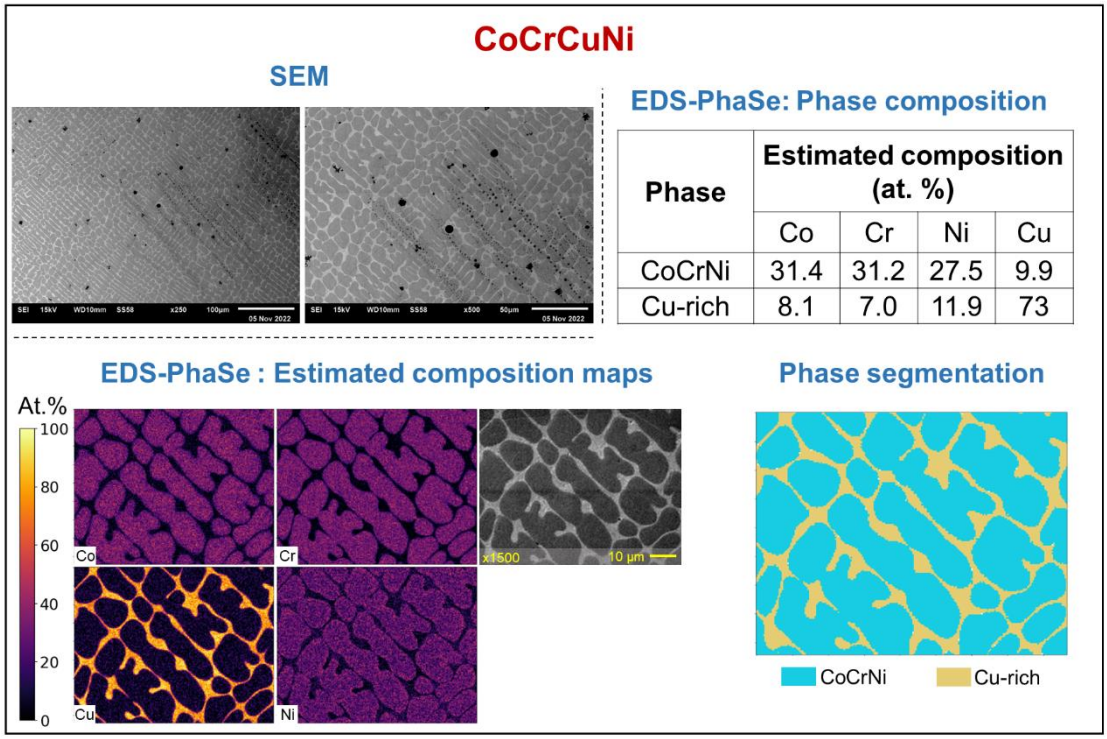

Phase	Estimated composition (at. %)			
	Co	Cr	Ni	Cu
CoCrNi	31.4	31.2	27.5	9.9
Cu-rich	8.1	7.0	11.9	73

Figure 6.7 SEM-EDS and EDS-PhaSe results of CoCrCuNi alloy along with the phase information. The quantitative analysis of EDS data and subsequent phase segmentation was done using EDS-PhaSe [235] software that was developed as part of this thesis (Appendix B).

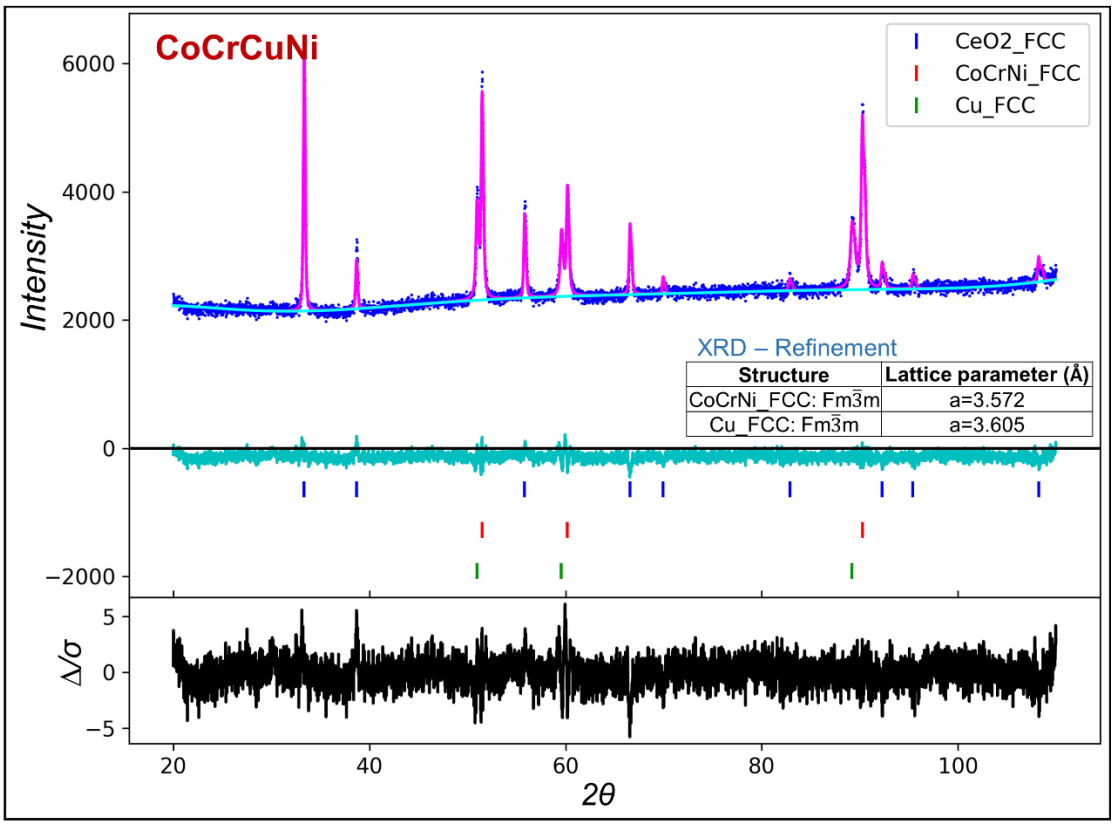

Figure 6.8 XRD pattern and Rietveld-refined structures for CoCrCuNi equiatomic quaternary.

6.3.4 CoCrCuNi-Al

Al has a larger radius and significantly lower VEC compared to Co, Cr, Ni and Cu. Moreover, as seen in Figure 6.1b, Al has negative interaction parameters with all elements here. The Al-Ni interaction parameters are especially negative, as is Al-Co (though to a lesser extent than Al-Ni), which could be sufficient to promote ordering of these elements with the elastic interaction parameters being only slightly positive and not enough to overcome the effects of the chemical interaction parameters. In contrast to the highly negative Al-Ni and Al-Co interactions, the Al-Cr or Al-Cu chemical interaction parameters are only moderately negative, while the elastic interaction parameters are comparable to Al-Ni and Al-Co pairs. This would suggest that Al would mostly tend to stay with Ni and Co, allowing the Cr-Cu pair to cluster resulting potentially in a three-phase mixture of an AlNiCo rich phase, a Cr rich phase (or potentially a Co-Cr rich phase, if the Al-Ni ordering tendency drives the formation of an intermetallic phase) and a Cu rich phase.

It is now instructive to compare the line of reasoning developed above with our ML (Figure 6.2) and Thermo-Calc results (Figure 6.9). The ML model indicates the existence of BCC, FCC and intermetallic phases. The Thermo-Calc differs slightly, showing the presence of a CoCr rich BCT sigma phase (which is essentially a distortion of the BCC structure), an FCC phase that is Cu rich and an Al-Ni intermetallic showing a B2 ordering. This is observed in experimental results also (Figure 6.10) wherein, similar to CoCrCuNi alloy, we see the formation of Co-Cr rich dendrites with Cu segregating to form a Cu rich ID phase. The Al-Ni rich phase forms at the interface of the dendritic and interdendritic region. The placement of this phase can be understood when we consider that Al has the negative interaction parameters with all other elements (and hence can stay adjoining to all of the atoms, individually, without destabilizing the system) while Ni has the lowest positive interaction with Cu while having low negative interactions with Co and Cr. Our XRD analysis (Figure 6.11) indicates the presence of an FCC phase (a=3.626 Å), which matches reasonably well with the lattice parameter of Cu (3.604 Å, possibly

owing to the larger atomic size of Al) and likely corresponds to the Cu rich phase. The diffraction pattern also shows a minor B2 phase (a=2.882 Å) whose lattice parameter matches closely with the well-known Al-Ni B2 and is therefore likely corresponding to the B2 phase. The major phase observed in the XRD is a BCC phase (a=2.868 Å). This would, therefore, map onto the third phase seen via phase segmentation of the SEM images, i.e., the Co-Cr rich phase. Apparently, the incorporation of Al in CoCrNi rich phase causes it to transform into CoCr-rich phase. This may be driven by two factors – firstly, the depletion of Ni (which is the only FCC element in CoCrNi rich phase) due to the formation of NiAl rich phase and secondly, the incorporation of a significant amount of Al (~21 at. %) which is known to induce FCC → BCC transition owing to its low VEC.

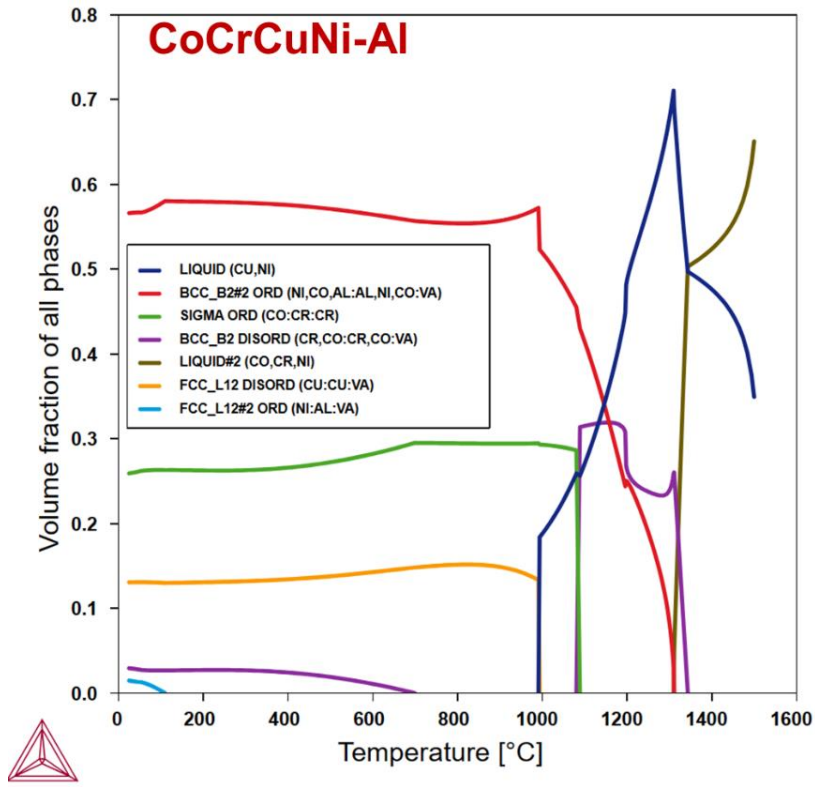

Figure 6.9 Thermo-Calc predicted phase fractions in CoCrCuNi-Al equiatomic quinary as a function of temperature.

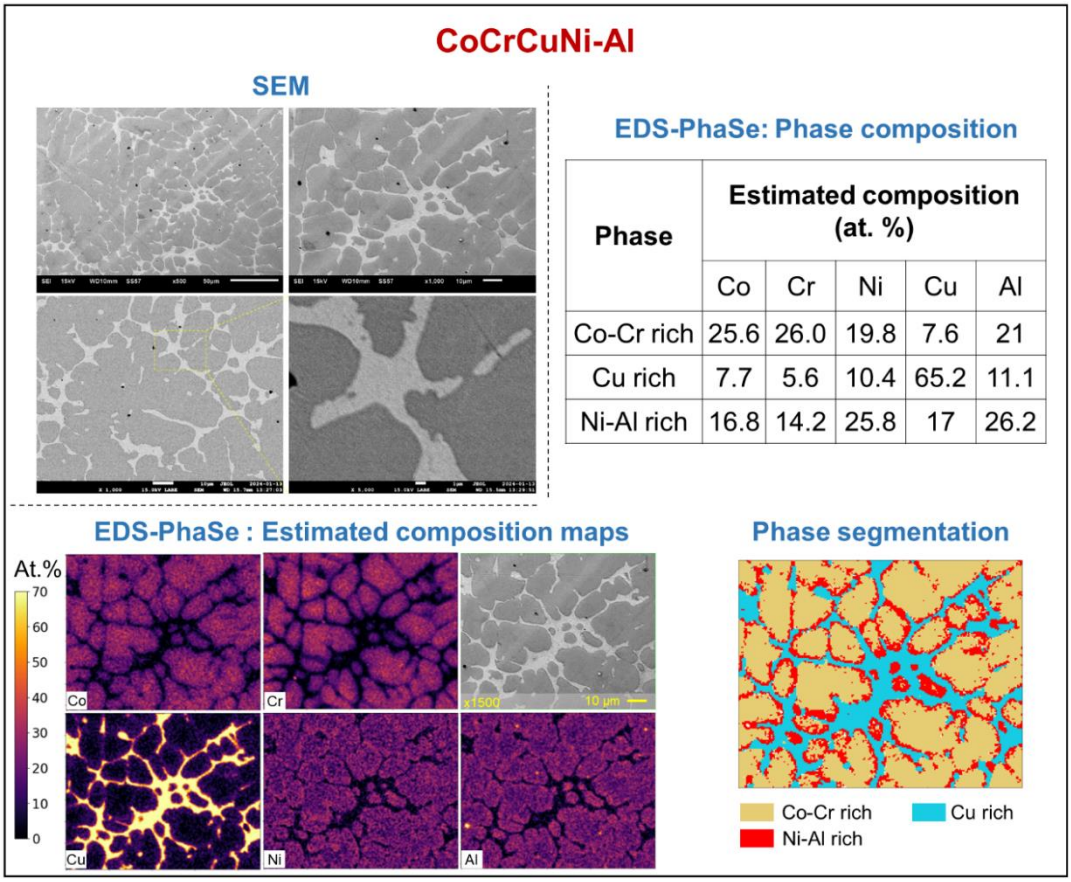

Phase	Estimated composition (at. %)				
	Co	Cr	Ni	Cu	Al
Co-Cr rich	25.6	26.0	19.8	7.6	21
Cu rich	7.7	5.6	10.4	65.2	11.1
Ni-Al rich	16.8	14.2	25.8	17	26.2

Figure 6.10 SEM-EDS and EDS-PhaSe results of CoCrCuNi-Al alloy along with the phase information. The quantitative analysis of EDS data and subsequent phase segmentation was done using EDS-PhaSe [235] software that was developed as part of this thesis (Appendix B)

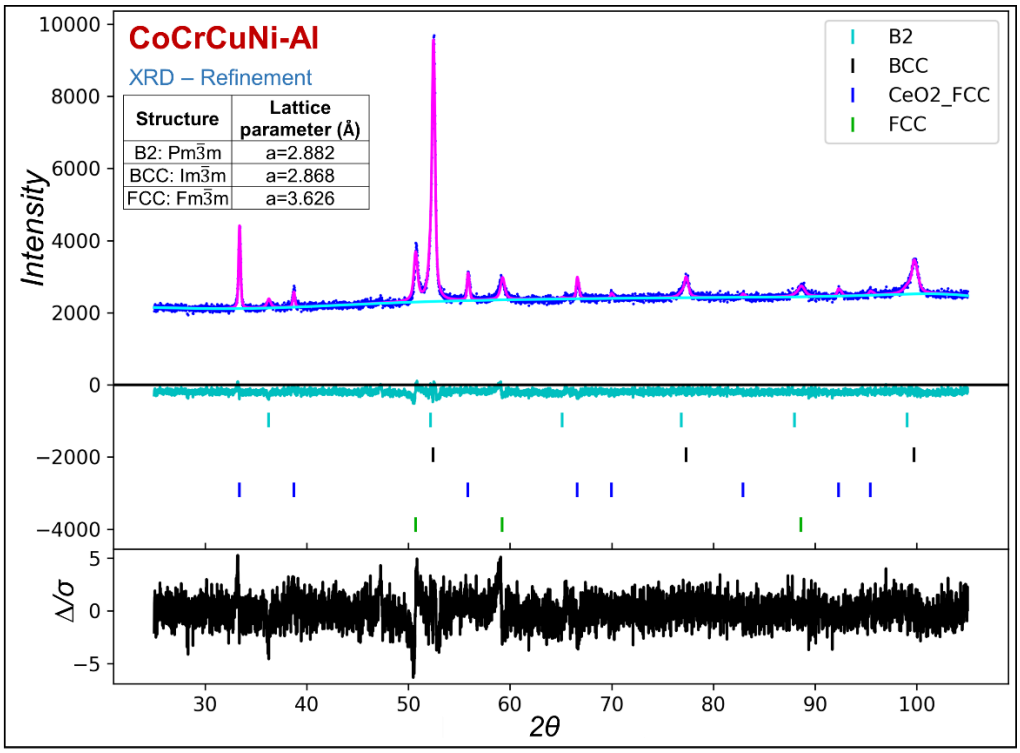

Figure 6.11 XRD pattern and Rietveld-refined structures for CoCrCuNi-Al equiatomic quinary.

6.3.5 CoCrCuNi-Ti

Similar to Al, Ti has a larger atomic size and lower VEC than Co, Cr, Cu and Ni. Also, Ti-(Co/Cr/Cu/Ni) have similar chemical and elastic interaction parameters as Al-pairs, as seen in Figure 6.1b. But there are three key differences between Al and Ti addition that can potentially affect the overall phase evolution. Firstly, Ti is larger than Al, with higher elastic modulii and consequently, Ti-pairs have more positive elastic interactions than Al-pairs. Secondly, while the chemical interaction parameters of Ti-(Co/Ni/Cu) pairs are more negative than same Al-pairs, the chemical interaction parameter of Ti-Cr is less negative than Al-Cr. This, accompanied by the higher elastic interactions for Ti-pairs, results in just a slightly negative solution interaction parameter (ΔH^{sol}) of Ti-Cr pair. Thirdly, Ti has HCP crystal structure unlike Al which has FCC structure. The combined effect of these factors implies that if a Ti-rich phase forms, which is quite probable owing to exceptionally strong Ti-(Co,Ni) ordering. It can accommodate Cu preferentially over Cr, given a stronger Ti-Cu interaction as opposed to Ti-Cr interactions, and since Cu-Cr cluster strongly, any Cu that goes into these phases can effectively make it more and more difficult for Cr to be accommodated. This can potentially result in Cr being pushed out completely to form a separate Cr-rich phase.

The ML predictions, Figure 6.2a, indicate that the addition of Ti to CoCrCuNi result in presence of FCC and intermetallic phases. This aligns with the strong ordering of Ti-Ni and Ti-Co pairs that may drive intermetallic formation. The Thermo-Calc calculations (Figure 6.12) also indicate formation of a variety of intermetallic phases that include Co_2Ti-type C15 Laves, Ni_3Ti-type $D0_{24}$ and Ti-Co rich B2 phase. But Thermo-Calc also predicts a pure Cr BCC phase and a pure Cu FCC phase. While the binary interaction parameters support formation of a Cr rich phase here, there is no apparent reason why Cu should cluster out completely; especially if Cr has already clustered into a separate phase since the primary driver for Cu segregation here is the Cr-Cu pair.

The experimental results (Figure 6.13) are in partial agreement with the ML and Thermo-Calc predictions as the phase segmented micrograph and EDS-PhaSe analysis shows the formation of a Cr rich phase, a Co-Ti rich phase and two CoCrNiTi phases (one of which has higher Ni while one has higher Cu and Ti). The Cr rich phase appears as separate dendrites while the Ni-enriched CoCrNiTi phase forms the dominant matrix phase that embeds the Co-Ti rich phase and a tiny amount of Cu-Ti enriched CoCrNiTi phase. The formation of Cr rich phase matches with the Thermo-Calc predictions but we did not find any evidence of a Cu rich phase that was predicted by Thermo-Calc. This makes sense as it is quite unlikely (based on binary interactions) that Cu would cluster out in this system, especially if Cr already forms a Cr rich phase.

The XRD patterns (Figure 6.14) show two major phases – a BCC phase, a=2.886 Å and an FCC phase, a=3.621 Å. The microstructural analysis also shows two major phases – a Cr rich phase and a Ni-enriched CoCrNiTi phase. Based on the composition of Cr rich phase (~74% Cr) and the fact that the lattice parameter of BCC phase (a=2.886 Å) is quite close to that of Cr (a=2.879 Å) in addition to the BCC structure of Cr, it would appear that it is the Cr rich phase that has crystallized with a BCC structure. Hence, the other major phase i.e., the FCC phase, a=3.621 Å, very likely corresponds to the Ni rich CoCrNiTi matrix phase. We also observe a Laves C15, a=6.689 Å minor phase in the XRD analysis. Based on the Thermo-Calc calculations which predict formation of a Co_2Ti-type C15 Laves phase, it is quite likely that the Co-Ti rich phase in the microstructure corresponds to the Laves C15, a=6.689 Å structure.

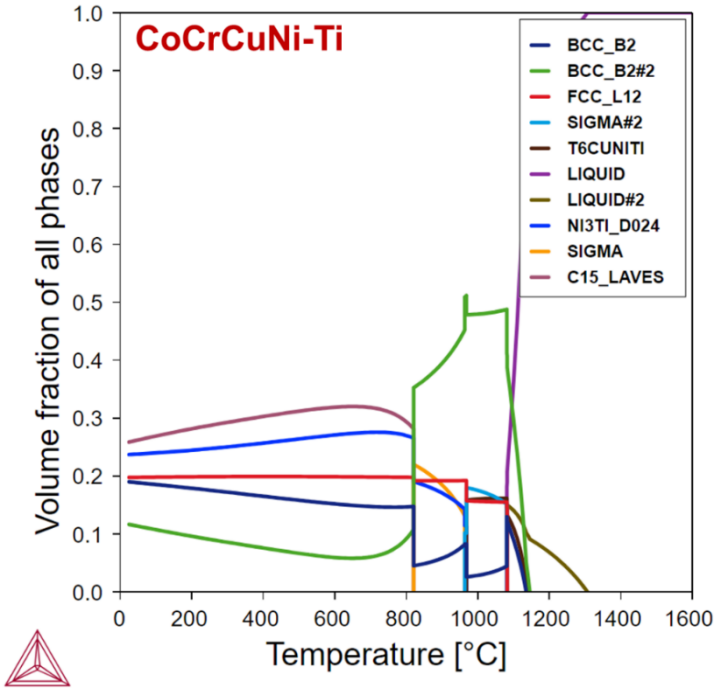

Figure 6.12 Thermo-Calc predicted phase fractions in CoCrCuNi-Ti equiatomic quinary as a function of temperature.

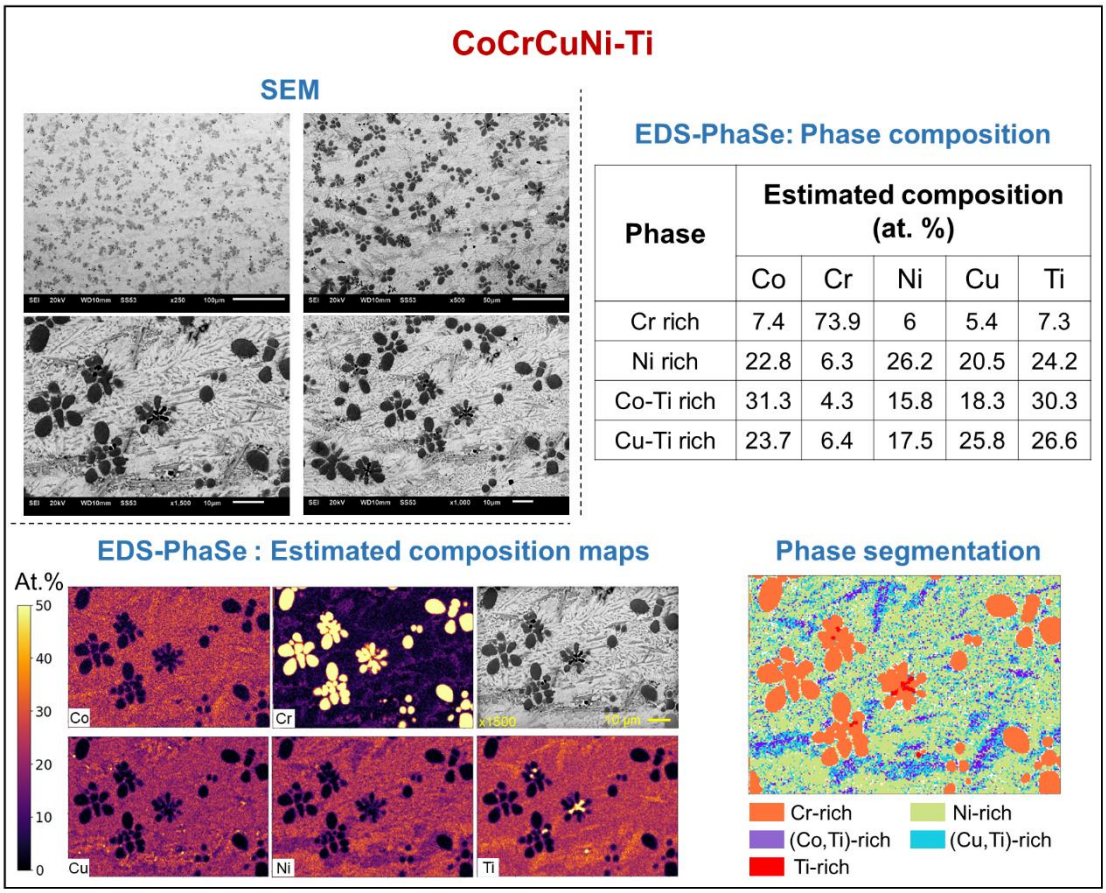

EDS-PhaSe: Phase composition

Phase	Estimated composition (at. %)				
	Co	Cr	Ni	Cu	Ti
Cr rich	7.4	73.9	6	5.4	7.3
Ni rich	22.8	6.3	26.2	20.5	24.2
Co-Ti rich	31.3	4.3	15.8	18.3	30.3
Cu-Ti rich	23.7	6.4	17.5	25.8	26.6

Figure 6.13 SEM-EDS and EDS-PhaSe results of CoCrCuNi-Ti alloy along with the phase information. The quantitative analysis of EDS data and subsequent phase segmentation was done using EDS-PhaSe [235] software that was developed as part of this thesis (Appendix B).

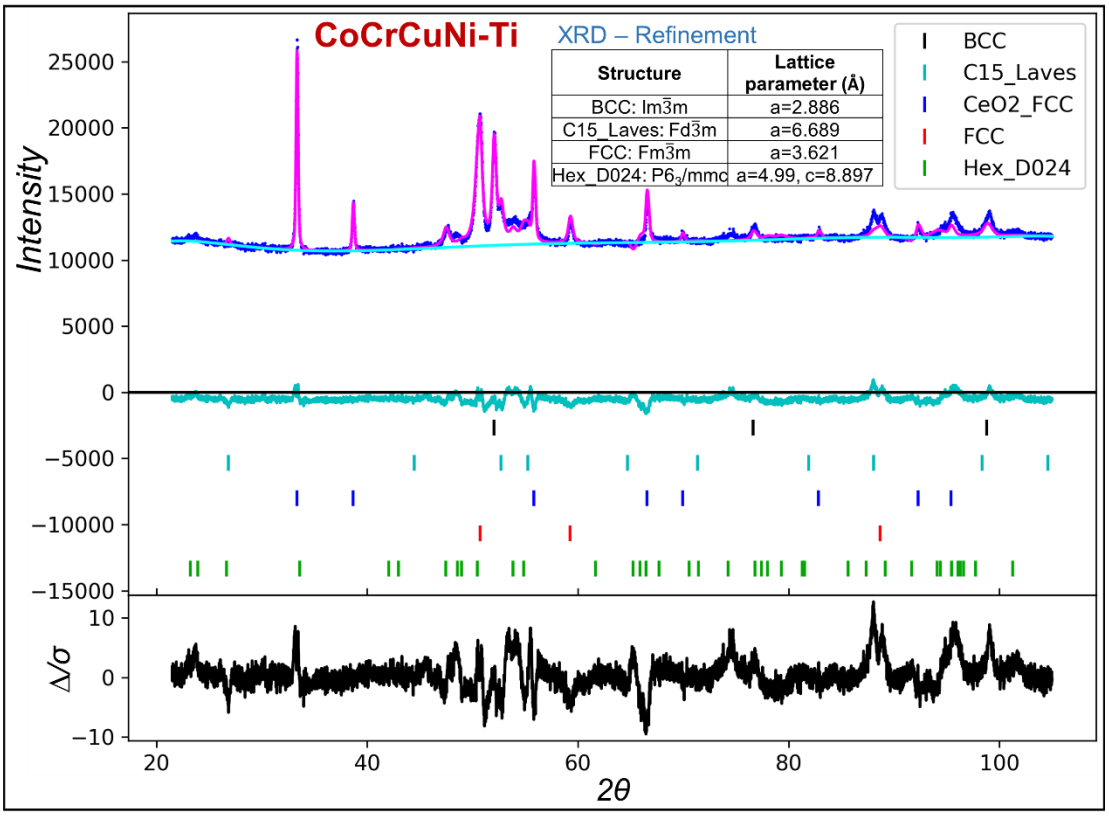

Figure 6.14 XRD pattern and Rietveld-refined structures for CoCrCuNi-Ti equiatomic quinary

6.3.6 CoCrCuNi-Zr

As seen in Figure 6.1, Zr has the same VEC and crystal structure as Ti. The chemical interaction parameters of Zr-pairs in CoCrCuNi-Zr are also similar to Ti-pairs albeit the magnitude of Zr-(Co/Ni/Cu) pairs has increased significantly compared to same Ti-pairs whereas as that of Zr-Cr pair is only slightly more negative than Ti-Cr. But the major difference is the significantly larger atomic size of Zr as compared to Ti which results in exceptionally high elastic interaction parameters of Zr-pairs. This leads to – (a) only slightly more negative solution interaction parameters (ΔH^{sol}) of Zr-(Co/Ni) pairs as compared to Ti-(Co/Ni) pairs, and (b) a positive solution interaction parameter (ΔH^{sol}) of Zr-Cr pair. This implies that the addition of Zr to CoCrCuNi should result in formation of Cr-rich phases, possibly even more pronounced than what we saw with Ti addition. It also suggests strong possibility of formation of Zr-Ni-Co rich intermetallic phases.

The ML predictions, Figure 6.2a, indicate that the addition of Zr to CoCrCuNi results in the presence of mostly BCC and intermetallic phases with a small amount of FCC phase. This aligns with the formation of a Cr-rich and Zr-(Ni/Co) rich intermetallics that can be reasoned based on the binary interaction parameters. The Zr-Ni and Zr-Co binary phase diagrams also show an exceptionally intermetallic formation tendencies with the presence of many different line compounds. The Thermo-Calc calculations predict the formation of only three phases – a Cr rich BCC phase, a pure Cu FCC phase and a CoNiZr Laves C15 phase. This is in line with the ML predictions.

The experimental results (Figure 6.16) show good agreement with the ML and ThermoCalc predictions as the phase segmented micrograph and EDS-PhaSe analysis shows the formation of a Cr rich phase, a CoZrNi rich phase and a Cu rich phase. This matches very closely with the Thermo-Calc predictions as in both the cases CoNiZr phase is by far the most dominant, followed by the Cu rich phase and the Cr rich phase.

The XRD pattern, Figure 6.17, also shows a Laves C15 phase, a=12.364 Å, as the major phase accompanied by two minor phases – a BCC phase, a= 2.878 Å and a hexagonal phase, a=3.82 Å, c=4.685 Å. Since the CoZrNi rich phase appears as the dominant phase from phase segmentation, it is reasonable to assign the Laves C15, a=12.364 Å structure to this phase. It is further supported by the Thermo-Calc calculations that predict a CoNiZr Laves C15 as the dominant phase. The Cr-rich phase identified from microstructural analysis very likely corresponds to the BCC structure, similar to what was observed with Ti addition. The remaining hexagonal structure most likely belongs to the Cu-rich phase which has a significant amount of Co present in it.

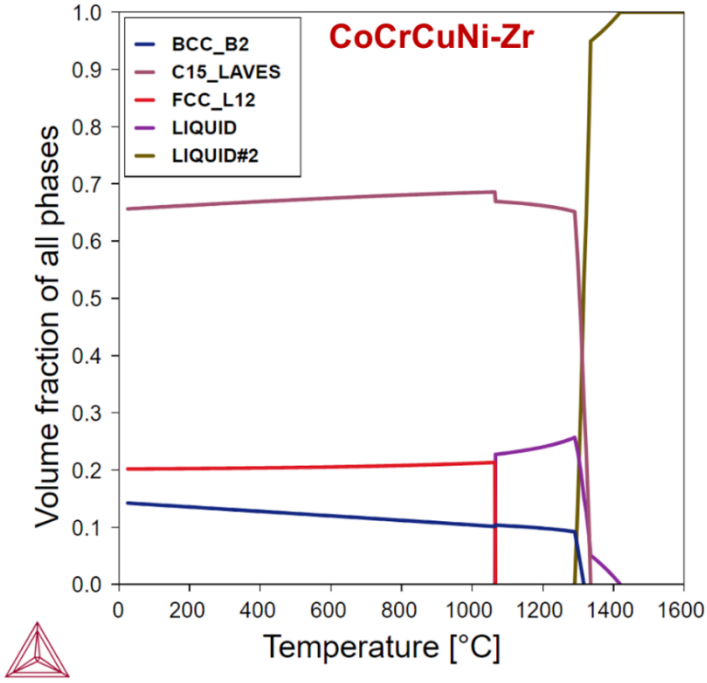

Figure 6.15 Thermo-Calc predicted phase fractions in CoCrCuNi-Zr equiatomic quinary as a function of temperature.

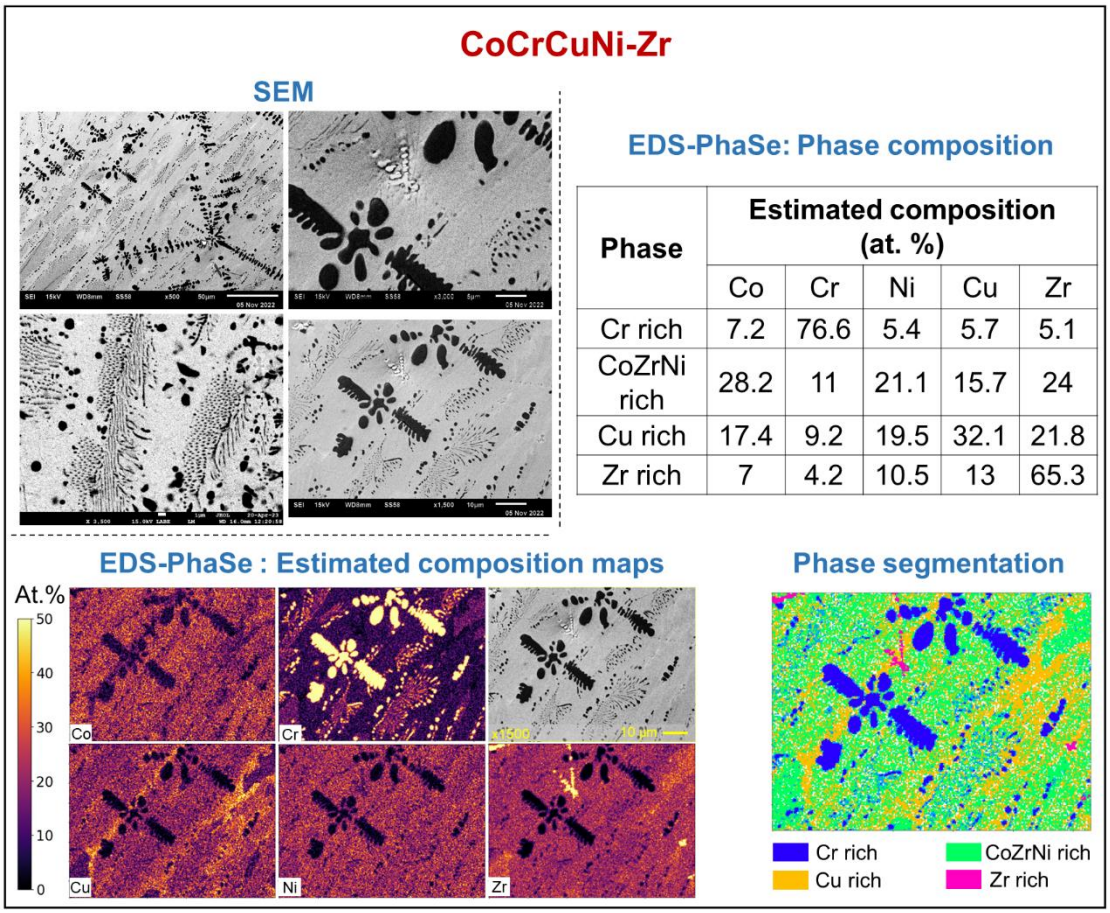

Phase	Estimated composition (at. %)				
	Co	Cr	Ni	Cu	Zr
Cr rich	7.2	76.6	5.4	5.7	5.1
CoZrNi rich	28.2	11	21.1	15.7	24
Cu rich	17.4	9.2	19.5	32.1	21.8
Zr rich	7	4.2	10.5	13	65.3

Figure 6.16 SEM-EDS and EDS-PhaSe results of CoCrCuNi-Zr alloy along with the phase information. The quantitative analysis of EDS data and subsequent phase segmentation was done using EDS-PhaSe [235] software that was developed as part of this thesis (Appendix B).

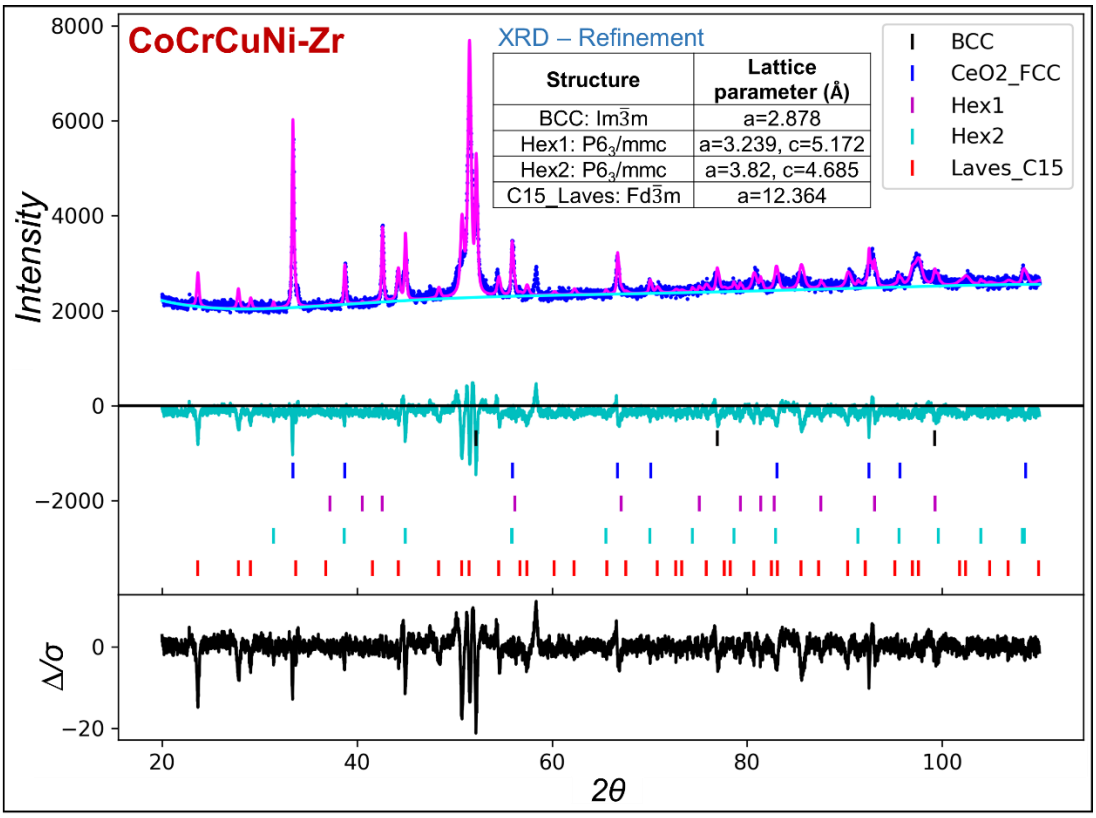

Figure 6.17 XRD pattern and Rietveld-refined structures for CoCrCuNi-Zr equiatomic quinary

6.3.7 CoCrCuNi-Nb

Unlike Ti and Zr, which exhibit close-packed (HCP) structures at the room temperature, Nb has a BCC structure. As seen in Figure 6.1b, similar to Ti and Zr, Nb-(Co/Cr/Ni) pairs also have negative chemical interaction parameters, with the Nb-Co and Nb-Ni interactions being highly negative. Nb-Cu, however, shows positive interaction parameters (unlike the Cu-Ti and Cu-Zr interaction parameters). The Nb atom is significantly larger than the late transition metals in the system which results in significantly positive elastic interaction parameters. In the case of Nb-Co and Nb-Ni, the magnitude of the elastic interaction parameters is much lower than the chemical interaction parameters, while in case of Nb-Cr, the elastic and chemical interaction parameters are comparable in magnitude. The Nb-Cu not only has positive chemical interaction parameters, but also strongly positive elastic parameters, which suggests that Nb and Cu would prefer to stay apart – something which

the Nb-Cu binary phase diagram readily shows with significant immiscibility in the liquid state leading to a monotectic reaction. With Cu clustering with other elements in the system as well, the formation of a Cu rich phase is only logical – something borne out experimentally also, as seen in Figure 6.19. With Ni-Cr interactions being significantly stronger than Co-Cr, we would anticipate a Ni-Cr rich phase with some Co and a Nb-Co rich phase.

The ML predictions, Figure 6.2, indicate the formation of FCC and intermetallic phases, which would be in agreement with a Cu rich phase (FCC) and a CoCrNi rich phase (which, based on the analysis of the CoCrNi ternary, is known to be an FCC phase). The strong chemical interactions between Nb and Co would then drive the intermetallic formation. The ML predictions also show a minor amount of BCC forming potentially. With Cr being the only BCC element which does not show strong intermetallic forming tendency (as evidenced from relatively low negative chemical interaction parameters), one can only surmise that a Cr rich phase might be a minor BCC phase (if at all present). The Thermo-Calc calculations, Figure 6.18, are broadly aligned with these predictions with a Co-Nb C15 Laves phase intermetallic featuring prominently with a Cu rich FCC phase and Cr rich BCC phase. Interestingly, the Thermo-Calc simulation doesn't indicate a second FCC phase and this is where the ML predictions deviate from the Thermo-Calc result.

The experimental results (Figure 6.19) also show a significant formation of a Cu-rich phase (~78% Cu) – which is in agreement with both the ML and ThermoCalc results, but the morphology of this phase is quite different from what was observed in CoCrCuNi and CoCrCuNi-Al alloys. In these systems, the Cu-rich phase formed the ID region but with Nb addition, it forms isolated globules. This is characteristic of liquid phase separation that occurs in monotectic systems. This is quite likely given that the binary Cu-Nb system is known to show a monotectic reaction. In the Cu-Nb system, as we cool through the monotectic, the Nb rich solid solution is the primary solidifying phase in a dendritic morphology, with Cu rich globules solidifying later. Here, we observe something similar, with the formation of Nb-Co rich dendritic

structures encompassing the globular Cu rich regions. Of the minor solutes present in this Cu rich phase, Nb content is the lowest and Ni content the highest – which is in agreement with the chemical interaction parameters of the individual Cu containing binary pairs. The matrix is the major phase, rich in Co and Nb, with significant amounts of Ni and Cr being present. The interdendritic region is enriched in Ni and Cr.

The diffraction pattern (Figure 6.20) shows the major phase to be a C36 Laves phase (a=4.819 Å, c=7.813 Å). Given the Thermo-Calc/ML predictions of the intermetallic phase and EDS phase segmentation results, it is quite likely that this corresponds to the Co-Nb rich phase where the chemical interaction parameters are strongly negative (and hence, more amenable to intermetallic formation). The second major phase is an FCC solid solution, a=3.616 Å, quite similar to Cu and likely corresponds to the Cu rich solid solution. A second FCC phase (in minor amounts) is seen to have a lattice parameter of a=3.607 Å, which is nearly identical to the CoCrNi ternary alloy and likely corresponds to the CoCrNi phase. This is a situation where the Thermo-Calc actually misses out the minor FCC phase and predicts a second $D0_A$ intermetallic which is not observed experimentally.

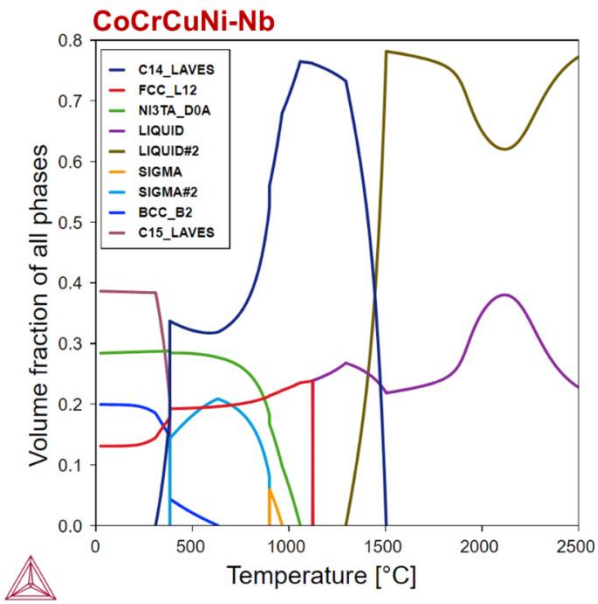

Figure 6.18 Thermo-Calc predicted phase fractions in CoCrCuNi-Nb equiatomic quinary as a function of temperature.

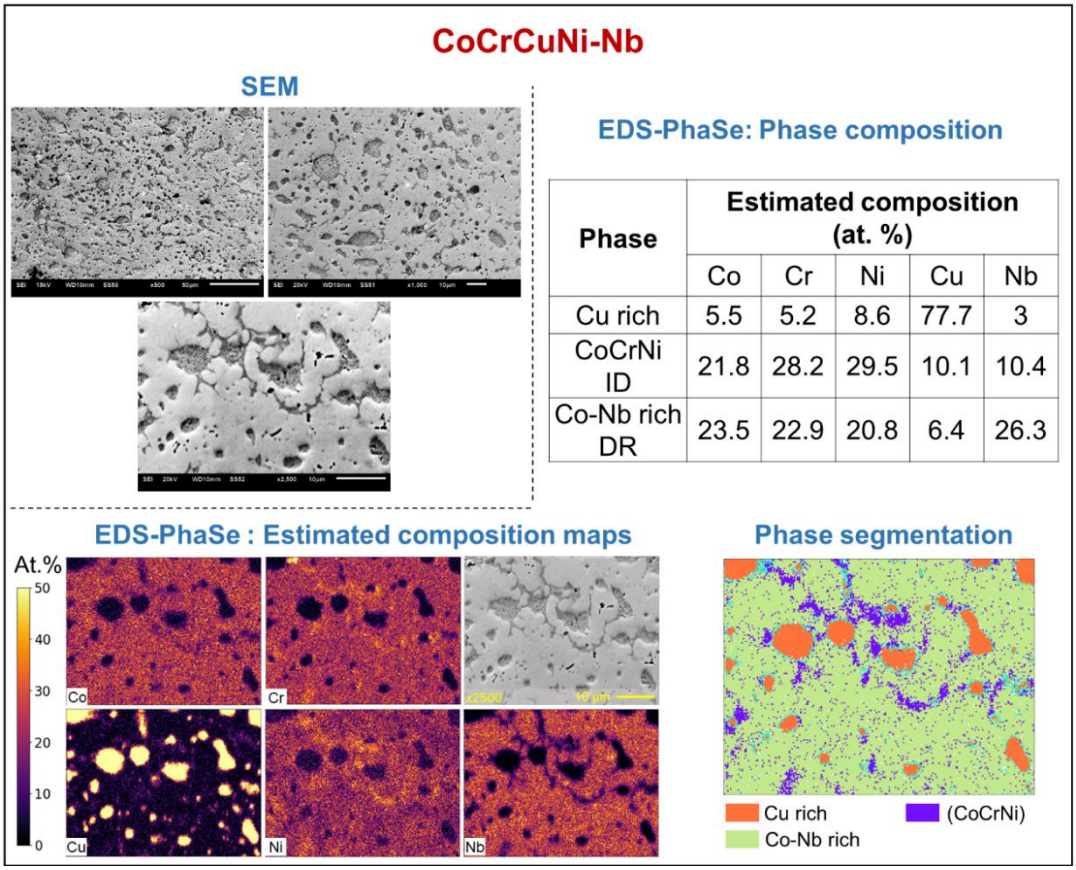

Phase	Estimated composition (at. %)				
	Co	Cr	Ni	Cu	Nb
Cu rich	5.5	5.2	8.6	77.7	3
CoCrNi ID	21.8	28.2	29.5	10.1	10.4
Co-Nb rich DR	23.5	22.9	20.8	6.4	26.3

Figure 6.19 SEM-EDS and EDS-PhaSe results of CoCrCuNi-Nb alloy along with the phase information. The quantitative analysis of EDS data and subsequent phase segmentation was done using EDS-PhaSe [235] software that was developed as part of this thesis (Appendix B).

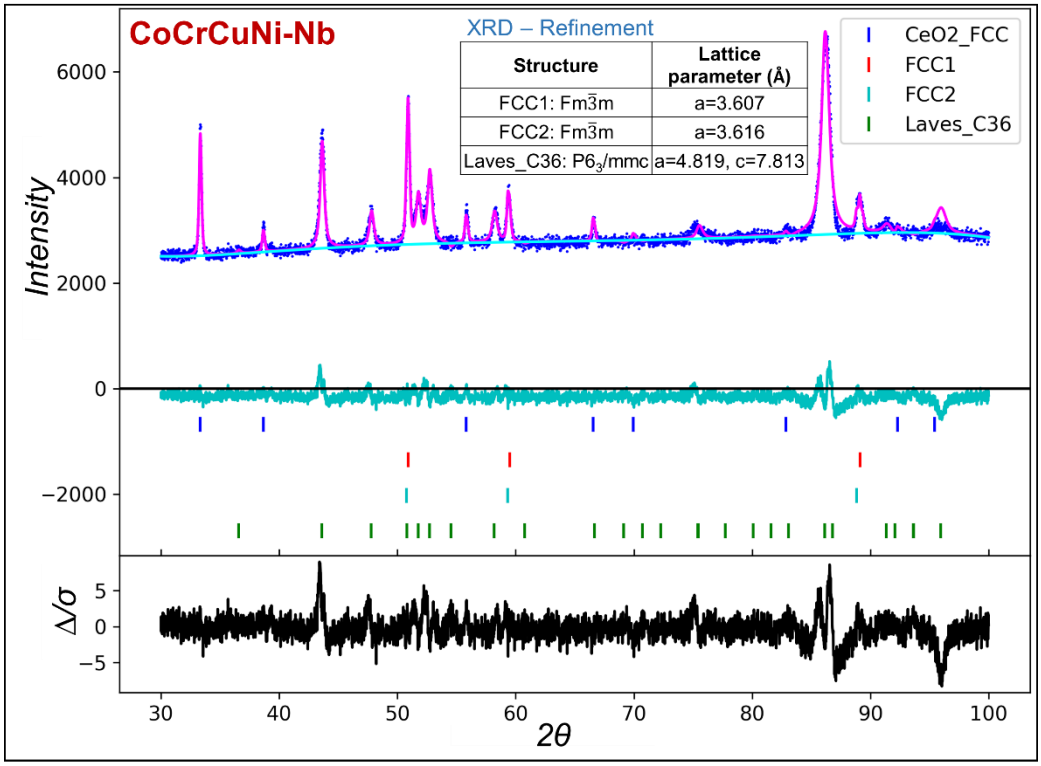

Structure	Lattice parameter (Å)
FCC1: $Fm\bar{3}m$	a=3.607
FCC2: $Fm\bar{3}m$	a=3.616
Laves_C36: $P6_3/mmc$	a=4.819, c=7.813

Figure 6.20 XRD pattern and Rietveld-refined structures for CoCrCuNi-Nb equiatomic quinary

6.3.8 CoCrCuNi-Mo

As seen in Figure 6.1, Mo has many similarities with Cr as they both have BCC structure, are in the same group and hence have the same VEC (=6). The chemical interaction parameters of Mo-(Co/Ni/Cu) pairs are very similar to Cr-pairs. But the major difference is the much larger size of Mo atom as compared to Cr which leads to significantly higher elastic interaction parameters of Mo-pairs. This is in fact the reason why Mo-Cr binary, which forms an isomorphous system at high temperatures, breaks down into Mo rich and Cr rich solids at low temperatures. The overall solution interaction parameters (ΔH^{sol}) of all Mo-pairs are positive with that of Mo-Cu pair being exceptionally large. In terms of interaction with Cu, Mo is similar to Nb as the Mo-Cu binary also shows monotectic reaction with significant immiscibility in the liquid state. But due to an additional valence electron, the chemical interaction parameters of Mo-(Co/Cr/Ni) pairs are significantly weaker as compared to same Nb-pairs. Since both Mo and Cu cluster strongly with all the other elements in this system, it would be fair to expect the formation of separate Mo rich and Cu rich phases in this alloy which should then drive the formation of a third CoCrNi phase since both Cu and Mo cluster with Co, Cr and Ni.

The ML predictions, Figure 6.2, indicate the presence of FCC and Intermetallic phases which aligns with the possible formation of a Cu rich phase (FCC) and a CoCrNi rich phase (FCC) deduced from binary interaction parameters. The expected Mo-rich phase could very well align with the intermetallic phase formation since Zhou et al. have recently reported the formation of a Mo-rich intermetallic phase in a CoCrNiMo quaternary [239]. The Thermo-Calc calculations, Figure 6.21, also closely match these predictions as they predict the formation of a Cu rich phase (FCC), a NiCoCr phase (FCC) and a Mo-Cr rich sigma phase (BCT). That said, we do see a discrepancy in the quantitative phase estimation since Thermo-Calc predicts a significantly more amount of intermetallic phase than what is suggested by the ML model.

The experimental results (Figure 6.22) are in agreement with the ML and Thermo-Calc predictions as the phase segmented micrograph and EDS-PhaSe analysis shows the formation of a Cu rich phase, a CoCrNi phase and a Mo rich phase. Similar to the CoCrCuNi-Nb system, the Cu rich phase here is also present as isolated globules encompassed by Mo rich dendrites and marks the liquid phase separation that may have been driven by the well-known monotectic reaction in Cu-Mo system. It appears that as the melt cools, it may have separated into Cu rich and Mo rich liquid phases, and since Mo has significantly higher melting point, the Mo-rich dendrites may have solidified first thereby trapping the Cu rich liquid which has significantly lower melting point. As the Mo-rich dendrites grew, the interdendritic region may have gotten enriched in Ni and Co (owing to the positive interaction parameters of Mo-Ni and Mo-Co pairs). Since Ni-Cr is by the far the strongest ordering pair in this alloy system, the Ni may have pulled some Cr from the Mo-rich dendrites into the interdendritic region. The interdendritic region may have finally solidified as the CoCrNi FCC phase.

The XRD pattern (Figure 6.23) shows the major phase (~87 wt.%) to be a tetragonal σ-phase, a=9.013 Å, c=4.696 Å. Since the Mo-rich intermetallic is by far the most dominant phase present in both the microstructure and Thermo-Calc calculations, we can safely assign Mo-rich phase as the tetragonal σ-phase. The second major phase is an FCC solid solution, a=3.614 Å. This matches with the lattice parameter of Cu and may be assigned to the Cu-rich phase which has been observed both experimentally and in Thermo-Calc simulations. The expected peak positions of CoCrNi FCC phase overlap with the peaks of tetragonal Mo-rich phase and cannot be deconvoluted reliably. Thus, while we see clearly observe the CoCrNi phase as the interdendritic phase and can confidently expect it to be an FCC phase based on Thermo-Calc simulations as well as analysis of previous alloy systems, we cannot conclusively declare its structure or the lattice parameter here. We also observe some minor peaks in the XRD which match with a Cr rich BCC phase. While we did not observe any such phase in microstructural characterization, it could very well be that a

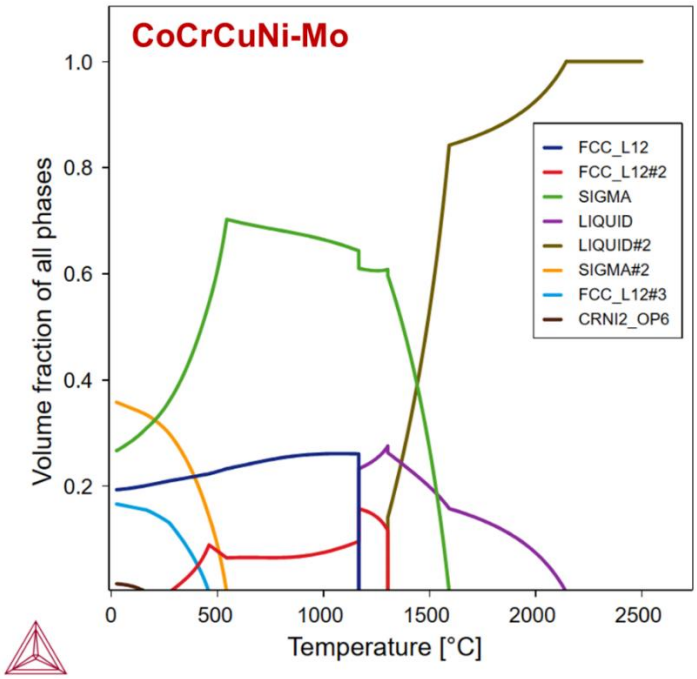

Figure 6.21 Thermo-Calc predicted phase fractions in CoCrCuNi-Mo equiatomic quinary as a function of temperature.

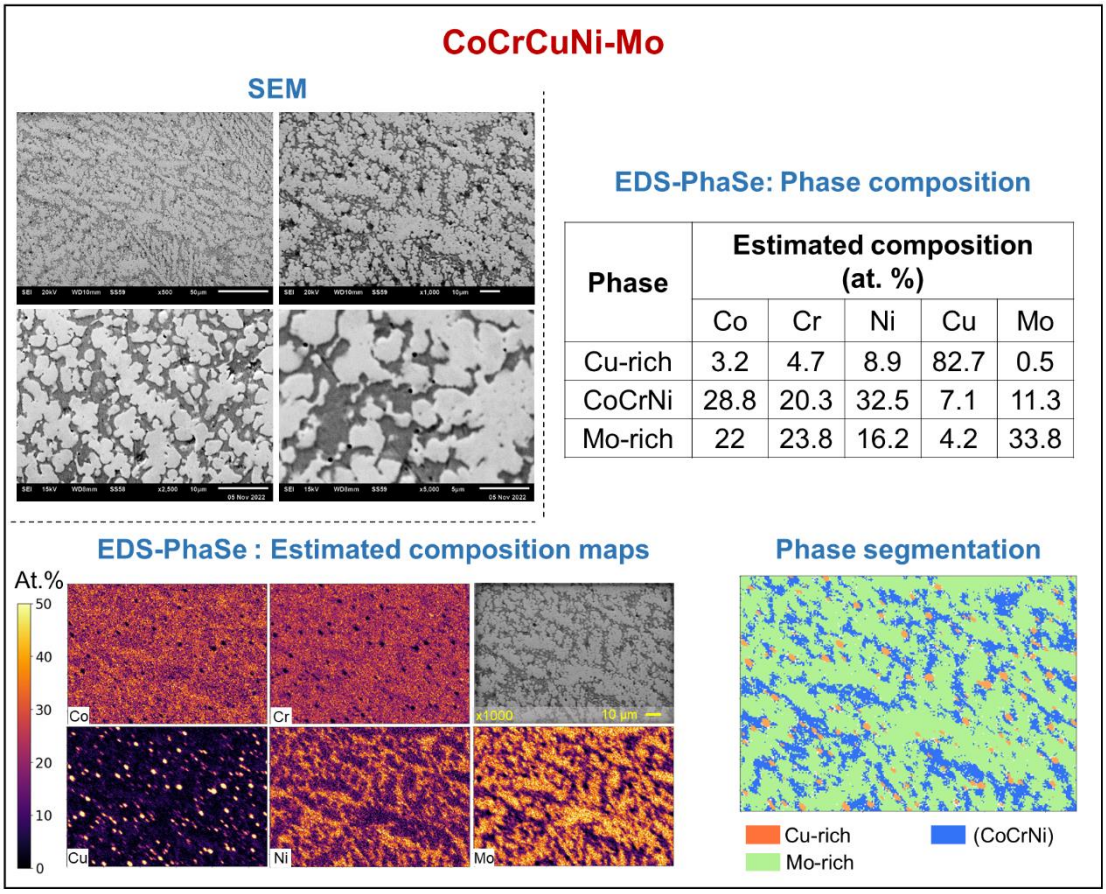

EDS-PhaSe: Phase composition

Phase	Estimated composition (at. %)				
	Co	Cr	Ni	Cu	Mo
Cu-rich	3.2	4.7	8.9	82.7	0.5
CoCrNi	28.8	20.3	32.5	7.1	11.3
Mo-rich	22	23.8	16.2	4.2	33.8

Figure 6.22 SEM-EDS and EDS-PhaSe results of CoCrCuNi-Mo alloy along with the phase information. The quantitative analysis of EDS data and subsequent phase segmentation was done using EDS-PhaSe [235] software that was developed as part of this thesis (Appendix B).

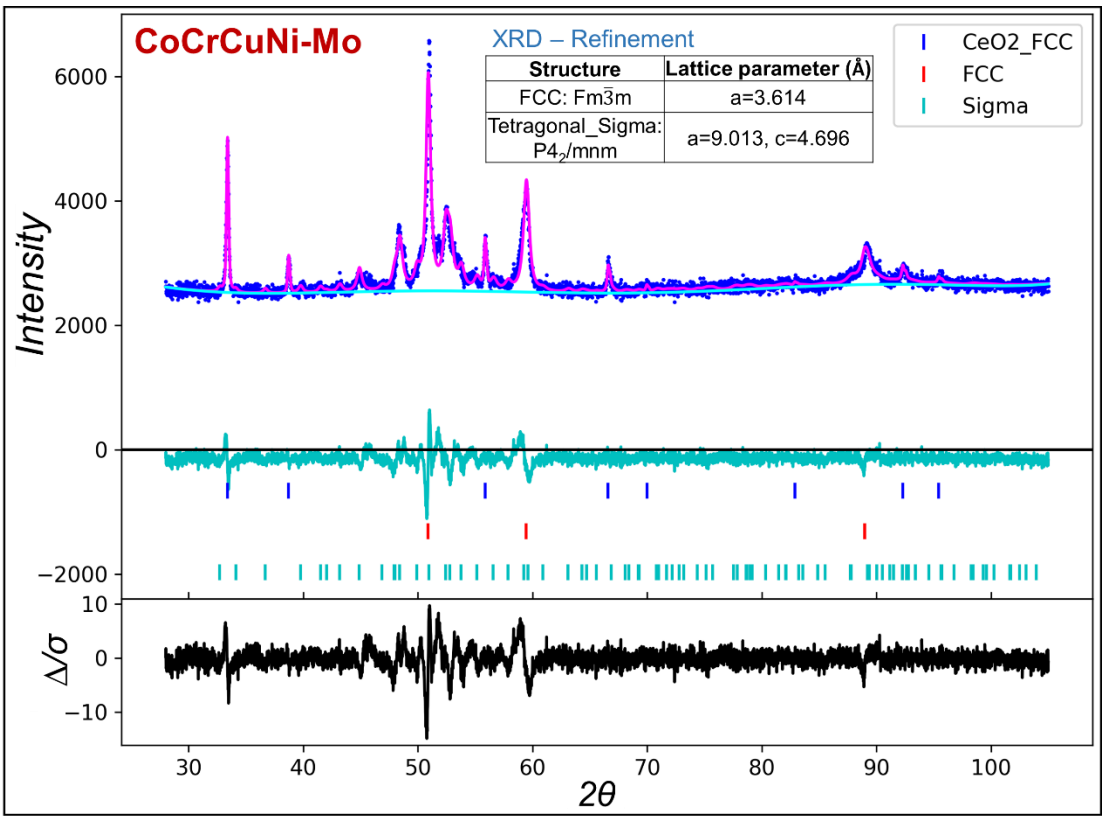

Figure 6.23 XRD pattern and Rietveld-refined structures for CoCrCuNi-Mo equiatomic quinary

small amount of Cr-rich BCC phase separates out from the Mo-rich phase since we do know that Mo-Cr binary phase separates at low temperatures.

6.4 Conclusions

In this chapter, we carried out experimental studies on CoCrNi ternary, CoCrCuNi quaternary and CoCrCuNi-M (M={Al, Ti, Zr, Nb, Mo}) quinary alloys to study the phase evolution in these alloys. The coexistence of Cu with 3d and 4d transition metals introduces a broad spectrum of ordering and clustering behavior which makes these alloys a good test bed for a systematic study on the role of binary interactions in phase selection in CCAs. Moreover, these compositions are not only helpful in validating the phase selection and hardness prediction ML models developed earlier in this dissertation, but are also vital in identifying the limits of these models. The binary interactions here change from strongly ordering (in Ti and Zr systems) to strongly clustering (in Nb and Mo systems) and thus push the ML models to their limits; which is

especially true for Nb and Mo systems since the training datasets had only alloy with Cu-Mo pair and no alloy with Cu-Nb pair. The structural and microstructural characterization of as-cast alloys was done through XRD (with Rietveld refinement) and SEM-EDS measurements. EDS-PhaSe was used for the phase analysis from SEM-EDS data. The CoCrNi ternary exhibits a single-phase FCC structure whereas the addition of Cu causes phase separation into a CoCrNi rich FCC phase and a Cu rich phase in CoCrCuNi quaternary. The addition of Al to CoCrCuNi causes the formation of an additional Al-Ni rich B2 phase at the interface of dendritic and interdendritic regions that drives the CoCrNi-rich dendritic phase to transition into a Co-Cr BCT phase. The addition of either Ti or Zr to CoCrCuNi leads to intermetallic formation and completely flips the clustering behavior wherein now we have Cr (instead of Cu) clustering to a separate Cr rich phase. This is driven by the formation of Ti and Zr rich phases which, combined with the higher ordering of Ti-Cu and Zr-Cu pairs compared to Ti-Cr and Zr-Cr pairs, drives the Cr out instead of Cu. The addition of either Nb or Mo to CoCrCuNi leads to a major intermetallic phase that solidifies as dendritic region and a minor CoCrNi rich phase that forms in the interdendritic region. Also, for both alloys, Cu segregates into separate globular regions encompassed by Mo rich and Nb rich dendrites indicating liquid phase separation between Cu-rich and Mo-rich liquids; which is not surprising as both Cu-Mo and Cu-Nb binaries exhibit a monotectic reaction. The formation of intermetallic phases in all CoCrCuNi-M quinary alloys here results in a significant increase in their hardness as compared to the CoCrCuNi quaternary. The hardness ML model quite reliably predicts this increase for Al, Ti and Zr alloys but is quite off in Nb and Mo alloys (especially Mo). Similarly, the phase selection model correctly predicts the intermetallic formation in all of the quinary alloys, but underpredicts the phase fraction of intermetallic phases in Nb and Mo alloys (especially Mo). This stems from the fact that the behavior seen in Nb and Mo alloys here was not well represented in the training datasets as they have an exceptionally high chemical enthalpy of mixing owing to their strong clustering tendencies wherein Nb-(Co/Cr) and Mo-(Co/Cr/Cu/Ni) pairs all have positive interaction parameters. Thus, this

highlights an important limitation of the ML models wherein they can be expected to break down when operating near or outside the limits of the feature values that were encountered in the training process. Going forward, we will design and incorporate these limitations into MAPAL (Appendix A) so that, whenever these models are used, appropriate warnings and confidence estimates are generated based on the feature space that is being probed by the user.

Chapter 7: Conclusions and future outlook

7.1 Research summary and general conclusions

Since the initial reports by Brian Cantor and Jien-Wei Yeh in 2004, compositionally complex alloys (CCAs) have come a long way in the last two decades and are amongst the most widely researched class of alloys today. A fundamental challenge associated with the exploration of CCAs is the astronomical compositional space (more than 10^{100} possible compositions) that is presented by these alloys. In recent years, machine learning (ML) has appeared as a promising tool to aid material discovery and has immense potential to enable the efficient exploration of compositional spaces in CCAs. But the black-box treatment that is often accorded to these models makes it difficult to extract any physical insights from the decision-making process of these models. Thus, the scope of this thesis is to build data-driven models and explainability frameworks that can not only accelerate the design of CCAs but can also decode the decision-making process of these models to provide fundamental physical insights into the factors that lead to certain properties in CCAs. Prior to this thesis, we published an ML model for predicting the phase selection in CCAs and validated it using ab initio, atomistic, experimental and Thermo-Calc results for a wide variety of alloy systems. But despite the excellent performance, it was treated as a black-box model since it deployed an ensemble of deep neural-networks which cannot be visualized or decoded directly. Thus, in Chapter 2, we started out this thesis by reducing the complex neural network model into a simplified and interpretable mathematical function for the probability of occurrence of FCC and BCC phases in CCAs. We

used a logistic function to isolate the effect of valence electron count on FCC and BCC phase occurrence and modeled the residuals as a function of six other physical and thermodynamic descriptors. This enabled a direct quantitative estimation of feature contributions towards the phase occurrence probabilities. We also showed that the physics-guided mathematical form (wherever possible) is superior to the brute-force deduction of mathematical expression through symbolic regression. That said, there are often scenarios where one may not have any idea as to what type of mathematical expression may be suitable for a problem. Thus, to enable interpretation in such scenarios, in Chapter 3, we developed a model-agnostic interpretational methodology termed as Compositional-Stimulus and Model-Response (CoSMoR) framework. CoSMoR can be applied to any composition-based ML model (irrespective of the algorithm used) to calculate the exact contribution of each feature towards the manifestation of target material property along a continuous compositional pathway. It utilizes the local partial dependencies of target property with respect to each feature and combines it with feature variations associated with discretized compositional variations to measure exact feature contributions. We showcased the importance of CoSMoR in this chapter through its implementation on the phase selection problem in CCAs wherein it provided materials-specific physical insights into phase transitions. Now that we had an interpretation methodology that can be applied to any composition-based model, we next developed ML models for predicting the short-range order (Chapter 4) and hardness (Chapter 5) in CCAs. From ML perspective, short-range order (SRO) prediction has unique challenges since – (a) SRO data is not a single value for any given alloy but is instead a matrix containing one SRO value for each unique binary pair, and (b) the SRO is controlled by the competing nature of binary pair interactions and not by the consolidated alloy features. We addressed these challenges in Chapter 4 by devising a new methodology wherein all of the information pertaining to an alloy and its constituent binary pairs was encoded into a three-dimensional array which was then mapped to a two-dimensional SRO matrix using variational autoencoders. In Chapter 5, we developed a neural network

ensemble model that captures the essential physical and thermodynamic features that contribute to hardness and allows high-throughput exploration of multi-dimensional compositional space. The model was used to explore and successfully predict hardness in $Al_xTi_y(CrFeNi)_{1-x-y}$, $Hf_xCo_y(CrFeNi)_{1-x-y}$ and $Al_x(TiZrHf)_{1-x}$ systems. Using the DFT calculations done by our collaborators at Ames Lab, USA, we showed that the model is able to capture both linear and non-linear hardness variations that are associated with the composition-dependent SRO and phase stabilities. For both SRO and hardness model, we used CoSMoR to extract physical insights from the decision-making process of the model. Finally, in Chapter 6, we undertook experimental study of CoCrNi, CoCrCuNi and CoCrCuNi-M (M={Al, Ti, Zr, Nb, Mo}) alloys to – a) assess the capability of phase selection and hardness prediction ML models developed earlier in this thesis, and b) study the effect of strong ordering/clustering binary pairs on phase evolution in CCAs. We performed the structural and microstructural characterization using XRD and SEM-EDS to study the phase evolution in these alloys and measured the Vicker's hardness for comparison with our ML predictions. To assist the microstructural analysis from SEM-EDS data, we developed the EDS-PhaSe software as part of this thesis, included as Appendix B, to enable quantitative analysis of EDS data. It converts the EDS elemental maps into estimated composition maps and allows interactive phase segmentation and phase analysis based on various markers of elemental segregation. All feature generation programs, trained ML models and interpretation routines developed as part of this thesis have been packaged into a Python library viz., MAPAL, that has been included as Appendix A. Overall, this thesis encompasses the development of ML models and computational frameworks for the study of CCAs to – a) enable reliable, efficient and targeted exploration of compositional spaces in CCAs, b) decode the decision-making process of ML model to provide physical insights, and c) enhance the microstructural characterization from SEM-EDS data to add new dimensions to the insights that can be gained from experimental results.

7.2 Future outlook

Even though the extensive research on CCAs over the last decade has uncovered many compositions with unique and improved properties such as excellent high temperature resistance, cryogenic strength and extreme toughness, we have barely scratched the surface of what these alloys have to offer. In the years and decades to come, CCAs have the potential to revolutionize many technologies that are impeded by the limitations imposed by existing alloys. This thesis makes several contributions towards the exploration of these alloys and there are several avenues in which it can be taken forward. Firstly, as is true for any data-driven approach, the accuracy and applicability of the model is strongly dictated by the quality, quantity and diversity of the data on which it was trained. As CCAs are still fairly new materials (compared to the steels and superalloys), the volume of experimental data is significantly lacking. But in the time to come, this will change due to both the exponentially growing research interest in these alloys as well as the high-throughput automated experimental facilities that have started appearing recently. As more data becomes available, the ML models must be retrained and reevaluated to improve their performance. Secondly, there is an urgent need for implementation and automation of web-scraping and text-mining to develop exhaustive databases for CCAs using the published literature. This would ensure that the ML models can learn from as much data as possible and can also actively adapt to new research as it appears. Thirdly, majority of the ML models for CCAs, including those developed in this thesis, are microstructure agnostic. While it is not difficult to build multi-modal ML models that incorporate images, the main difficulties with the incorporation of microstructures from published literature include – a) lack of uniform reporting standards that ensure availability of annotation-free images along with the associated metadata, b) immense length scales that are spanned by microstructural images, and c) lack of labelled microstructures that contain layers/masks representing distinct phases or features. There is an immense scope in future to develop methodologies that can circumvent these problems and enable effective utilization of microstructural information for improving

ML models. Finally, as the field of CCAs matures, it would be immensely helpful to combine machine learning with various computational approaches viz., ab initio calculations, atomistic simulations, theoretical modeling and thermodynamic modeling, to form synergistic frameworks that can perform much better than the standalone methods. We are also developing a package for high-throughput calculations in MAPAL that would use the pre-trained models developed in this thesis to efficiently generate and explore the properties of CCAs over large compositional spaces spanning millions of compositions.

References

[1] B. Cantor, I.T.H. Chang, P. Knight, A.J.B. Vincent, Microstructural development in equiatomic multicomponent alloys, Materials Science and Engineering: A 375–377 (2004) 213–218. https://doi.org/10.1016/j.msea.2003.10.257.

[2] J.-W. Yeh, S.-K. Chen, S.-J. Lin, J.-Y. Gan, T.-S. Chin, T.-T. Shun, C.-H. Tsau, S.-Y. Chang, Nanostructured High-Entropy Alloys with Multiple Principal Elements: Novel Alloy Design Concepts and Outcomes, Advanced Engineering Materials 6 (2004) 299–303. https://doi.org/10.1002/adem.200300567.

[3] P. Singh, A.V. Smirnov, A. Alam, D.D. Johnson, First-principles prediction of incipient order in arbitrary high-entropy alloys: exemplified in Ti0.25CrFeNiAlx, Acta Mater. 189 (2020) 248–254. https://doi.org/10.1016/j.actamat.2020.02.063.

[4] Y. Zhang, T.T. Zuo, Z. Tang, M.C. Gao, K.A. Dahmen, P.K. Liaw, Z.P. Lu, Microstructures and properties of high-entropy alloys, Progress in Materials Science 61 (2014) 1–93. https://doi.org/10.1016/j.pmatsci.2013.10.001.

[5] P. Singh, S. Gupta, S. Thimmaiah, B. Thoeny, P.K. Ray, A.V. Smirnov, D.D. Johnson, M.J. Kramer, Vacancy-mediated complex phase selection in high entropy alloys, Acta Mater. 194 (2020) 540–546. https://doi.org/10.1016/j.actamat.2020.04.063.

[6] W. Li, D. Xie, D. Li, Y. Zhang, Y. Gao, P.K. Liaw, Mechanical behavior of high-entropy alloys, Progress in Materials Science 118 (2021) 100777. https://doi.org/10.1016/j.pmatsci.2021.100777.

[7] P. Singh, A. Marshal, A.V. Smirnov, A. Sharma, G. Balasubramanian, K.G. Pradeep, D.D. Johnson, Tuning phase stability and short-range order through Al doping in (CoCrFeMn)100-x (Al)x high-entropy alloys, Phys. Rev. Materials 3 (2019) 075002. https://doi.org/10.1103/PhysRevMaterials.3.075002.

[8] B. Cantor, Multicomponent high-entropy Cantor alloys, Prog. Mater. Sci. 120 (2021) 100754. https://doi.org/10.1016/j.pmatsci.2020.100754.

[9] P. Singh, A.V. Smirnov, D.D. Johnson, Ta-Nb-Mo-W refractory high-entropy alloys: anomalous ordering behavior and its intriguing electronic origin, Phys. Rev. Mater. 2 (2018) 055004. https://doi.org/10.1103/PhysRevMaterials.2.055004.

[10] R. Singh, A. Sharma, P. Singh, G. Balasubramanian, D.D. Johnson, Accelerating computational modeling and design of high-entropy alloys, Nature Computational Science 1 (2021) 54–61. https://doi.org/10.1038/s43588-020-00006-7.

[11] E.P. George, D. Raabe, R.O. Ritchie, High-entropy alloys, Nat. Rev. Mater. 4 (2019) 515–534. https://doi.org/10.1038/s41578-019-0121-4.
[12] N. Walker, S. Lee, J. Dagdelen, K. Cruse, S. Gleason, A. Dunn, G. Ceder, A. Paul Alivisatos, K. A. Persson, A. Jain, Extracting structured seed-mediated gold nanorod growth procedures from scientific text with LLMs, Digital Discovery 2 (2023) 1768–1782. https://doi.org/10.1039/D3DD00019B.
[13] K. Cruse, V. Baibakova, M. Abdelsamie, K. Hong, C.J. Bartel, A. Trewartha, A. Jain, C.M. Sutter-Fella, G. Ceder, Text Mining the Literature to Inform Experiments and Rationalize Impurity Phase Formation for BiFeO3, Chem. Mater. (2023). https://doi.org/10.1021/acs.chemmater.3c02203.
[14] M. Abdelsamie, K. Hong, K. Cruse, C.J. Bartel, V. Baibakova, A. Trewartha, A. Jain, G. Ceder, C.M. Sutter-Fella, Combining text mining, in situ characterization, and ab initio calculations to rationalize BiFeO3 crystallization pathways, Matter 6 (2023) 4291–4305. https://doi.org/10.1016/j.matt.2023.10.002.
[15] A. Dunn, J. Dagdelen, N. Walker, S. Lee, A.S. Rosen, G. Ceder, K. Persson, A. Jain, Structured information extraction from complex scientific text with fine-tuned large language models, (2022). https://doi.org/10.48550/arXiv.2212.05238.
[16] K. Cruse, A. Trewartha, S. Lee, Z. Wang, H. Huo, T. He, O. Kononova, A. Jain, G. Ceder, Text-mined dataset of gold nanoparticle synthesis procedures, morphologies, and size entities, Sci Data 9 (2022) 234. https://doi.org/10.1038/s41597-022-01321-6.
[17] S. Gorsse, M.H. Nguyen, O.N. Senkov, D.B. Miracle, Database on the mechanical properties of high entropy alloys and complex concentrated alloys, Data Brief 21 (2018) 2664–2678. https://doi.org/10.1016/j.dib.2018.11.111.
[18] C.K.H. Borg, C. Frey, J. Moh, T.M. Pollock, S. Gorsse, D.B. Miracle, O.N. Senkov, B. Meredig, J.E. Saal, Expanded dataset of mechanical properties and observed phases of multi-principal element alloys, Sci Data 7 (2020) 430. https://doi.org/10.1038/s41597-020-00768-9.
[19] D. Beniwal, P.K. Ray, Learning phase selection and assemblages in High-Entropy Alloys through a stochastic ensemble-averaging model, Comput. Mater. Sci. 197 (2021) 110647. https://doi.org/10.1016/j.commatsci.2021.110647.
[20] A. Jain, S.P. Ong, G. Hautier, W. Chen, W.D. Richards, S. Dacek, S. Cholia, D. Gunter, D. Skinner, G. Ceder, K.A. Persson, Commentary: The Materials Project: A materials genome approach to accelerating materials innovation, APL Materials 1 (2013) 011002. https://doi.org/10.1063/1.4812323.
[21] S. Curtarolo, W. Setyawan, G.L.W. Hart, M. Jahnatek, R.V. Chepulskii, R.H. Taylor, S. Wang, J. Xue, K. Yang, O. Levy, M.J. Mehl, H.T. Stokes, D.O. Demchenko, D. Morgan, AFLOW: An automatic framework

for high-throughput materials discovery, Computational Materials Science 58 (2012) 218–226. https://doi.org/10.1016/j.commatsci.2012.02.005.

[22] M. Esters, C. Oses, S. Divilov, H. Eckert, R. Friedrich, D. Hicks, M.J. Mehl, F. Rose, A. Smolyanyuk, A. Calzolari, X. Campilongo, C. Toher, S. Curtarolo, aflow.org: A web ecosystem of databases, software and tools, Computational Materials Science 216 (2023) 111808. https://doi.org/10.1016/j.commatsci.2022.111808.

[23] S. Kirklin, J.E. Saal, B. Meredig, A. Thompson, J.W. Doak, M. Aykol, S. Rühl, C. Wolverton, The Open Quantum Materials Database (OQMD): assessing the accuracy of DFT formation energies, Npj Comput Mater 1 (2015) 1–15. https://doi.org/10.1038/npjcompumats.2015.10.

[24] J.E. Saal, S. Kirklin, M. Aykol, B. Meredig, C. Wolverton, Materials Design and Discovery with High-Throughput Density Functional Theory: The Open Quantum Materials Database (OQMD), JOM 65 (2013) 1501–1509. https://doi.org/10.1007/s11837-013-0755-4.

[25] M. Scheidgen, L. Himanen, A.N. Ladines, D. Sikter, M. Nakhaee, Á. Fekete, T. Chang, A. Golparvar, J.A. Márquez, S. Brockhauser, S. Brückner, L.M. Ghiringhelli, F. Dietrich, D. Lehmberg, T. Denell, A. Albino, H. Näsström, S. Shabih, F. Dobener, M. Kühbach, R. Mozumder, J.F. Rudzinski, N. Daelman, J.M. Pizarro, M. Kuban, C. Salazar, P. Ondračka, H.-J. Bungartz, C. Draxl, NOMAD: A distributed web-based platform for managing materials science research data, Journal of Open Source Software 8 (2023) 5388. https://doi.org/10.21105/joss.05388.

[26] scipy.stats.pearsonr — SciPy v0.14.0 Reference Guide, (2021). https://docs.scipy.org/doc/scipy-0.14.0/reference/generated/scipy.stats.pearsonr.html#scipy.stats.pearsonr (accessed December 1, 2021).

[27] scipy.stats.spearmanr — SciPy v0.14.0 Reference Guide, (2021). https://docs.scipy.org/doc/scipy-0.14.0/reference/generated/scipy.stats.spearmanr.html#scipy.stats.spearmanr (accessed December 1, 2021).

[28] scipy.stats.pointbiserialr — SciPy v0.14.0 Reference Guide, (2021). https://docs.scipy.org/doc/scipy-0.14.0/reference/generated/scipy.stats.pointbiserialr.html#scipy.stats.pointbiserialr (accessed December 1, 2021).

[29] Permutation Importance with Multicollinear or Correlated Features, Scikit-Learn (2021). https://scikit-learn/stable/auto_examples/inspection/plot_permutation_importance_multicollinear.html (accessed December 2, 2021).

[30] K.T. Butler, D.W. Davies, H. Cartwright, O. Isayev, A. Walsh, Machine learning for molecular and materials science, Nature 559 (2018) 547–555. https://doi.org/10.1038/s41586-018-0337-2.

[31] J. Wei, X. Chu, X.-Y. Sun, K. Xu, H.-X. Deng, J. Chen, Z. Wei, M. Lei, Machine learning in materials science, InfoMat 1 (2019) 338–358. https://doi.org/10.1002/inf2.12028.

[32] J. Cai, X. Chu, K. Xu, H. Li, J. Wei, Machine learning-driven new material discovery, Nanoscale Advances 2 (2020) 3115–3130. https://doi.org/10.1039/D0NA00388C.
[33] R. Ramprasad, R. Batra, G. Pilania, A. Mannodi-Kanakkithodi, C. Kim, Machine learning in materials informatics: recent applications and prospects, Npj Comput. Mater. 3 (2017) 1–13. https://doi.org/10.1038/s41524-017-0056-5.
[34] R. Batra, L. Song, R. Ramprasad, Emerging materials intelligence ecosystems propelled by machine learning, Nat Rev Mater (2020) 1–24. https://doi.org/10.1038/s41578-020-00255-y.
[35] A. Géron, Hands-On Machine Learning with Scikit-Learn, Keras, and TensorFlow: Concepts, Tools, and Techniques to Build Intelligent Systems, 2nd edition, O'Reilly Media, Beijing China ; Sebastopol, CA, 2019.
[36] D. Beniwal, P.K. Ray, CoSMoR: Decoding decision-making process along continuous composition pathways in machine learning models trained for material properties, Phys. Rev. Mater. 7 (2023) 043802. https://doi.org/10.1103/PhysRevMaterials.7.043802.
[37] K. Lee, M.V. Ayyasamy, P. Delsa, T.Q. Hartnett, P.V. Balachandran, Phase classification of multi-principal element alloys via interpretable machine learning, Npj Comput Mater 8 (2022) 1–12. https://doi.org/10.1038/s41524-022-00704-y.
[38] S. Sun, R. Ouyang, B. Zhang, T.-Y. Zhang, Data-driven discovery of formulas by symbolic regression, MRS Bulletin 44 (2019) 559–564. https://doi.org/10.1557/mrs.2019.156.
[39] B. Rozemberczki, L. Watson, P. Bayer, H.-T. Yang, O. Kiss, S. Nilsson, R. Sarkar, The Shapley Value in Machine Learning, (2022). https://doi.org/10.48550/arXiv.2202.05594.
[40] A. Takeuchi, A. Inoue, Calculations of Mixing Enthalpy and Mismatch Entropy for Ternary Amorphous Alloys, Materials Transactions, JIM 41 (2000) 1372–1378. https://doi.org/10.2320/matertrans1989.41.1372.
[41] A.R. Miedema, P.F. de Châtel, F.R. de Boer, Cohesion in alloys — fundamentals of a semi-empirical model, Physica B+C 100 (1980) 1–28. https://doi.org/10.1016/0378-4363(80)90054-6.
[42] R.F. Zhang, S.H. Zhang, Z.J. He, J. Jing, S.H. Sheng, Miedema Calculator: A thermodynamic platform for predicting formation enthalpies of alloys within framework of Miedema's Theory, Computer Physics Communications 209 (2016) 58–69. https://doi.org/10.1016/j.cpc.2016.08.013.
[43] P.K. Ray, M. Akinc, M.J. Kramer, Applications of an extended Miedema's model for ternary alloys, J. Alloys Compd. 489 (2010) 357–361. https://doi.org/10.1016/j.jallcom.2009.07.062.
[44] M.S. Mousavi, R. Abbasi, S.F. Kashani-Bozorg, A Thermodynamic Approach to Predict Formation Enthalpies of Ternary Systems Based on Miedema's Model, Metall and Mat Trans A 47 (2016) 3761–3770. https://doi.org/10.1007/s11661-016-3533-4.

[45] J.-H. Li, M.-H. Tsai, Theories for predicting simple solid solution high-entropy alloys: Classification, accuracy, and important factors impacting accuracy, Scripta Materialia 188 (2020) 80–87. https://doi.org/10.1016/j.scriptamat.2020.06.064.
[46] S. Guo, C. Ng, J. Lu, C.T. Liu, Effect of valence electron concentration on stability of fcc or bcc phase in high entropy alloys, J. Appl. Phys. 109 (2011) 103505. https://doi.org/10.1063/1.3587228.
[47] M. Liu, W. Xu, S. Zhang, Z. Wang, Z. Wang, B. Wang, D. Wang, F. Li, Microstructures and hardnesses of AlCoCr0.5FexNi2.5 high entropy alloys with equal valence electron concentration, Journal of Alloys and Compounds 824 (2020) 153881. https://doi.org/10.1016/j.jallcom.2020.153881.
[48] D. Beniwal, Jhalak, P.K. Ray, Data-Driven Phase Selection, Property Prediction and Force-Field Development in Multi-Principal Element Alloys, in: A. Verma, S. Mavinkere Rangappa, S. Ogata, S. Siengchin (Eds.), Forcefields for Atomistic-Scale Simulations: Materials and Applications, Springer Nature, Singapore, 2022: pp. 315–347. https://doi.org/10.1007/978-981-19-3092-8_16.
[49] X. Yang, Y. Zhang, Prediction of high-entropy stabilized solid-solution in multi-component alloys, Mater. Chem. Phys. 132 (2012) 233–238. https://doi.org/10.1016/j.matchemphys.2011.11.021.
[50] S. Guo, Q. Hu, C. Ng, C.T. Liu, More than entropy in high-entropy alloys: Forming solid solutions or amorphous phase, Intermetallics 41 (2013) 96–103. https://doi.org/10.1016/j.intermet.2013.05.002.
[51] Z. Wang, Y. Huang, Y. Yang, J. Wang, C.T. Liu, Atomic-size effect and solid solubility of multicomponent alloys, Scripta Materialia 94 (2015) 28–31. https://doi.org/10.1016/j.scriptamat.2014.09.010.
[52] A.K. Singh, N. Kumar, A. Dwivedi, A. Subramaniam, A geometrical parameter for the formation of disordered solid solutions in multi-component alloys, Intermetallics 53 (2014) 112–119. https://doi.org/10.1016/j.intermet.2014.04.019.
[53] Y.F. Ye, Q. Wang, J. Lu, C.T. Liu, Y. Yang, Design of high entropy alloys: A single-parameter thermodynamic rule, Scripta Materialia 104 (2015) 53–55. https://doi.org/10.1016/j.scriptamat.2015.03.023.
[54] Y.F. Ye, Q. Wang, J. Lu, C.T. Liu, Y. Yang, The generalized thermodynamic rule for phase selection in multicomponent alloys, Intermetallics 59 (2015) 75–80. https://doi.org/10.1016/j.intermet.2014.12.011.
[55] M.C. Troparevsky, J.R. Morris, P.R.C. Kent, A.R. Lupini, G.M. Stocks, Criteria for Predicting the Formation of Single-Phase High-Entropy Alloys, Phys. Rev. X 5 (2015) 011041. https://doi.org/10.1103/PhysRevX.5.011041.
[56] O.N. Senkov, D.B. Miracle, A new thermodynamic parameter to predict formation of solid solution or intermetallic phases in high entropy alloys, J. Alloys Compd. 658 (2016) 603–607. https://doi.org/10.1016/j.jallcom.2015.10.279.

[57] D.J.M. King, S.C. Middleburgh, A.G. McGregor, M.B. Cortie, Predicting the formation and stability of single phase high-entropy alloys, Acta Materialia 104 (2016) 172–179. https://doi.org/10.1016/j.actamat.2015.11.040.
[58] A. Roy, T. Babuska, B. Krick, G. Balasubramanian, Machine learned feature identification for predicting phase and Young's modulus of low-, medium- and high-entropy alloys, Scripta Materialia 185 (2020) 152–158. https://doi.org/10.1016/j.scriptamat.2020.04.016.
[59] N. Islam, W. Huang, H.L. Zhuang, Machine learning for phase selection in multi-principal element alloys, Computational Materials Science 150 (2018) 230–235. https://doi.org/10.1016/j.commatsci.2018.04.003.
[60] W. Huang, P. Martin, H.L. Zhuang, Machine-learning phase prediction of high-entropy alloys, Acta Materialia 169 (2019) 225–236. https://doi.org/10.1016/j.actamat.2019.03.012.
[61] Y. Li, W. Guo, Machine-learning model for predicting phase formations of high-entropy alloys, Phys. Rev. Materials 3 (2019) 095005. https://doi.org/10.1103/PhysRevMaterials.3.095005.
[62] Z. Zhou, Y. Zhou, Q. He, Z. Ding, F. Li, Y. Yang, Machine learning guided appraisal and exploration of phase design for high entropy alloys, Npj Comput. Mater. 5 (2019) 1–9. https://doi.org/10.1038/s41524-019-0265-1.
[63] Y. Zhang, C. Wen, C. Wang, S. Antonov, D. Xue, Y. Bai, Y. Su, Phase prediction in high entropy alloys with a rational selection of materials descriptors and machine learning models, Acta Mater. 185 (2020) 528–539. https://doi.org/10.1016/j.actamat.2019.11.067.
[64] U.K. Jaiswal, Y. Vamsi Krishna, M.R. Rahul, G. Phanikumar, Machine learning-enabled identification of new medium to high entropy alloys with solid solution phases, Computational Materials Science 197 (2021) 110623. https://doi.org/10.1016/j.commatsci.2021.110623.
[65] S.Y. Lee, S. Byeon, H.S. Kim, H. Jin, S. Lee, Deep learning-based phase prediction of high-entropy alloys: Optimization, generation, and explanation, Materials & Design 197 (2021) 109260. https://doi.org/10.1016/j.matdes.2020.109260.
[66] A. Roy, G. Balasubramanian, Predictive descriptors in machine learning and data-enabled explorations of high-entropy alloys, Computational Materials Science 193 (2021) 110381. https://doi.org/10.1016/j.commatsci.2021.110381.
[67] J.M. Rickman, H.M. Chan, M.P. Harmer, J.A. Smeltzer, C.J. Marvel, A. Roy, G. Balasubramanian, Materials informatics for the screening of multi-principal elements and high-entropy alloys, Nat. Commun. 10 (2019) 1–10. https://doi.org/10.1038/s41467-019-10533-1.
[68] Y.-J. Chang, C.-Y. Jui, W.-J. Lee, A.-C. Yeh, Prediction of the Composition and Hardness of High-Entropy Alloys by Machine Learning, JOM 71 (2019) 3433–3442. https://doi.org/10.1007/s11837-019-03704-4.
[69] C. Wen, Y. Zhang, C. Wang, D. Xue, Y. Bai, S. Antonov, L. Dai, T. Lookman, Y. Su, Machine learning assisted design of high entropy alloys

with desired property, Acta Mater. 170 (2019) 109–117. https://doi.org/10.1016/j.actamat.2019.03.010.
[70] V. Revi, S. Kasodariya, A. Talapatra, G. Pilania, A. Alankar, Machine learning elastic constants of multi-component alloys, Computational Materials Science 198 (2021) 110671. https://doi.org/10.1016/j.commatsci.2021.110671.
[71] H. Khakurel, M.F.N. Taufique, A. Roy, G. Balasubramanian, G. Ouyang, J. Cui, D.D. Johnson, R. Devanathan, Machine learning assisted prediction of the Young's modulus of compositionally complex alloys, Sci Rep 11 (2021) 17149. https://doi.org/10.1038/s41598-021-96507-0.
[72] C. Yang, C. Ren, Y. Jia, G. Wang, M. Li, W. Lu, A machine learning-based alloy design system to facilitate the rational design of high entropy alloys with enhanced hardness, Acta Materialia 222 (2022) 117431. https://doi.org/10.1016/j.actamat.2021.117431.
[73] L.R. Owen, H.Y. Playford, H.J. Stone, M.G. Tucker, A new approach to the analysis of short-range order in alloys using total scattering, Acta Materialia 115 (2016) 155–166. https://doi.org/10.1016/j.actamat.2016.05.031.
[74] J. Yin, Z. Pei, M.C. Gao, Neural network-based order parameter for phase transitions and its applications in high-entropy alloys, Nat Comput Sci 1 (2021) 686–693. https://doi.org/10.1038/s43588-021-00139-3.
[75] C. Doersch, Tutorial on Variational Autoencoders, arXiv:1606.05908 [Cs, Stat] (2021). http://arxiv.org/abs/1606.05908 (accessed November 26, 2021).
[76] D.P. Kingma, M. Welling, Auto-Encoding Variational Bayes, arXiv:1312.6114 [Cs, Stat] (2014). http://arxiv.org/abs/1312.6114 (accessed November 26, 2021).
[77] C.C. Aggarwal, A. Hinneburg, D.A. Keim, On the Surprising Behavior of Distance Metrics in High Dimensional Space, in: J. Van den Bussche, V. Vianu (Eds.), Database Theory — ICDT 2001, Springer, Berlin, Heidelberg, 2001: pp. 420–434. https://doi.org/10.1007/3-540-44503-X_27.
[78] C. Zhang, M.C. Gao, CALPHAD modeling of high-entropy alloys, in: High-Entropy Alloys, Springer, 2016: pp. 399–444.
[79] P. Singh, A.V. Smirnov, D.D. Johnson, Atomic short-range order and incipient long-range order in high-entropy alloys, Physical Review B 91 (2015) 224204.
[80] P.K. Ray, M. Akinc, M.J. Kramer, Applications of an extended Miedema's model for ternary alloys, Journal of Alloys and Compounds 489 (2010) 357–361.
[81] A.R. Miedema, P.F. De Chatel, F.R. De Boer, Cohesion in alloys—fundamentals of a semi-empirical model, Physica B+ c 100 (1980) 1–28.
[82] D.G. Pettifor, A quantum-mechanical critique of the Miedema rules for alloy formation, in: Solid State Physics, Elsevier, 1987: pp. 43–92.
[83] D. Beniwal, P.K. Ray, Learning phase selection and assemblages in High-Entropy Alloys through a stochastic ensemble-averaging model,

Computational Materials Science 197 (2021) 110647. https://doi.org/10.1016/j.commatsci.2021.110647.
[84] J.M. Rickman, H.M. Chan, M.P. Harmer, J.A. Smeltzer, C.J. Marvel, A. Roy, G. Balasubramanian, Materials informatics for the screening of multi-principal elements and high-entropy alloys, Nat Commun 10 (2019) 1–10. https://doi.org/10.1038/s41467-019-10533-1.
[85] V. Shivam, D. Beniwal, Y. Shadangi, P. Singh, V.S. Hariharan, G. Phanikumar, D.D. Johnson, P.K. Ray, N.K. Mukhopadhyay, Effect of Zn Addition on Phase Selection in AlCrFeCoNiZn High-Entropy Alloy, (2022). https://doi.org/10.2139/ssrn.4263461.
[86] N. Islam, W. Huang, H.L. Zhuang, Machine learning for phase selection in multi-principal element alloys, Computational Materials Science 150 (2018) 230–235. https://doi.org/10.1016/j.commatsci.2018.04.003.
[87] W. Huang, P. Martin, H.L. Zhuang, Machine-learning phase prediction of high-entropy alloys, Acta Materialia 169 (2019) 225–236. https://doi.org/10.1016/j.actamat.2019.03.012.
[88] Y. Li, W. Guo, Machine-learning model for predicting phase formations of high-entropy alloys, Phys. Rev. Materials 3 (2019) 095005. https://doi.org/10.1103/PhysRevMaterials.3.095005.
[89] Z. Zhou, Y. Zhou, Q. He, Z. Ding, F. Li, Y. Yang, Machine learning guided appraisal and exploration of phase design for high entropy alloys, Npj Comput Mater 5 (2019) 1–9. https://doi.org/10.1038/s41524-019-0265-1.
[90] A. Roy, T. Babuska, B. Krick, G. Balasubramanian, Machine learned feature identification for predicting phase and Young's modulus of low-, medium- and high-entropy alloys, Scripta Materialia 185 (2020) 152–158. https://doi.org/10.1016/j.scriptamat.2020.04.016.
[91] Y. Zhang, C. Wen, C. Wang, S. Antonov, D. Xue, Y. Bai, Y. Su, Phase prediction in high entropy alloys with a rational selection of materials descriptors and machine learning models, Acta Materialia 185 (2020) 528–539. https://doi.org/10.1016/j.actamat.2019.11.067.
[92] U.K. Jaiswal, Y. Vamsi Krishna, M.R. Rahul, G. Phanikumar, Machine learning-enabled identification of new medium to high entropy alloys with solid solution phases, Computational Materials Science 197 (2021) 110623. https://doi.org/10.1016/j.commatsci.2021.110623.
[93] S.Y. Lee, S. Byeon, H.S. Kim, H. Jin, S. Lee, Deep learning-based phase prediction of high-entropy alloys: Optimization, generation, and explanation, Materials & Design 197 (2021) 109260. https://doi.org/10.1016/j.matdes.2020.109260.
[94] K. Lee, M.V. Ayyasamy, Y. Ji, P.V. Balachandran, A comparison of explainable artificial intelligence methods in the phase classification of multi-principal element alloys, Sci Rep 12 (2022) 11591. https://doi.org/10.1038/s41598-022-15618-4.
[95] D. Beniwal, P. Singh, S. Gupta, M.J. Kramer, D.D. Johnson, P.K. Ray, Distilling physical origins of hardness in multi-principal element alloys

directly from ensemble neural network models, Npj Comput Mater 8 (2022) 1–11. https://doi.org/10.1038/s41524-022-00842-3.
[96] J. Xiong, S.-Q. Shi, T.-Y. Zhang, Machine learning of phases and mechanical properties in complex concentrated alloys, Journal of Materials Science & Technology 87 (2021) 133–142. https://doi.org/10.1016/j.jmst.2021.01.054.
[97] C. Kim, G. Pilania, R. Ramprasad, From Organized High-Throughput Data to Phenomenological Theory using Machine Learning: The Example of Dielectric Breakdown, Chem. Mater. 28 (2016) 1304–1311. https://doi.org/10.1021/acs.chemmater.5b04109.
[98] R. Ouyang, S. Curtarolo, E. Ahmetcik, M. Scheffler, L.M. Ghiringhelli, SISSO: A compressed-sensing method for identifying the best low-dimensional descriptor in an immensity of offered candidates, Phys. Rev. Materials 2 (2018) 083802. https://doi.org/10.1103/PhysRevMaterials.2.083802.
[99] Y. Wang, N. Wagner, J.M. Rondinelli, Symbolic regression in materials science, MRS Communications 9 (2019) 793–805. https://doi.org/10.1557/mrc.2019.85.
[100] B. Weng, Z. Song, R. Zhu, Q. Yan, Q. Sun, C.G. Grice, Y. Yan, W.-J. Yin, Simple descriptor derived from symbolic regression accelerating the discovery of new perovskite catalysts, Nat Commun 11 (2020) 3513. https://doi.org/10.1038/s41467-020-17263-9.
[101] Z. Guo, S. Hu, Z.-K. Han, R. Ouyang, Improving Symbolic Regression for Predicting Materials Properties with Iterative Variable Selection, J. Chem. Theory Comput. 18 (2022) 4945–4951. https://doi.org/10.1021/acs.jctc.2c00281.
[102] X. Yang, Y. Zhang, Prediction of high-entropy stabilized solid-solution in multi-component alloys, Materials Chemistry and Physics 132 (2012) 233–238. https://doi.org/10.1016/j.matchemphys.2011.11.021.
[103] S. Guo, Q. Hu, C. Ng, C.T. Liu, More than entropy in high-entropy alloys: Forming solid solutions or amorphous phase, Intermetallics 41 (2013) 96–103. https://doi.org/10.1016/j.intermet.2013.05.002.
[104] Z. Wang, Y. Huang, Y. Yang, J. Wang, C.T. Liu, Atomic-size effect and solid solubility of multicomponent alloys, Scripta Materialia 94 (2015) 28–31. https://doi.org/10.1016/j.scriptamat.2014.09.010.
[105] A.K. Singh, N. Kumar, A. Dwivedi, A. Subramaniam, A geometrical parameter for the formation of disordered solid solutions in multi-component alloys, Intermetallics 53 (2014) 112–119. https://doi.org/10.1016/j.intermet.2014.04.019.
[106] Y.F. Ye, Q. Wang, J. Lu, C.T. Liu, Y. Yang, Design of high entropy alloys: A single-parameter thermodynamic rule, Scripta Materialia 104 (2015) 53–55. https://doi.org/10.1016/j.scriptamat.2015.03.023.
[107] M.C. Troparevsky, J.R. Morris, P.R.C. Kent, A.R. Lupini, G.M. Stocks, Criteria for Predicting the Formation of Single-Phase High-Entropy Alloys, Phys. Rev. X 5 (2015) 011041. https://doi.org/10.1103/PhysRevX.5.011041.

[108]O.N. Senkov, D.B. Miracle, A new thermodynamic parameter to predict formation of solid solution or intermetallic phases in high entropy alloys, Journal of Alloys and Compounds 658 (2016) 603–607. https://doi.org/10.1016/j.jallcom.2015.10.279.
[109]D.J.M. King, S.C. Middleburgh, A.G. McGregor, M.B. Cortie, Predicting the formation and stability of single phase high-entropy alloys, Acta Materialia 104 (2016) 172–179. https://doi.org/10.1016/j.actamat.2015.11.040.
[110]J.-H. Li, M.-H. Tsai, Theories for predicting simple solid solution high-entropy alloys: Classification, accuracy, and important factors impacting accuracy, Scripta Materialia 188 (2020) 80–87. https://doi.org/10.1016/j.scriptamat.2020.06.064.
[111]S. Guo, C. Ng, J. Lu, C.T. Liu, Effect of valence electron concentration on stability of fcc or bcc phase in high entropy alloys, Journal of Applied Physics 109 (2011) 103505. https://doi.org/10.1063/1.3587228.
[112]R. Chen, G. Qin, H. Zheng, L. Wang, Y. Su, Y. Chiu, H. Ding, J. Guo, H. Fu, Composition design of high entropy alloys using the valence electron concentration to balance strength and ductility, Acta Materialia 144 (2018) 129–137. https://doi.org/10.1016/j.actamat.2017.10.058.
[113]S. Yang, J. Lu, F. Xing, L. Zhang, Y. Zhong, Revisit the VEC rule in high entropy alloys (HEAs) with high-throughput CALPHAD approach and its applications for material design-A case study with Al–Co–Cr–Fe–Ni system, Acta Materialia 192 (2020) 11–19. https://doi.org/10.1016/j.actamat.2020.03.039.
[114]M. Liu, W. Xu, S. Zhang, Z. Wang, Z. Wang, B. Wang, D. Wang, F. Li, Microstructures and hardnesses of AlCoCr0.5FexNi2.5 high entropy alloys with equal valence electron concentration, Journal of Alloys and Compounds 824 (2020) 153881. https://doi.org/10.1016/j.jallcom.2020.153881.
[115]A.R. Miedema, P.F. de Châtel, F.R. de Boer, Cohesion in alloys — fundamentals of a semi-empirical model, Physica B+C 100 (1980) 1–28. https://doi.org/10.1016/0378-4363(80)90054-6.
[116]R.F. Zhang, S.H. Zhang, Z.J. He, J. Jing, S.H. Sheng, Miedema Calculator: A thermodynamic platform for predicting formation enthalpies of alloys within framework of Miedema's Theory, Computer Physics Communications 209 (2016) 58–69. https://doi.org/10.1016/j.cpc.2016.08.013.
[117]P.K. Ray, M. Akinc, M.J. Kramer, Applications of an extended Miedema's model for ternary alloys, J. Alloys Compd. 489 (2010) 357–361. https://doi.org/10.1016/j.jallcom.2009.07.062.
[118]J.D. Eshelby, The Continuum Theory of Lattice Defects, in: F. Seitz, D. Turnbull (Eds.), Solid State Physics, Academic Press, 1956: pp. 79–144. https://doi.org/10.1016/S0081-1947(08)60132-0.
[119]A. Takeuchi, A. Inoue, Calculations of Amorphous-Forming Composition Range for Ternary Alloy Systems and Analyses of Stabilization of

Amorphous Phase and Amorphous-Forming Ability, Mater. Trans. 42 (2001) 1435–1444. https://doi.org/10.2320/matertrans.42.1435.
[120] M. Wagih, C.A. Schuh, Spectrum of grain boundary segregation energies in a polycrystal, Acta Materialia 181 (2019) 228–237. https://doi.org/10.1016/j.actamat.2019.09.034.
[121] M. Wagih, P.M. Larsen, C.A. Schuh, Learning grain boundary segregation energy spectra in polycrystals, Nature Communications 11 (2020) 6376. https://doi.org/10.1038/s41467-020-20083-6.
[122] R.H. Byrd, P. Lu, J. Nocedal, C. Zhu, A Limited Memory Algorithm for Bound Constrained Optimization, SIAM J. Sci. Comput. 16 (1995) 1190–1208. https://doi.org/10.1137/0916069.
[123] C. Zhu, R.H. Byrd, P. Lu, J. Nocedal, Algorithm 778: L-BFGS-B: Fortran subroutines for large-scale bound-constrained optimization, ACM Trans. Math. Softw. 23 (1997) 550–560. https://doi.org/10.1145/279232.279236.
[124] SciPy Documentation (https://docs.scipy.org/doc/scipy/reference/optimize.minimize-lbfgsb.html#optimize-minimize-lbfgsb), minimize(method='L-BFGS-B') — SciPy v1.8.0 Manual, (n.d.). https://docs.scipy.org/doc/scipy/reference/optimize.minimize-lbfgsb.html#optimize-minimize-lbfgsb (accessed February 13, 2022).
[125] W.-R. Wang, W.-L. Wang, S.-C. Wang, Y.-C. Tsai, C.-H. Lai, J.-W. Yeh, Effects of Al addition on the microstructure and mechanical property of AlxCoCrFeNi high-entropy alloys, Intermetallics 26 (2012) 44–51. https://doi.org/10.1016/j.intermet.2012.03.005.
[126] S. Gao, T. Kong, M. Zhang, X. Chen, Y.W. Sui, Y.J. Ren, J.Q. Qi, F.X. Wei, Y.Z. He, Q.K. Meng, Z. Sun, Effects of titanium addition on microstructure and mechanical properties of CrFeNiTi $_x$ (x = 0.2–0.6) compositionally complex alloys, J. Mater. Res. 34 (2019) 819–828. https://doi.org/10.1557/jmr.2019.40.
[127] P. Singh, A. Sharma, A.V. Smirnov, M.S. Diallo, P.K. Ray, G. Balasubramanian, D.D. Johnson, Design of high-strength refractory complex solid-solution alloys, Npj Comput. Mater. 4 (2018) 1–8. https://doi.org/10.1038/s41524-018-0072-0.
[128] K.R. Broløs, M.V. Machado, C. Cave, J. Kasak, V. Stentoft-Hansen, V.G. Batanero, T. Jelen, C. Wilstrup, An Approach to Symbolic Regression Using Feyn, (2021). https://doi.org/10.48550/arXiv.2104.05417.
[129] P. Singh, S. Gupta, S. Thimmaiah, B. Thoeny, P.K. Ray, A.V. Smirnov, D.D. Johnson, M.J. Kramer, Vacancy-mediated complex phase selection in high entropy alloys, Acta Materialia 194 (2020) 540–546.
[130] J. Schmidt, M.R.G. Marques, S. Botti, M.A.L. Marques, Recent advances and applications of machine learning in solid-state materials science, Npj Comput. Mater. 5 (2019) 1–36. https://doi.org/10.1038/s41524-019-0221-0.

[131]K. Choudhary, B. DeCost, C. Chen, A. Jain, F. Tavazza, R. Cohn, C.W. Park, A. Choudhary, A. Agrawal, S.J.L. Billinge, E. Holm, S.P. Ong, C. Wolverton, Recent advances and applications of deep learning methods in materials science, Npj Comput Mater 8 (2022) 1–26. https://doi.org/10.1038/s41524-022-00734-6.
[132]G.L.W. Hart, T. Mueller, C. Toher, S. Curtarolo, Machine learning for alloys, Nat Rev Mater 6 (2021) 730–755. https://doi.org/10.1038/s41578-021-00340-w.
[133]V. Shivam, D. Beniwal, Y. Shadangi, P. Singh, V.S. Hariharan, G. Phanikumar, D.D. Johnson, P.K. Ray, N.K. Mukhopadhyay, Effect of Zn Addition on Phase Selection in AlCrFeCoNiZn High-Entropy Alloy, SSRN Electronic Journal (Preprint) (2022). https://doi.org/10.2139/ssrn.4263461.
[134]I. Roy, P.K. Ray, G. Balasubramanian, Modeling Oxidation of AlCoCrFeNi High-Entropy Alloy Using Stochastic Cellular Automata, Entropy 24 (2022) 1263. https://doi.org/10.3390/e24091263.
[135]C.D. Taylor, B.M. Tossey, High temperature oxidation of corrosion resistant alloys from machine learning, Npj Mater Degrad 5 (2021) 1–10. https://doi.org/10.1038/s41529-021-00184-3.
[136]N. Birbilis, S. Choudhary, J.R. Scully, M.L. Taheri, A perspective on corrosion of multi-principal element alloys, Npj Mater Degrad 5 (2021) 1–8. https://doi.org/10.1038/s41529-021-00163-8.
[137]A. Roy, M.F.N. Taufique, H. Khakurel, R. Devanathan, D.D. Johnson, G. Balasubramanian, Machine-learning-guided descriptor selection for predicting corrosion resistance in multi-principal element alloys, Npj Mater Degrad 6 (2022) 1–10. https://doi.org/10.1038/s41529-021-00208-y.
[138]S.Kr. Bhattacharya, R. Sahara, T. Narushima, Predicting the Parabolic Rate Constants of High-Temperature Oxidation of Ti Alloys Using Machine Learning, Oxid Met 94 (2020) 205–218. https://doi.org/10.1007/s11085-020-09986-3.
[139]C.J. Bartel, S.L. Millican, A.M. Deml, J.R. Rumptz, W. Tumas, A.W. Weimer, S. Lany, V. Stevanović, C.B. Musgrave, A.M. Holder, Physical descriptor for the Gibbs energy of inorganic crystalline solids and temperature-dependent materials chemistry, Nat Commun 9 (2018) 1–10. https://doi.org/10.1038/s41467-018-06682-4.
[140]C.J. Bartel, A. Trewartha, Q. Wang, A. Dunn, A. Jain, G. Ceder, A critical examination of compound stability predictions from machine-learned formation energies, Npj Comput Mater 6 (2020) 1–11. https://doi.org/10.1038/s41524-020-00362-y.
[141]Y. Liu, T. Zhao, W. Ju, S. Shi, Materials discovery and design using machine learning, J. Materiomics 3 (2017) 159–177. https://doi.org/10.1016/j.jmat.2017.08.002.
[142]Y. Yan, D. Lu, K. Wang, Accelerated discovery of single-phase refractory high entropy alloys assisted by machine learning, Computational

Materials Science 199 (2021) 110723.
https://doi.org/10.1016/j.commatsci.2021.110723.
[143]Y. Iwasaki, I. Takeuchi, V. Stanev, A.G. Kusne, M. Ishida, A. Kirihara, K. Ihara, R. Sawada, K. Terashima, H. Someya, K. Uchida, E. Saitoh, S. Yorozu, Machine-learning guided discovery of a new thermoelectric material, Sci Rep 9 (2019) 2751. https://doi.org/10.1038/s41598-019-39278-z.
[144]K. Kaufmann, D. Maryanovsky, W.M. Mellor, C. Zhu, A.S. Rosengarten, T.J. Harrington, C. Oses, C. Toher, S. Curtarolo, K.S. Vecchio, Discovery of high-entropy ceramics via machine learning, Npj Comput Mater 6 (2020) 1–9. https://doi.org/10.1038/s41524-020-0317-6.
[145]S. Lu, Q. Zhou, L. Ma, Y. Guo, J. Wang, Rapid Discovery of Ferroelectric Photovoltaic Perovskites and Material Descriptors via Machine Learning, Small Methods 3 (2019) 1900360. https://doi.org/10.1002/smtd.201900360.
[146]D. Khatamsaz, B. Vela, P. Singh, D.D. Johnson, D. Allaire, R. Arróyave, Bayesian optimization with active learning of design constraints using an entropy-based approach, Npj Comput Mater 9 (2023) 1–14. https://doi.org/10.1038/s41524-023-01006-7.
[147]B. Vela, C. Acemi, P. Singh, T. Kirk, W. Trehern, E. Norris, D.D. Johnson, I. Karaman, R. Arróyave, High-throughput exploration of the WMoVTaNbAl refractory multi-principal-element alloys under multiple-property constraints, Acta Materialia 248 (2023) 118784. https://doi.org/10.1016/j.actamat.2023.118784.
[148]B. Kailkhura, B. Gallagher, S. Kim, A. Hiszpanski, T.Y.-J. Han, Reliable and explainable machine-learning methods for accelerated material discovery, Npj Comput Mater 5 (2019) 1–9. https://doi.org/10.1038/s41524-019-0248-2.
[149]F. Oviedo, J.L. Ferres, T. Buonassisi, K.T. Butler, Interpretable and Explainable Machine Learning for Materials Science and Chemistry, Acc. Mater. Res. 3 (2022) 597–607. https://doi.org/10.1021/accountsmr.1c00244.
[150]G. Pilania, Machine learning in materials science: From explainable predictions to autonomous design, Computational Materials Science 193 (2021) 110360. https://doi.org/10.1016/j.commatsci.2021.110360.
[151]X. Zhong, B. Gallagher, S. Liu, B. Kailkhura, A. Hiszpanski, T.Y.-J. Han, Explainable machine learning in materials science, Npj Comput Mater 8 (2022) 1–19. https://doi.org/10.1038/s41524-022-00884-7.
[152]Z.C. Lipton, The Mythos of Model Interpretability: In machine learning, the concept of interpretability is both important and slippery., Queue 16 (2018) 31–57. https://doi.org/10.1145/3236386.3241340.
[153]D. Beniwal, P.K. Ray, FCC vs. BCC phase selection in high-entropy alloys via simplified and interpretable reduction of machine learning models, Materialia (2022) 101632. https://doi.org/10.1016/j.mtla.2022.101632.

[154]C.K.H. Borg, C. Frey, J. Moh, T.M. Pollock, S. Gorsse, D.B. Miracle, O.N. Senkov, B. Meredig, J.E. Saal, Expanded dataset of mechanical properties and observed phases of multi-principal element alloys, Sci Data 7 (2020) 430. https://doi.org/10.1038/s41597-020-00768-9.
[155]B. Cantor, Multicomponent high-entropy Cantor alloys, Progress in Materials Science (2020) 100754. https://doi.org/10.1016/j.pmatsci.2020.100754.
[156]S. Guo, C. Ng, Z. Wang, C.T. Liu, Solid solutioning in equiatomic alloys: Limit set by topological instability, Journal of Alloys and Compounds 583 (2014) 410–413. https://doi.org/10.1016/j.jallcom.2013.08.213.
[157]B. Cantor, I.T.H. Chang, P. Knight, A.J.B. Vincent, Microstructural development in equiatomic multicomponent alloys, Materials Science and Engineering: A 375–377 (2004) 213–218. https://doi.org/10.1016/j.msea.2003.10.257.
[158]L. Tang, K. Yan, B. Cai, Y. Wang, B. Liu, S. Kabra, M.M. Attallah, Y. Liu, Deformation mechanisms of FeCoCrNiMo0.2 high entropy alloy at 77 and 15 K, Scripta Materialia 178 (2020) 166–170. https://doi.org/10.1016/j.scriptamat.2019.11.026.
[159]A.-C. Fan, J.-H. Li, M.-H. Tsai, On the phase constituents of three CoCrFeNiX (X = V, Nb, Ta) high-entropy alloys after prolonged annealing, Journal of Alloys and Compounds 823 (2020) 153524. https://doi.org/10.1016/j.jallcom.2019.153524.
[160]C. Dai, T. Zhao, C. Du, Z. Liu, D. Zhang, Effect of molybdenum content on the microstructure and corrosion behavior of FeCoCrNiMox high-entropy alloys, Journal of Materials Science & Technology 46 (2020) 64–73. https://doi.org/10.1016/j.jmst.2019.10.020.
[161]C. Ai, F. He, M. Guo, J. Zhou, Z. Wang, Z. Yuan, Y. Guo, Y. Liu, L. Liu, Alloy design, micromechanical and macromechanical properties of CoCrFeNiTax eutectic high entropy alloys, Journal of Alloys and Compounds 735 (2018) 2653–2662. https://doi.org/10.1016/j.jallcom.2017.12.015.
[162]Y. Cai, S.M. Manladan, Z. Luo, Tribological behaviour of the double FeCoNiCrCux middle-entropy alloy coatings, Surface Engineering 35 (2019) 14–21. https://doi.org/10.1080/02670844.2018.1444548.
[163]J. Cieslak, J. Tobola, K. Berent, M. Marciszko, Phase composition of AlxFeNiCrCo high entropy alloys prepared by sintering and arc-melting methods, Journal of Alloys and Compounds 740 (2018) 264–272. https://doi.org/10.1016/j.jallcom.2017.12.333.
[164]K.A. Christofidou, E.J. Pickering, P. Orsatti, P.M. Mignanelli, T.J.A. Slater, H.J. Stone, N.G. Jones, On the influence of Mn on the phase stability of the CrMnxFeCoNi high entropy alloys, Intermetallics 92 (2018) 84–92. https://doi.org/10.1016/j.intermet.2017.09.011.
[165]U. Dahlborg, J. Cornide, M. Calvo-Dahlborg, T.C. Hansen, Z. Leong, L. Asensio Dominguez, S. Chambreland, A. Cunliffe, R. Goodall, I. Todd, Crystalline structures of some high entropy alloys obtained by neutron

and X-ray diffraction, Acta Physica Polonica A 128 (2015) 552–556. https://doi.org/10.12693/APhysPolA.128.552.
[166]F. Tian, L. Delczeg, N. Chen, L.K. Varga, J. Shen, L. Vitos, Structural stability of NiCoFeCrAl${}_{x}$ high-entropy alloy from ab initio theory, Phys. Rev. B 88 (2013) 085128. https://doi.org/10.1103/PhysRevB.88.085128.
[167]C. Li, J.C. Li, M. Zhao, Q. Jiang, Effect of alloying elements on microstructure and properties of multiprincipal elements high-entropy alloys, Journal of Alloys and Compounds 475 (2009) 752–757. https://doi.org/10.1016/j.jallcom.2008.07.124.
[168]Y.-J. Hsu, W.-C. Chiang, J.-K. Wu, Corrosion behavior of FeCoNiCrCux high-entropy alloys in 3.5% sodium chloride solution, Materials Chemistry and Physics 92 (2005) 112–117. https://doi.org/10.1016/j.matchemphys.2005.01.001.
[169]H.-P. Chou, Y.-S. Chang, S.-K. Chen, J.-W. Yeh, Microstructure, thermophysical and electrical properties in AlxCoCrFeNi (0≤x≤2) high-entropy alloys, Materials Science and Engineering: B 163 (2009) 184–189. https://doi.org/10.1016/j.mseb.2009.05.024.
[170]P. Singh, A. Sharma, A.V. Smirnov, M.S. Diallo, P.K. Ray, G. Balasubramanian, D.D. Johnson, Design of high-strength refractory complex solid-solution alloys, Npj Computational Materials 4 (2018) 1–8. https://doi.org/10.1038/s41524-018-0072-0.
[171]Y. Zhang, Y.J. Zhou, J.P. Lin, G.L. Chen, P.K. Liaw, Solid-Solution Phase Formation Rules for Multi-component Alloys, Advanced Engineering Materials 10 (2008) 534–538. https://doi.org/10.1002/adem.200700240.
[172]F.E. Wang, Bonding theory for metals and alloys, 1. ed, Elsevier, Amsterdam, 2005.
[173]J.D. Eshelby, The Continuum Theory of Lattice Defects, in: F. Seitz, D. Turnbull (Eds.), Solid State Physics, Academic Press, 1956: pp. 79–144. https://doi.org/10.1016/S0081-1947(08)60132-0.
[174]J. Friedel, Electronic structure of primary solid solutions in metals, Advances in Physics 3 (1954) 446–507. https://doi.org/10.1080/00018735400101233.
[175]R.F. Zhang, S.H. Zhang, Z.J. He, J. Jing, S.H. Sheng, Miedema Calculator: A thermodynamic platform for predicting formation enthalpies of alloys within framework of Miedema's Theory, Computer Physics Communications 209 (2016) 58–69. https://doi.org/10.1016/j.cpc.2016.08.013.
[176]O.N. Senkov, G.B. Wilks, J.M. Scott, D.B. Miracle, Mechanical properties of Nb25Mo25Ta25W25 and V20Nb20Mo20Ta20W20 refractory high entropy alloys, Intermetallics 19 (2011) 698–706. https://doi.org/10.1016/j.intermet.2011.01.004.
[177]P. Singh, A.V. Smirnov, D.D. Johnson, Atomic short-range order and incipient long-range order in high-entropy alloys, Phys. Rev. B 91 (2015) 224204. https://doi.org/10.1103/PhysRevB.91.224204.

[178]A. Ferrari, F. Körmann, M. Asta, J. Neugebauer, Simulating short-range order in compositionally complex materials, Nat Comput Sci 3 (2023) 221–229. https://doi.org/10.1038/s43588-023-00407-4.
[179]T. Abe, Effect of Short-Range Ordering in High-Entropy Alloys, Materials Transactions 62 (2021) 711–718. https://doi.org/10.2320/matertrans.MT-M2021022.
[180]J.M. Cowley, An Approximate Theory of Order in Alloys, Phys. Rev. 77 (1950) 669–675. https://doi.org/10.1103/PhysRev.77.669.
[181]J.M. Cowley, Short-Range Order and Long-Range Order Parameters, Phys. Rev. 138 (1965) A1384–A1389. https://doi.org/10.1103/PhysRev.138.A1384.
[182]Y. Rao, W.A. Curtin, Analytical models of short-range order in FCC and BCC alloys, Acta Mater. 226 (2022) 117621. https://doi.org/10.1016/j.actamat.2022.117621.
[183]S. Chen, Z.H. Aitken, S. Pattamatta, Z. Wu, Z.G. Yu, R. Banerjee, D.J. Srolovitz, P.K. Liaw, Y.-W. Zhang, Chemical-Affinity Disparity and Exclusivity Drive Atomic Segregation, Short-Range Ordering, and Cluster Formation in High-Entropy Alloys, Acta Materialia 206 (2021) 116638. https://doi.org/10.1016/j.actamat.2021.116638.
[184]B. Cantor, Multicomponent high-entropy Cantor alloys, Prog. Mater. Sci. 120 (2021) 100754. https://doi.org/10.1016/j.pmatsci.2020.100754.
[185]D. Ma, B. Grabowski, F. Körmann, J. Neugebauer, D. Raabe, Ab initio thermodynamics of the CoCrFeMnNi high entropy alloy: Importance of entropy contributions beyond the configurational one, Acta Mater. 100 (2015) 90–97. https://doi.org/10.1016/j.actamat.2015.08.050.
[186]P. Singh, S. Gupta, S. Thimmaiah, B. Thoeny, P.K. Ray, A.V. Smirnov, D.D. Johnson, M.J. Kramer, Vacancy-mediated complex phase selection in high entropy alloys, Acta Mater. 194 (2020) 540–546. https://doi.org/10.1016/j.actamat.2020.04.063.
[187]L. Himanen, A. Geurts, A.S. Foster, P. Rinke, Data-Driven Materials Science: Status, Challenges, and Perspectives, Adv. Sci. 6 (2019) 1900808. https://doi.org/10.1002/advs.201900808.
[188]J. Schmidt, M.R.G. Marques, S. Botti, M.A.L. Marques, Recent advances and applications of machine learning in solid-state materials science, Npj Comput. Mater. 5 (2019) 1–36. https://doi.org/10.1038/s41524-019-0221-0.
[189]K.T. Butler, D.W. Davies, H. Cartwright, O. Isayev, A. Walsh, Machine learning for molecular and materials science, Nature 559 (2018) 547–555. https://doi.org/10.1038/s41586-018-0337-2.
[190]R. Ramprasad, R. Batra, G. Pilania, A. Mannodi-Kanakkithodi, C. Kim, Machine learning in materials informatics: recent applications and prospects, Npj Comput. Mater. 3 (2017) 1–13. https://doi.org/10.1038/s41524-017-0056-5.
[191]J.J. de Pablo, N.E. Jackson, M.A. Webb, L.-Q. Chen, J.E. Moore, D. Morgan, R. Jacobs, T. Pollock, D.G. Schlom, E.S. Toberer, J. Analytis, I. Dabo, D.M. DeLongchamp, G.A. Fiete, G.M. Grason, G. Hautier, Y. Mo,

K. Rajan, E.J. Reed, E. Rodriguez, V. Stevanovic, J. Suntivich, K. Thornton, J.-C. Zhao, New frontiers for the materials genome initiative, Npj Comput. Mater. 5 (2019) 1–23. https://doi.org/10.1038/s41524-019-0173-4.

[192] Y. Dong, Y. Lu, J. Kong, J. Zhang, T. Li, Microstructure and mechanical properties of multi-component AlCrFeNiMox high-entropy alloys, J. Alloys Compd. 573 (2013) 96–101. https://doi.org/10.1016/j.jallcom.2013.03.253.

[193] J.M. Rickman, H.M. Chan, M.P. Harmer, J.A. Smeltzer, C.J. Marvel, A. Roy, G. Balasubramanian, Materials informatics for the screening of multi-principal elements and high-entropy alloys, Nat Commun 10 (2019) 1–10. https://doi.org/10.1038/s41467-019-10533-1.

[194] Y.-J. Chang, C.-Y. Jui, W.-J. Lee, A.-C. Yeh, Prediction of the Composition and Hardness of High-Entropy Alloys by Machine Learning, JOM 71 (2019) 3433–3442. https://doi.org/10.1007/s11837-019-03704-4.

[195] F.-Z. Dai, B. Wen, Y. Sun, H. Xiang, Y. Zhou, Theoretical prediction on thermal and mechanical properties of high entropy (Zr0.2Hf0.2Ti0.2Nb0.2Ta0.2)C by deep learning potential, Journal of Materials Science & Technology (2020). https://doi.org/10.1016/j.jmst.2020.01.005.

[196] G. Kim, H. Diao, C. Lee, A.T. Samaei, T. Phan, M. de Jong, K. An, D. Ma, P.K. Liaw, W. Chen, First-principles and machine learning predictions of elasticity in severely lattice-distorted high-entropy alloys with experimental validation, Acta Materialia 181 (2019) 124–138. https://doi.org/10.1016/j.actamat.2019.09.026.

[197] C. Wen, Y. Zhang, C. Wang, D. Xue, Y. Bai, S. Antonov, L. Dai, T. Lookman, Y. Su, Machine learning assisted design of high entropy alloys with desired property, Acta Materialia 170 (2019) 109–117. https://doi.org/10.1016/j.actamat.2019.03.010.

[198] K. Lee, M.V. Ayyasamy, P. Delsa, T.Q. Hartnett, P.V. Balachandran, Phase classification of multi-principal element alloys via interpretable machine learning, Npj Comput Mater 8 (2022) 1–12. https://doi.org/10.1038/s41524-022-00704-y.

[199] E.P. George, D. Raabe, R.O. Ritchie, High-entropy alloys, Nature Reviews Materials 4 (2019) 515–534. https://doi.org/10.1038/s41578-019-0121-4.

[200] M.Z. Ghomsheh, G. Khatibi, B. Weiss, M. Lederer, S. Schwarz, A. Steiger-Thirsfeld, M.A. Tikhonovsky, E.D. Tabachnikova, E. Schafler, High cycle fatigue deformation mechanisms of a single phase CrMnFeCoNi high entropy alloy, Materials Science and Engineering: A 777 (2020) 139034. https://doi.org/10.1016/j.msea.2020.139034.

[201] Q. Rizzardi, G. Sparks, R. Maaß, Fast Slip Velocity in a High-Entropy Alloy, JOM 70 (2018) 1088–1093. https://doi.org/10.1007/s11837-018-2856-6.

[202] T. Borkar, B. Gwalani, D. Choudhuri, C.V. Mikler, C.J. Yannetta, X. Chen, R.V. Ramanujan, M.J. Styles, M.A. Gibson, R. Banerjee, A

combinatorial assessment of AlxCrCuFeNi2 (0 < x < 1.5) complex concentrated alloys: Microstructure, microhardness, and magnetic properties, Acta Materialia 116 (2016) 63–76. https://doi.org/10.1016/j.actamat.2016.06.025.

[203]Z. Li, K.G. Pradeep, Y. Deng, D. Raabe, C.C. Tasan, Metastable high-entropy dual-phase alloys overcome the strength–ductility trade-off, Nature 534 (2016) 227–230. https://doi.org/10.1038/nature17981.

[204]E. Ma, X. Wu, Tailoring heterogeneities in high-entropy alloys to promote strength–ductility synergy, Nature Communications 10 (2019) 5623. https://doi.org/10.1038/s41467-019-13311-1.

[205]I. Basu, V. Ocelík, J.ThM. De Hosson, BCC-FCC interfacial effects on plasticity and strengthening mechanisms in high entropy alloys, Acta Materialia 157 (2018) 83–95. https://doi.org/10.1016/j.actamat.2018.07.031.

[206]J.Y. He, H. Wang, H.L. Huang, X.D. Xu, M.W. Chen, Y. Wu, X.J. Liu, T.G. Nieh, K. An, Z.P. Lu, A precipitation-hardened high-entropy alloy with outstanding tensile properties, Acta Materialia 102 (2016) 187–196. https://doi.org/10.1016/j.actamat.2015.08.076.

[207]H. Lee, W.Y. Huen, V. Vimonsatit, P. Mendis, An Investigation of Nanomechanical Properties of Materials using Nanoindentation and Artificial Neural Network, Scientific Reports 9 (2019) 13189. https://doi.org/10.1038/s41598-019-49780-z.

[208]W.A. Saidi, W. Shadid, I.E. Castelli, Machine-learning structural and electronic properties of metal halide perovskites using a hierarchical convolutional neural network, Npj Computational Materials 6 (2020) 1–7. https://doi.org/10.1038/s41524-020-0307-8.

[209]A. Cecen, H. Dai, Y.C. Yabansu, S.R. Kalidindi, L. Song, Material structure-property linkages using three-dimensional convolutional neural networks, Acta Materialia 146 (2018) 76–84. https://doi.org/10.1016/j.actamat.2017.11.053.

[210]Y. Liu, T. Zhao, W. Ju, S. Shi, Materials discovery and design using machine learning, Journal of Materiomics 3 (2017) 159–177. https://doi.org/10.1016/j.jmat.2017.08.002.

[211]S. Gorsse, M.H. Nguyen, O.N. Senkov, D.B. Miracle, Database on the mechanical properties of high entropy alloys and complex concentrated alloys, Data in Brief 21 (2018) 2664–2678. https://doi.org/10.1016/j.dib.2018.11.111.

[212]D.D. Johnson, D.M. Nicholson, F.J. Pinski, B.L. Gyorffy, G.M. Stocks, Density-functional theory for random alloys: total energy within the coherent-potential approximation, Physical Review Letters 56 (1986) 2088.

[213]A.R. Miedema, P.F. de Châtel, F.R. de Boer, Cohesion in alloys — fundamentals of a semi-empirical model, Physica B+C 100 (1980) 1–28. https://doi.org/10.1016/0378-4363(80)90054-6.

[214] P.K. Ray, M. Akinc, M.J. Kramer, Applications of an extended Miedema's model for ternary alloys, Journal of Alloys and Compounds 489 (2010) 357–361. https://doi.org/10.1016/j.jallcom.2009.07.062.
[215] J.-W. Yeh, S.-J. Lin, T.-S. Chin, J.-Y. Gan, S.-K. Chen, T.-T. Shun, C.-H. Tsau, S.-Y. Chou, Formation of simple crystal structures in Cu-Co-Ni-Cr-Al-Fe-Ti-V alloys with multiprincipal metallic elements, Metall and Mat Trans A 35 (2004) 2533–2536. https://doi.org/10.1007/s11661-006-0234-4.
[216] Y. LeCun, Y. Bengio, G. Hinton, Deep learning, Nature 521 (2015) 436–444. https://doi.org/10.1038/nature14539.
[217] S. Guo, C.T. Liu, Phase stability in high entropy alloys: Formation of solid-solution phase or amorphous phase, Progress in Natural Science: Materials International 21 (2011) 433–446. https://doi.org/10.1016/S1002-0071(12)60080-X.
[218] J.P. Perdew, K. Burke, M. Ernzerhof, Generalized gradient approximation made simple, Physical Review Letters 77 (1996) 3865.
[219] J. Ding, Q. Yu, M. Asta, R.O. Ritchie, Tunable stacking fault energies by tailoring local chemical order in CrCoNi medium-entropy alloys, Proceedings of the National Academy of Sciences 115 (2018) 8919–8924.
[220] P. Singh, A.V. Smirnov, D.D. Johnson, Ta-Nb-Mo-W refractory high-entropy alloys: anomalous ordering behavior and its intriguing electronic origin, Physical Review Materials 2 (2018) 055004.
[221] S.-H. Jhi, J. Ihm, S.G. Louie, M.L. Cohen, Electronic mechanism of hardness enhancement in transition-metal carbonitrides, Nature 399 (1999) 132–134.
[222] P. Singh, D. Sauceda, R. Arroyave, The effect of chemical disorder on defect formation and migration in disordered max phases, Acta Materialia 184 (2020) 50–58.
[223] M. Zhang, Y. Ma, W. Dong, X. Liu, Y. Lu, Y. Zhang, R. Li, Y. Wang, P. Yu, Y. Gao, G. Li, Phase evolution, microstructure, and mechanical behaviors of the CrFeNiAlxTiy medium-entropy alloys, Materials Science and Engineering: A 771 (2020) 138566. https://doi.org/10.1016/j.msea.2019.138566.
[224] S. Gao, T. Kong, M. Zhang, X. Chen, Y.W. Sui, Y.J. Ren, J.Q. Qi, F.X. Wei, Y.Z. He, Q.K. Meng, Z. Sun, Effects of titanium addition on microstructure and mechanical properties of CrFeNiTi $_x$ (x = 0.2–0.6) compositionally complex alloys, J. Mater. Res. 34 (2019) 819–828. https://doi.org/10.1557/jmr.2019.40.
[225] H. Ma, C.H. Shek, Effects of Hf on the microstructure and mechanical properties of CoCrFeNi high entropy alloy, Journal of Alloys and Compounds 827 (2020) 154159. https://doi.org/10.1016/j.jallcom.2020.154159.
[226] C. Xiang, H.M. Fu, Z.M. Zhang, E.-H. Han, H.F. Zhang, J.Q. Wang, G.D. Hu, Effect of Cr content on microstructure and properties of Mo0.5VNbTiCrx high-entropy alloys, Journal of Alloys and Compounds 818 (2020) 153352. https://doi.org/10.1016/j.jallcom.2019.153352.

[227]P. Singh, A.V. Smirnov, A. Alam, D.D. Johnson, First-principles prediction of incipient order in arbitrary high-entropy alloys: exemplified in Ti0.25CrFeNiAlx, Acta Materialia 189 (2020) 248–254. https://doi.org/10.1016/j.actamat.2020.02.063.
[228]W.-R. Wang, W.-L. Wang, S.-C. Wang, Y.-C. Tsai, C.-H. Lai, J.-W. Yeh, Effects of Al addition on the microstructure and mechanical property of AlxCoCrFeNi high-entropy alloys, Intermetallics 26 (2012) 44–51. https://doi.org/10.1016/j.intermet.2012.03.005.
[229]A. Roy, P. Sreeramagiri, T. Babuska, B. Krick, P.K. Ray, G. Balasubramanian, Lattice distortion as an estimator of solid solution strengthening in high-entropy alloys, Mater. Charact. 172 (2021) 110877. https://doi.org/10.1016/j.matchar.2021.110877.
[230]Q. Ding, Y. Zhang, X. Chen, X. Fu, D. Chen, S. Chen, L. Gu, F. Wei, H. Bei, Y. Gao, M. Wen, J. Li, Z. Zhang, T. Zhu, R.O. Ritchie, Q. Yu, Tuning element distribution, structure and properties by composition in high-entropy alloys, Nature 574 (2019) 223–227. https://doi.org/10.1038/s41586-019-1617-1.
[231]S. Bajpai, B.E. MacDonald, T.J. Rupert, H. Hahn, E.J. Lavernia, D. Apelian, Recent progress in the CoCrNi alloy system, Materialia 24 (2022) 101476. https://doi.org/10.1016/j.mtla.2022.101476.
[232]B. Gludovatz, A. Hohenwarter, D. Catoor, E.H. Chang, E.P. George, R.O. Ritchie, A fracture-resistant high-entropy alloy for cryogenic applications, Science 345 (2014) 1153–1158. https://doi.org/10.1126/science.1254581.
[233]N. Derimow, T. Clark, C. Roach, S. Mathaudhu, R. Abbaschian, Processing pathway effects in CoCrCuNi+X (Fe, Mn) high-entropy alloys, Philosophical Magazine 99 (2019) 1899–1913. https://doi.org/10.1080/14786435.2019.1616121.
[234]B.H. Toby, R.B. Von Dreele, GSAS-II: the genesis of a modern open-source all purpose crystallography software package, J Appl Cryst 46 (2013) 544–549. https://doi.org/10.1107/S0021889813003531.
[235]D. Beniwal, V. Shivam, O. Palasyuk, M.J. Kramer, G. Phanikumar, P.K. Ray, EDS-PhaSe: Phase Segmentation and Analysis from EDS Elemental Map Images Using Markers of Elemental Segregation, Metallogr. Microstruct. Anal. (2023). https://doi.org/10.1007/s13632-023-01020-7.
[236]A.K. Niessen, A.R. Miedema, F.R. de Boer, R. Boom, Enthalpies of formation of liquid and solid binary alloys based on 3d metals: V. Alloys of nickel, Physica B: Condensed Matter 152 (1988) 303–346. https://doi.org/10.1016/0921-4526(88)90002-6.
[237]L. Kaufman, H. Bernstein, Computer calculation of phase diagrams With special reference to refractory metals, Academic Press Inc, United States, 1970.
[238]G. Guisbiers, S. Khanal, F. Ruiz-Zepeda, J.R. de la Puente, M. José-Yacaman, Cu–Ni nano-alloy: mixed, core–shell or Janus nano-particle?, Nanoscale 6 (2014) 14630–14635. https://doi.org/10.1039/C4NR05739B.

[239] C. Zhou, L. Zhou, M. Li, Y. Tong, Z. Zhou, Microstructure and mechanical properties of multi-principal component CoCrNiMo medium entropy alloys, Materials Today Communications 38 (2024) 108180. https://doi.org/10.1016/j.mtcomm.2024.108180.

Appendix A

MAPAL: A python library for mapping features and properties of alloys over compositional spaces

A.1 Introduction

Alloy design involves mixing of multiple elements together to get improved or unique properties. The alloy composition controls the type and extent of atomic interactions as well as the phases that are possible in an alloy; and thus, compositional tuning is a critical part of any alloy design process. While deciding the composition, a preliminary conceptualization of the expected alloy properties often requires extension of elemental properties to the alloy composition space. The perfect example is Hume-Rothery rules that provide approximate conditions for formation of solid-solutions in binary alloys based on the individual elemental properties viz. atomic size, crystal structure, electronegativity and valency. Similarly, for compositionally complex alloys (CCAs), we have highlighted in previous chapters various composition-based features that play a significant role in phase selection and hardness. Thus, despite the simplistic nature of such composition-based metrics, their relevance and importance in alloy design has been cemented by a plethora of empirical, semi-empirical and machine learning models that have been successfully

---

D Beniwal and PK Ray, MAPAL: A python library for mapping features and properties of alloys over compositional spaces, **Under preparation**

deployed to predict the phase selection, mechanical properties and oxidation behaviour in a wide-variety of materials. With this in mind, we have built **MAPAL** (**Map**ping **Al**loys) as a tool to assist the compositional design of alloys through three key implementations: (a) mapping of alloy features to a variety of compositional regimes within binary, ternary and multi-component alloy systems, (b) parametrizing alloy compositions into a wide variety of physical and thermodynamic descriptors that act as input for machine learning models, and (c) mapping of alloy properties such as hardness, phase selection and yield strength over compositional spaces using pre-trained models. **MAPAL** is distributed as an open-source Python library that can be easily integrated with machine learning workflows and can thus be used for both creating new ML models as well as using trained models for exploration of new compositional spaces.

A.2 Design methodology and programming environment

As **MAPAL** predominantly focuses on compositional mapping, we elaborate here the nuances associated with how the alloy composition is represented in **MAPAL**. An alloy is represented by a 'string' variable for alloy name which captures its composition. This string consists of a sequence of elements wherein each element is followed by a number suffix that denotes its stoichiometry. If an element does not have a numeric suffix, stoichiometry of '1' is assumed for that element. This terminology is in line with the commonly used representation for compounds and CCAs. Some examples are:

- 'AlTi', 'Al1Ti1', 'Al50Ti50' are equivalent and represent an equiatomic binary alloy of Al and Ti; whereas 'Al2Ti' or 'AlTi0.5' or 'Al66.6Ti33.3' represent a binary alloy where the number of atoms of Al : Ti are in a ratio of 2 : 1
- 'CoCrFeNi' or 'Co1Cr1Fe1Ni1' is an equiatomic quaternary whereas 'CoCr2FeNi2.5' is a quaternary alloy where number of atoms of (Co : Cr : Fe : Ni) are present in a ratio of (1 : 2 : 1 : 2.5)

MAPAL library comprises several packages and Figure A.1 shows the schematic flowchart of how the features or ML predicted properties are mapped either to user-defined compositional regimes (Figure A.1a) or to a list of alloy compositions (Figure A.1b) that are being used for training new ML models.

MAPAL was developed using Python | 3.10.2 and has been tested on Windows 10, 11 and Ubuntu 20.04. For different functionalities, it uses following open-source python libraries: numpy | 1.26.1, pandas | 2.1.2, tqdm | 4.66.1, tensorflow | 2.8.0, matplotlib | 3.8.0, plotly | 5.18.0, scikit-image | 0.22.0.

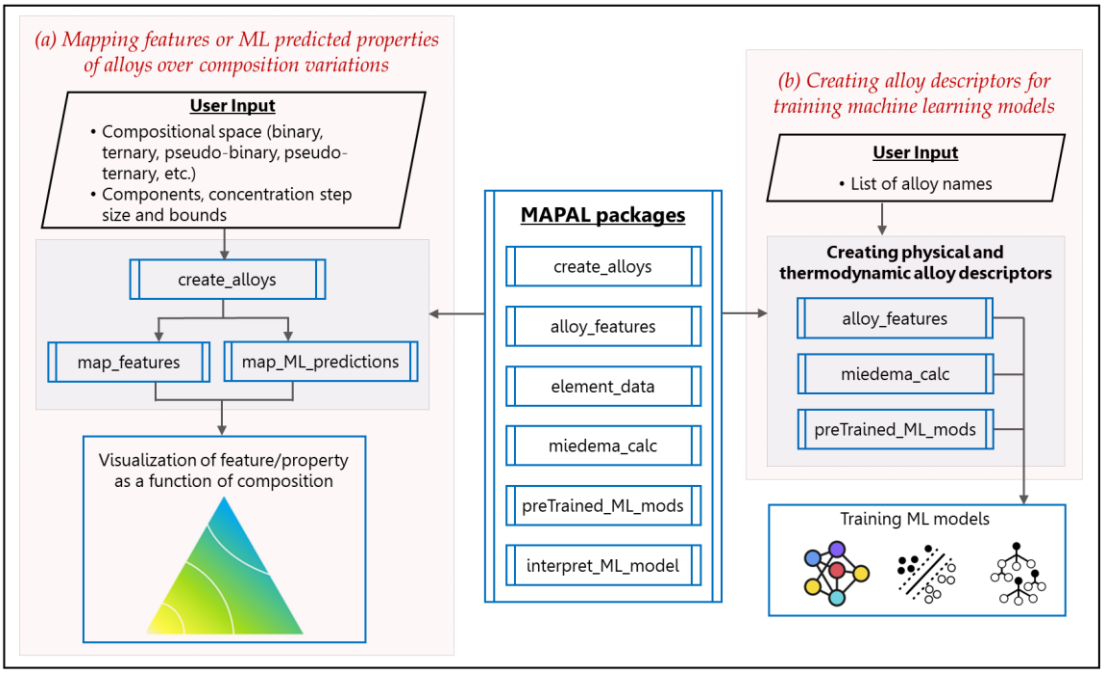

Figure A.1 Flowchart showing the use of MAPAL packages for: (a) mapping features or machine learning predictions as a function of composition, and (b) creating alloy descriptors for training machine learning models.

A.3 MAPAL packages

MAPAL contains different packages with dedicated functionalities. While the implementation of each package has been detailed (with examples) in the documentation, we briefly describe each package here to highlight its contents and usage.

A.3.1 mapal.element_data

MAPAL contains an in-built database of elemental properties that are used for calculating alloy features. The parameters for implementation of Miedema's model (§A.3.4) are also included in this database. The element properties currently available are listed in Table A.1 along with their '*prop_key*' which is used to call any property from the database. Since new workflows may require customization of the element database, the user can both update the values as well as add new element properties to the in-built database by following a simple process shown in the documentation. The key functions available in the '*element_data*' package are:

- *mapal.element_data.**el_properties**()*: prints list of all properties available in the element database
- *mapal.element_data.**el_prop_info**(prop_key)*: prints the information about any particular '*prop_key*'
- *mapal.element_data.**get_el_property**(el, prop_key)*: returns the value of property '*prop_key*' for element '*el*'

A.3.2 mapal.create_alloys

A pre-requisite for mapping features over compositions is to have a functionality that can create the compositional space in the first place. This role is filled by the '*create_alloys*' package in **MAPAL**. A compositional space represents a map of the concentration of alloy components. In a true binary and ternary system, each component is a single element e.g., Al_xTi_{1-x} or $Al_xTi_yZr_{1-x-y}$, whereas in a pseudo binary or ternary system, the components can be a stoichiometric combination of multiple elements e.g., $(Al)_x(Ti2Zr)_{1-x}$ or $(AlNi)_x(TiZr)_y(MoNb)_{1-x-y}$. Thus, to enable creation of both true as well as pseudo binary/ternary systems, the components can be defined as either a single element (e.g., A='Al', B='Ti') or a stoichiometric combination of multiple elements (e.g., A='AlNi', B='Ti2Zr'). It should be noted that the inputs/outputs for compositions and composition step sizes in '*create_alloys*' are represented in atomic fraction units (and not in atomic percent). The key functions available

Table A.1 List of element properties available in the built-in element database of MAPAL library.

#	Element property (prop_key)	#	Element property (prop_key)
1	Crystal structure (crys_struct)	13	Valence electron count (VEC)
2	Work function (phi_workFunc)	14	Pauling Electronegativity (EN_Pauling)
3	Electron density at Wigner-Seitz cell boundary (nWS)	15	Allen Electronegativity (EN_Allen)
4	Molar volume (Vm)	16	Density (density_S)
5	Elastic modulus (E)	17	Melting temperature (Tm)
6	Shear modulus (G)	18	Cohesive energy (Coh_E)
7	Bulk modulus (K)	19	Compressibility (Compressibility)
8	Surface energy (Sf_E)	20	Number of unpaired electrons (n_unpaired)
9	Vacancy formation energy (Hf_vac)	21	Spin magnetic moment (spin_mag_moment)
10	R/P ratio in Miedema's model (R_P_ratio)	22	Vickers hardness number (VHN)
11	Metallic radius (r_met)	23	Poisson number (poisson_num)
12	Covalent radius (r_cov)		

in '*create_alloys*' package are:

- *mapal.create_alloys.**binary**(A, B, dc=0.01, cAmin=0, cAmax=1)*: creates alloy compositions for a A_xB_{1-x} binary system with a composition (atomic fraction) step size of '*dc*' (default=0.01). The lower and upper bounds for concentration of component *A* are '*cAmin*' (default=0) and '*cAmax*' (default=1)
- *mapal.create_alloys.**ternary**(A, B, C, dc=0.01)*: creates alloy compositions for a $A_xB_yC_{1-x-y}$ ternary system with a composition (atomic fraction) step size of '*dc*' (default=0.01)
- *mapal.create_alloys.**ternary_1Cfixed**(A, B, C, Cfix, dc=0.01, cAmin=0, cAmax='')*: creates alloy compositions for a $A_xB_{1-x}C_{Cfix}$ ternary system with a composition (atomic fraction) step size of '*dc*' (default=0.01). The

concentration (atomic fraction) of component *C* is fixed as '*Cfix*'. The lower and upper bounds for concentration of component A are '*cAmin*' (default=0) and '*cAmax*' (default=1 – *Cfix*)

- *mapal.create_alloys.**equiatomic_alloys**(el_list, n_el)*: creates all possible equiatomic compositions containing '*n_el*' number of elements from the '*el_list*' list of elements
- *mapal.create_alloys.**all_possible_compositions**(el_list, dc=0.01, cmin=0.0)*: creates all possible compositions from '*el_list*' list of elements with a composition (atomic fraction) step size of '*dc*' (default=0.01). The minimum possible concentration of any element is '*cmin*' (default=0)

A.3.3 mapal.alloy_features

One of the primary goals behind development of **MAPAL** is to enable creation of alloy features over compositional space. While the compositional space (alloy compositions) is created using '*create_alloys*' package, the parametrization of these compositions into alloy descriptors is achieved through '*alloy_features*' package. There are two methodologies for creating features:

a) *Operator-based features*: An operator mutates the properties of constituent elements based on the alloy composition to create an alloy feature. An operator represents just the mathematical function and thus, when creating operator-based features, user must also provide the element property ('prop_key' from Table A.1) to which the operator will be applied. The operators available in **MAPAL** are listed in Table A.2 along with their mathematical expression and '*operator_key*' that is used to call a specific operator function.

b) *Defined features*: These are strictly defined functions that require only the alloy composition as an input. The defined features available in **MAPAL** are listed in Table A.3 along with their mathematical expression and '*feature_key*' that is used to call them.

The key functions available in '*alloy_features*' package are:

- *mapal.alloy_features.**list_operators()***: returns list of operators available to mutate elemental properties to alloy features
- *mapal.alloy_features.**list_features()***: returns list of defined features available in **MAPAL**
- *mapal.alloy_features.**get_feat_value**(alloy_list, feature)*: serves as a single access function to calculate all the features available in **MAPAL** for a list of alloys ('*alloy_list*'). If the feature to be calculated is an operator-based feature (Table A.2), then '*feature*' is defined as a tuple of *('operator_key', 'el_prop')*. For example, composition weighted average VEC will be expressed as *feature = ('comp_avg', 'VEC')*. If the feature is a defined feature (Table A.3), then '*feature*' is defined simply as the '*feature_key*'; for example, configurational entropy will be expressed as *feature* = '*S_config*'
- *mapal.alloy_features.**get_comp_dict**(alloy_name)*: converts alloy name string ('*alloy_name*') into a dictionary containing alloy composition

A.3.4 mapal.miedema_calc

MAPAL contains an in-built Miedema calculator that implements Miedema's model [1,2] to calculate the chemical and elastic enthalpy of mixing associated with mixing of two elements. While the original Miedema's model was built for binary alloys only, the Miedema calculator in **MAPAL** extends it to multi-component alloys using the extended regular solution model [3].

Despite the simplistic nature of Miedema's model, owing to the use of a macroscopic atom picture that is not backed by quantum mechanics, it has been widely used due to its – (a) good agreement with the experimental mixing enthalpy values for binary alloys, and (b) ease of implementation in calculating enthalpy estimates that can act as a feature for data-driven models. In fact, over the last decade (including the work in this thesis), Miedema's enthalpy values have featured as key variables in many empirical, semi-empirical and ML models for CCAs. Since the Miedema's approach has been documented

Table A.2 List of operator-based features available in MAPAL. The operator-based features use the alloy composition to mutate any element property X (extracted from in-built element database) into an alloy feature. The calculation of these features requires two inputs – (i) alloy composition, and (ii) the elemental property to be transformed (X). They 'operator_key' for each feature represents the notation using which it can be called in MAPAL.

#	Operator based features	operator_key	Mathematical expression
1	Composition weighted average	comp_avg	$\bar{X} = \sum_{i=1}^{N} c_i X_i$
2	Asymmetry	asymmetry	$\delta_X = \sqrt{\sum_{i=1}^{N} c_i \left(1 - \frac{X_i}{\bar{X}}\right)^2}$
3	Local mismatch	local_mismatch	$\mathrm{LM}_X = \sum_{i=1}^{N} \sum_{j=1, j\neq i}^{N} c_i c_j \lvert X_i - X_j \rvert$
4	Square difference	sqdiff	$\mathrm{SD}_X = \sqrt{\sum_{i=1}^{N} c_i (X_i - \bar{X})^2}$
5	Modulus mismatch	modulus_mismatch	$\eta_X = \sum_{i=1}^{N} \left(\frac{c_i \frac{2(X_i - \bar{X})}{X_i + \bar{X}}}{1 + 0.5\left(c_i \frac{2(X_i - \bar{X})}{X_i + \bar{X}}\right)} \right)$

Table A.3 List of defined features available in MAPAL. The calculation of these features requires only the alloy composition as an input and the relevant elemental properties are extracted automatically from the built-in element database. They 'feature_key' for each feature represents the notation using which it can be called in MAPAL.

#	Defined features	feature_key	Mathematical expression
1	Configurational entropy of mixing	S_config	$\Delta S^{config} = -R \sum_{i=1}^{N} c_i \log(c_i)$
2	Singh's geometrical parameter	Singh_parameter	$\Lambda = \frac{\Delta S^{config}}{(\delta_r)^2}$
3	Wang's geometrical parameter	Wang_parameter	$\gamma = \frac{1 - \sqrt{1 - \left(\frac{\bar{r}}{r_S + \bar{r}}\right)^2}}{1 - \sqrt{1 - \left(\frac{\bar{r}}{r_L + \bar{r}}\right)^2}}$
4	Lattice distortion energy	latt_dist_energy	$\mu = 0.5\, \bar{E}\, \delta_r$
5	Energy term in alloy strengthening model	energy_strength_model	$A = \bar{G}\, \delta_r \left(\frac{1+\bar{\mu}}{1-\bar{\mu}}\right)$
6	Peierls-Nabarro factor	Peierl_Nabarro_factor	$F = \frac{2\bar{G}}{1-\bar{\mu}}$

extensively in the literature, we will not discuss all of its nuances here and will instead just briefly highlight the step-by-step methodology used by the Miedema calculator in **MAPAL**. All of the elemental parameters required for

the implementation of Miedema's model have been incorporated in the in-built element database of **MAPAL** and are called directly from there by the program.

When mixing two elements A and B in concentrations c_A and c_B respectively, the chemical enthalpy of mixing (ΔH_{AB}^{chem}) is calculated using a series of steps highlighted below:

<u>*Step 1*</u>: Calculating surface concentrations (c_A^s and c_B^s):

$$c_A^s = \frac{c_A \bar{V}_A^{2/3}}{c_A \bar{V}_A^{2/3} + c_B \bar{V}_B^{2/3}} \qquad and \quad c_B^s = \frac{c_B \bar{V}_B^{2/3}}{c_A \bar{V}_A^{2/3} + c_B \bar{V}_B^{2/3}}$$

where $\bar{V}_A$ and $\bar{V}_B$ are molar volumes of element A and B respectively

<u>*Step 2*</u>: Implementing volume corrections to calculate effective molar volumes of elements A and B in A-B alloy:

$$\Delta \bar{V}_A = \frac{P_o\, f_B^A\, \bar{V}_A^{2/3}\, (\phi_A^* - \phi_B^*)}{2\left(n_{ws}^{-1/3}\right)_{av}} \; [(n_{WS}^B)^{-1} - (n_{WS}^A)^{-1})]$$

$$\Delta \bar{V}_B = \frac{P_o\, f_A^B\, \bar{V}_B^{2/3}\, (\phi_B^* - \phi_A^*)}{2\left(n_{ws}^{-1/3}\right)_{av}} \; [(n_{WS}^A)^{-1} - (n_{WS}^B)^{-1})]$$

where ϕ_A^* and ϕ_B^* are work functions for A & B, n_{WS}^A and n_{WS}^B are average electron density parameters over the entire Wigner-Seitz cell boundary, $(n_{ws}^{-1/3})_{av}$ is equal to $\frac{(n_{WS}^A)^{-1/3} + (n_{WS}^B)^{-1/3}}{2}$, and P_o is an empirical constant that is equal to 1.5 when molar volume is expressed in *cm*^{3}, work function in *Volts* and n_{WS} in *density units*. If A-B is assumed to form solid solution, then $f_B^A = c_B^s$ *and* $f_A^B = c_A^s$.

The corrected molar volumes are then calculated as:

$$(\bar{V}_A)_{in\ alloy} = (\bar{V}_A)_{pure} + \Delta \bar{V}_A \quad \& \quad (\bar{V}_B)_{in\ alloy} = (\bar{V}_B)_{pure} + \Delta \bar{V}_B$$

Step 3: Calculating the parameter Γ:

$$\Gamma = \frac{1}{\left(n_{ws}^{-1/3}\right)_{av}}\left[-\boldsymbol{P}(\Delta\phi^*)^2 + \boldsymbol{Q}\left(\Delta n_{ws}^{1/3}\right)^2 - \boldsymbol{R}\right]$$

where $\Delta n_{ws}^{1/2} = (n_{ws}^{A})^{1/2} - (n_{ws}^{\mathrm{B}})^{1/2}$ and $\Delta\phi^* = \phi_A^* - \phi_B^*$

$\boldsymbol{P}$, $\boldsymbol{Q}$ and $\boldsymbol{R}$ are all constants and their value is selected as following:

Case 1: If both A & B are transition metals, then $\boldsymbol{P}$=14.1, $\boldsymbol{R}$=0 & $\boldsymbol{Q}$=9.4*$\boldsymbol{P}$

Case 2: If both A & B are non-transition metals, then $\boldsymbol{P}$=10.6, $\boldsymbol{R}$=0 & $\boldsymbol{Q}$=9.4*$\boldsymbol{P}$

Case 3: If one of the elements is a transition metal and the other is a non-transition metal, then $\boldsymbol{P}$=12.3 and $\boldsymbol{Q}$=9.4*$\boldsymbol{P}$. The value of $\boldsymbol{R}$ is calculated as $\boldsymbol{R} = 12.3\left(\frac{R}{P}\right)_A\left(\frac{R}{P}\right)_B\left(\frac{R}{P}\right)_{phase}$ where $\left(\frac{R}{P}\right)_{phase}$=1 (for solid state) and 0.73 (for liquid state). The values of $\left(\frac{R}{P}\right)_A$ and $\left(\frac{R}{P}\right)_B$ are obtained from the built-in element database.

Step 4: Calculating chemical enthalpy of mixing (ΔH_{AB}^{chem}) for A-B binary pair:

$$\Delta H_{AB}^{chem} = (c_A . c_B)(c_B^s\,\bar{V}_A^{2/3} + c_A^s\,\bar{V}_B^{2/3})\,.\,\Gamma$$

where $\bar{V}_A$ and $\bar{V}_B$ are corrected molar volumes of element A and B calculated in step 2.

When mixing two elements A and B in concentrations c_A and c_B respectively, the elastic enthalpy of mixing (ΔH_{AB}^{el}) is calculated as:

$$\Delta H_{AB}^{el} = c_A c_B\left(c_B\,\Delta\bar{H}_{A\,in\,B}^{el} + c_A\,\Delta\bar{H}_{B\,in\,A}^{el}\right)$$

The $\Delta\bar{H}_{A\,in\,B}^{elast}$ and $\Delta\bar{H}_{B\,in\,A}^{elast}$ values in above equation are calculated as:

$$\Delta\bar{H}^{elast}_{A\ in\ B} = \frac{2K_A G_B(\bar{V}_A - \bar{V}_B)^2}{3K_A\bar{V}_B + 4G_B\bar{V}_A} \quad \& \quad \Delta\bar{H}^{elast}_{B\ in\ A} = \frac{2K_B G_A(\bar{V}_A - \bar{V}_B)^2}{3K_B\bar{V}_A + 4G_A\bar{V}_B}$$

where K_A & K_B are bulk modulus of A & B, G_B & G_B are shear modulus of A & B, and $\bar{V}_A$ & $\bar{V}_B$ are corrected molar volumes of A & B.

For multi-component alloys containing three or more elements, the Miedema calculator in **MAPAL** calculates the enthalpy values using the extended regular solution model [3] as shown below:

$$\Delta H_{alloy} = \sum_{i=1}^{N} \sum_{j=1, j\neq i}^{N} 4\, c_i c_j\, \Delta H_{ij}^{mix}$$

where N is the number of elements present in the alloy and ΔH_{ij}^{mix} is the mixing enthalpy for $i - j$ equiatomic alloy.

The key functions available in 'miedema_calc' package are:

- *mapal.miedema_calc.**get_miedema_enthalpy**(alloy_name)*: returns mixing enthalpy for solid solution and formation enthalpy for intermetallic for an alloy ('*alloy_name*') using Miedema's model
- *mapal.miedema_calc.**get_miedema_vol_correction**(alloy_name)*: calculates overall effective volume correction applied to elements in Miedema's model. It can be considered as an estimate of the distortion in atomic volumes due to alloying

A.3.5 mapal.preTrained_ML_mods

With the has built-in functionalities for calculating compositional spaces and alloy features, **MAPAL** can seamlessly support deployment of trained ML models to map predictions over different compositional regimes to aid the alloy design process. This becomes especially helpful when **MAPAL** was used to create features for training of the ML model. Currently, we have included two pre-trained ML models in **MAPAL** (as shown in Table A.4) – (a) Neural

network ensemble model for predicting Vicker's hardness in multi-principal component alloys [4], and (b) a neural network ensemble model for predicting phase fractions of FCC, BCC and intermetallic phases in high-entropy alloys [5]. We have also developed an yield strength prediction model for multi-principal element alloys that will be included in a future update. The key functions available in '*preTrained_ML_mods*' package are:

- *mapal.preTrained_ML_mods.**mods_list**()*: prints the list of pre-trained ML models available in **MAPAL** along with their 'model_key' that is used to access them
- *mapal.preTrained_ML_mods.**info**(mod)*: returns detailed information about any model ('*mod*')
- *mapal.preTrained_ML_mods.**predict_hardness**(alloy_names_list)*: creates Vicker's hardness predictions for a list of alloys ('*alloy_names_list*')
- *mapal.preTrained_ML_mods.**predict_phase_fractions**(alloy_names_list)*: creates predicted phase fractions of FCC, BCC and Intermetallic phases for a list of alloys ('*alloy_names_list*')

Table A.4 List of pre-trained machine learning models available in the MAPAL.

#	Pre-trained Machine Learning model	model _key	Predicted property	Reference
1	Neural network ensemble model for predicting hardness of as-cast multi-principal element alloys	M1	Vickers Hardness (HV)	[4] Beniwal et al., npj Computational Materials, 8 (2022) 153 DOI: 10.1038/s41524-022-00842-3
2	Neural network ensemble model for predicting phase fraction of FCC, BCC & Intermetallic phases in as-cast high-entropy alloys	M2	Phase fraction of FCC, BCC and Intermetallic phase	[5] Beniwal and Ray, Computational Materials Science, 197 (2021) 110647 DOI: 10.1016/j.commatsci.2021.110647
3	Neural network ensemble model for predicting yield strength of as-cast multi-principal element alloys	-	Yield strength (MPa)	Not published currently. The model will be added to MAPAL in future update

A.3.6 mapal.map_features

The '*map_features*' package combines various functionalities in **MAPAL** (as discussed above) with plotting functions to enable visualization of features as a function of composition in different type of alloy systems, as shown in Figure A.2. Both the operator-based features and defined features (as discussed earlier in §A.3.3) can be visualized using this package. The key functions available in '*map_features*' package are:

- *mapal.map_features.**binary**(feats, A, B, dc=0.01, cAmin=0, cAmax=1)*: plots all features in input feature list ('*feats*') for an A_xB_{1-x} binary system with a composition (atomic fraction) step size of '*dc*' (default=0.01), as shown in Figure A.2a. The lower and upper bounds for concentration of component *A* are '*cAmin*' (default=0) and '*cAmax*' (default=1)
- *mapal.map_features.**ternary**(feats, A, B, C, dc=0.01, colorscale='Viridis')*: creates a ternary plot for all features in input feature list ('*feats*') over an $A_xB_yC_{1-x-y}$ ternary system with a composition (atomic fraction) step size of '*dc*' (default=0.01), as shown in Figure A.2b
- *mapal.map_features.**ternary1Cfixed**(feats, A, B, C, Cfix, dc=0.01, cAmin=0, cAmax='')*: plots all features in input feature list ('*feats*') for an $A_xB_{1-x}C_{Cfix}$ ternary system with a composition (atomic fraction) step size of '*dc*' (default=0.01), as shown in Figure A.2c. The concentration (atomic fraction) of component *C* is fixed as '*Cfix*'. The lower and upper bounds for concentration of component A are '*cAmin*' (default=0) and '*cAmax*' (default=1 – *Cfix*)

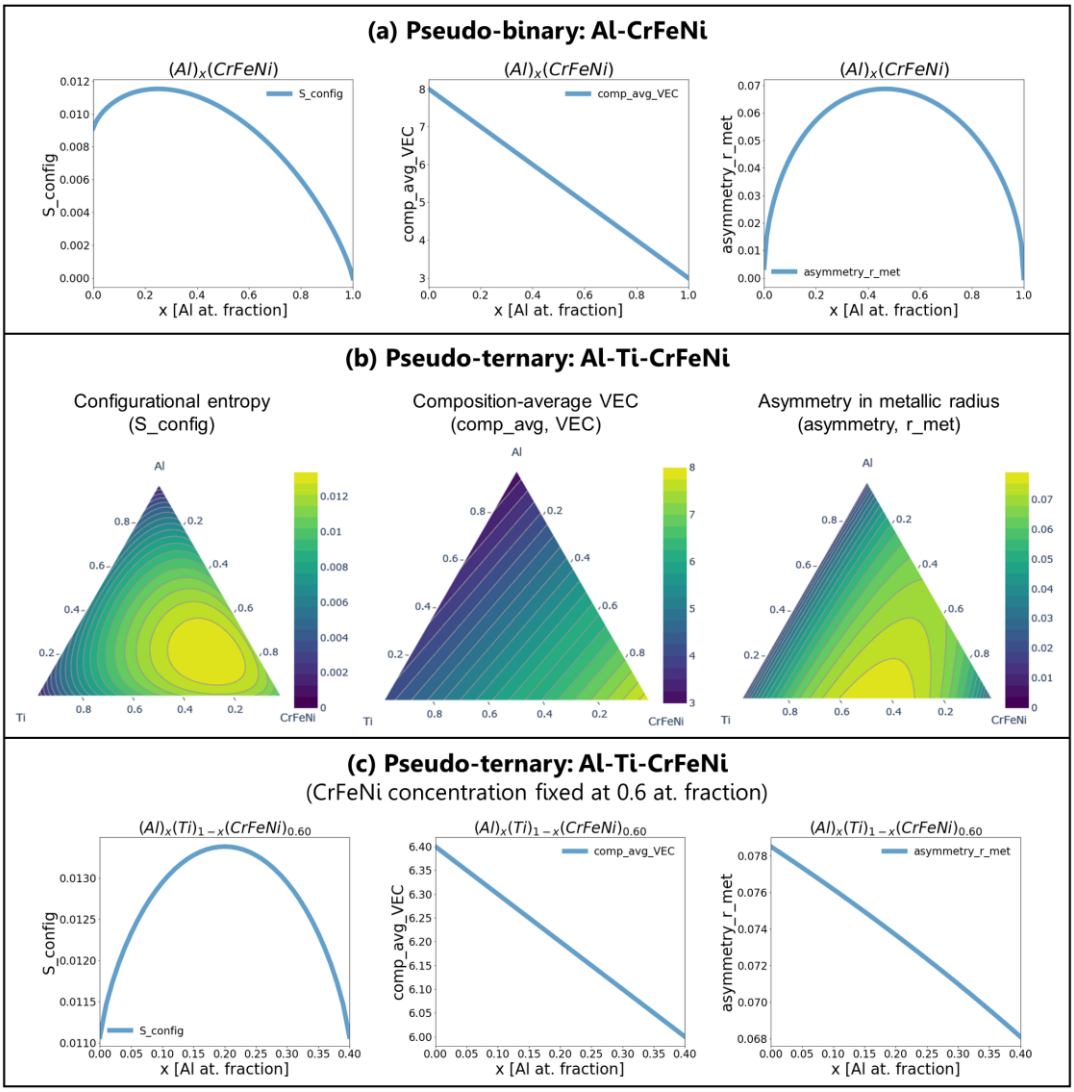

Figure A.2 Different types of feature-composition maps created using '*map_features*' package. (a) Features maps for $Al_x(CrFeNi)_{1-x}$ pseudo-binary system. (b) Feature maps for $Al_xTi_y(CrFeNi)_{1-x-y}$ pseudo-ternary system. (c) Feature maps for $Al_xTi_{1-x}(CrFeNi)_{0.6}$ pseudo-ternary system where the concentration of (CrFeNi) is fixed at 0.6 atomic fraction. In all (a-c), the left, middle and right figures are for configurational entropy, composition-weighted average valence electron count (VEC) and asymmetry in metallic radius respectively.

A.3.7 mapal.map_ML_predictions

Trained ML models can potentially guide the alloy design process by enabling identification of composition-of-interests based on how the predictions change over continuous compositional variations. To enable this, '*map_ML_predictions*' package in **MAPAL** uses the pre-trained ML models (as listed in Table A.4) to map the predictions over different type of compositional regimes including binary, pseudo-binary, ternary and pseudo-ternary compositional spaces. The key functions available in '*map_ML_predictions*' package are:

- *mapal.map_ML_predictions.**HV_binary**(A, B, dc=0.01, cAmin=0, cAmax=1)*: plots the Vicker's hardness predictions for an A_xB_{1-x} binary system with a composition (atomic fraction) step size of '*dc*' (default=0.01), as shown in Figure A.3a. The lower and upper bounds for concentration of component *A* are '*cAmin*' (default=0) and '*cAmax*' (default=1)
- *mapal.map_ML_predictions.**fPhase_binary**(A, B, dc=0.01, cAmin=0, cAmax=1)*: plots the predicted phase fractions of FCC, BCC and Intermetallic phases over an $A_xB_yC_{1-x-y}$ ternary system with a composition (atomic fraction) step size of '*dc*' (default=0.01), as shown in Figure A.3a
- *mapal.map_ML_predictions.**HV_ternary**(A, B, C, dc=0.01)*: plots the Vicker's hardness predictions over an $A_xB_yC_{1-x-y}$ ternary system with a composition (atomic fraction) step size of '*dc*' (default=0.01), as shown in Figure A.3b
- *mapal.map_ML_predictions.**fPhase_ternary**(A, B, C, dc=0.01)*: plots the predicted phase fractions of FCC, BCC and Intermetallic phases over an $A_xB_yC_{1-x-y}$ ternary system with a composition (atomic fraction) step size of '*dc*' (default=0.01), as shown in Figure A.3b
- *mapal.map_ML_predictions.**HV_ternary1Cfixed**(A, B, C, Cfix, dc=0.01, cAmin=0, cAmax='')*: plots the Vicker's hardness predictions over an $A_xB_{1-x}C_{Cfix}$ ternary system with a composition (atomic fraction) step size of '*dc*' (default=0.01), as shown in Figure A.3c. The concentration (atomic fraction) of component *C* is fixed as '*Cfix*'. The lower and upper bounds for concentration of component A are '*cAmin*' (default=0) and '*cAmax*' (default=1 – *Cfix*)
- *mapal.map_ML_predictions.**fPhase_ternary1Cfixed**(A, B, C, Cfix, dc=0.01, cAmin=0, cAmax'')*: plots the predicted phase fractions of FCC, BCC and Intermetallic phases over an $A_xB_{1-x}C_{Cfix}$ ternary system with a composition (atomic fraction) step size of '*dc*' (default=0.01), as shown in Figure A.3c. The concentration (atomic fraction) of component *C* is fixed as '*Cfix*'. The lower and upper bounds for concentration of component A are '*cAmin*' (default=0) and '*cAmax*' (default=1 – *Cfix*)

A.4 Conclusions

In summary, we have built **MAPAL** to enable parametrization of alloy compositions into physically relevant features that can be used to develop new machine learning models for predicting properties and behaviour of materials. **MAPAL** can also help in the alloy design process through – (a) visualization of a wide variety of thermodynamic and physical alloy descriptors over compositional spaces including binary, pseudo-binary, ternary and pseudo-ternary alloy systems, and (b) mapping of machine learning predictions from pre-trained models over compositional spaces. These visualizations provide insights for the selection of compositions-of-interest that can be further studied experimentally or through first-principles calculations. **MAPAL** has been developed as an open-source Python library and can support not only the training of new ML models but also the use of pre-trained ML models for exploration of compositional spaces. As the source code for **MAPAL** has published online, users can easily modify or expand the existing functions and element database for new case-specific functionalities.

A.5 Code availability

The documentation of **MAPAL** is available at https://ideas-db.notion.site/ideas-db/mapal-3c83308bf94140f6a5bb9ff12dd47543. The source code for **MAPAL** is available on 'IDEAsLab-Materials-Informatics' organization page on GitHub (https://github.com/IDEAsLab-Materials-Informatics). The library is currently available for download as a wheel package that can be installed locally using pip. Soon, it will also be hosted on PyPI repository to enable direct pip installation through web.

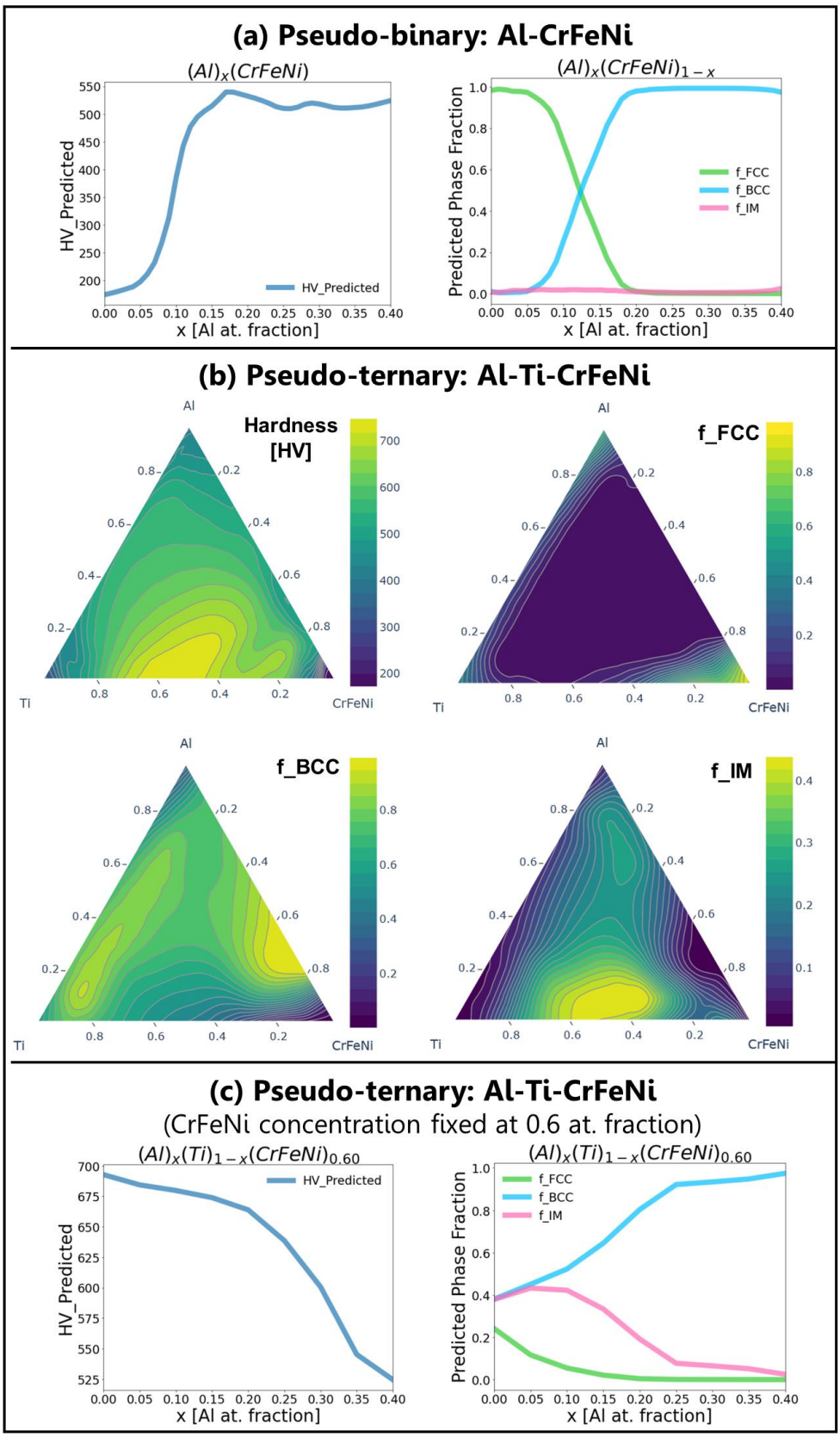

Figure A.3 Different types of property-composition maps created using '*map_ML_predictions*' package. Predicted hardness and phase fractions maps for (a) $Al_x(CrFeNi)_{1-x}$ pseudo-binary system, (b $Al_xTi_y(CrFeNi)_{1-x-y}$ pseudo-ternary system, and (c) $Al_xTi_{1-x}(CrFeNi)_{0.6}$ pseudo-ternary system where the concentration of (CrFeNi) is fixed at 0.6 atomic fraction. In all (a-c), f_FCC, f_BCC and f_IM represent phase fractions of FCC, BCC and Intermetallic phases respectively.

A.6 References

[1] A.R. Miedema, P.F. de Châtel, F.R. de Boer, Cohesion in alloys — fundamentals of a semi-empirical model, Physica B+C. 100 (1980) 1–28. https://doi.org/10.1016/0378-4363(80)90054-6.

[2] A.K. Niessen, A.R. Miedema, The "Macroscopic Atom" Model: An Easy Tool to Predict Thermodynamic Quantities, in: H. Brodowsky, H.-J. Schaller (Eds.), Thermochemistry of Alloys: Recent Developments of Experimental Methods, Springer Netherlands, Dordrecht, 1989: pp. 29–54. https://doi.org/10.1007/978-94-009-1027-0_2.

[3] A. Takeuchi, A. Inoue, Calculations of Mixing Enthalpy and Mismatch Entropy for Ternary Amorphous Alloys, Materials Transactions, JIM. 41 (2000) 1372–1378. https://doi.org/10.2320/matertrans1989.41.1372.

[4] D. Beniwal, P. Singh, S. Gupta, M.J. Kramer, D.D. Johnson, P.K. Ray, Distilling physical origins of hardness in multi-principal element alloys directly from ensemble neural network models, Npj Comput Mater. 8 (2022) 1–11. https://doi.org/10.1038/s41524-022-00842-3.

[5] D. Beniwal, P.K. Ray, Learning phase selection and assemblages in High-Entropy Alloys through a stochastic ensemble-averaging model, Comput. Mater. Sci. 197 (2021) 110647. https://doi.org/10.1016/j.commatsci.2021.110647.

Appendix B

EDS-PhaSe: Phase segmentation and analysis from EDS elemental map images using markers of elemental segregation

B.1 Introduction

Scanning Electron Microscopy (SEM), combined with Energy Dispersive Spectroscopy (EDS) mapping, is commonly used for gaining a qualitative understanding of elemental and phase distribution in materials. While SEM imaging (especially with back-scattered electrons) enables visualization of phase distribution in the sample surface due to the average Z-contrast, EDS elemental maps provide a visualization of the elemental distribution within the sample. However, extracting quantitative data that allows for chemical mapping of phases is rarely attempted. A key impediment in such efforts lies in the self-scaling nature of the individual element map, i.e., the intensities scale between the highest and lowest concentration of that element vis-à-vis the microstructure instead of scaling according to the absolute concentrations within the alloy. A wealth of such data exists in the microscopy literature where qualitative analysis is done without quantifying the results. The present work

This appendix has been published as a research article in 'Metallography, Microstructure and Analysis'

D Beniwal, V Shivam, O Palasyuk, MJ Kramer, G Phanikumar, PK Ray, *EDS-PhaSe: Phase segmentation and analysis from EDS elemental map images using markers of elemental segregation*, **Metallography, Microstructure, and Analysis**, 12 (2023) 924–933

DOI: https://doi.org/10.1007/s13632-023-01020-7

seeks to address this challenge via appropriate scaling of intensity, normalized for the actual chemical compositions.

Usually, the separate phases are identified based on the contrast in SEM images (typically using backscattered electrons with some visual cues from EDS maps) and the phase compositions are estimated by sampling small regions within the separate phases. This becomes challenging in scenarios where the phase contrast is not clearly apparent from the backscattered images due to low overall Z contrast. In this work, we present the **EDS-Pha**se **Se**gmentation (**EDS-PhaSe**) tool that enables phase segmentation and phase analysis using the EDS elemental map images. It converts the EDS map images into estimated composition maps for calculating markers of selective elemental redistribution in the scanned area and creates a phase segmented micrograph while providing approximate fraction and composition of each identified phase.

EDS is a quantitative technique wherein the chemical composition of any region on the sample surface can be calculated from the analysis of the characteristic X-ray spectrum emitted by that region when it is impacted by high-energy fast-moving electrons [1]. EDS mapping over a selected area is often used to generate elemental maps, the color intensity of which is scaled according to the relative abundance of the element within that region. However, given the self-scaling nature of the individual elemental maps, a measure of the overall composition is not obtainable by direct visual observation, which in turns becomes an impediment for extracting quantitative data from the EDS maps. The major reason behind such treatment is the fact that statistical accuracy of EDS quantification is strongly linked to the number of signals (photon counts) received, which can be very low at a single pixel due to the short dwell time per pixel while mapping large areas. Since phase separation is usually associated with elemental redistribution, EDS elemental maps can be used to identify compositionally different phases. Various commercial software packages are in fact available for automated phase segmentation, but these are coupled with the respective spectroscopic imaging systems and thus cannot work with the elemental mapping data available only

as images (for example, data obtained from published literature). Various approaches have been implemented by researchers for EDS assisted phase segmentation [2–6]. Some of these lack capabilities for generalized implementation for phase analysis, while others are built only for specific use-case scenarios. The *edxia* tool developed by Georget et al. [4] is especially interesting, albeit it is targeted towards microstructural analysis of cementitious materials only.

The **EDS-PhaSe** framework presented in this work enables phase segmentation and phase analysis using the EDS data to obtain estimates of phase fractions and phase compositions. The algorithms presented here are available as an interactive workflow with an easy-to-use interface and can be implemented directly to the EDS elemental map images for any material without requiring access to any raw data or proprietary software. The application of **EDS-PhaSe** is demonstrated here for microstructural analysis in AlCoCrFeNi alloy.

B.2 Methodology

The **EDS-PhaSe** framework developed in this work enables phase segmentation and phase analysis from raw EDS elemental map images. It was implemented using the Python programming language and associated open-source libraries. '*OpenCV*' was used for reading and processing the raw EDS maps, '*numpy*' was used for manipulation and conversion of pixel map arrays, and '*matplotlib*' was used for plotting the pixel maps, phase masks and segmented microstructures. The codes were wrapped into jupyter notebooks wherein interactive controls were incorporated using '*ipywidgets*'. This enables a user-friendly access to the **EDS-PhaSe** (akin to a graphical user interface) so that it can be used for analyzing new data and EDS maps without any coding. The code for **EDS-PhaSe** is available at GitHub (§B.5 Research data).

The SEM micrograph and raw EDS elemental maps of AlCoCrFeNi used in this work correspond to equiatomic AlCoCrFeNi CCA that was prepared using Mechanical Alloying (MA) followed by sintering in the published work of

Shivam et al. [7]. The microstructure and EDS elemental maps for AlCoCrFeNi alloy were captured using FEI Quanta 200 F SEM equipped with AMETEK EDS detector operated at 20 kV. The accuracy of this approach was also demonstrated on a commercial Ni-based Haynes 282 superalloy using the actual raw data from the EDS maps as well as the images derived from the commercial software package (Oxford's AZtec).

B.3 Results

B.3.1 Creating estimated composition maps

The elemental maps obtained from EDS capture the distribution of each element within the scan area which is most commonly represented in the form of RGB color images wherein the intensity of each pixel is scaled relative to the spectral contribution of that pixel to the overall spectrum of a given element. Figure B.1 shows the methodology used for converting raw EDS maps into estimated composition maps. Suppose a sample has N number of raw EDS elemental maps (one for each element) and the size of each map is $m \times n$. The intensity of any (i, j) pixel in the raw EDS map of any element k is denoted here as I_{ij}^{k}. The raw EDS map of any element k is converted to a scaled map wherein the scaled intensity of any (i, j) pixel (S_{ij}^{k}) is given as:

$$S_{ij}^{k} = \frac{\bar{X}^{k}}{\sum_{i=1}^{m} \sum_{j=1}^{n} I_{ij}^{k}} \times I_{ij}^{k}$$

Equation B.1

where, $\bar{X}^{k}$ is the average concentration of element k in the overall area mapped using EDS and the denominator ($\sum_{i=1}^{m} \sum_{j=1}^{n} I_{ij}^{k}$) is the sum of all pixel intensities in the raw EDS map of element k. $\bar{X}^{k}$ can be in either atomic percent or weight percent and must match the mode used for creating raw EDS maps. In essence, the scaled map is a representation of how the total quantity of any given element present in the overall scanned area is redistributed to each pixel. This assumes a linear relationship between the pixel intensity at a given spatial

location and the relative quantity of the element present (here, relative refers to the maximum quantity of the element within the region captured in the map).

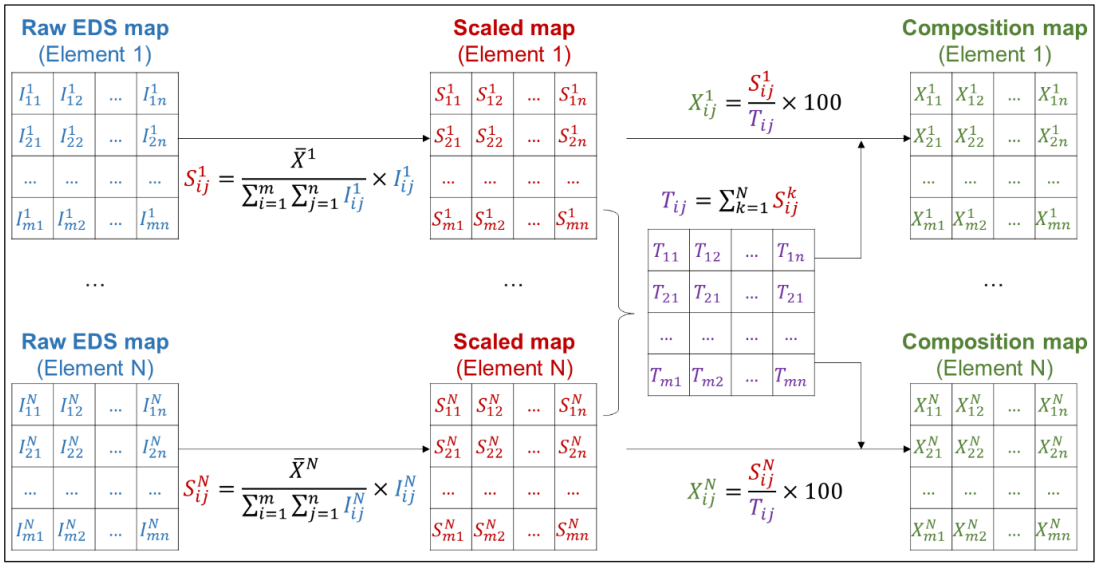

Figure B.1 Methodology for conversion of raw EDS maps into composition maps.

The scaled map of any element k is then converted to an estimated composition map wherein the estimated concentration (X_{ij}^k) of element k in any (i, j) pixel is given as:

$$X_{ij}^k = \frac{S_{ij}^k}{T_{ij}} \times 100$$

Equation B.2

where, T_{ij} is the summation of scaled intensities for all elements at the (i, j) pixel and is calculated as $T_{ij} = \sum_{k=1}^N S_{ij}^k$. The units of estimated composition maps thus obtained are same as the mode used for capturing the raw EDS elemental maps. Figure B.2 shows the raw elemental EDS maps along with the transformed composition maps (atomic percent and weight percent) for AlCoCrFeNi alloy.

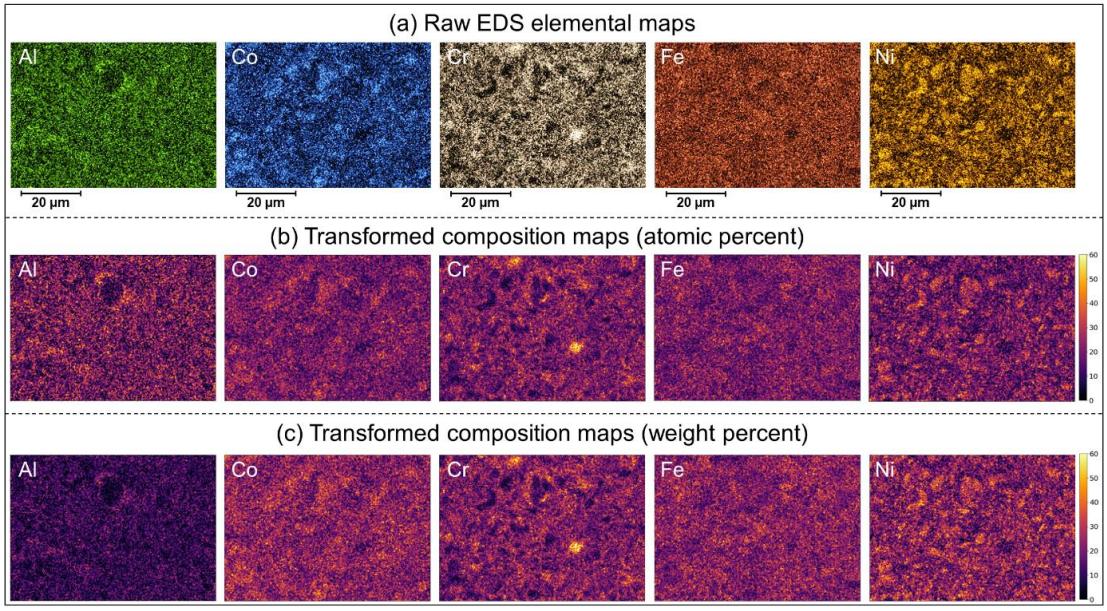

Figure B.2 EDS elemental maps and transformed compositional maps for AlCoCrFeNi.

B.3.2 Elemental segregation markers

Phase separation in alloys, whether it be during solidification or heat treatment, is often marked by the redistribution of elements into different phases. EDS maps capture this elemental redistribution; but, while they give visual cues on the nature of segregation in different regions, the lack of quantitative analysis often makes it difficult to: **(a)** precisely phase segment the microstructure when phase contrast is lacking in SEM micrographs [8], **(b)** estimate the extent of elemental redistribution, and **(c)** differentiate between the Z contrast (due to average atomic number difference) and grain orientation contrast. Thus, we use two markers that provide quantitative information on the selective redistribution of all element pairs at each pixel in a given alloy and can act as parameters for performing phase segmentation.

The first parameter is a proxy order-parameter (α_{ij}^{A-B}) that is a measure of elemental ordering on a microscopic scale (decided by pixel size in EDS scan) and is calculated at any (i, j) pixel for any binary pair A-B as:

$$\alpha_{ij}^{A-B} = \frac{X_{ij}^{A}\, X_{ij}^{B}}{\bar{X}^{A}\, \bar{X}^{B}} - 1$$

Equation B.3

where, X_{ij}^{A} and X_{ij}^{B} are estimated atomic percent of element A and B respectively at (i,j) pixel, and $\bar{X}^{A}$ and $\bar{X}^{B}$ are the average atomic percent of element A and B respectively in the overall area mapped using EDS. Here, $X_{ij}^{A}\,X_{ij}^{B}$ is a measure of co-occurrence of the A and B in the (i,j) pixel whereas $\bar{X}^{A}\,\bar{X}^{B}$ is a measure of co-occurrence of A and B under assumption that A and B elements are distributed uniformly throughout the mapped area. Consequently, α_{ij}^{A-B} takes positive value in pixels where co-occurrence of A-B is higher than what would be obtained with uniform distribution of elements and vice-versa. Thus, α_{ij}^{A-B}>0 suggests ordering behavior of A-B binary at the (i,j) pixel whereas α_{ij}^{A-B}>0 suggests either clustering of A-B binary at (i,j) pixel or rejection of both A & B elements from (i,j) pixel. The formulation of α_{ij}^{A-B} parameter here is inspired from the Warren-Cowley parameter [9–12] used extensively for characterizing the short-range order. Since the formation of new phases is often associated with selective redistribution of elements (while total amount of each element is conserved), it is reasonable to expect that the α_{ij}^{A-B} parameter for at least one binary pair would undergo a strong transition as we move from one phase to the next. Thus, mapping of α_{ij}^{A-B} parameter for all binaries over the entire scan area, as shown in Figure B.3, can provide contrast for identifying phases that may not be easily distinguishable from SEM images.

The second parameter is the absolute concentration difference (ΔX_{ij}^{A-B}) that is calculated at any (i,j) pixel for a binary pair A-B as:

$$\Delta X_{ij}^{A-B} = |X_{ij}^{A} - X_{ij}^{B}|$$

Equation B.4

where, X_{ij}^{A} and X_{ij}^{B} are the estimated concentration of element A and B respectively at (i,j) pixel. It is a fairly straight-forward metric that quantifies the difference between concentrations of element A and B at each pixel; and

thus, when mapped over the entire scanned area (as shown in Figure B.3), it can create contrast useful for phase identification.

While these parameters are useful in most cases, there are instances where the use of single element concentration (X_{ij}^{k}) by itself may be preferable for phase identification. For e.g., suppose we have formation of two phases that correspond approximately to A_2B and AB_2 stoichiometry. The α_{ij}^{A-B} and ΔX_{ij}^{A-B} parameter maps over these phases will look identical, but these can be easily distinguished by the elemental concentration of either A or B. Thus, the choice of exact parameter for phase segmentation will vary not only from one sample to another, but also from one phase to another within the same sample. To enable this, **EDS-PhaSe** framework developed in this work provides the flexibility to use different parameters for identification of different phases within the same sample.

B.3.3 Creating phase masks

Here we are looking at the AlCoCrFeNi alloy that was prepared through mechanical alloying route. For this alloy, it is difficult to identify phases directly from the SEM micrograph (Figure B.5b) since these don't exhibit great contrast. The binary parameter maps (Figure B.3) and estimated composition maps (Figure B.2) provide clear insights into what type of phases are present and what parameters may be ideal for their separate identification.

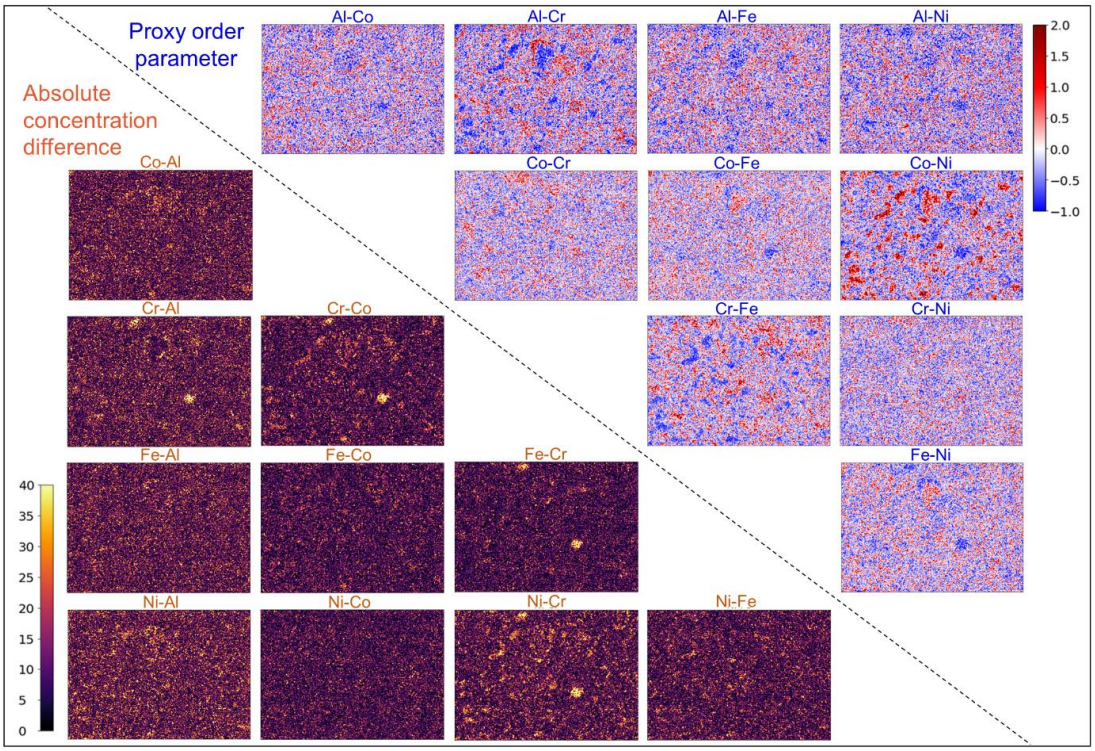

Figure B.3 Proxy-order parameter maps and absolute concentration difference maps for all binary pairs.

From Figure B.3, we can see three separate (non-overlapping) regions which show a strong ordering parameter for different binary pairs. The strongest one is the Co-Ni ordering, followed by Al-Cr and Cr-Fe, thereby indicating that we have three major phases present in the alloy: a (Co, Ni)-rich phase, a (Al, Cr)-rich phase and a (Fe, Cr)-rich phase. **EDS-PhaSe** allows interactive mask creation for a phase that gets overlaid on top of the SEM micrograph. First, a condition is defined for each phase using three user inputs: **(a)** parameter type, **(b)** operator type, and (c) threshold value. For e.g., the mask for (Co, Ni)-rich phase in Figure B.4a has been created using 'α_{ij}^{Co-Ni}' parameter and '>' (i.e., 'greater than') operator for different threshold values viz. {0.1, 0.3, 0.5, 1}. Similarly, the mask for (Al, Cr)-rich phase in Figure B.4b has been created using 'α_{ij}^{Al-Cr}' parameter and '>' (i.e., 'greater than') operator for different threshold values viz. {0.1, 0.3, 0.5, 1}.

Once the condition is defined, the phase mask is created by assigning a value of '1' or '0' at each pixel based on whether the condition is satisfied or not satisfied respectively. The interactive controls allow creation and visualization

of the masks (Figure B.4) in real time so that appropriate parameter choice can be made for final phase segmentation and analysis.

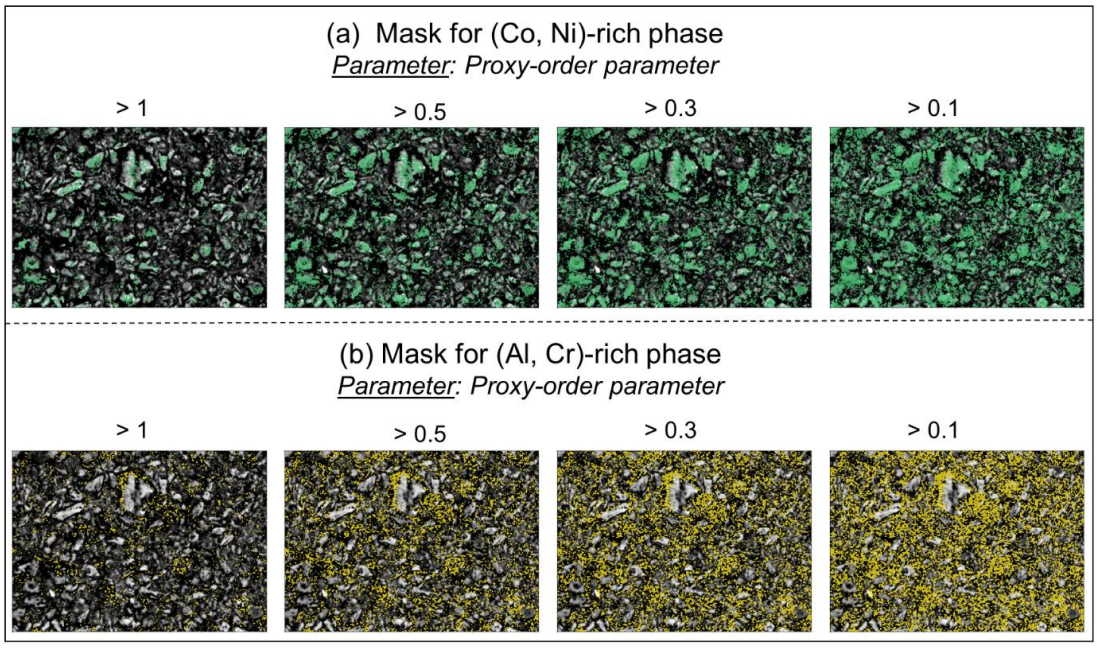

Figure B.4 Phase segmentation masks for different threshold values.

B.3.4 Phase segmentation and analysis

Once the conditions for identification of each phase are finalized, these are used to create the individual phase masks. The overall phase segmented image is created by layering the individual phase masks on top of each other. The analysis of these phase masks yields important information pertaining to: **(a)** the volume (or area) fraction of each phase, and **(b)** the estimated average composition of each phase.

The phase fraction (f^p) of any phase p is calculated as:

$$f^p = \left(\frac{1}{m \times n}\right) \sum_{i=1}^{m} \sum_{j=1}^{n} \boldsymbol{\delta}_{M_{ij}^p = 1}$$

Equation B.5

where, $(m \times n)$ is the total number of pixels in image of size $(m \times n)$, M_{ij}^p is the value of phase mask for phase p at (i, j) pixel, and $\boldsymbol{\delta}_{M_{ij}^p = 1}$ is a delta function that returns 1 if $M_{ij}^p = 1$ or else 0. Figure B.5a shows the individual phase masks and

phase fractions of three phases identified in the AlCoCrFeNi. The estimated phase fractions of (Co, Ni)-rich phase, (Al, Cr)-rich phase and Fe-rich phase in the scanned area are 0.36, 0.34 and 0.3 respectively.

The average concentration ($\bar{X}^{k,p}$) of any element k in any phase p is calculated as:

$$\bar{X}^{k,p} = \left(\frac{1}{f^p}\right)\left(\frac{1}{m \times n}\right) \sum_{i=1}^{m} \sum_{j=1}^{n} X_{ij}^{k} \, M_{ij}^{p}$$

Equation B.6

where, f^p is the phase fraction of phase p, $(m \times n)$ is the total number of pixels in image of size $(m \times n)$, X_{ij}^{k} is the estimated concentration of element k at (i, j) pixel, and M_{ij}^{p} is the value of phase mask of phase p at (i, j) pixel. Implementing this phase analysis on the AlCoCrFeNi results in the estimated average compositions (in atomic percent) of (Co, Ni)-rich, (Al, Cr)-rich and Fe-rich phases as {Al: 13.6, Co: 25.5, Cr: 16, Fe: 17.6, Ni: 27.3}, {Al: 27.6, Co: 15.8, Cr: 24.6, Fe: 17.7, Ni: 14.3} and {Al: 16.7, Co: 18.7, Cr: 21.1, Fe: 26, Ni: 17.5} respectively. To highlight the significance of phase analysis enabled by **EDS-PhaSe** framework, it must be noted that in the original work [7], the authors had identified three phases through XRD, but could sample only two phases during SEM-EDS due to a lack of clear phase contrast in SEM micrographs. **EDS-PhaSe** shines especially in such scenarios where the phase identification is otherwise difficult.

The estimated phase fractions and phase compositions through **EDS-PhaSe** are especially sensitive to the threshold values used while creating the phase masks, and thus represent only rough estimates of what the actual phase compositions might be. But that said, the type of elemental redistribution indicated by the analysis would still be accurate, i.e., (Co, Ni)-rich phase identified here would be rich in Co and Ni in actual sample also, even though the extent of segregation may be under- or over-estimated based on the choice of threshold values.

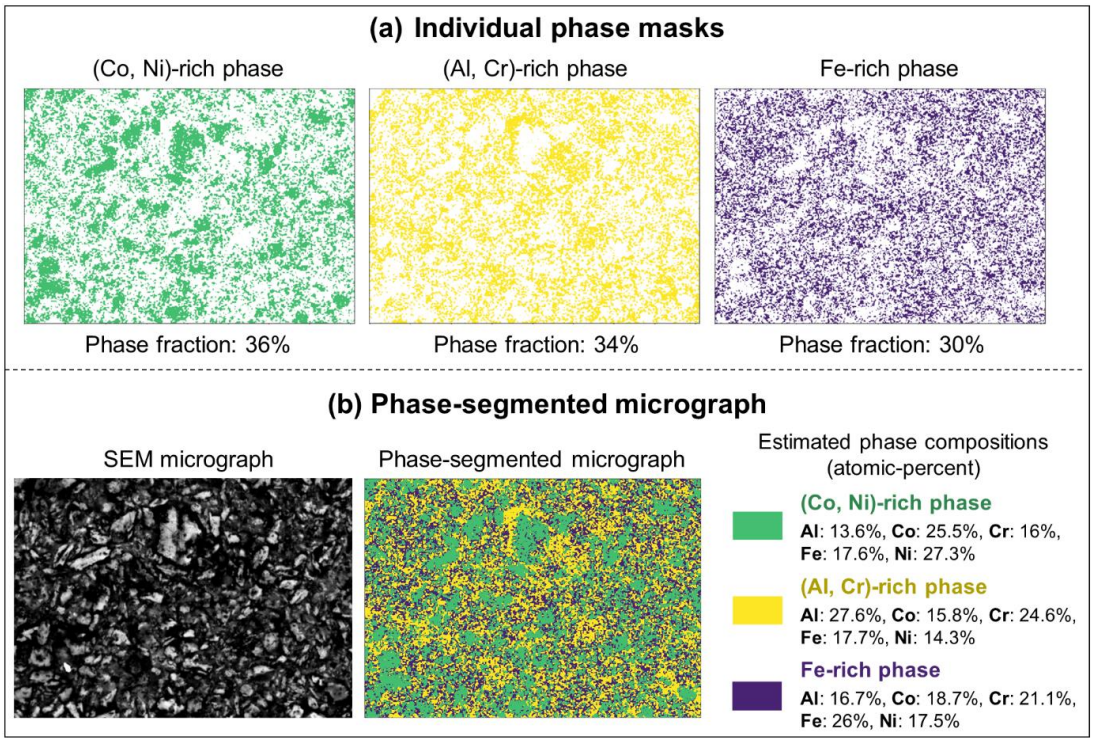

Figure B.5 Phase segmentation and phase analysis. (a) Phase masks for individual phases. (b) SEM micrograph and phase-segmented micrograph along with the estimated phase compositions in atomic-percent.

B.3.5 Using raw count maps for EDS-PhaSe analysis

The vast majority of EDS elemental mapping data is collected and distributed as graphic images and thus, in §B.3.1-B.3.4, we focused on the methodology (Figure B.1) and implementation (Figure B.2-Figure B.5) of **EDS-PhaSe** for analyzing EDS images. But some EDS software (such as AZtec by Oxford Instruments) provide easy access to raw count maps, containing the counts of characteristic X-rays used for quantification of each element, that can be exported in a tabular format as excel or csv files. **EDS-PhaSe** has the capability to analyze these raw count maps in a manner similar to how graphic images are analyzed above. To showcase this, we have analyzed Haynes 282 alloy (Figure B.6) using two different data sources – **(a)** the raw count maps created using $K\alpha_1$ and $L\alpha_1$ energies for mapping of {Al, Co, Cr, Ni, Si, Ti} and Mo, respectively and **(b)** graphic images of elemental maps. We further calculated the compositions of various regions, as marked in Figure B.6c, with **EDS-PhaSe** using both data sources and compared these with the compositions measured directly through EDS region scans (Figure B.6d) to address three key

questions:– **(a)** How accurate are the compositions calculated by **EDS-PhaSe** model as compared to actual EDS region scans?, **(b)** What is the extent of improvement (if any) obtained when raw count maps are used instead of graphic images?, and **(c)** How sensitive are the EDS-PhaSe calculations to size of the scanned area?. To quantify the difference between calculated and actual concentration, the error metric (Figure B.6d) has been calculated as:

$$Error = \sum_{i=1}^{N} |X_{model}^{i} - X_{EDS}^{i}|$$

Equation B.7

where N is the number of elements, X_{model}^{i} is the concentration of ith element as calculated by the **EDS-PhaSe** model and X_{EDS}^{i} is the concentration of ith element as determined by the EDS region scan.

As seen in Figure B.6d, the overall error in **EDS-PhaSe** calculated compositions is quite small; ranging between 0.46 and 2.24 at. % with raw count maps and between 0.17 and 2.69 at. % with graphic images as the data source. These error values are small since these are not average errors in concentration of elements, but are instead cumulative errors representing summation over absolute errors in concentration of all elements. The accuracy of **EDS-PhaSe** calculated compositions shows a direct relation to the area of the scanned region (represented by number of pixels lying within the region) as the accuracy decreases with decrease in the size of sampled region and vice-versa, as seen in Figure B.6d.

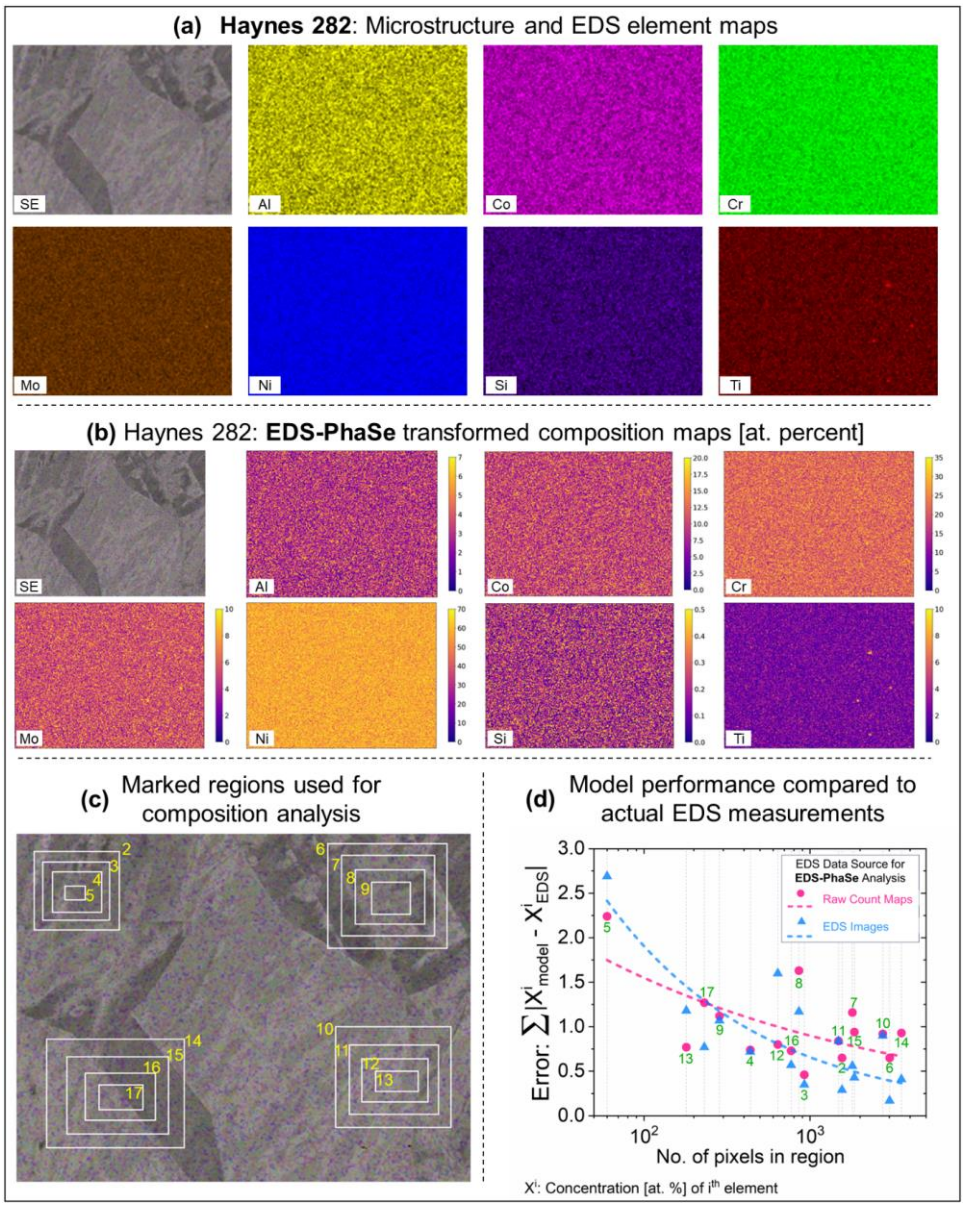

Figure B.6 Comparing performance of EDS-PhaSe model using different data sources (EDS images and raw count maps) over scan areas of varying size. (a) Microstructure and elemental maps of Haynes 282 alloy. EDS element maps were collected as both graphic images as well as raw count maps. (b) Composition maps [atomic percent] created using EDS-PhaSe. (c) Marked regions with region id varying from 02 to 17). The composition of each of these regions was measured first using the EDS software and then using the EDS-PhaSe tool presented in this work. (c) Error in composition of regions marked in (b) as calculated by EDS-PhaSe model using two different data sources – raw count maps ($L\alpha_1$ for Mo and $K\alpha_1$ for all other elements) and EDS images. The labels (2-17) in (c) correspond to respective region id marked in (b). The error is calculated as sum of absolute difference between composition of each element measured by EDS-PhaSe Model ($\mathbf{X^i_{model}}$) vs. the actual concentration measured by EDS software ($\mathbf{X^i_{EDS}}$).

B.4 Conclusions

This chapter presents the **EDS-PhaSe** framework that incorporates an interactive workflow for phase segmentation and phase analysis using the EDS elemental map images. It converts the EDS map images into estimated composition maps that are used for calculating markers of selective elemental redistribution in the scanned area. The proxy order parameter, defined as a measure of deviation in occurrence frequency of binary atom pairs, is especially helpful in highlighting chemical contrast between different phases. **EDS-PhaSe** creates individual phase masks with the additional flexibility of using different identification parameter and conditions for each phase. It further creates a phase segmented micrograph and provides approximate fraction and composition of each phase. The approach offers two unique advantages. Firstly, it enables the direct processing of EDS elemental map images without requiring any raw or proprietary data/software; thereby enabling analysis of EDS results available in the published literature as images or in cases where either the raw data is not available/collected or the access to proprietary software is limited. Secondly, it enables segmentation and analysis of phases even when the phase contrast is missing in SEM micrographs; thereby assisting in correlating the XRD and SEM-EDS data as shown in this work for AlCoCrFeNi alloy. The quantitative phase analysis obtained from **EDS-PhaSe**, comprising phase fractions and phase compositions, can be further integrated with insights obtained from other computational techniques such as: **(a)** phase selection, phase fractions and phase constitutions predicted by machine learning models and CALPHAD calculations [13–20], **(b)** ordering and clustering tendencies predicted by ab-initio calculations and atomistic simulations [21–23], and **(c)** microstructural changes such as phase separation and precipitate formation predicted by phase field modelling [16,24,25].

The current implementation of **EDS-PhaSe** has certain limitations also – **(a)** the phase masks are very sensitive to the threshold value, which is a user-input parameter, and thus, the phase fractions and phase compositions should only be treated as rough estimates, **(b) EDS-PhaSe** does not perform any spectrum

correction and assumes that the EDS software has taken into account all corrections (such as ZAF correction) while capturing the elemental maps, which is often the case, and **(c)** it is assumed that no post-processing has been done on the input EDS element map images post-acquisition; but that said, linear adjustment of the intensity spectrum (brightness and contrast adjustments) in input images will not make a difference as long as the thresholds are kept above (below) the maximum (minimum) intensity values in raw spectrum.

The best use case scenario, and the future thrust, for **EDS-PhaSe** framework is its integration with the EDS software so that the phase segmentation and analysis is done simultaneously in real time during the acquisition of EDS elemental maps. This would provide critical insights to the operator as to which areas should be sampled further for accurate quantification of phase compositions. As **EDS-PhaSe** code is available as open-access with this article, there are various other collaborative avenues for improvements such as – **(a)** while **EDS-PhaSe** is capable of analyzing raw count maps, these are not readily accessible from all EDS software and thus there is scope for development of algorithms that can break down the raw spectrum into count maps, **(b)** development of new and innovative markers using the composition maps to create unique masks, **(c)** development of algorithms to guide selection of appropriate threshold parameters, and **(d)** unique masking techniques to probe different microstructural features such as grain boundary segregation.

B.5 Research data

EDS-PhaSe code, wrapped in interactive Jupyter notebooks, is available at 'IDEAsLab-Computational-Microstructure' organization page on GitHub:

https://github.com/IDEAsLab-Computational-Microstructure/EDS-PhaSe

B.6 References

[1] J.I. Goldstein, D.E. Newbury, J.R. Michael, N.W.M. Ritchie, J.H.J. Scott, D.C. Joy, Scanning Electron Microscopy and X-Ray Microanalysis, Springer New York, New York, NY, 2018. https://doi.org/10.1007/978-1-4939-6676-9.

[2] B. Münch, L. h. j. Martin, A. Leemann, Segmentation of elemental EDS maps by means of multiple clustering combined with phase identification, J. Microsc. 260 (2015) 411–426. https://doi.org/10.1111/jmi.12309.

[3] R. Juránek, J. Výravský, M. Kolář, D. Motl, P. Zemčík, Graph-based deep learning segmentation of EDS spectral images for automated mineral phase analysis, Comput. Geosci. 165 (2022) 105109. https://doi.org/10.1016/j.cageo.2022.105109.

[4] F. Georget, W. Wilson, K.L. Scrivener, edxia: Microstructure characterisation from quantified SEM-EDS hypermaps, Cem. Concr. Res. 141 (2021) 106327. https://doi.org/10.1016/j.cemconres.2020.106327.

[5] J.B. Byrnes, A.A. Gazder, S.A. Yamini, Assessing phase discrimination via the segmentation of an elemental energy dispersive X-ray spectroscopy map: a case study of Bi2Te3 and Bi2Te2S, RSC Adv. 8 (2018) 7457–7464. https://doi.org/10.1039/C7RA08594J.

[6] P.T. Durdziński, C.F. Dunant, M.B. Haha, K.L. Scrivener, A new quantification method based on SEM-EDS to assess fly ash composition and study the reaction of its individual components in hydrating cement paste, Cem. Concr. Res. 73 (2015) 111–122. https://doi.org/10.1016/j.cemconres.2015.02.008.

[7] V. Shivam, Y. Shadangi, J. Basu, N.K. Mukhopadhyay, Evolution of phases, hardness and magnetic properties of AlCoCrFeNi high entropy alloy processed by mechanical alloying, J. Alloys Compd. 832 (2020) 154826. https://doi.org/10.1016/j.jallcom.2020.154826.

[8] V. Shivam, D. Beniwal, Y. Shadangi, P. Singh, V.S. Hariharan, G. Phanikumar, D.D. Johnson, P.K. Ray, N.K. Mukhopadhyay, Effect of Zn Addition on Phase Selection in AlCrFeCoNiZn High-Entropy Alloy, SSRN Electronic Journal (Preprint) (2022). https://doi.org/10.2139/ssrn.4263461.

[9] J.M. Cowley, Short-Range Order and Long-Range Order Parameters, Phys. Rev. 138 (1965) A1384–A1389. https://doi.org/10.1103/PhysRev.138.A1384.

[10] Y. Rao, W.A. Curtin, Analytical models of short-range order in FCC and BCC alloys, Acta Mater. 226 (2022) 117621. https://doi.org/10.1016/j.actamat.2022.117621.

[11] P. Singh, A.V. Smirnov, D.D. Johnson, Atomic short-range order and incipient long-range order in high-entropy alloys, Phys. Rev. B 91 (2015) 224204. https://doi.org/10.1103/PhysRevB.91.224204.

[12] D. Porter, K. Easterling, Phase Transformations in Metals and Alloys (Revised Reprint), CRC Press, 2009. https://doi.org/10.1201/9781439883570.

[13] D. Beniwal, P.K. Ray, Learning phase selection and assemblages in High-Entropy Alloys through a stochastic ensemble-averaging model, Comput. Mater. Sci. 197 (2021) 110647. https://doi.org/10.1016/j.commatsci.2021.110647.

[14] M. Wu, S. Wang, H. Huang, D. Shu, B. Sun, CALPHAD aided eutectic high-entropy alloy design, Mater. Lett. 262 (2020) 127175. https://doi.org/10.1016/j.matlet.2019.127175.

[15] D. Beniwal, P.K. Ray, FCC vs. BCC phase selection in high-entropy alloys via simplified and interpretable reduction of machine learning models, Materialia 26 (2022) 101632. https://doi.org/10.1016/j.mtla.2022.101632.

[16] C. Liu, A. Garner, H. Zhao, P.B. Prangnell, B. Gault, D. Raabe, P. Shanthraj, CALPHAD-informed phase-field modeling of grain boundary microchemistry and precipitation in Al-Zn-Mg-Cu alloys, Acta Mater. 214 (2021) 116966. https://doi.org/10.1016/j.actamat.2021.116966.

[17] D. Beniwal, Jhalak, P.K. Ray, Data-Driven Phase Selection, Property Prediction and Force-Field Development in Multi-Principal Element Alloys, in: A. Verma, S. Mavinkere Rangappa, S. Ogata, S. Siengchin (Eds.), Forcefields for Atomistic-Scale Simulations:

Materials and Applications, Springer Nature, Singapore, 2022: pp. 315–347. https://doi.org/10.1007/978-981-19-3092-8_16.
[18] W. Wang, H.-L. Chen, H. Larsson, H. Mao, Thermodynamic constitution of the Al–Cu–Ni system modeled by CALPHAD and ab initio methodology for designing high entropy alloys, Calphad 65 (2019) 346–369. https://doi.org/10.1016/j.calphad.2019.03.011.
[19] Q. Han, Z. Lu, S. Zhao, Y. Su, H. Cui, Data-driven based phase constitution prediction in high entropy alloys, Comput. Mater. Sci 215 (2022) 111774. https://doi.org/10.1016/j.commatsci.2022.111774.
[20] D. Beniwal, P.K. Ray, CoSMoR: Decoding decision-making process along continuous composition pathways in machine learning models trained for material properties, Phys. Rev. Mater. 7 (2023) 043802. https://doi.org/10.1103/PhysRevMaterials.7.043802.
[21] P. Singh, A.V. Smirnov, A. Alam, D.D. Johnson, First-principles prediction of incipient order in arbitrary high-entropy alloys: exemplified in Ti0.25CrFeNiAlx, Acta Mater. 189 (2020) 248–254. https://doi.org/10.1016/j.actamat.2020.02.063.
[22] P. Singh, A.V. Smirnov, D.D. Johnson, Ta-Nb-Mo-W refractory high-entropy alloys: anomalous ordering behavior and its intriguing electronic origin, Phys. Rev. Mater. 2 (2018) 055004. https://doi.org/10.1103/PhysRevMaterials.2.055004.
[23] D. Beniwal, P. Singh, S. Gupta, M.J. Kramer, D.D. Johnson, P.K. Ray, Distilling physical origins of hardness in multi-principal element alloys directly from ensemble neural network models, Npj Comput Mater 8 (2022) 1–11. https://doi.org/10.1038/s41524-022-00842-3.
[24] L. Gránásy, G.I. Tóth, J.A. Warren, F. Podmaniczky, G. Tegze, L. Rátkai, T. Pusztai, Phase-field modeling of crystal nucleation in undercooled liquids – A review, Prog. Mater Sci. 106 (2019) 100569. https://doi.org/10.1016/j.pmatsci.2019.05.002.
[25] X.J. Zuo, Y. Coutinho, S. Chatterjee, N. Moelans, Phase field simulations of FCC to BCC phase transformation in (Al)CrFeNi medium entropy alloys, Mater. Theory 6 (2022) 12. https://doi.org/10.1186/s41313-021-00034-4.